Effects of Ligand-Constraints on the Reactivity of Biomimetic Thiolate-Ligated Transition Metal Complexes

Alexandra Downing

A dissertation

submitted in partial fulfillment of the

requirements for the degree of

Doctor of Philosophy

University of Washington

2021

Reading Committee:

Julie A. Kovacs, Chair

Brandi Cossairt

Alexandra Velian

Program Authorized to Offer Degree:

Chemistry

University of Washington

Abstract

Effects of Ligand-Constraints on the Reactivity of Biomimetic

Thiolate-Ligated Transition Metal Complexes

Alexandra Downing

Chair of the Supervisory Committee:

Julie A. Kovacs

Chemistry

The addition of steric constraints to thiolate-ligated transition metal complexes was explored herein, with particular focus on the addition of a tertiary amine to the backbone to form complexes [$Fe^{II}(S_2^{Me2}N_2N^{Me}(Pr,Pr))$] and [$Co^{II}(S_2^{Me2}N_2N^{Me}(Pr,Pr))$]. The coordination environment of these complexes serves as a biomimetic model applicable to cysteinate-ligated enzymes cysteine dioxygenase (CDO), nitrile hydratase (NHase), and Isopenicillin-*N*-synthase (IPNS). The dioxygen reactivity of these complexes was investigated and multiple dioxygen derived intermediates were isolated and characterized in both the Fe and Co systems. The intermediates included a hydroxy-sulfenate -Fe^{III} species, [$Fe^{III}(S\text{-}O)S^{Me2}N_2N^{Me}(Pr,Pr))(OH)$], applicable to the

proposed CDO mechanism, which indicated the formation of an unobserved peroxythiolate species [Fe^{II}(S-OO)$S^{Me2}N_2N^{Me}$(Pr,Pr))]. Sulfur oxygenation processes are of particular interest in studying both CDO, which transforms cysteine to cysteine sulfinic acid, and NHase, which contains two oxygenated cysteines in its coordination sphere.

Two singly-oxygenated sulfenate species [Fe^{III}(η^2-S^{Me2}O)($S^{Me2}N_2N^{Me}$(Pr,Pr)]$^+$ and [Co^{III}(η^2-S^{Me2}O)($S^{Me2}N_2N^{Me}$(Pr,Pr))]$^+$ were crystallographically characterized from the addition of oxo-atom donor PhIO. The kinetics of both the dioxygen reactivity and oxo-atom donor addition were explored, and revealed a spin-state dependence for the formation of [Fe^{III}(η^2-S^{Me2}O)($S^{Me2}N_2N^{Me}$(Pr,Pr)]$^+$. In order to study the effects of steric constraints on the reactivity of thiolate-ligated transition metal complexes, the Fe/Co sterically constrained complexes and products were compared to their predecessor analogues that contained a secondary amine in the coordination sphere.

To further explore and isolate the effect of the thiolate in the inner coordination sphere, DFT calculations of a thiolate-ligated Mn-alkylperoxo species and an alkoxide-ligated Mn-alkylperoxo species were carried out. The alkoxide-ligated RO-Mn^{III}-OOR complex was an order of magnitude more stable than its thiolate-ligated RS-Mn^{III}-OOR derivative. The highest occupied molecular orbital of the thiolate-ligated derivative possesses significant sulfur character and π-backdonation from the thiolate competes with π-backdonation from the peroxo π^*(O–O). DFT-calculated Mulliken charges show that the Mn ion Lewis acidity of alkoxide-ligated RO-Mn^{III}-OOR (+0.451) is greater than that of thiolate-ligated RS-Mn^{III}-OOR (+0.306), thereby facilitating π-backdonation from the antibonding peroxo π^*(O–O) orbital and increasing its stability. This helps

to explain why the photosynthetic oxygen-evolving Mn complex, which catalyzes O−O bond formation as opposed to cleavage, incorporates O- and/or N-ligands as opposed to ^{cys}S-ligands.

Dedication

For my grandmothers:

Laverne Downing

&

Josie Hill

Acknowledgements

First and foremost I am grateful to my advisor, Professor Julie Kovacs for her invaluable advice, continuous encouragement, and patience during my PhD study. The opportunity to work in her group with access to her immense knowledge and plentiful experience in transition metal thiolate chemistry and beyond has been a pleasure. I would also like to thank the senior group members, Dr. Ben Leipzig, Dr. Maike Blakely, and Dr. Penny Poon who served as valuable scientific sounding boards throughout my research. I would especially like to thank Dr. Penny Poon for all of the editing work that went into creating the following dissertation. The rest of the current Kovacs group members; Dylan Rogers, Maria Greiner, Bennet Karel, Paige Gannon, Douglas Baumgardner, Chris Lowe, and Chris Woodburn, have been a valuable source of support through practice talks, lab equipment emergencies, and discovering new results.

The scientific community of the University of Washington as a whole, and the Inorganic Chemistry division have offered key opportunities to further my research. In particular, I would like to thank my reading committee members, Professors Brandi Cossairt and Alexandra Velian, who also graciously served on all of my exam committees. I would also like to thank Professors Stefan Stoll, Gerald Seidler, and AJ Boydston for serving on exam committees throughout my PhD. The scientific discussion from division meetings and exams improved the quality of my scientific work.

Finally, I would like to express my gratitude to my family for their continuous support in my working towards this goal. My parents, Micah and Lisa, my sister, Gabrielle, my mother-in-law, Sharon, and my sister-in-law, Crystal, have all been supporting and understanding from a distance throughout the challenges of the past 5 years. Without the tremendous support and encouragement of my husband, Brandon, over the past few years, it would have been impossible for me to complete my study.

Contents

Glossary

Å	Ångström
ACV	l-valine, l-cysteine, and l-α-aminoadipic acid
$^{Asp}O^-$	aspartic acid
ATR	attenuated total reflection
BDFE	bond dissociation free energy
CDO	cysteine dioxygenase
CT	charge transfer
CV	cyclic voltammetry
$^{Cys}S^-$	cysteine
DCM	dichloromethane
DFT	density functional theory
EAS	electron absorbance spectroscopy
EPR	electron paramagnetic resonance
ESI-MS	electrospray-ionization mass spectroscopy
Et_2O	diethyl ether
EtOH	ethanol
FT	Fourier transform
H_2O_2	hydrogen peroxide
HAT	hydrogen atom transfer
^{His}N	histidine
HOMO	highest occupied molecular orbital
HS	high-spin
Hz	Hertz
IBX-ester	iodoxybenzoate
IPNS	isopenicillin-N-synthase
KO_2	potassium superoxide

LS	low-spin
LUMO	lowest occupied molecular orbital
^{m}CPBA	meta-chloroperoxybenzoic acid
MeCN	acetonitrile
MeOH	methanol
MnLO	managanese lipoxygenase
MnSOD	superoxide dismutase
N_3^-	azide anion
NHase	nitrile hydratase
NMR	nuclear magnetic resonance
NTO	natural transition orbital
$O^{\bullet}$	oxyl radical
$O_2^{\bullet -}$	superoxide anion
OAD	oxo-atom donor
PDB	protein data bank
PFIB	pentafluoroiodosylbenzene
PhI	iodobenzene
PhIO	iodosylbenzene
$PhIO_2$	iodoxybenzene
PNO	pyridine-N-oxide
ppm	parts per million
ROS	reactive oxygen species
rRaman	resonance Raman
SCE	saturated calomel electrode
SCO	spin crossover
$t_{1/2}$	half-life
TD-DFT	time-dependent density functional theory
TEA	triethylamine

TEMPOH	1-hydroxy-2,2,6,6-tetramethyl-piperidine
THF	tetrahydrofuran
UV-Vis	UV-visible
XAS	X-ray absorption spectroscopy
$\Delta H^{\ddagger}$	enthalpy of activation
$\Delta S^{\ddagger}$	entropy of activation
μ_{eff}	magnetic moment
σ^2_{oct}	variance in the octahedral angles
τ	five-coordinate geometry index
$\chi_{(T)}$	magnetic susceptibility

List of Numbered Complexes

Numbered Complexes for Chapter 1

1	$[Fe^{II}(S_2{}^{Me2}N_2N^{H}(Pr,Pr))]$
1-O₂	$[Fe^{III}(S_2{}^{Me2}N_2N^{H}(Pr,Pr))(O_2)]$
1-OOH	$[Fe^{III}(S_2{}^{Me2}N_2N^{H}(Pr,Pr))(OOH)]$
1-O	$[Fe^{III}(\eta^2\text{-}S^{Me2}O)(S^{Me2})N_2N^{H}(Pr,Pr)]^+$
1^{ox}	$[Fe^{III}(S_2{}^{Me2}N_2N^{H}(Pr,Pr))]^+$
2	$[Fe^{II}(S_2{}^{H2}N_2N^{H}(Pr,Pr))]$
3	$[Fe^{III}(ADIT)_2]^+$
3-O	$[Fe^{III}(ADIT)(ADIT\text{-}O)]^+$
4	$[Co^{III}(ADIT)_2]^+$
5	$[Co^{III}(S_2{}^{Me2}N_2N^{H}(Pr,Pr))]^+$
6	$[Co^{III}(S^{Me2}O_2)(S^{Me2})N_2N^{H}(Pr,Pr))]^+$
7	$[Co^{III}(S^{Me2}O_2)(\eta^2\text{-}S^{Me2}O)N_2N^{H}(Pr,Pr))]^+$

Numbered Complexes for Chapter 2

1	$[Fe^{II}(S_2{}^{Me2}N_2N^{H}(Pr,Pr))]$
1-O₂	$[Fe^{III}(S_2{}^{Me2}N_2N^{H}(Pr,Pr))(O_2)]$
1-OOH	$[Fe^{III}(S_2{}^{Me2}N_2N^{H}(Pr,Pr))(OOH)]$
1^{ox}	$[Fe^{III}(S_2{}^{Me2}N_2N^{H}(Pr,Pr))]^+$
2	$[Fe^{III}(\eta^2\text{-}S^{Me2}O)(S^{Me2})N_2N^{H}(Pr,Pr)]^+$
3	$[Fe^{II}(S_2{}^{Me2}N_2N^{Me}(Pr,Pr))]$
3^{ox}	$[Fe^{III}(S_2{}^{Me2}N_2N^{Me}(Pr,Pr))]^+$
3-O₂	$[Fe^{III}(S_2{}^{Me2}N_2N^{Me}(Pr,Pr))(O_2)]$
3-OOH	$[Fe^{III}(S_2{}^{Me2}N_2N^{Me}(Pr,Pr))(OOH)]$
3-OH	$[Fe^{III}(S_2{}^{Me2}N_2N^{Me}(Pr,Pr))(OH)]$

4 $[Fe^{II}(S_2{}^{H2}N_2N^{H}(Pr,Pr))]$

5 $[Fe^{II}(S_2{}^{H2}N_2N^{Me}(Pr,Pr))]$

6 $[Fe^{II}(S_2{}^{Me2}N_2N^{H}(Et,Pr))]$

7 $[Fe^{III}(\eta^2\text{-}S^{Me2}O)(S^{Me2}N_2N^{Me}(Pr,Pr)]^{+}$

8 $[Fe^{IV}(S_2{}^{Me2}N_2N^{Me}(Pr,Pr))(O)]$

9 $[Fe^{II}(S\text{-}OO)S^{Me2}N_2N^{Me}(Pr,Pr))]$

10 $[Fe^{IV}(S\text{-}O)S^{Me2}N_2N^{Me}(Pr,Pr))(O)]$

11 $[Fe^{III}(S\text{-}O)S^{Me2}N_2N^{Me}(Pr,Pr))(OH)]$

12 $[Zn^{II}(S_2{}^{Me2}N_2N^{Me}(Pr,Pr))]$

Numbered Complexes for Chapter 3

1 $[Fe^{III}(S_2{}^{Me2}N_2N^{H}(Pr,Pr))](PF_6)$

1-PNO $[Fe^{III}(S_2{}^{Me2}N_2N^{H}(Pr,Pr))(PNO)](PF_6)$

1-IBX-ester $[Fe^{III}(S_2{}^{Me2}N_2N^{H}(Pr,Pr))(IBX\text{-}ester)](PF_6)$

1-PFIB $[Fe^{III}(S_2{}^{Me2}N_2N^{H}(Pr,Pr))(PFIB)](PF_6)$

2 $[Fe^{III}(\eta^2\text{-}S^{Me2}O)(S^{Me2}N_2N^{H})(Pr,Pr))](PF_6)$

3 $[Fe^{III}(S_2{}^{Me2}N_2N^{H}(Pr,Pr))(N_3)]$

4 $[Fe^{V}(O)(S_2{}^{Me2}N_2N^{H}(Pr,Pr))](PF_6)$

5 $[Fe^{III}(S_2{}^{Me2}N_2N^{Me}(Pr,Pr))](PF_6)$

5-IBX-ester $[Fe^{III}(S_2{}^{Me2}N_2N^{Me}(Pr,Pr))(IBX\text{-}ester)](PF_6)$

5-PhIO $[Fe^{III}(S_2{}^{Me2}N_2N^{Me}(Pr,Pr))(PhIO)](PF_6)$

6 $[Fe^{III}((\eta^2\text{-}S^{Me2}O)S^{Me2}N_2N^{Me}(Pr,Pr))](PF_6)$

7 $[Fe^{V}(O)(S_2{}^{Me2}N_2N^{Me}(Pr,Pr))](PF_6)$

8 $[Fe^{III}(S_2{}^{Me2}N_2N^{Me}(Pr,Pr)(N_3)]$

Numbered Complexes for Chapter 4

1 $[Co^{III}(S_2{}^{Me2}N_2N^{H}(Pr,Pr))]^+$

2 $[Co^{III}(S^{Me2}(S^{O2})N_2N^{H}(Pr,Pr))]^+$

3 $[Co^{III}((\eta^2\text{-}S^{Me2}O)(S^{O2})N_2N^{H}(Pr,Pr))]^+$

4 $[Co^{II}(S_2{}^{Me2}N_2N^{Me}(Pr,Pr))]$

4^{ox} $[Co^{III}(S_2{}^{Me2}N_2N^{Me}(Pr,Pr))]^+$

5 $[Co^{II}(S_2{}^{Me2}N_2N^{H}(Et,Pr))]$

5^{ox} $[Co^{III}(S^{Me2}\ N_2N^{H}(Et,Pr)(\eta^2\text{-}S_2)](PF_6)$

6 $[Co^{II}(S_2{}^{\beta H2}N_2N^{H}(Pr,Pr))]$

7 $[Co^{II}(S_2{}^{Me2}N_2N^{H}(Pr,Pr))]$

8 $[Co^{III}(S^{Me2}N_2N^{Me}(Pr,Pr)(TK))]^+$

9 $[Co^{III}(\eta^2\text{-}S^{Me2}O)(S^{Me2}N_2N^{Me}(Pr,Pr))]^+$

10 $[Co^{III}((\eta^2\text{-}S^{Me2}O)(S^{O2})N_2N^{Me}(Pr,Pr))]^+$

Numbered Complexes for Chapter 5

1 $[Mn^{III}(O^{Me2}N_4(6\text{-Me-DPEN})(OO^{t}Bu))^+$

2 $[Mn^{III}(S^{Me2}N_4(6\text{-Me-DPEN})(OO^{t}Bu))^+$

3 $[Mn^{II}(S^{Me2}N_4(6\text{-Me-DPEN}))]^+$

4 $[Mn^{II}(S^{Me2}N_4(6\text{-MeDPPN}))]^+$

5 $[Mn^{III}(S^{Me2}N_4(6\text{-Me-DPPN})(OO^{t}Bu))^+$

6 $[Mn^{II}(O^{Me2}N_4(6\text{-Me-DPPN}))]^+$

7 $[Mn^{II}(HO^{Me2}N_4(6\text{-Me-DPEN})(MeCN))]^{2+}$

8 $[Mn^{II}(HO^{Me2}N_4(6\text{-Me-DPEN})(CHO_2))]^+$

9 $[Mn^{III}(dpaq^{2Me})(OO^{t}Bu)]^+$

10 $[Mn^{III}(S^{Me2}N_4(quinoEN))(OO^{t}Bu)]^+$

11 $[Mn^{III}(S^{Me2N}{}_4(quinoPN))(OO^{t}Bu)]^+$

List of Figures

Chapter 1 Figures

Chapter 2 Figures

Chapter 3 Figures

Chapter 4 Figures

Chapter 5 Figures

List of Schemes

Chapter 1 Schemes

Chapter 2 Schemes

Chapter 3 Schemes

List of Tables

Chapter 2 Tables

Chapter 3 Tables

Chapter 4 Tables

Chapter 5 Tables

Chapter 1: Biomimetic Models of Transition Metal Metalloenzymes and Investigations of Dioxygen Reactivity

1.1 Overview of Metalloenzyme Reactivity

Nature carries out varied, rich chemical processes by utilizing metalloenzymes. First row transition metals such as manganese, iron, cobalt, nickel, copper and zinc are often employed by nature to facilitate key natural processes.[1,2] The metal co-factors are able to facilitate a multitude of chemical transformations. The selectivity and sensitivity for substrates and products is controlled in part by the unique set of ligating residues, which form the coordination environments around different transition metal ions.[2] The common binding motif can be highly conserved, within an enzyme family, even as the metal ion changes, as in the case of nitrile hydratases (NHase).[3,4] The chemical processes of enzymes and their biomimetic models include thermodynamically challenging processes such as dioxygen activation,[5,6] C—H bond activation,[7] green chemical transformations,[8] and signal transduction pathways.[9,10] Naturally found enzymatic systems have been studied in the native enzyme, and through the development of small-molecule biomimetic models. The study of these demonstrated natural processes can be applied towards the improvement of green chemical synthesis,[8] as well as to the development of health insights and the identification of potential therapeutic targets.[9]

The structural environments of metalloenzymes are directly related to their specific chemical functions. Across metalloenzymes, there are two broad categories of structural distinctions, heme and non-heme environments. Heme-Fe and corrin-Co environments (***Figure 1.1***) provide a rigid coordination plane, over which electron density can be delocalized.[11] Both structures

illustrated in ***Figure 1.1***, show the metal ion is ligated with four N ligands in the plane,[12] leaving a *trans* binding site open for various substrates to interact with the metal ion. The redox non-innocence of the heme and corrinoid systems can be key to their reactivity, such as in the case of cytochrome P450.[11] The other broad class of structural distinction is labeled as non-heme or non-corrinoid systems, which have a more flexible environment around the metal ion (***Figure 1.2***).[13,14] Common coordinating residues include, histidine (^{His}N), and aspartic acid ($^{Asp}O^-$), often in a 2-His-1-carbolxylate facial triad pocket as well as cysteine ($^{Cys}S^-$).[14–16] A brief discussion of enzymes from these different classes will be described below to highlight the rich chemical processes carried out by metalloenzymes, especially as they relate to the activation and utilization of dioxygen as an oxidant. In addition, the advantages of biomimetic models, which seek to recreate a small molecule transition metal complex that mimic enzymatic active sites in structure and/or function will be discussed. Examples of key biomimetic complexes and their reactivity will be highlighted as well. The rest of the dissertation focuses on biomimetic models for enzymes that contain either thiolate-ligated Fe- (**Chapter 2- 3**) or Co-cofactors (**Chapter 4**) in non-heme or non-corrinoid environments.

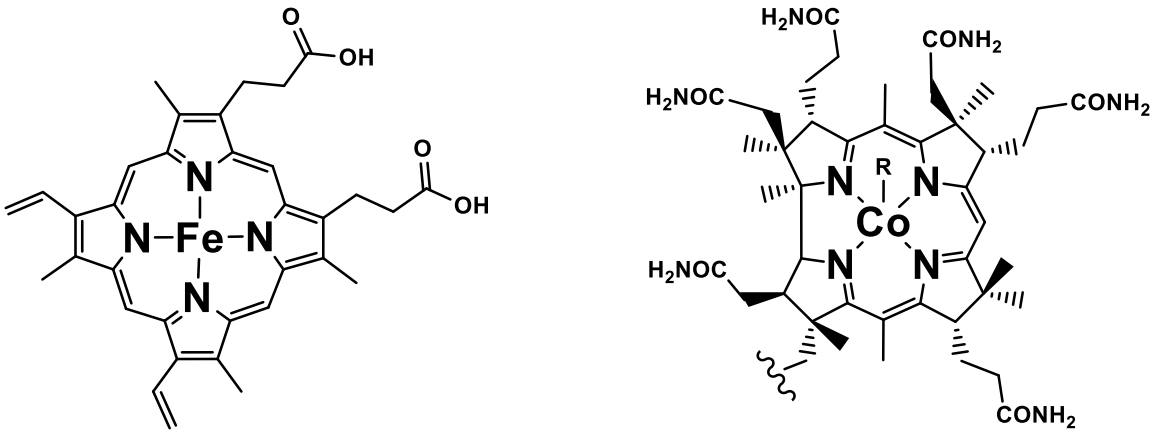

Figure 1.1 ChemDraw structures for a heme-Fe site from hemoglobin (left)[17] and a corrin-Co site from cobalamin (right)[18].

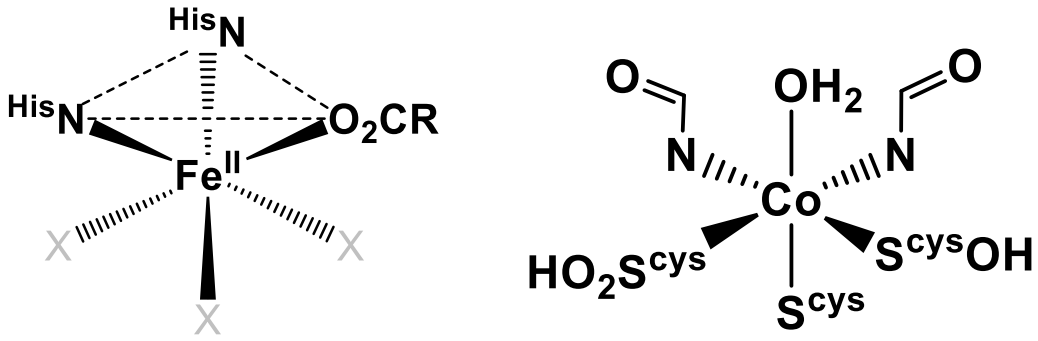

Figure 1.2 ChemDraw structures for non-heme Fe^{II} with the 2-His-1-carboxylate facial triad[16] (left) and non-corrinoid Co^{III} ion site of NHase family, with post-translationally modified cysteinate ligands[19] (right).

1.1.1 Introduction to Mechanisms of Dioxygen Activation

Dioxygen activation has been observed in enzymes containing either a monomeric Fe^{II} center, or a dimeric Fe center.[14,19–22] However, the enzymes and biomimetic models of focus here are proposed to follow the single Fe^{II} metal cofactor pathways. A general scheme for the activation of dioxygen by a single Fe^{II} center is outlined in **Scheme 1.1**.[23] In order to activate dioxygen, the Fe^{II} center first binds the dioxygen molecule and undergoes a one electron oxidation to form an Fe^{III}-superoxo (Fe^{III}-$O_2^{\bullet}$). The transition of dioxygen to superoxo is a spin-forbidden process and

therein requires the presence of the metal cofactor to efficiently transfer the electron.[24] With an available H-atom, the Fe^{III}-superoxo is then proposed to perform an H-atom abstraction (HAT) from a substrate to form an Fe^{III}-hydroperoxo (Fe^{III}-OOH), further weakening and thus activating the O—O bond. The O—O bond can then undergo either homolytic or heterolytic cleavage to form a high-valent Fe^{IV}- or Fe^{V}-oxo, respectively. $Fe^{IV/V}$-oxo species have been shown to be competent oxidants.[25,26] The $Fe^{IV/V}$-oxo species can perform another HAT (intermolecular) to form a Fe^{III}-hydroxide, or, in the presence of a thiolate ligand, the $Fe^{IV/V}$-oxo could be trapped by an interaction with the thiolate (intramolecular) to form an oxygenated sulfur species.[27] The structural differences of the metal active sites can have large effects on which specific steps of the dioxygen activation pathway are followed.

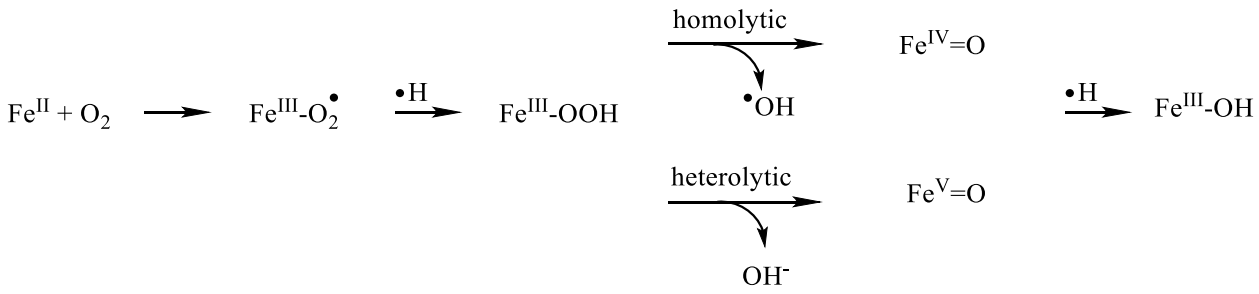

Scheme 1.1 General scheme for dioxygen activation by a monomeric Fe^{II} active site.

1.1.2 Heme-Iron Enzymes

Cytochrome P450s are a superfamily of enzymes that utilize a heme-Fe cofactor to function as monooxygenases.[12] The enzyme participates in oxidative metabolism as protection against reactive oxygen species (ROS), such as superoxide ($O_2^{\bullet-}$), hydrogen peroxide (H_2O_2) , and oxyl ($O^{\bullet}$) radicals, as these ROS are generated during oxidation-reduction processes involving the utilization of dioxygen by aerobic life.[11] The first-sphere coordination environment of the Fe

cofactor includes a thiolate arm *trans* to the active site in addition to the 4 N-heme coordination motif.[12] The mechanistic investigation of cytochrome P450 by Green and coworkers resulted in the identification of key dioxygen derived oxidants, Compound 0 (Fe^{III}-hydroperoxo),[28] Compound I (Fe^{IV}-oxo),[28] and Compound II (Fe^{IV}-hydroxo)[29] (**Scheme 1.2**). The study and utilization of the cytochrome P450 architecture has also expanded with the Nobel prize winning work of Arnold and coworkers in the use of directed evolution.[7,30,31] These cytochrome P450-like catalysts do specific chemical reactions that demonstrate the power of enzymatic systems carrying out selective and high turnover chemical transformations.

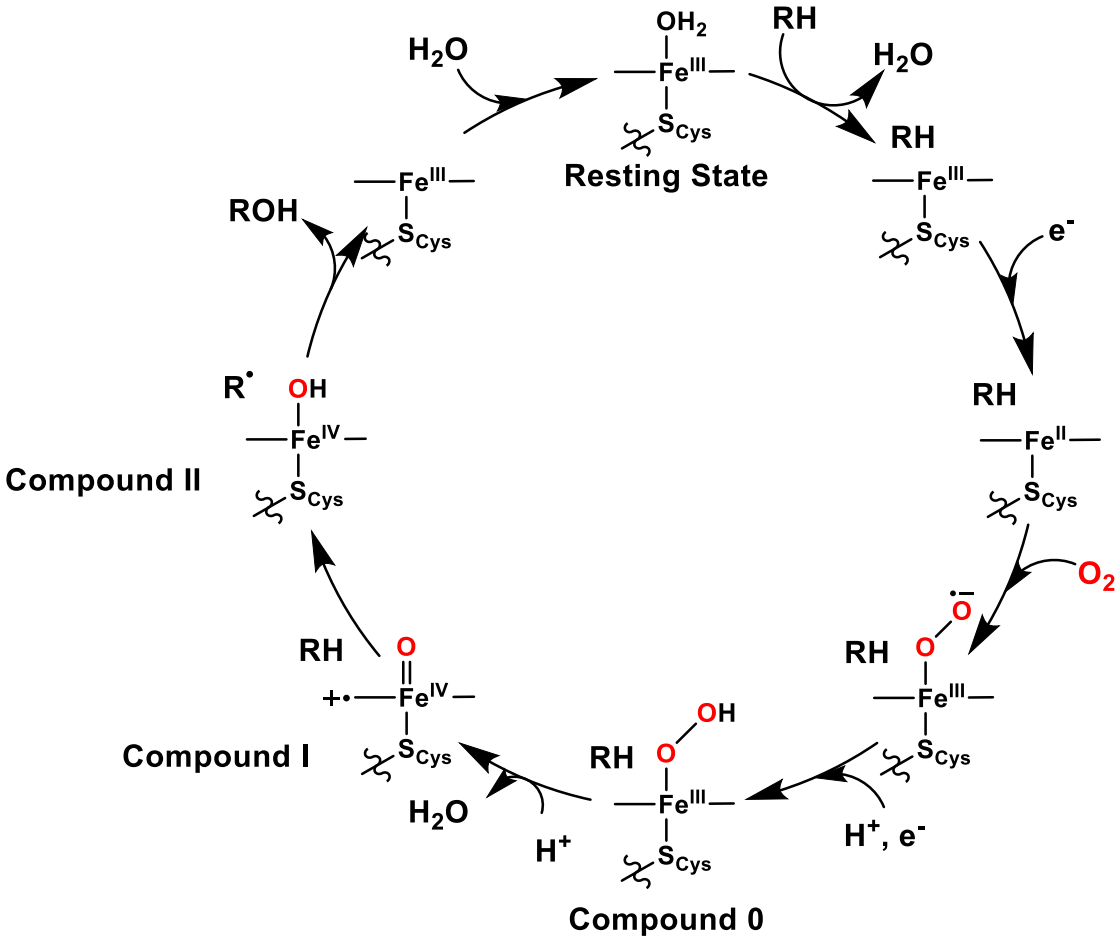

Scheme 1.2 Reaction cycle of dioxygen activation by cytochrome P450, highlighting the structures of the key dioxygen derived species, Compounds 0, I, and II.[12,28,29]

1.1.3 Corrinoid-Cobalt Enzymes

The ligation environment of cobalamin or vitamin B12, a corrinoid Co complex often found as an enzyme cofactor, is illustrated in ***Figure 1.1***.[18] The planar 4-N ligation of the cobalt ion is similar to the heme-Fe coordination environment. Corrinoid-dependent methyltransferases are found in all three kingdoms of life.[18] Methionine synthase is the only one found in humans. The ligand architecture of the cobalt cofactor binding site (***Figure 1.1***) must stabilize a Co^{I} state and allow for conformational rearrangements, which are involved in the complicated reaction cycle.[18] The enzyme transforms the substrate L-homocysteine to the essential amino acid, L-methionine as shown in **Scheme 1.3.**

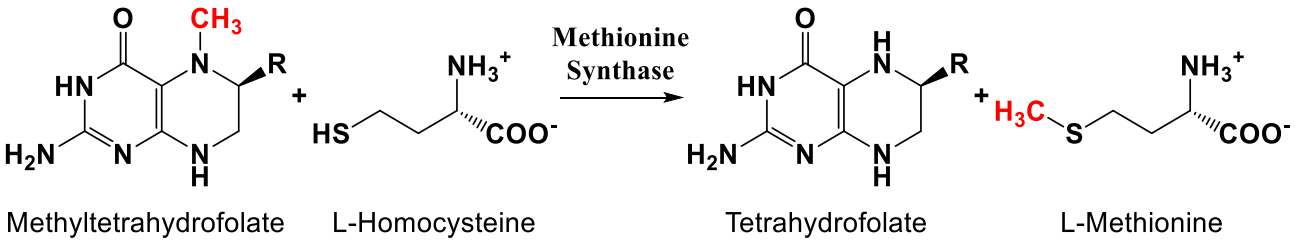

Scheme 1.3 Chemical transformation carried out by methionine synthase utilizing cobalamin (Vitamin B12).

1.1.4 Non-Heme Iron Enzymes

Nature utilizes many non-heme Fe cofactors as key mediators of thermodynamically challenging chemical processes.[15] A key residue pattern that appears frequently includes the 2-histidine-1 carboxylate facial triad family of non-heme Fe^{II} enzymes (***Figure 1.2***). The open face of the coordination sphere allows for the binding of dioxygen to take place and then the specificity/selectivity of the reactivity diverges based on the various flexible arrangements the substrate binding pockets provide.[15] This class of enzymes includes extradiol catecholic

dioxygenases, Rieske *cis*-diol-forming dioxygenases, dioxygenases that utilize a 2-oxo acid as a co-substrate, tetrahydropterin-containing oxygenases, and oxidase enzymes among many others. All of the enzymes promote specific chemical transformations that utilize the oxidative power of activated dioxygen (***Figure 1.3***).

Specifically, there are non-heme enzymes that incorporate a thiolate (usually a cysteinate or post-translationally modified cysteinate) in the coordination sphere of the Fe^{II} similar to cytochrome P450. Non-heme enzymes also utilize dioxygen as the oxidant for their chemical processes.[14,20,32,33] Enzymes of particular interest to the following dissertation include iso-penicillin-N-synthase (IPNS), cysteine dioxygenase (CDO), and nitrile hydratase (NHase). The similarities and differences between the two structural classes of non-heme and heme enzymes make it important to understand the basic functions and structures of each, as the biomimetic models can be relevant to both systems, especially when they incorporate thiolate ligands. The majority of this dissertation will focus on biomimetic modeling to elucidate mechanistic details and comparisons to these three thiolate-ligated non-heme (non-corrinoid) enzymes (**Chapters 2-4**). The specific details of the structure and function of the non-heme and non-corrinoid enzymes, as well as proposed mechanisms will be outlined in the following sections.

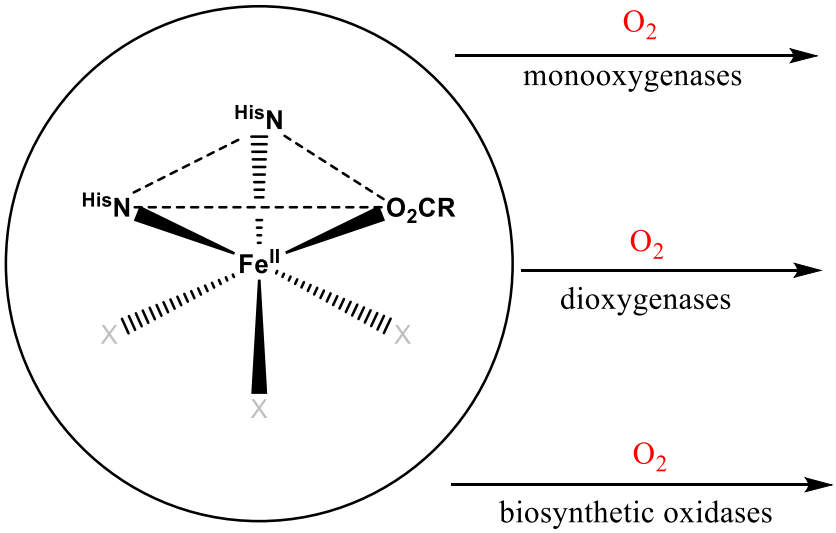

Figure 1.3 General reactivity functions of non-heme enzymes.

1.1.4.1 Iso-penicillin- N-Synthase

Iso-penicillin-N-Synthase (IPNS) is involved in the synthesis of antibiotic precursor iso-penicillin-N.[34] Amidst the growing crisis of antibiotic resistance, a greater understanding of the mechanism for the synthesis of key antibiotic precursors is necessary to ensure a the advancement of novel antibiotic compounds.[35–37] The reaction mechanism was observed with X-ray crystallography by Baldwin and coworkers and shown to demonstrate a two-step ring closure promoted upon the exposure of the Fe center to dioxygen.[38] The current proposed mechanism begins with an Fe^{II} resting state, which is proposed to activate dioxygen to form an Fe^{III}-superoxo intermediate.[20] The Fe^{III}-superoxo is proposed to abstract the β-hydrogen atom, resulting in one of the ring closures of the tripeptide substrate, l-valine, l-cysteine, and l-α-aminoadipic acid (ACV) (**Scheme 1.4**). A high-valent Fe^{IV}-oxo species is proposed to be the second oxidative species in the reaction pathway. The Bollinger and Krebs groups were able to elucidate more of this active species by deuterating the protein environment around the Fe site.[20] An electronic absorbance

spectrum was obtained with stopped-flow absorbance experiments for the superoxo species by the Bollinger group with λ_{max} = 630 nm.[20] Our group had previously characterized an Fe^{III}-superoxo species in a small molecule model, which was antiferromagnetically coupled to form a diamagnetic species, that demonstrated a similar electronic absorbance spectrum with λ_{max} = 409, 520, 707 nm.[27] While high-valent Fe-oxo species have been demonstrated as strong oxidants, examples of Fe^{III}-superoxo species, demonstrating C—H bond activation reactivity are rare.[27,39–42] The demonstration of the biomimetic Fe^{III}-superoxo completing the HAT to form an Fe^{III}-hydroperoxo species[27] was an important step to supporting the proposed HAT mechanism for IPNS and other enzymes. The information provided by the model complex was a strong demonstration of the utility of biomimetic modeling.

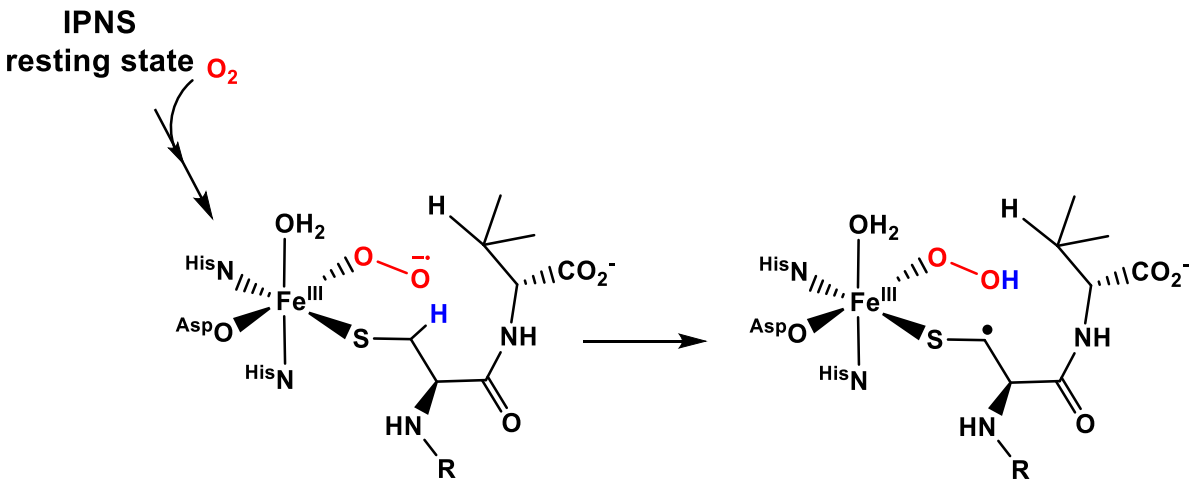

Scheme 1.4 Proposed HAT step from the β-hydrogen (blue) accomplished by the IPNS-dioxygen derived Fe^{III}-superoxo species (C-$^{\beta}$**H** BDFE = 96 kcal, mol^{-1}).

1.1.4.2 Cysteine Dioxygenase

Another non-heme Fe enzyme, cysteine dioxygenase (CDO), catalyzes the oxidation of cysteinate (RS^-) to cysteine sulfinic acid ($RS(O)_2^-$).[32,43–49] High levels of cysteine in the body have been implicated in the development of neurological disorders, such as Alzheimer's, and Parkinson's diseases,[47,49] as well as the metastases of cancerous tumors.[50] The cysteine sulfinic acid is also a key molecule for the cell signal transduction pathways.[51]

The catalytically active Fe^{II} site is ligated by three histidine residues and a water molecule.[47,52] The mechanism of CDO-promoted cysteine oxidation is not yet fully understood. One proposed mechanism is illustrated below (**Scheme 1.5**), based on theoretical calculations by deVisser and coworkers[32] as well as theoretical studies of Fe-centered model complexes.[43,47] First, the free cysteine substrate must bind to the Fe^{II} ion in the active site of CDO, to form the resting state. With the binding of cysteine to the Fe^{II}-center, the nephelauxetic effect due to the sulfur further lowers the energy barrier for the binding of dioxygen *cis* to the cysteine. The Fe^{II} is oxidized by the dioxygen to form an Fe^{III}-superoxo intermediate. The superoxo intermediate is followed by the reduction of the Fe ion and the formation of a unique, unobserved bicyclic intermediate, an Fe^{II}-peroxythiolate species. The O—O bond is likely to heterolytically cleave to form a high-valent Fe^{IV}-oxo species with one singly oxygenated sulfenate, ($^{Cys}RSO^-$). A controlled oxo-atom addition by the high valent oxo would add a second oxygen to the sulfenate creating the cysteine-sulfinic acid bound to the Fe^{II} center.

Spectroscopic observation of the proposed intermediates has proven to be difficult in the enzyme environment due to the temperature and solvent limitations of enzymatic systems.

Through transient absorbance experiments, one intermediate (λ_{max} ~ 500, 650 nm) was observed in CDO,[21] and assigned as either the Fe^{III}-superoxo species or the Fe^{II}-peroxythiolate cyclic intermediate. The TD-DFT calculated spectra and experimental electronic absorption spectra of rare Fe^{III}-superoxo species, $[Fe^{III}(S_2{}^{Me2}N_2N^H(Pr,Pr))(O_2)]$[27] (**1-O₂**), were found to be similar to that of the observed intermediate in CDO supporting the assignment of the transient species to the Fe^{III}-superoxo. Neither of the other proposed intermediates (the high-valent Fe^{IV}-oxo with sulfenate or the Fe^{II}-peroxythiolate) have been spectroscopically observed in the native enzyme. **Chapter 2** of this dissertation will discuss new results in the characterization of dioxygen derived intermediates relevant to CDO.

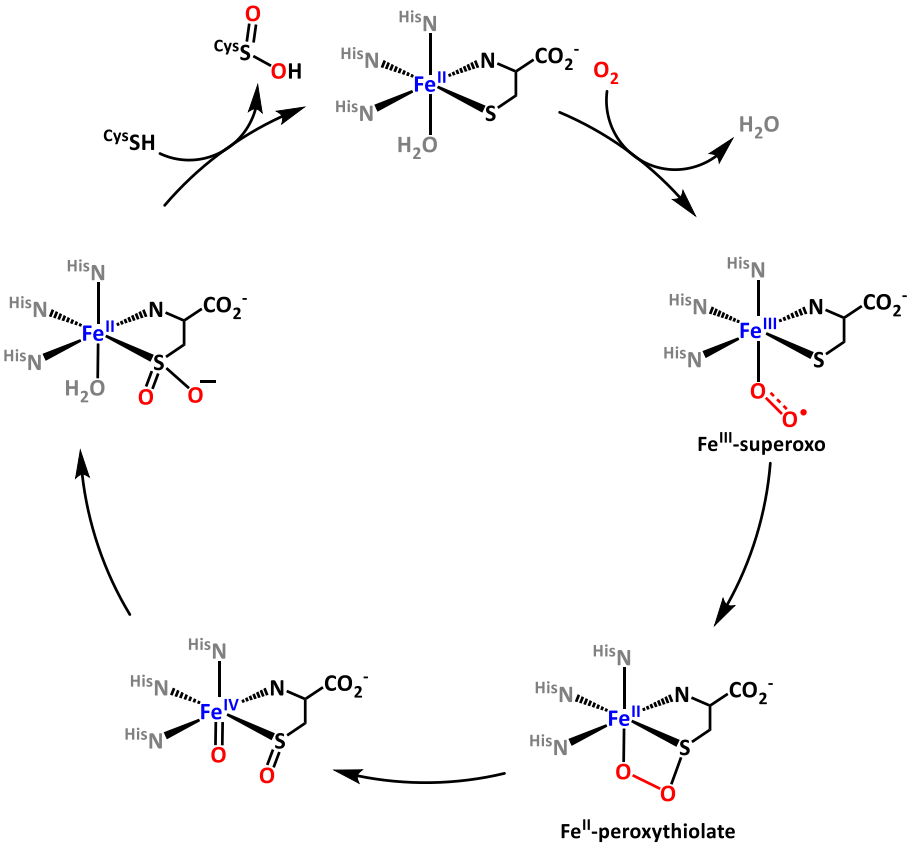

Scheme 1.5 Proposed mechanism for cysteine dioxygenase (CDO).

1.1.5 Non-Corrinoid Cobalt Systems

1.1.5.1 Nitrile Hydratase

Nitrile hydratases (NHase) are non-heme Fe^{III}-containing, or non-corrinoid Co^{III}-containing, enzymes, which catalyze stereoselective, hydration of nitriles to amides[53] and are widely used in industry;[54–59] they are also responsible for decontamination or bioremediation of nitrile polluted sites.[60,61] The industrial process is utilized in the production of plastic precursor molecules that originate from monomers, such as acrylamide, demonstrating the green applications of enzymes.[54–57] The Fe- and Co-versions of the enzyme differ in the selected substrates, where in general, the Fe derivatives will catalyze the transformation of alkyl-nitriles and Co derivatives are selective for aromatic-nitrile substrates.[14]

The coordination environment of the Co or Fe ion is highly conserved[4] and includes two post-translationally modified cysteinates.[62] Structural characterization of Co-NHase using X-ray crystallography, shows that the active site consists of a six coordinate low-spin $S = 0$ Co^{III} ion[63–66] ligated by three cysteinates, two of which have been oxidized, one to a singly oxygenated sulfenic acid ($^{Cys}S—OH$)[33,67–69] and the other to a sulfinate ($^{Cys}S(O)_2^-$).[70] In addition, the Co^{III} ion is ligated by two amide nitrogens, and a water molecule, (***Figure 1.2***, *right*).[71] The low-spin Co^{III} environment increases metal ion Lewis acidity, relative to high-spin Co^{III}, and this facilitates the binding of nitrile substrate to the metal ion.[22] The process of sulfur oxygenation in these enzymes is also not well understood, although a recent study involving EPR spectroscopy and mass spectrometry of an Fe peptide has shed some light on the maturation process of sequential oxidations.[62]

The proposed mechanism for NHase implicates the ^{Cys}S—OH moiety (**Scheme 1.6 B**) in the formation of a unique, unobserved intermediate containing a five-membered ring (**Scheme 1.6 C**), through nucleophilic attack of the ^{Cys}S—OH at the carbon of the bound nitrile substrate.[33] NHase is inactivated when an additional oxygen atom is added to the ^{Cys}S—OH, implying that the ^{Cys}S—OH plays a key role in the mechanism.[72] Examples of singly oxygenated thiolate-ligated transition metal complexes, and in particular, examples that incorporate cobalt as the central metal ion are rare.[73–77] Once the five-membered ring intermediate **B** is formed, water is proposed to interact with either the nitrile-carbon or the sulfur, forming either intermediate species preceding the formation of the metal-bound amide product (**Scheme 1.6 D**). The final step is the release of the fully formed amide product from the Fe^{III} or Co^{III} ion to reform the resting state **A**.

Enzymatic studies have shown the binding of isobutyronitrile to the active site,[33] but the other intermediates have not been fully characterized or observed. In alkoxide thiolate ligated model complexes, Co^{III}-amidate and Co^{III}-iminol intermediates derived from MeCN were observed.[78] The sulfenic acid species is also of great interest to study within a biomimetic model complex and spectroscopically characterized Fe-sulfenate[79,80] and Co-sulfenate[73,74] species are also rare.

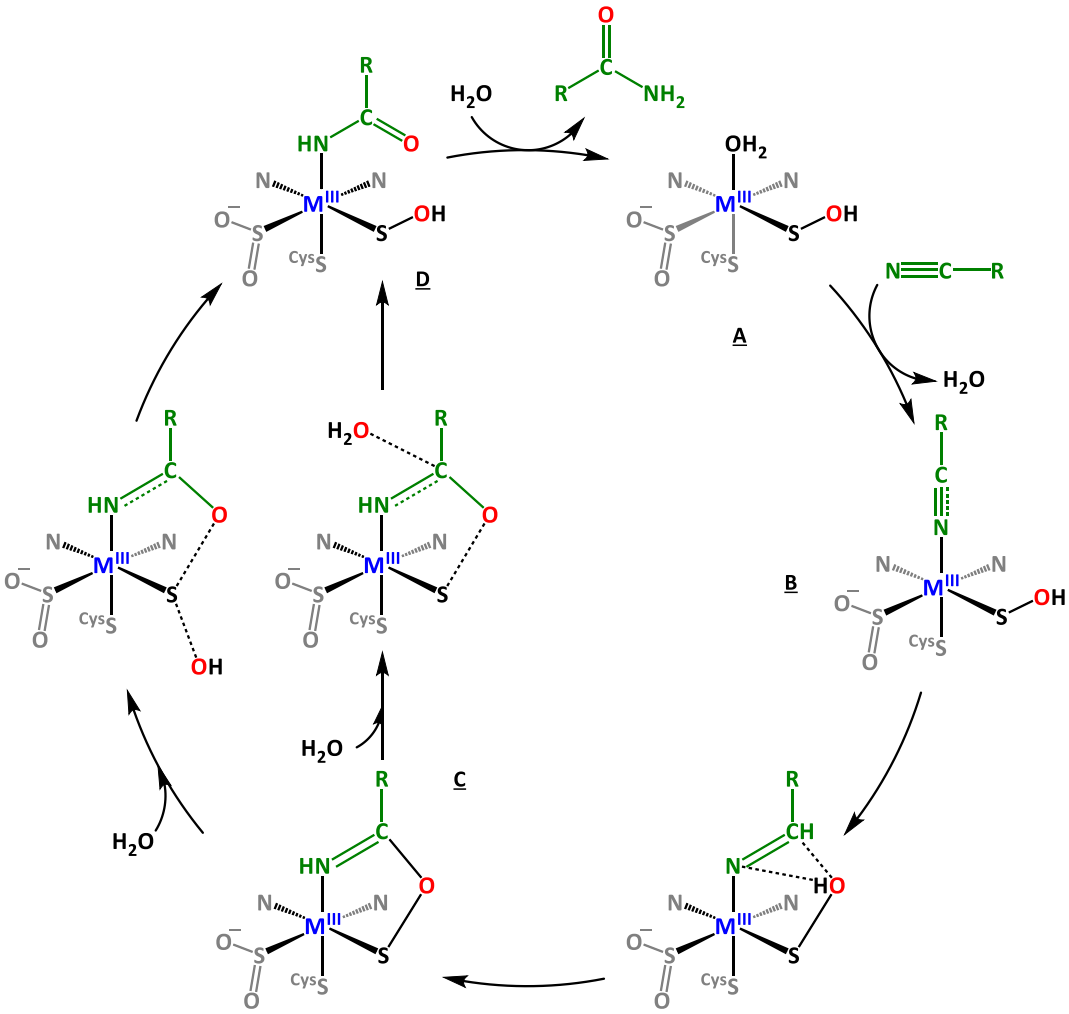

Scheme 1.6 Proposed mechanism of NHase (M = Fe or Co).

1.1.5.2 Bleomycin

Another biologically relevant application of non-corrinoid Co complexes include the anti-tumor drug Co-bleomycin (***Figure 1.4***),[81] which is able to cleave chemical bonds in DNA.[82–84] Bleomycin has been studied with various metal ions widely chelated as a class of complexes capable of cleaving DNA to treat various cancers. The metal-chelated bleomycin will activate O_2 to form reactive oxygen species that become cytotoxic to cells. A crystal structure of DNA-bound Co bleomycin highlights the ligand coordinating in a conformation favorable for an H atom

abstraction to take place.[84] Further investigation of Co-complex dioxygen reactivity in non-heme systems will broaden the understanding of these ROS that are stabilized by the cobalt ion due to the limitations of the oxo-wall.[85] In order for a cobalt ion to form a high valent oxo species, similar to iron, an electron would have to be held in an antibonding orbital, therein reducing the bond order of the metal-oxo species and destabilizing the electronic arrangement.

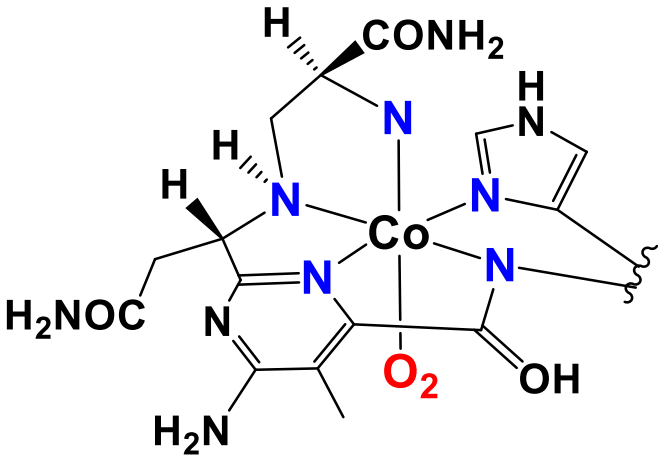

Figure 1.4 ChemDraw structure of metal ion binding site of bleomycin.

1.1.6 Manganese Enzymes

Manganese ions are readily available in Nature as one of the most abundant transition row elements available from the Earth's crust and Mn-dependent enzymes are commonly observed. Many of these enzymes utilize Mn-peroxo species as key intermediates for their oxidative transformations. [86–103] For example, lipoxygenases (MnLO) oxidize fatty acids via a Mn^{III}-OOR intermediate, [88,89,94,103] superoxide dismutase (MnSOD)[104,105] breaks down superoxide ($O_2^{\bullet-}$) radicals, a toxic ROS associated with Alzheimer's[106,107] and Parkinson's disease,[108] via a Mn^{III}-OOH intermediate, and Mn-catalases[101] break down H_2O_2. A Mn-peroxo intermediate is also involved

as an intermediate in photosynthetic water oxidation.[96,109–111] These natural catalysts contain O- or N-ligands in the Mn ion's primary coordination sphere (***Figure 1.5***).[112] The inherent instability of transition-metal peroxo intermediates precludes their structural characterization in most cases, and despite their significant role, very few well-characterized Mn-peroxo compounds have been reported.[93,113–124] Unlike for Co and Fe metal cofactors, cysteinate ligands are not regularly incorporated into the active sites of Mn cofactors. Although there is one example of a Mn ion dependent NHase found in a sea sponge that would include the common binding motif of modified cysteinates.[125] **Chapter 5** will discuss how the primary coordination affects the stability of in Mn^{III}-peroxo complexes.

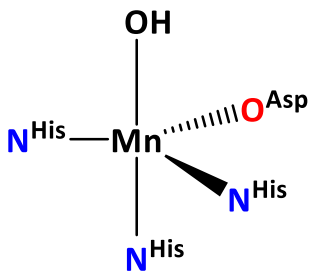

MnSOD

Figure 1.5 ChemDraw structure illustrating the N and O binding residues of MnSOD (PDB: 1VEW).[112]

1.2 The Effect of Thiolates

Thiolates in the coordination sphere of transition metal ions are able to affect the electronics of the metal ion through the nephelauxetic effect of the S-atom orbitals.[126,127] The nephelauxetic effect results in highly covalent metal-sulfur bonds, reduces the Lewis acidity of the metal ion and in turn, lowers the reduction potential of the metal ion. The 'cloud sharing' effect

demonstrates the ability of the thiolate ligand to act as a shared partner in handling electron density with the metal center. The delocalization can balance the reduction potential of the metal species while the oxidation state of the metal changes.[80] Combined, these effects can result in the stabilization of higher metal oxidation states that are required for the rich chemical process such as dioxygen activation and C—H bond cleavage by "blow torch" metal-oxo species that are regularly found to be active oxidants.[14,128,129]

Cytochrome P450 utilizes the *trans* thiolate to aid in cleaving the O—O bond through the "push effect".[130–133] The thiolate donates electron density onto the metal center, which is then pushed into the π O—O antibonding orbital to promote heterolytic bond cleavage. Modeling complexes that include thiolates in the coordination sphere of Fe is of interest to compare to the P450 system, especially if they support a high-valent oxo species. Comparisons between the thiolate ligand and either oxygen or nitrogen ligands is also of interest to fully understand the role of the thiolate. The comparison of alkoxide versus thiolate ligands will be further discussed in **Chapter 5**. However, in a method similar to the P450 "push effect", the thiolate ligand of Mn^{III}-OOR complexes resulted in the destabilization of the O—O bond compared to the alkoxide ligated Mn^{III}-OOR complex (***Figure 1.6***).

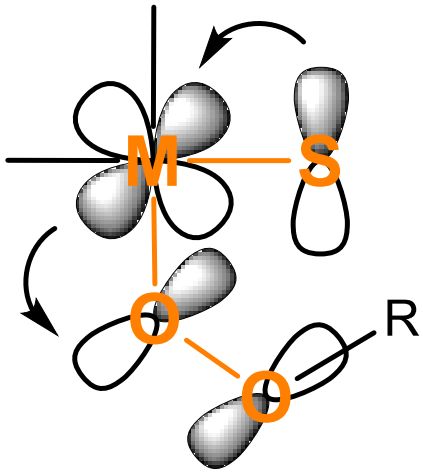

Figure 1.6 Destabilization of the O—O bond by thiolate donation to the metal ion.

1.3 Advantages of Biomimetic Modeling

A variety of spectroscopic and other characterization techniques can be applied to protein and enzymatic systems, such as X-ray crystallography and electron paramagnetic resonance (EPR) spectroscopy.[134,135] However, there are limitations in studying the proteins/enzymes in isolation. Small molecules are more easily soluble in a host of organic solvents, which aid their observation at lower temperatures and without potentially interfering effects of dioxygen and water, as is the case in native protein environments. While proteins are usually more water soluble, the tertiary/quaternary structure of proteins often ensures the active sites of the enzymes are in a hydrophobic pocket more akin to an organic solvent environment. The intermediates of dioxygen activation are more isolable in small molecule environments, yielding them to more vigorous characterization techniques.[136]

1.4 A Selection of Biomimetic Models from the Kovacs Group

1.4.1 Iron-Thiolate Complexes

In the previous section discussing the enzymes IPNS and CDO, [$Fe^{II}(S_2{}^{Me2}N_2N^H(Pr,Pr))$] (**1**) and key dioxygen derived intermediates were mentioned. [$Fe^{II}(S_2{}^{H2}N_2N^H(Pr,Pr))$] (**2**) was previously characterized but not found to form a stable Fe^{III} species. The first example of an Fe^{III}-sulfenate species, [Fe^{III}(ADIT)(ADIT-O)]$^+$ (**3-O**), was characterized by our group, and required a strong *N*-sulfonyloxaziridine oxidant to convert the thiolate to a singly oxygenated sulfenate.[80] The sulfenate species is of especial interest to the mechanisms of NHase, where the sulfenic acid is a key nucleophile.

Chapters 2-3 will discuss the effects of adding additional steric restraints to the constrained helical ligand backbone found in complexes **1** and **2**, as the addition of a methyl group to the amine N, in the equatorial plane, results in a divergence from the reactivity established for **1** and **2**. Thiolate-ligated **1** was previously shown to react with mild oxidants (O_2 or H_2O_2) to form a rare example of a singly oxygenated Fe^{III}-sulfenate complex [$Fe^{III}(\eta^2\text{-}S^{Me2}O)(S^{Me2})N_2N^H(Pr,Pr)]^+$ (**1-O**), leaving the other thiolate arm unmodified.[79] The sulfenate species is also formed from the addition of oxo-atom donors, including iodosylbenzene (PhIO) to the oxidized complex [$Fe^{III}(S_2{}^{Me2}N_2N^H(Pr,Pr))]^+$ (**1^{ox}**).[27,79]

As small molecule models of enzymes facilitate observation of intermediates at cryogenic temperatures, the dioxygen reactivity of **1** was also studied at low temperatures. Two dioxygen-derived intermediates are observed before the formation of the final sulfenate **1-O.** The first was a rare example of an alkyl-thiolate ligated Fe^{III}-superoxo species [$Fe^{III}(S_2{}^{Me2}N_2N^H(Pr,Pr))(O_2)$] (**1-($O_2$)**). The species demonstrated key electronic absorbances at λ_{max} = 409, 520, and 707 nm and

is antiferromagnetically coupled showing no signal with EPR experiments. Resonance Raman (rRaman) experiments identified the key O—O stretching frequencies as a Fermi doublet at 1093 and 1122 cm^{-1} that shift to 1022 cm^{-1} when generated from $^{18}O_2$. The superoxo species **1-O₂** was also demonstrated to be a strong oxidant, able to cleave a C—H bond from THF (BDFE = 92 kcal mol^{-1}) to form a putative hydroperoxo [$Fe^{III}(S_2{}^{Me2}N_2N^H(Pr,Pr))(OOH)$] (**1-OOH**), λ_{max} = 696 nm).[27]

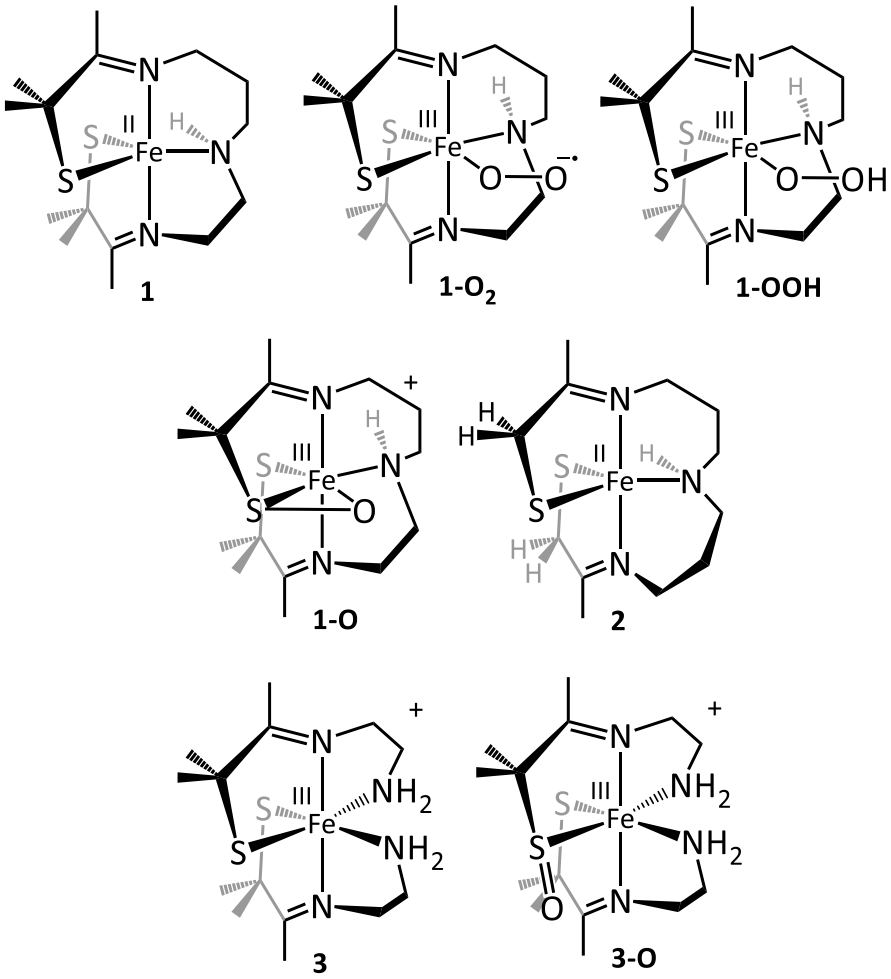

Figure 1.7 ChemDraw structures for selected Fe-thiolate biomimetic complexes: [$Fe^{II}(S_2{}^{Me2}N_2N^H(Pr,Pr))$] (**1**);[27] [$Fe^{III}(S_2{}^{Me2}N_2N^H(Pr,Pr))(O_2)$] (**1-(O₂)**);[27] [$Fe^{III}(S_2{}^{Me2}N_2N^H(Pr,Pr))(OOH)$] (**1-OOH**);[27] [$Fe^{II}(\eta^2\text{-}S^{Me2}O)(S^{Me2})N_2N^H(Pr,Pr)]^+$ (**1-O**);[79] [$Fe^{II}(S_2{}^{H2}N_2N^H(Pr,Pr))$] (**2**);[137] [$Fe^{III}(ADIT)_2]^+$ (**3**);[80] [$Fe^{III}(ADIT)(ADIT\text{-}O)]^+$ (**3-O**).[80]

1.4.2 Cobalt-Thiolate Complexes

The Co^{III} derivative of **3**, $[Co^{III}(ADIT)_2]^+$ (**4**) was shown to be unreactive with oxidants although it demonstrates a band at λ_{max} = 279 nm,[138] close to that found for the native enzyme, λ_{max} = 280 nm.[63] The Co^{III} derivative with the PrPr ligand framework $[Co^{III}(S_2{}^{Me2}N_2N^H(Pr,Pr))]^+$ (**5**) was shown to react with dioxygen from air to form a doubly oxygenated, a Co^{III}-sulfinate, $[Co^{III}(S^{Me2}(S^{O2})N_2N^H(Pr,Pr))]^+$ (**6**). The addition of H_2O_2 to **6** installed an additional oxygen on the remaining unmodified thiolate sulfur to form an η^2-sulfenate-ligated complex, $[Co^{III}((\eta^2\text{-}S^{Me2}O)(S^{O2})N_2N^H(Pr,Pr))]^+$ (**7**).[73] While the Kovacs group reported the first sulfenate-ligated Co^{III} complex, it had, in addition to the sulfenate, a doubly oxygenated sulfur and no unmodified thiolates. The latter is likely to play an important role in subsequent reactivity. **Chapter 4** will discuss sterically constrained cobalt complexes and their dioxygen reactivity, including rare examples of Co-sulfenate species.

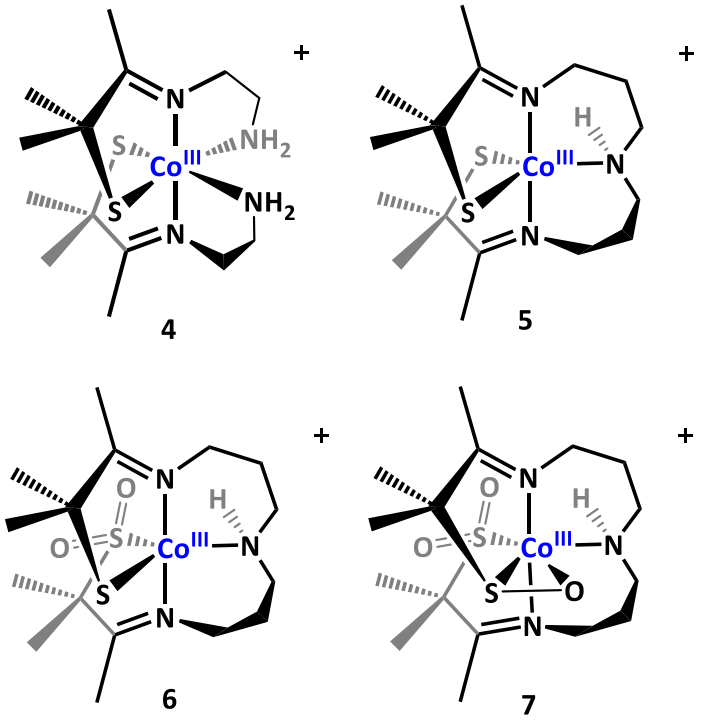

Figure 1.8 ChemDraw structures of selected Co-thiolate biomimetic complexes: $[Co^{III}(ADIT)_2]^+$ (**4**);[138] $[Co^{III}(S_2{}^{Me2}N_2N^H(Pr,Pr))]^+$ (**5**);[73,138] $[Co^{III}(S^{Me2}O_2)(S^{Me2})N_2N^H(Pr,Pr))]^+$ (**6**);[73] $[Co^{III}(S^{Me2}O_2)(\eta^2\text{-}S^{Me2}O)N_2N^H(Pr,Pr))]^+$ (**7**).[73]

1.4.3 Manganese Complexes

Previous work in the group focused on a series of structurally analogous five-coordinate, thiolate-ligated Mn^{II} complexes ($[Mn^{II}(S^{Me2}N_4(\mathbf{L}\text{-DPEN})]^+$), which incorporate readily derivatized *N*- heterocycle amines (N^{Ar} = 6-H-pyridine (**L**$^{\mathbf{Py}}$), 6-Me-pyridine (**L**$^{\mathbf{Mepy}}$), 6-OMe-pyridine (**L**$^{\mathbf{OMepy}}$) and quinoline (**L**$^{\mathbf{Quino}}$)), providing a method to tune the steric and electronic properties while including a thiolate ligand allowing fora better spectroscopic handle to observe dioxygen intermediates.[118–120,139] The low-temperature dioxygen reactivity of these complexes was investigated with methods including EPR and stopped-flow spectroscopy in order to obtain more information regarding the mechanism of the O—O bond cleaving step. The presence of the

thiolate also lowers the activation barrier to O_2 binding. The first example of a crystallographically characterized binuclear peroxo-bridged dimer, $\{[Mn^{III}(S^{Me2}N_4(6\text{-Me-DPEN})]_2(\mu\text{-}O_2)\}^{2+}$ (**$8^{Mepy}(\mu\text{-}O_2)$**)[140] was identified with this ligand system. A series of alkylperoxo species were also isolated and the correlations between their structural properties and their spectroscopic properties were established.[141] Two of the Mn complexes were found to form $Mn^{IV}Mn^{IV}$-$(\mu\text{-}O)_2$ species as their isolable final product.[142] **Chapter 5** will discuss a comparison of alkylperoxo species ligated with thiolate and alkoxide ligands and their electronic structures investigated with density functional theory calculations.

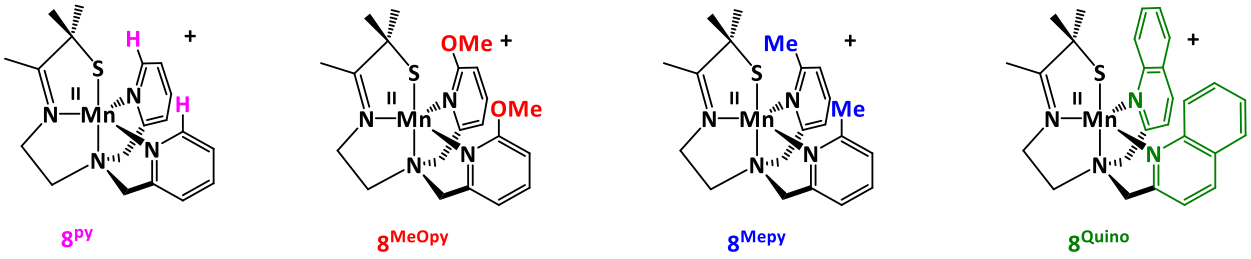

Figure 1.9 ChemDraw structures of selected Mn^{II}-thiolate complexes: $[Mn^{II}(S^{Me2}N_4(6\text{-H-DPEN})]^+$ (**8^{py}**); $[Mn^{II}(S^{Me2}N_4(6\text{-MeO-DPEN})]^+$ (**8^{MeOpy}**); $[Mn^{II}(S^{Me2}N_4(6\text{-Me-DPEN})]^+$ (**8^{Mepy}**); $[Mn^{II}(S^{Me2}N_4(\text{Quino-DPEN})]^+$ (**8^{Quino}**).[119,140]

1.5 A Selection of Relevant Biomimetic Models

1.5.1 Iron Complexes

High valent Fe-oxos have been isolated and characterized to model enzymatic systems by other groups. The following discussion cannot address all of the characterized species but highlights some significant findings that are relevant comparisons to the systems described in this dissertation. The Que group was the first to isolate a crystal structure of a high valent Fe-oxo species in the 'diamond core' motif, $[Fe(\mu\text{-}O)_2(5\text{-}Et_3\text{-TPA})_2]^{3+}$.[143] Nam and Que identified the first

crystal structure of a terminal high-valent oxo with the TMC ligand system, $[Fe^{IV}(O)(TMC)(OTf)]^{+}$.[144] The addition of a thiolate arm to the *trans* position of the TMC ligand system resulted in the identification of new species, including an Fe^{IV}-oxo, $[Fe^{IV}(O)(TMCS)]^{+}$,[145] and a η^{1} bound peroxy dianion, $[Fe^{III}(TMCS)(\eta^{1}\text{-}OO^{-})]^{+}$,[146] that were too reactive to be crystallographically analyzed. Fe complexes with five- and six-coordinate environments studied in the Goldberg group incorporate aromatic thiolate ligand arms including $[Fe^{II}(LN_3S)(OTf)]$, $[Fe^{II}(Me_3TACN)(abt^{x})(OTf)]$, and $Fe^{II}(iPr_3TACN)(abt^{x})(OTf)]$, where abt includes derivatives of 2-aminobenzenethiolate. Upon interaction with dioxygen the complexes demonstrate sulfur oxidation, in some cases form high valent Fe-oxos.[147,148]

1.5.2 Cobalt Complexes

Masuda and coworkers reported several Co^{III} complexes $PPh_4[Co^{III}(L)]$, $PPh_4[Co^{III}(L\text{-}O_3)]$, and $PPh_4[Co^{III}(L\text{-}O_4)]$, with N_2S_3-type ligands, where L = bis(*N*-(2-mercapto-2-methylpropionyl)-aminopropyl)sulfide (***Figure 1.10***)**.** The complexes have a very similar ligand architecture to the $Pr,Pr^{amide}N^{Me}$ series synthesized by the Kovacs group.[79] The ligand backbone is a closer match to the native enzymatic system coordination sphere. The dioxygen reactivity, from air, demonstrates sulfur oxygenation adding a total of four O-atoms to the S-atoms of the complexes to form $PPh_4[Co^{III}(L\text{-}O_4)]$. The addition of hydrogen peroxide to $PPh_4[Co^{III}(L)]$ results in the formation of an η^{2}-bound Co^{III}-sulfenate complex, $PPh_4[Co^{III}(L\text{-}O_3)]$. However, the complex does not continue to undergo any further sulfur oxidation from exposure to air.[74] The previous Kovacs group complexes that demonstrated sulfur oxygenation added two oxygens from air and then an additional oxygen from the addition of H_2O_2.

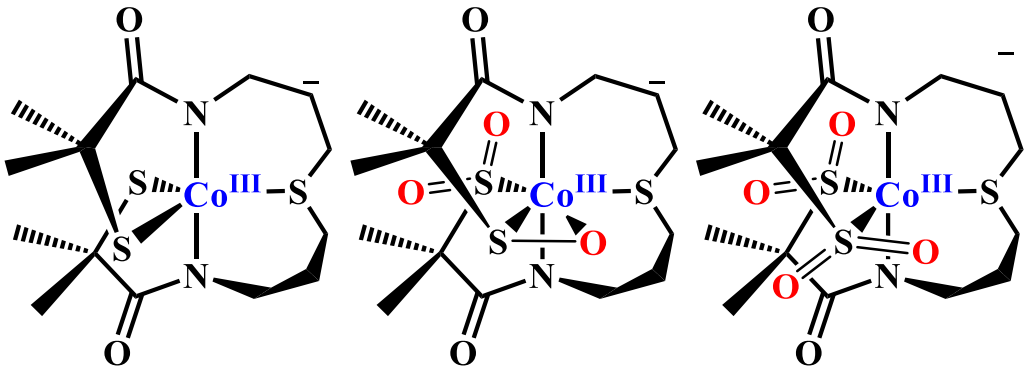

Figure 1.10 Masuda and coworkers N_2S_3-type cobalt complexes.[74]

1.6 Spin-Crossover and Relation to Enzymatic Systems

Spin-Crossover (SCO) is a research area useful in the development and control of molecular machines[149,150] and key to reactivity of metalloenzymes, such as in the case of cytochrome P450.[151] In the case of cytochrome P450, the substrate binds to the enzyme, which causes the six-coordinate, high-spin Fe center to rearrange to the low-spin five-coordinate Fe geometry that is crucial to the next step of the reactivity. The substrate does not bind at the metal center, yet the rearrangement affects the metal ion and is key to its catalytic reactivity. In the case of NHase, the metal centers are low-spin Fe and Co, aided by the covalency of the M-S bonds in the coordination sphere. Investigation of the maturation process has shown changes in the spin state of the metal center as the cysteinates are modified, from high-spin Fe^{II} to intermediate spin (S = 3/2) Fe^{III} and then finally to the active low spin (S = 1/2) Fe^{III} system.[62]

The majority of complexes known to exhibit SCO behavior are octahedral Fe^{II} complexes.[152] The d^7 ion in an octahedral field negates the interelectron repulsion and make the transition of the energy gap in the ligand field possible. There are known Fe^{III} complexes known to exhibit SCO

but also usually in octahedral geometries.[153] Recent research has been investigating the potential of developing SCO compounds with lower coordination geometries (>5). The utilization of strong field ligands ($[PhB(CH_2PPh_2)_3]^-$,[154] $[CN^-]$[155]) with low coordination numbers results in different metal complexes with an "umbrella" distortion, keeping the complex in a trigonal geometry, which allows for SCO behavior.[155–157] A series of four-coordinate Fe complexes, (derivatives of bis(formazanate) Fe^{II} complexes) accomplished SCO behavior by utilizing an inverted tetrahedral ligand field due to the high-covalency and π-backbonding to lower the effect of the interelectronic repulsion that would force a high-spin state in other geometries.[158,159] The relationship between the structure and spin state is applicable to the thiolate-ligated complexes discussed in this dissertation. The nephelauxetic effect of the thiolate ligands alters the electronics to allow for unique spin states and SCO behavior to be experimentally observed and computationally investigated.

1.7 Chapter 1 References

(1) Mounicou, S.; Szpunar, J.; Lobinski, R. Metallomics: The Concept and Methodology. *Chem. Soc. Rev.* **2009**, *38*, 1119–1138.

(2) Tainer, J. A.; Roberts, V. A.; Getzoff, E. D. Metal-Binding Sites in Proteins. *Curr. Opin. Biotechnol.* **1991**, *2* (4), 582–591.

(3) Miyanaga, A.; Fushinobu, S.; Ito, K.; Wakagi, T. Crystal Structure of Cobalt-Containing Nitrile Hydratase. *Biochem. Biophys. Res. Commun.* **2001**, *288* (5), 1169–1174.

(4) Nishiyama, M.; Horinouchi, S.; Kobayashi, M.; Nagasawa, T.; Yamada, H.; Beppu, T. Cloning and Characterization of Genes Responsible for Metabolism of Nitrile Compounds from Pseudomonas Chloraraphis B23. *J. Bacteriol.* **1991**, *173* (8), 2465–2472.

(5) Jasniewski, A. J.; Que, L. Dioxygen Activation by Nonheme Diiron Enzymes: Diverse Dioxygen Adducts, High-Valent Intermediates, and Related Model Complexes. *Chem. Rev.* **2018**, *118* (5), 2554–2592.

(6) Ray, K.; Lee, Y. M.; Nam, W. Dioxygen Activation Chemistry by Synthetic Mononuclear Nonheme Iron, Copper and Chromium Complexes. *Coord. Chem. Rev.* **2017**, *334*, 25–42.

(7) Lewis, J. C.; Coelho, P. S.; Arnold, F. H. Enzymatic Functionalization of Carbon–Hydrogen Bonds. *Chem. Soc. Rev.* **2011**, *40* (4), 2003–2021.

(8) Blamey, J. M.; Fischer, F.; Meyer, H. P.; Sarmiento, F.; Zinn, M. Enzymatic Biocatalysis in Chemical Transformations: A Promising and Emerging Field in Green Chemistry Practice. In *Biotechnology of Microbial Enzymes: Production, Biocatalysis and Industrial Applications*; Brahmachari, G., Ed.; Academic Press, 2017; pp 347–403.

(9) Chen, A. Y.; Adamek, R. N.; Dick, B. L.; Credille, C. V.; Morrison, C. N.; Cohen, S. M. Targeting Metalloenzymes for Therapeutic Intervention. *Chem. Rev.* **2019**, *119* (2), 1323–1455.

(10) Dent, M. R.; DeMartino, A. W.; Tejero, J.; Gladwin, M. T. Endogenous Hemoprotein-Dependent Signaling Pathways of Nitric Oxide and Nitrite. *Inorg. Chem.* **2021**, Article ASAP.

(11) Huang, X.; Groves, J. T. Oxygen Activation and Radical Transformations in Heme Proteins and Metalloporphyrins. *Chem. Rev.* **2018**, *118* (5), 2491–2553.

(12) Finnigan, J. D.; Young, C.; Cook, D. J.; Charnock, S. J.; Black, G. W. Cytochromes P450 (P450s): A Review of the Class System with a Focus on Prokaryotic P450s. *Adv. Protein Chem. Struct. Biol.* **2020**, *122*, 289–320.

(13) Solomon, E. I.; Decker, A.; Lehnert, N. Non-Heme Iron Enzymes: Contrasts to Heme Catalysis. *Proc. Natl. Acad. Sci. U. S. A.* **2003**, *100* (7), 3589–3594.

(14) Kovacs, J. A. Synthetic Analogues of Cysteinate-Ligated Non-Heme Iron and Non-Corrinoid Cobalt Enzymes. *Chem. Rev.* **2004**, *104* (2), 825–848.

(15) Kovaleva, E. G.; Lipscomb, J. D. Versatility of Biological Non-Heme Fe(II) Centers in Oxygen Activation Reactions. *Nat. Chem. Biol.* **2008**, *4* (3), 186–193.

(16) Bruijnincx, P. C. A.; van Koten, G.; Klein Gebbink, R. J. M. Mononuclear Non-Heme Iron Enzymes with the 2-His-1-Carboxylate Facial Triad: Recent Developments in Enzymology and Modeling Studies. *Chem. Soc. Rev.* **2008**, *37* (12), 2716–2744.

(17) Marengo-Rowe, A. J. Structure-Function Relations of Human Hemoglobins. *Baylor Univ. Med. Cent. Proc.* **2006**, *19* (3), 239–245.

(18) Matthews, R. G. Cobalamin- and Corrinoid-Dependent Enzymes. *Met Ions Life Sci.* **2009**, *6*, 53–114.

(19) Murakami, T.; Nojiri, M.; Nakayama, H.; Odaka, M.; Yohda, M.; Dohmae, N.; Takio, K.; Nagamune, T.; Endo, I. Post-Translational Modification Is Essential for Catalytic Activity of Nitrile Hydratase. *Protein Sci.* **2000**, *9*, 1024–1030.

(20) Tamanaha, E.; Zhang, B.; Guo, Y.; Chang, W. C.; Barr, E. W.; Xing, G.; St Clair, J.; Ye, S.; Neese, F.; Bollinger, J. M.; et al. Spectroscopic Evidence for the Two C-H-Cleaving Intermediates of Aspergillus Nidulans Isopenicillin N Synthase. *J. Am. Chem. Soc.* **2016**, *138* (28), 8862–8874.

(21) Tchesnokov, E. P.; Faponle, A. S.; Davies, C. G.; Quesne, M. G.; Turner, R.; Fellner, M.; Souness, R. J.; Wilbanks, S. M.; De Visser, S. P.; Jameson, G. N. L. An Iron–Oxygen Intermediate Formed during the Catalytic Cycle of Cysteine Dioxygenase. *Chem. Commun.* **2016**, *52*, 8814–8817.

(22) Light, K. M.; Yamanaka, Y.; Odaka, M.; Solomon, E. I. Spectroscopic and Computational Studies of Nitrile Hydratase: Insights into Geometric and Electronic Structure and the Mechanism of Amide Synthesis. *Chem. Sci.* **2015**, *6*, 6280–6294.

(23) Hong, S.; Lee, Y.-M.; Ray, K.; Nam, W. Dioxygen Activation Chemistry by Synthetic Mononuclear Nonheme Iron, Copper and Chromium Complexes. *Coord. Chem. Rev.* **2017**, *334*, 25–42.

(24) Minaev, B. F.; Ågren, H.; Minaeva, V. O. Spin-Orbit Coupling in Enzymatic Reactions and the Role of Spin in Biochemistry. In *Handbook of Computational Chemistry*; Springer

Netherlands, 2016; pp 1–31.

(25) Krebs, C.; Galoni´, D. G.; Fujimori, G.; Walsh, C. T.; Bollinger, J. M. Non-Heme Fe(IV)-Oxo Intermediates. *Acc. Chem. Res.* **2007**, *40* (7), 484–492.

(26) Hohenberger, J.; Ray, K.; Meyer, K. The Biology and Chemistry of High-Valent Iron-Oxo and Iron-Nitrido Complexes. *Nat. Commun.* **2012**, *3* (1), 1–13.

(27) Blakely, M. N.; Dedushko, M. A.; Chaau, P.; Poon, Y.; Villar-Acevedo, G.; Kovacs, J. A. Formation of a Reactive, Alkyl Thiolate-Ligated Fe III-Superoxo Intermediate Derived from Dioxygen. *J. Am. Chem. Soc* **2019**, *141* (5), 1867–1870.

(28) Rittle, J.; Green, M. T. Cytochrome P450 Compound I: Capture, Characterization, and C-H Bond Activation Kinetics. *Science.* **2010**, *330* (6006), 933–937.

(29) Krest, C. M.; Onderko, E. L.; Yosca, T. H.; Calixto, J. C.; Karp, R. F.; Livada, J.; Rittle, J.; Green, M. T. Reactive Intermediates in Cytochrome P450 Catalysis. *J. Biol. Chem.* **2013**, *288* (24), 17074–17081.

(30) Dunham, N. P.; Arnold, F. H. Nature's Machinery, Repurposed: Expanding the Repertoire of Iron-Dependent Oxygenases. *ACS Catal.* **2020**, *10* (20), 12239–12255.

(31) Hammer, S. C.; Knight, A. M.; Arnold, F. H. Design and Evolution of Enzymes for Non-Natural Chemistry. *Curr. Opin. Green Sustain. Chem.* **2017**, *7*, 23–30.

(32) Swathi, A.; Visser, S. P. de. The Mechanism of Cysteine Oxygenation by Cysteine Dioxygenase Enzymes. *J. Am. Chem. Soc* **2007**, *129* (48), 14846–14847.

(33) Yamanaka, Y.; Kato, Y.; Hashimoto, K.; Iida, K.; Nagasawa, K.; Nakayama, H.; Dohmae, N.;

Noguchi, K.; Noguchi, T.; Yohda, M.; et al. Time-Resolved Crystallography of the Reaction Intermediate of Nitrile Hydratase: Revealing a Role for the Cysteinesulfenic Acid Ligand as a Catalytic Nucleophile. *Angew. Chemie Int. Ed.* **2015**, *54* (37), 10763–10767.

(34) Baldwin, J. E.; Abraham, E. The Biosynthesis of Penicillins and Cephalosporins. *Nat. Prod. Rep.* **1988**, *5* (2), 129–145.

(35) Perry, J.; Waglechner, N.; Wright, G. The Prehistory of Antibiotic Resistance. *Cold Spring Harb. Perspect. Med.* **2016**, *6* (6), 1–8.

(36) Smalla, K.; Cook, K.; Djordjevic, S. P.; Klümper, U.; Gillings, M. Environmental Dimensions of Antibiotic Resistance: Assessment of Basic Science Gaps. *FEMS Microbiol. Ecol.* **2018**, *94* (12), 195.

(37) Neu, H. C. The Crisis in Antibiotic Resistance. *Science (80-.).* **1992**, *257* (5073), 1064–1073.

(38) Burziaff, N. I.; Rutledge, P. J.; Clifton, I. J.; Hensgens, C. M. H.; Pickford, M.; Adlington, R. M.; Roach, P. L.; Baldwin, J. E. The Reaction Cycle of Isopenicillin N Synthase Observed by X-Ray Diffraction. *Nature* **1999**, *401* (6754), 721–724.

(39) Chiang, C.-W.; Kleespies, S. T.; Stout, H. D.; Meier, K. K.; Li, P.-Y.; Bominaar, E. L.; Lawrence Que, J.; Münck, E.; Lee, W.-Z. Characterization of a Paramagnetic Mononuclear Nonheme Iron-Superoxo Complex. *J. Am. Chem. Soc.* **2014**, *136* (31), 10846–10849.

(40) Fischer, A. A.; Lindeman, S. V.; Fiedler, A. T. A Synthetic Model of the Nonheme Iron–Superoxo Intermediate of Cysteine Dioxygenase. *Chem. Commun.* **2018**, *54* (80), 11344–11347.

(41) Oddon, F.; Chiba, Y.; Nakazawa, J.; Ohta, T.; Ogura, T.; Hikichi, S. Characterization of Mononuclear Non-Heme Iron(III)-Superoxo Complex with a Five-Azole Ligand Set. *Angew. Chemie Int. Ed.* **2015**, *54* (25), 7336–7339.

(42) Hong, S.; Sutherlin, K. D.; Park, J.; Kwon, E.; Siegler, M. A.; Solomon, E. I.; Nam, W. Crystallographic and Spectroscopic Characterization and Reactivities of a Mononuclear Non-Haem Iron(III)-Superoxo Complex. *Nat. Commun. 2014 51* **2014**, *5* (1), 1–7.

(43) Kumar, D.; Sastry, G. N.; Goldberg, D. P.; de Visser, S. P. Mechanism of S-Oxygenation by a Cysteine Dioxygenase Model Complex. *J. Phys. Chem. A* **2012**, *116* (1), 582–591.

(44) McQuilken, A. C.; Jiang, Y.; Siegler, M. A.; Goldberg, D. P. Addition of Dioxygen to an N4S(Thiolate) Iron(II) Cysteine Dioxygenase Model Gives a Structurally Characterized Sulfinato–Iron(II) Complex. *J. Am. Chem. Soc.* **2012**, *134* (21), 8758–8761.

(45) Badiei, Y. M.; Siegler, M. A.; Goldberg, D. P. O2 Activation by Bis(Imino)Pyridine Iron(II)-Thiolate Complexes. *J. Am. Chem. Soc.* **2011**, *133* (5), 1274–1277.

(46) Jiang, Y.; Widger, L. R.; Kasper, G. D.; Siegler, M. A.; Goldberg, D. P. Iron(II)-Thiolate *S* -Oxygenation by O_2 : Synthetic Models of Cysteine Dioxygenase. *J. Am. Chem. Soc.* **2010**, *132* (35), 12214–12215.

(47) Kumar, D.; Thiel, W.; De Visser, S. P. Theoretical Study on the Mechanism of the Oxygen Activation Process in Cysteine Dioxygenase Enzymes. *J. Am. Chem. Soc.* **2011**, *133*, 3869–3882.

(48) Simmons, C. R.; Krishnamoorthy, K.; Granett, S. L.; Schuller, D. J.; Dominy, J. E.; Begley, T. P.; Stipanuk, M. H.; Karplus, P. A. A Putative Fe(2+) Bound Persulfenate Intermediate in

Cysteine Dioxygenase. *Biochemistry* **2008**, *47* (44), 11390–11392.

(49) Ray, K.; Pfaff, F. F.; Wang, B.; Nam, W. Status of Reactive Non-Heme Metal–Oxygen Intermediates in Chemical and Enzymatic Reactions. *J. Am. Chem. Soc.* **2014**, *136* (40), 13942–13958.

(50) Jeschke, J.; O'Hagan, H. M.; Zhang, W.; Vatapalli, R.; Calmon, M. F.; Danilova, L.; Nelkenbrecher, C.; Van Neste, L.; Bijsmans, I. T. G. W.; Van Engeland, M.; et al. Frequent Inactivation of Cysteine Dioxygenase Type 1 Contributes to Survival of Breast Cancer Cells and Resistance to Anthracyclines. *Clin. Cancer Res.* **2013**, *19* (12), 3201–3211.

(51) Jacob, C.; Holme, A. L.; Fry, F. H. The Sulfinic Acid Switch in Proteins. *Org. Biomol. Chem.* **2004**, *2* (14), 1953–1956.

(52) Driggers, C. M.; Kean, K. M.; Hirschberger, L. L.; Cooley, R. B.; Stipanuk, M. H.; Karplus, P. A. Structure-Based Insights into the Role of the Cys–Tyr Crosslink and Inhibitor Recognition by Mammalian Cysteine Dioxygenase. *J. Mol. Biol.* **2016**, *428* (20), 3999–4012.

(53) Kobayashi, M.; Shimizu, S. Metalloenzyme Nitrile Hydratase: Structure, Regulation, and Application to Biotechnology. *Nat. Biotechnol.* **1998**, *16* (8), 733–736.

(54) Mitra, S.; Holz, R. C. Unraveling the Catalytic Mechanism of Nitrile Hydratases. *J. Biol. Chem.* **2007**, *282* (10), 7397–7404.

(55) Kobayashi, M.; Shimizu, S. Metalloenzyine Nitrile Hydratase: Structure, Regulation, and Application to Biotechnology. *Nat. Biotechnol.* **1998**, *16*, 733–736.

(56) Sugiura, Y.; Kuwahara, J. Nitrile Hydratase: The First Non-Heme Iron Enzyme with a Typical

Low-Spin Fe(III)-Active Center. *J. Am. Chem. Soc.* **1987**, *109*, 5848–5850.

(57) Stolz, A.; Trott, S.; Binder, M.; Bauer, R.; Hirrlinger, B.; Layh, N.; Knackmuss, H.-J. Enantioselective Nitrile Hydratases and Amidases from Different Bacterial Isolates. *J. Mol. Catal. B Enzym.* **1998**, *5*, 137–141.

(58) Prasad, S.; Chand Bhalla, T. Nitrile Hydratases (NHases): At the Interface of Academia and Industry. *Biotechnol. Adv.* **2010**, *28*, 725–741.

(59) Petrillo, K. L.; Wu, S.; Hann, E. C.; Cooling, F. B.; Ben-Bassat, A.; Gavagan, J. E.; DiCosimo, R.; Payne, M. S. Over-Expression in Escherichia Coli of a Thermally Stable and Regio-Selective Nitrile Hydratase from Comamonas Testosteroni 5-MGAM-4D. *Appl. Microbiol. Biotechnol.* **2005**, *67* (5), 664–670.

(60) Kohyama, E.; Yoshimura, A.; Aoshima, D.; Yoshida, T.; Kawamoto, H.; Nagasawa, T. Convenient Treatment of Acetonitrile-Containing Wastes Using the Tandem Combination of Nitrile Hydratase and Amidase-Producing Microorganisms. *Appl. Microbiol. Biotechnol.* **2006**, *72*, 600–606.

(61) Baxter, J.; Cummings, S. P. The Current and Future Applications of Microorganism in the Bioremediation of Cyanide Contamination. *Antonie Van Leeuwenhoek* **2006**, *90*, 1–17.

(62) Ogutu, I. R. A. M.; Holz, R. C.; Bennett, B. Insight into the Maturation Process of the Nitrile Hydratase Active Site. *Inorg. Chem.* **2021**, *60* (8), 5432–5435.

(63) Brennan, B. A.; Alms, G.; Nelson, M. J.; Durney, L. T.; Scarrow, R. C. Nitrile Hydratase from Rhodococcus Rhodochrous J1 Contains a Non-Corrin Cobalt Ion with Two Sulfur Ligands. *J. Am. Chem. Soc.* **1996**, *118* (38), 9194–9195.

(64) Nagasawa, T.; Takeuchi, K.; Yamada, H. Characterization of a New Cobalt-Containing Nitrile Hydratase Purified from Urea-Induced Cells of Rhodococcus Rhodochrous J1. *Eur. J. Biochem.* **1991**, *196* (3), 581–589.

(65) Nojiri, M.; Nakayama, H.; Odaka, M.; Yohda, M.; Takio, K.; Endo, I. Cobalt-Substituted Fe-Type Nitrile Hydratase of Rhodococcus Sp. N-771. *FEBS Lett.* **2000**, *465* (2–3), 173–177.

(66) Payne, M. S.; Wu, S.; Fallon, R. D.; Tudor, G.; Stieglitz, B.; Turner, I. M.; Nelson, M. J. A Stereoselective Cobalt-Containing Nitrile Hydratase. *Biochemistry* **1997**, *36* (18), 5447–5454.

(67) Martinez, S.; Wu, R.; Sanishvili, R.; Liu, D.; Holz, R. The Active Site Sulfenic Acid Ligand in Nitrile Hydratases Can Function as a Nucleophile. *J. Am. Chem. Soc.* **2014**, *136* (4), 1186–1189.

(68) Dey, A.; Chow, M.; Taniguchi, K.; Lugo-Mas, P.; Davin, S.; Maeda, M.; Kovacs, J. A.; Odaka, M.; Hodgson, K. O.; Hedman, B.; et al. Sulfur K-Edge XAS and DFT Calculations on Nitrile Hydratase: Geometric and Electronic Structure of the Non-Heme Iron Active Site. *J. Am. Chem. Soc.* **2006**, *128*, 533–541.

(69) Song, L.; Wang, M.; Shi, J.; Xue, Z.; Wang, M.-X.; Qian, S. High Resolution X-Ray Molecular Structure of the Nitrile Hydratase from Rhodococcus Erythropolis AJ270 Reveals Posttranslational Oxidation of Two Cysteines into Sulfinic Acids and a Novel Biocatalytic Nitrile Hydration Mechanism. *Biochem. Biophys. Res. Commun.* **2007**, *362*, 319–324.

(70) Nagashima, S.; Nakasako, M.; Dohmae, N.; Tsujimura, M.; Takio, K.; Odaka, M.; Yohda, M.; Kamiya, N.; Endo, L. Novel Non-Heme Iron Center of Nirtile Hydratase with a Claw Setting

of Oxygen Atoms. *Nat. Struct. Biol.* **1998**, *5* (5), 347–351.

(71) Miyanaga, A.; Fushinobu, S.; Ito, K.; Wakagi, T. Crystal Structure of Cobalt-Containing Nitrile Hydratase. *Biochem. Biophys. Res. Commun.* **2001**, *288* (5), 1169–1174.

(72) Tsujimura, M.; Odaka, M.; Nakayama, H.; Dohmae, N.; Koshino, H.; Asami, T.; Hoshino, M.; Takio, K.; Yoshida, S.; Maeda, M.; et al. A Novel Inhibitor for Fe-Type Nitrile Hydratase: 2-Cyano-2-Propyl Hydroperoxide. *J. Am. Chem. Soc.* **2003**, *125*, 11532–11538.

(73) Kung, I.; Schweitzer, D.; Shearer, J.; Taylor, W. D.; Jackson, H. L.; Lovell, S.; Kovacs, J. A. How Do Oxidized Thiolate Ligands Affect the Electronic and Reactivity Properties of a Nitrile Hydratase Model Compound? *J. Am. Chem. Soc.* **2000**, *122*, 8299–8300.

(74) Yano, T.; Wasada-Tsutsui, Y.; Ikeda, T.; Shibayama, T.; Kajita, Y.; Inomata, T.; Funahashi, Y.; Ozawa, T.; Masuda, H. Co(III) Complexes with N 2 S 3 -Type Ligands as Structural/Functional Models for the Isocyanide Hydrolysis Reaction Catalyzed by Nitrile Hydratase. *Inorg. Chem.* **2018**, *57* (8), 4277–4290.

(75) Heinrich, L. .; Mary-Verla, A. .; Li, Y. .; Vaissermann, J. .; Chottard, J.-C. Cobalt(III) Complexes with Carboxamido-N and Sulfenato-S or Sulfinato-S Ligands Suggest That a Coordinated Sulfenate-S Is Essential for the Catalytic Activity of Nitrile Hydratases. *Eur. J. Inorg. Chem.* **2001**, *2001* (9), 2203–2206.

(76) Lydon, J. D.; Deutsch, E. Chemistry and Reactivity of S-Bonded Sulfenato-Cobalt(III) Complexes. *Inorg. Chem* **1982**, *21*, 3180–3185.

(77) Adzamli, I. K.; Libson, K.; Lydon, J. D.; Elder, R. C.; Deutsch, E. Synthesis, Characterization, and Reactivity of Coordinated Sulfenic Acids. *Inorg. Chem.* **1979**, *18* (2), 303–311.

(78) Swartz, R. D.; Coggins, M. K.; Kaminsky, W.; Kovacs, J. A. Nitrile Hydration by Thiolate- and Alkoxide-Ligated Co-NHase Analogues. Isolation of Co(III)-Amidate and Co(III)-Iminol Intermediates. *J. Am. Chem. Soc.* **2011**, *133* (11), 3954–3963.

(79) Villar-Acevedo, G.; Lugo-Mas, P.; Blakely, M. N.; Rees, J. A.; Ganas, A. S.; Hanada, E. M.; Kaminsky, W.; Kovacs, J. A. Metal-Assisted Oxo Atom Addition to an Fe(III) Thiolate. *J. Am. Chem. Soc.* **2017**, *139*, 119–129.

(80) Lugo-Mas, P.; Dey, A.; Xu, L.; Davin, S. D.; Benedict, J.; Kaminsky, W.; Hodgson, K. O.; Hedman, B.; Solomon, E. I.; Kovacs, J. A. How Does Single Oxygen Atom Addition Affect the Properties of an Fe-Nitrile Hydratase Analogue? The Compensatory Role of the Unmodified Thiolate. *J. Am. Chem. Soc.* **2006**, *128* (34), 11211–11221.

(81) Lin, P.-S.; Kwock, L.; Hefter, K.; Misslbeck, G. Effects of Iron, Copper, Cobalt, and Their Chelators on the Cytotoxicity of Bleomycin. *Cancer Res.* **1983**, *43* (3).

(82) Rajani, C.; Kincaid, J. R.; Petering, D. H. Resonance Raman Studies of HOO-Co(III)Bleomycin and Co(III)Bleomycin: Identification of Two Important Vibrational Modes, ν(Co-OOH) and ν(O-OH). *J. Am. Chem. Soc.* **2004**, *126*, 3829–3836.

(83) Decker, A.; Chow, M. S.; Kemsley, J. N.; Lehnert, N.; Solomon, E. I. Direct Hydrogen-Atom Abstraction by Activated Bleomycin: An Experimental and Computational Study. *J. Am. Chem. Soc.* **2006**, *128*, 4719–4733.

(84) Goodwin, K. D.; Lewis, M. A.; Long, E. C.; Georgiadis, M. M. Crystal Structure of DNA-Bound Co(III)·bleomycin B2: Insights on Intercalation and Minor Groove Binding. *Proc. Natl. Acad. Sci. U. S. A.* **2008**, *105* (13), 5052–5056.

(85) Gray, H. B.; Winkler, J. R. Living with Oxygen. *Acc. Chem. Res.* **2018**, *51* (8), 1850–1857.

(86) Cotruvo, J. A.; Stubbe, J. An Active Dimanganese(III)-Tyrosyl Radical Cofactor in Escherichia Coli Class Ib Ribonucleotide Reductase. *Biochemistry* **2010**, *49* (6), 1297–1309.

(87) Jackson, T. A.; Karapetian, A.; Miller, A.-F.; Brunold, T. C. Probing the Geometric and Electronic Structures of the Low-Temperature Azide Adduct and the Product-Inhibited Form of Oxidized Manganese Superoxide Dismutase. *Biochemistry* **2005**, *44* (5), 1504–1520.

(88) Ewa Skrzypczak-Jankun, *; Rebecca A. Bross; Richard T. Carroll; Willam R. Dunham, and; Max O. Funk, J. . Three-Dimensional Structure of a Purple Lipoxygenase. *J. Am. Chem. Soc.* **2001**, *123* (44), 10814–10820.

(89) Oliw, E. H.; Jernerén, F.; Hoffmann, I.; Sahlin, M.; Garscha, U. Manganese Lipoxygenase Oxidizes Bis-Allylic Hydroperoxides and Octadecenoic Acids by Different Mechanisms. *Biochim. Biophys. Acta - Mol. Cell Biol. Lipids* **2011**, *1811* (3), 138–147.

(90) Kovaleva, E. G.; Lipscomb, J. D. Crystal Structures of Fe2+ Dioxygenase Superoxo, Alkylperoxo, and Bound Product Intermediates. *Science (80-.).* **2007**, *316* (5823), 453–457.

(91) Mbughuni, M. M.; Chakrabarti, M.; Hayden, J. A.; Meier, K. K.; Dalluge, J. J.; Hendrich, M. P.; Münck, E.; Lipscomb, J. D. Oxy Intermediates of Homoprotocatechuate 2,3-Dioxygenase: Facile Electron Transfer between Substrates. *Biochemistry* **2011**, *50* (47), 10262–10274.

(92) Liu, W.; Groves, J. T. Manganese Catalyzed C-H Halogenation. *Acc. Chem. Res.* **2015**, *48* (6), 1727–1735.

(93) Shook, R. L.; Peterson, S. M.; Greaves, J.; Moore, C.; Rheingold, A. L.; Borovik, A. S. Catalytic Reduction of Dioxygen to Water with a Monomeric Manganese Complex at Room Temperature. *J. Am. Chem. Soc.* **2011**, *133* (15), 5810–5817.

(94) Christian R. Goldsmith; Adam P. Cole, and; Stack*, T. D. P. C−H Activation by a Mononuclear Manganese(III) Hydroxide Complex: Synthesis and Characterization of a Manganese-Lipoxygenase Mimic? *J. Am. Chem. Soc.* **2005**, *127* (27), 9904–9912.

(95) Murphy, A.; Stack, T. D. P. Discovery and Optimization of Rapid Manganese Catalysts for the Epoxidation of Terminal Olefins. *J. Mol. Catal. A. Chem.* **2006**, *1–2* (251), 78–88.

(96) Cox, N.; Pantazis, D. A.; Neese, F.; Lubitz, W. Biological Water Oxidation. *Acc. Chem. Res.* **2013**, *46* (7), 1588–1596.

(97) Paul, S.; Neese, F.; Pantazis, D. A. Structural Models of the Biological Oxygen-Evolving Complex: Achievements, Insights, and Challenges for Biomimicry. *Green Chem.* **2017**, *19* (10), 2309–2325.

(98) Suga, M.; Akita, F.; Hirata, K.; Ueno, G.; Murakami, H.; Nakajima, Y.; Shimizu, T.; Yamashita, K.; Yamamoto, M.; Ago, H.; et al. Native Structure of Photosystem II at 1.95A° Resolution Viewed by Femtosecond X-Ray Pulses. *Nature* **2015**, *517* (7532), 99–103.

(99) Gilbert, N. C.; Bartlett, S. G.; Waight, M. T.; Neau, D. B.; Boeglin, W. E.; Brash, A. R.; Newcomer, M. E. The Structure of Human 5-Lipoxygenase. *Science.* **2011**, *331* (6014), 217–219.

(100) Sheng, Y.; Gralla, E. B.; Schumacher, M.; Cascio, D.; Cabelli, D. E.; Valentine, J. S. Six-Coordinate Manganese(3+) in Catalysis by Yeast Manganese Superoxide Dismutase. *Proc.*

Natl. Acad. Sci. U. S. A. **2012**, *109* (36), 14314–14319.

(101) Wu, A. J.; Penner-Hahn, J. E.; Pecoraro, V. L. Structural, Spectroscopic, and Reactivity Models for the Manganese Catalases. *Chem. Rev.* **2004**, *104* (2), 903–938.

(102) Gunderson, W. A.; Zatsman, A. I.; Emerson, J. P.; Farquhar, E. R.; Que, L.; Jr.; Lipscomb, J. D.; Hendrich, M. P. Electron Paramagnetic Resonance Detection of Intermediates in the Enzymatic Cycle of an Extradiol Dioxygenase. *J. Am. Chem. Soc.* **2008**, *130* (44), 14465.

(103) Hamberg, M.; Chao, S.; Oliw, E. Manganese Lipoxygenase. *J. Biol. Chem.* **1998**, *273* (21), 13080–13088.

(104) Jackson, T. A.; Brunold, T. C. Combined Spectroscopic/Computational Studies on Fe-and Mn-Dependent Superoxide Dismutases: Insights into Second-Sphere Tuning of Active Site Properties. *Acc. Chem. Res.* **2004**, *37* (7), 461–470.

(105) Vance, C. K.; Miller, A. F. Novel Insights into the Basis for Escherichia Coli Superoxide Dismutase's Metal Ion Specificity from Mn-Substituted FeSOD and Its Very High Em. *Biochemistry* **2001**, *40* (43), 13079–13087.

(106) Sen, A.; Hongpaisan, J. Hippocampal Microvasculature Changes in Association with Oxidative Stress in Alzheimer's Disease. *Free Radic. Biol. Med.* **2018**, *120*, 192–203.

(107) De Leo, M. E.; Borrello, S.; Passantino, M.; Palazzotti, B.; Mordente, A.; Daniele, A.; Filippini, V.; Galeotti, T.; Masullo, C. Oxidative Stress and Overexpression of Manganese Superoxide Dismutase in Patients with Alzheimer's Disease. *Neurosci. Lett.* **1998**, *250* (3), 173–176.

(108) Ihara, Y.; Chuda, D.; Kuroda, S.; Hayabara, T. Hydroxyl Radical and Superoxide Dismutase in Blood of Patients with Parkinson's Disease: Relationship to Clinical Data. *J. Neurol. Sci.* **1999**, *170* (2), 90–95.

(109) Yano, J.; Yachandra, V. Mn 4 Ca Cluster in Photosynthesis: Where and How Water Is Oxidized to Dioxygen. *Chem. Rev.* **2014**, *114*, 4175–4205.

(110) Cox, N.; Retegan, M.; Neese, F.; Pantazis, D. A.; Boussac, A.; Lubitz, W. Electronic Structure of the Oxygen-Evolving Complex in Photosystem II Prior to O-O Bond Formation. *Science.* **2014**, *345* (6198), 804–808.

(111) Umena, Y.; Kawakami, K.; Shen, J.-R.; Kamiya, N. Crystal Structure of Oxygen-Evolving Photosystem II at a Resolution of 1.9[Thinsp]A. *Nature* **2011**, *473* (7345), 55–60.

(112) Edwards, R. A.; Baker, H. M.; Whittaker, M. M.; Whittaker, J. W.; Jameson, G. B.; Baker, E. N. Manganese Superoxide Dismutase From Escherichia Coli. *Protein Data Bank* **1998**, 1VEW.

(113) Coggins, M. K.; Martin-Diaconescu, V.; DeBeer, S.; Kovacs, J. A. Correlation Between Structural, Spectroscopic, and Reactivity Properties Within a Series of Structurally Analogous Metastable Manganese(III)−Alkylperoxo Complexes. *J. Am. Chem. Soc.* **2013**, *135*, 4260–4272.

(114) Geiger, R. A.; Wijeratne, G. B.; Day, V. W.; Jackson, T. A. Steric and Electronic Influences on the Structures of Peroxomanganese(III) Complexes Supported by Tetradentate Ligands. *Eur. J. Inorg. Chem.* **2012**, *2012* (10), 1598–1608.

(115) Geiger, R. A.; Chattopadhyay, S.; Day, V. W.; Jackson, T. A. A Series of Peroxomanganese(III)

Complexes Supported by Tetradentate Aminopyridyl Ligands: Detailed Spectroscopic and Computational Studies. *J. Am. Chem. Soc.* **2010**, *132* (8), 2821–2831.

(116) Geiger, R. A.; Leto, D. F.; Chattopadhyay, S.; Dorlet, P.; Anxolabéhère-Mallart, E.; Jackson, T. A. Geometric and Electronic Structures of Peroxomanganese(III) Complexes Supported by Pentadentate Amino-Pyridine and -Imidazole Ligands. *Inorg. Chem.* **2011**, *50* (20), 10190–10203.

(117) Coggins, M. K.; Kovacs, J. A. Structural and Spectroscopic Characterization of Metastable Thiolate-Ligated Manganese(III)-Alkylperoxo Species. *J. Am. Chem. Soc.* **2011**, *133* (9), 12470–12473.

(118) Coggins, M. K.; Sun, X.; Kwak, Y.; Solomon, E. I.; Rybak-Akimova, E.; Kovacs, J. A. Characterization of Metastable Intermediates Formed in the Reaction between a Mn(II) Complex and Dioxygen, Including a Crystallographic Structure of a Binuclear Mn(III)−Peroxo Species. *J. Am. Chem. Soc.* **2013**, *135*, 5631–5640.

(119) Poon, P. C. Y.; Dedushko, M.; Sun, X.; Yang, G.; Toledo, S.; Hayes, E. C.; Johansen, A.; Rees, J. A.; Stoll, S.; Rybak-Akimova, E.; et al. How Metal Ion Lewis Acidity and Steric Properties Influence the Barrier to Dioxygen Binding, Peroxo O-O Bond Cleavage, and Reactivity. *J. Am. Chem. Soc.* **2019**, *141*, 15046–15057.

(120) Kovacs, J. A. Tuning the Relative Stability and Reactivity of Manganese Dioxygen and Peroxo Intermediates via Systematic Ligand Modification. *Acc. Chem. Res.* **2015**, *48* (10), 2744–2753.

(121) Borovik, A. S. Bioinspired Hydrogen Bond Motifs in Ligand Design: The Role of Noncovalent

Interactions in Metal Ion Mediated Activation of Dioxygen. *Acc. Chem. Res.* **2005**, *38* (1), 54–61.

(122) Stone, K. L.; Borovik, A. S. Lessons from Nature: Unraveling Biological C–H Bond Activation. *Curr. Opin. Chem. Biol.* **2009**, *13* (1), 114–118.

(123) Shook, R. L.; Gunderson, W. A.; Greaves, J.; Ziller, J. W.; Hendrich, M. P.; Borovik, A. S. A Monomeric MnIII-Peroxo Complex Derived Directly from Dioxygen. *J. Am. Chem. Soc.* **2008**, *130* (28), 8888–8889.

(124) Parham, J. D.; Wijeratne, G. B.; Rice, D. B.; Jackson, T. A. Spectroscopic and Structural Characterization of Mn(III)-Alkylperoxo Complexes Supported by Pentadentate Amide-Containing Ligands. *Inorg. Chem.* **2018**, *57* (5), 2489–2502.

(125) Lipowicz, B.; Hanekop, N.; Schmitt, L.; Proksch, P. Marine Drugs An Aeroplysinin-1 Specific Nitrile Hydratase Isolated from the Marine Sponge Aplysina Cavernicola. *Mar. Drugs* **2013**, *11*, 3046–3067.

(126) Downing, A. N.; Coggins, M. K.; Chaau Yan Poon, P.; Kovacs, J. A. Influence of Thiolate versus Alkoxide Ligands on the Stability of Crystallographically Characterized Mn(III)-Alkylperoxo Complexes. *J. Am. Chem. Soc.* **2021**, *143* (16), 6104–6113.

(127) Brown, C. D.; Neidig, M. L.; Neibergall, M. B.; Lipscomb, J. D.; Solomon, E. I. VTVH-MCD and DFT Studies of Thiolate Bonding to [FeNO]7/[FeO2]8 Complexes of Isopenicillin N Synthase: Substrate Determination of Oxidase versus Oxygenase Activity in Nonheme Fe Enzymes. *J. Am. Chem. Soc.* **2007**, *129* (23), 7427–7438.

(128) Kennepohl, P.; Neese, F.; Schweitzer, D.; Jackson, H. L.; Kovacs, J. A.; Solomon, E. I.

Spectroscopy of Non-Heme Iron Thiolate Complexes: Insight into the Electronic Structure of the Low-Spin Active Site of Nitrile Hydratase. *Inorg. Chem.* **2005**, *44*, 1826–1836.

(129) Green, M. T. Role of the Axial Ligand in Determining the Spin State of Resting Cytochrome P450. *J. Am. Chem. Soc.* **1998**, *120* (41), 10772–10773.

(130) Groves, J. T. Using Push to Get Pull. *Nat. Chem. 2014 62* **2014**, *6* (2), 89–91.

(131) Dawson, J. H.; Holm, R. H.; Trudell, J. R.; Barth, G.; Linder, R. E.; Bunnenberg, E.; Djerassi, C. Chloroperoxidase. Evidence for P-450 Type Heme Environment from Magnetic Circular Dichroism Spectroscopy. *J. Am. Chem. Soc.* **1976**, *98* (12), 3709–3710.

(132) Yamaguchi, K.; Watanabe, Y.; Morishima, I. Direct Observation of the Push Effect on the Oxygen-Oxygen Bond Cleavage of Acylperoxoiron(III) Porphyrin Complexes. *J. Am. Chem. Soc.* **2002**, *115* (10), 4058–4065.

(133) Geri, J. B.; Shanahan, J. P.; Szymczak, N. K. Testing the Push–Pull Hypothesis: Lewis Acid Augmented N2 Activation at Iron. *J. Am. Chem. Soc.* **2017**, *139* (16), 5952–5956.

(134) Jeschke, G. EPR Techniques for Studying Radical Enzymes. *Biochim. Biophys. Acta - Bioenerg.* **2005**, *1707* (1), 91–102.

(135) Šrajer, V.; Schmidt, M. Watching Proteins Function with Time-Resolved X-Ray Crystallography. *J. Phys. D. Appl. Phys.* **2017**, *50* (37).

(136) Groysman, S.; Holm, R. H. Biomimetic Chemistry of Iron, Nickel, Molybdenum, and Tungsten in Sulfur-Ligated Protein Sites. *Biochemistry* **2009**, *48* (11), 2310.

(137) Shoner, S. C.; Nienstedt, A. M.; Ellison, J. J.; Kung, I. Y.; Barnhart, D.; Kovacs, J. A. Structural

Comparison of Five-Coordinate Thiolate-Ligated MII = FeII, CoII, NiII, ZnII Ions Wrapped in a Chiral Helical Ligand. *Inorg. Chem.* **1998**, *9* (17), 5721–5726.

(138) Shearer, J.; Kung, I. Y.; Lovell, S.; Kaminsky, W.; Kovacs, J. A. Why Is There an " Inert " Metal Center in the Active Site of Nitrile Hydratase? Reactivity and Ligand Dissociation from a Five-Coordinate Co(III) Nitrile Hydratase Model. *J. Am. Chem. Soc.* **2001**, *16* (35), 733–736.

(139) Coggins, M. K.; Toledo, S.; Shaffer, E.; Kaminsky, W.; Shearer, J.; Kovacs, J. A. Characterization and Dioxygen Reactivity of a New Series of Coordinatively Unsaturated Thiolate-Ligated Manganese(II) Complexes. *Inorg. Chem.* **2012**, *51*, 6633–6644.

(140) Coggins, M. K.; Sun, X.; Kwak, Y.; Solomon, E. I.; Rybak-Akimova, E.; Kovacs, J. A. Characterization of Metastable Intermediates Formed in the Reaction between a Mn(II) Complex and Dioxygen, Including a Crystallographic Structure of a Binuclear Mn(III)-Peroxo Species. *J. Am. Chem. Soc.* **2013**, *135* (15), 5631–5640.

(141) Coggins, M. K.; Martin-Diaconescu, V.; Debeer, S.; Kovacs, J. A. Correlation Between Structural, Spectroscopic, and Reactivity Properties Within a Series of Structurally Analogous Metastable Manganese(III)-Alkylperoxo Complexes. *J. Am. Chem. Soc.* **2013**, *135*, 4260–4272.

(142) Coggins, M. K.; Downing, A. N.; Kaminsky, W.; Kovacs, J. A. Comparison of Two Mn^{IV} Mn^{IV} -Bis-μ-Oxo Complexes $\{[Mn^{IV}(N_4(6\text{-Me-DPEN}))]_2(\mu\text{-}O)_2\}^{2+}$ and $\{[Mn^{IV}(N_4(6\text{-Me-DPPN}))]_2(\mu\text{-}O)_2\}^{2+}$. *Acta Crystallogr. Sect. E Crystallogr. Commun.* **2020**, *76* (7), 1042–1046.

(143) Hua-Fen Hsu; Yanhong Dong; Lijin Shu; Victor G. Young, J. . and; Lawrence Que, J. . Crystal Structure of a Synthetic High-Valent Complex with an Fe2(μ-O)2 Diamond Core. Implications for the Core Structures of Methane Monooxygenase Intermediate Q and Ribonucleotide Reductase Intermediate X. *J. Am. Chem. Soc.* **1999**, *121* (22), 5230–5237.

(144) Rohde, J.-U.; In, J.-H.; Lim, M. H.; Brennessel, W. W.; Bukowski, M. R.; Stubna, A.; Münck, E.; Nam, W.; Que, L. Crystallographic and Spectroscopic Characterization of a Nonheme Fe(IV)=O Complex. *Science.* **2003**, *299* (5609), 1037–1039.

(145) Bukowski, M. R.; Koehntop, K. D.; Stubna, A.; Bominaar, E. L.; Halfen, J. A.; Münck, E.; Nam, W.; Que, L. A Thiolate-Ligated Nonheme Oxoiron(IV) Complex Relevant to Cytochrome P450. *Science.* **2005**, *310* (5750), 1000–1002.

(146) McDonald, A. R.; Van Heuvelen, K. M.; Guo, Y.; Li, F.; Bominaar, E. L.; Münck, E.; Que, L. Characterization of a Thiolato Iron(III) Peroxy Dianion Complex. *Angew. Chem. Int. Ed. Engl.* **2012**, *51* (36), 9132–9136.

(147) Jiang, Y.; Widger, L. R.; Kasper, G. D.; Siegler, M. A.; Goldberg, D. P. Iron(II)-Thiolate S-Oxygenation by O 2 : Synthetic Models of Cysteine Dioxygenase. *J. Am. Chem. Soc.* **2010**, *132*, 12214–12215.

(148) Gordon, J. B.; Mcgale, J. P.; Prendergast, J. R.; Shirani-Sarmazeh, Z.; Siegler, M. A.; Jameson, G. N. L.; Goldberg, D. P. Structures, Spectroscopic Properties, and Dioxygen Reactivity of 5-and 6-Coordinate Nonheme Iron(II) Complexes: A Combined Enzyme/Model Study of Thiol Dioxygenases. *J. Am. Chem. Soc.* **2018**, *140* (44), 14807–14822.

(149) Shepherd, H. J.; Gural'skiy, I. A.; Quintero, C. M.; Tricard, S.; Salmon, L.; Molnár, G.;

Bousseksou, A. Molecular Actuators Driven by Cooperative Spin-State Switching. *Nat. Commun. 2013 41* **2013**, *4* (1), 1–9.

(150) Dattler, D.; Fuks, G.; Heiser, J.; Moulin, E.; Perrot, A.; Yao, X.; Giuseppone, N. Design of Collective Motions from Synthetic Molecular Switches, Rotors, and Motors. *Chem. Rev.* **2019**, *120* (1), 310–433.

(151) Conner, K. P.; Woods, C.; Atkins, W. M. Interactions of Cytochrome P450s with Their Ligands. *Arch. Biochem. Biophys.* **2011**, *507* (1), 56.

(152) Gütlich, P.; Gaspar, A. B.; Garcia, Y. Spin State Switching in Iron Coordination Compounds. *Beilstein J. Org. Chem.* **2013**, *9* (1), 342–391.

(153) Nihei, M.; Shiga, T.; Maeda, Y.; Oshio, H. Spin Crossover Iron(III) Complexes. *Coord. Chem. Rev.* **2007**, *251*, 2606–2621.

(154) Jenkins, D. M.; Di Bilio, A. J.; Allen, M. J.; Betley, T. A.; Peters, J. C. Elucidation of a Low Spin Cobalt(II) System in a Distorted Tetrahedral Geometry. *J. Am. Chem. Soc.* **2002**, *124* (51), 15336–15350.

(155) Alvarez, S.; Cirera, J. How High the Spin? Allowed and Forbidden Spin States in Transition-Metal Chemistry. *Angew. Chemie Int. Ed.* **2006**, *45* (19), 3012–3020.

(156) Tangen, E.; Conradie, J.; Ghosh, A. Bonding in Low-Coordinate Environments: Electronic Structure of Pseudotetrahedral Iron-Imido Complexes. *J. Chem. Theory Comput.* **2007**, *3* (2), 448–457.

(157) Hoffmann, R.; Alvarez, S.; Mealli, C.; Falceto, A.; Thomas J. Cahill, I.; Zeng, T.; Manca, G.

From Widely Accepted Concepts in Coordination Chemistry to Inverted Ligand Fields. *Chem. Rev.* **2016**, *116* (14), 8173–8192.

(158) Milocco, F.; de Vries, F.; A Bartels, I. M.; A Havenith, R. W.; Cirera, J.; Demeshko, S.; Meyer, F.; Otten, E. Electronic Control of Spin-Crossover Properties in Four-Coordinate Bis(Formazanate) Iron(II) Complexes. **2020**, *19*, 30.

(159) Travieso-Puente, R.; Broekman, J. O. P.; Chang, M.-C.; Demeshko, S.; Meyer, F.; Otten, E. Spin-Crossover in a Pseudo-Tetrahedral Bis(Formazanate) Iron Complex. *J. Am. Chem. Soc.* **2016**, *138* (17), 5503–5506.

Chapter 2: Dioxygen Activation and Observation of Resulting Fe-Intermediates by a Sterically Constrained Thiolate-Ligated Fe^{II} Complex

2.1 Introduction

The mechanism of CDO-promoted cysteine oxidation is not yet well understood. The catalytically active Fe^{II} site of CDO is ligated by three histidine residues and a water molecule as discussed in **Chapter 1** (**Scheme 1.5**).[1,2] The proposed mechanism of CDO involves the initial binding of free cysteine substrate to the non-heme Fe^{II} active site to form the resting state. The cysteine bound to the Fe^{II}-center lowers the activation barrier to dioxygen binding, due to the thiolate-induced nephelauxetic effect.[3] Dioxygen binds to the Fe^{II} center, *cis* to the cysteine, resulting in the formation of an Fe^{III}-superoxo intermediate. The Fe^{III}-superoxo is then proposed to attack the adjacent thiolate sulfur to afford a unique bicyclic peroxythiolate Fe^{II} intermediate (***Figure 2.1***). Heterolytic cleavage of the peroxythiolate O—O bond is then proposed to afford a singly oxygenated sulfenate ($RS\text{-}O^{-}$)-ligated high-valent Fe^{IV}-oxo. The Fe^{IV}-oxo modality is then proposed to attack the sulfenate sulfur to form a second S—O bond resulting in the formation of a cysteine-sulfinic acid (RS(O)—O–)-Fe^{II} intermediate.

Observation of these Fe-dioxygen intermediates proposed for CDO has proven to be difficult in the enzymatic system. As CDO intermediates are difficult to isolate and characterize, biomimetic models have been utilized to further study and assign the transiently observed intermediate. In recent studies, the TD-DFT calculated and experimental electronic absorption spectrum of rare biomimetic Fe^{III}-superoxo species, $[Fe^{III}(S_2{}^{Me2}N_2N^{H}(Pr,Pr))(O_2)]$[4] (**1-$O_2$**), was found to be similar to that of the short-lived CDO intermediate supporting its identity as an Fe^{III}-

superoxo. The singly-oxygenated sulfenate intermediate for CDO has not yet been observed in the enzyme. However, our group has shown two Fe-sulfenate species $[Fe^{III}(ADIT\text{-}O(ADIT)]^{+}$ formed through the addition of tert-butyl N-sulfonyloxaziridine[5] and $[Fe^{III}(\eta^2\text{-}S^{Me2}O)(S^{Me2}N_2N^{H}(Pr,Pr)]^{+}$ (**2**) formed from the addition of an oxo-atom donor, PhIO, and/or dioxygen.[4,6] Dioxygen derived Fe^{III}-sulfenate species, with a thiolate in the coordination sphere, are applicable to studying the sulfur oxygenation process of CDO. The following chapter will discuss how the addition of steric constraints (N^{Me}) to form **3** promotes the formation of Fe-dioxygen derived intermediates that are applicable to the CDO system, including the implied formation of the peroxythiolate intermediate (***Figure 2.1***).

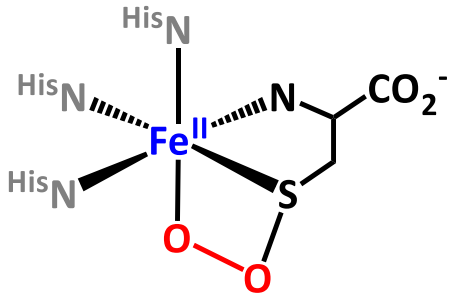

Figure 2.1 ChemDraw structure of the proposed peroxythiolate intermediate of CDO.

2.2 Sterically Constrained Thiolate-Ligated 3

To expand our understanding of how ligand constraints and thiolates control reactivity, Fe^{II} complexes containing various ligand constraints (either increasing or decreasing steric constraints compared to **1** have been synthesized in the Kovacs group, including the replacement of the secondary amine (N^{H}, **1**) to a tertiary amine (N^{Me} **3** and **5**), the *gem*-dimethyl groups to hydrogens ($[Fe^{II}(S_2{}^{H2}N_2N^{H}(Pr,Pr))]$ (**4**)), and the reduction of the propyl amine linker (**1**) to an ethyl

amine linker ([$Fe^{II}(S_2{}^{Me2}N_2N^H(Et,Pr))$] (**6**)). The focus of **Chapter 2** will be on the addition of steric bulk to the N^{amine} to form [$Fe^{II}(S_2{}^{Me2}N_2N^{Me}(Pr,Pr))$] (**3**, ***Figure 2.2***).

The addition of steric bulk to the N^{amine} was hypothesized to reduce the angle of the O_2 binding pocket, which would place the activated Fe^{III}-superoxo species in closer proximity to one of the thiolate arms of the ligand. The measured bond angles showed the expected reduction in the angle of the O_2 binding pocket from 125.7° in **1** to 114.8° in **3**. The smaller angle was expected to facilitate the formation of the peroxythiolate species proposed in the mechanism of CDO (***Figure 2.3***). A method analogous to that used to prepare thiolate ligated **1** was used to synthesize the complexes (**3**-**6**) described herein.[4,7]

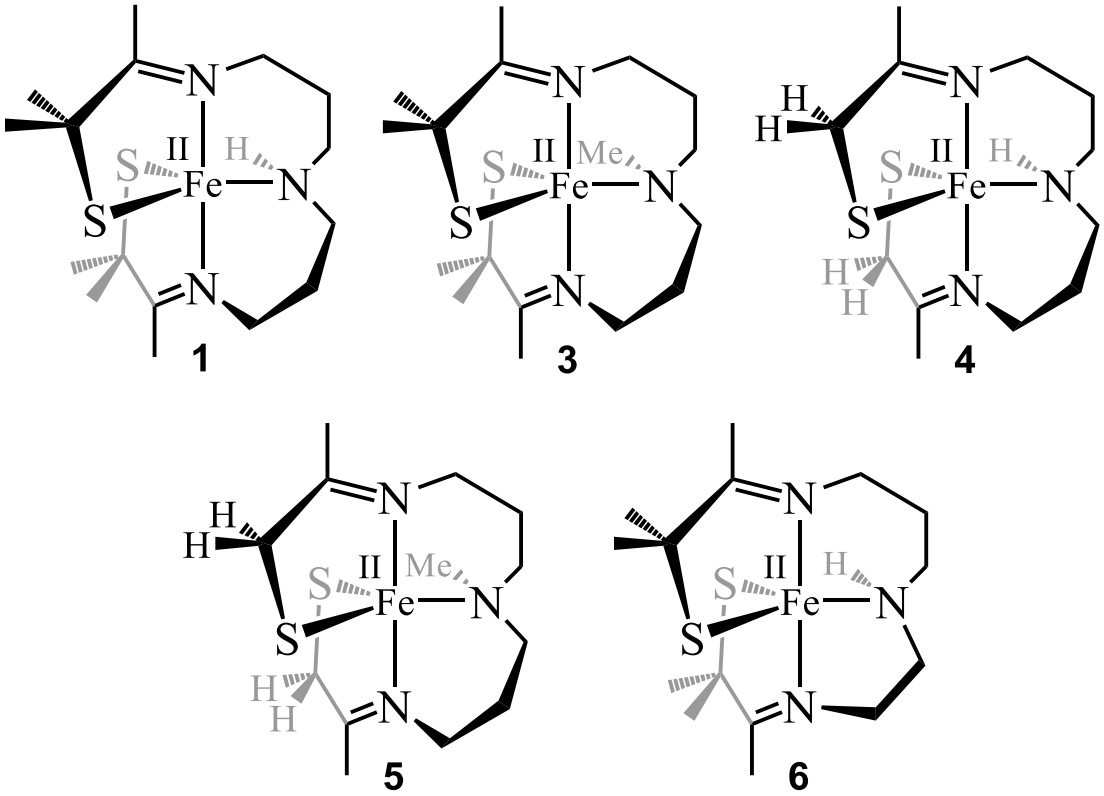

Figure 2.2 ChemDraw structures of the Kovacs group synthesized and crystallographically characterized thiolate-ligated Fe^{II} complexes: [$Fe^{II}(S_2{}^{Me2}N_2N^H(Pr,Pr))$] (**1**); [$Fe^{II}(S_2{}^{Me2}N_2N^{Me}(Pr,Pr))$] (**3**); [$Fe^{II}(S_2{}^{H2}N_2N^H(Pr,Pr))$] (**4**); [$Fe^{II}(S_2{}^{H2}N_2N^{Me}(Pr,Pr))$] (**5**); [$Fe^{II}(S_2{}^{Me2}N_2N^H(Et,Pr))$] (**6**).

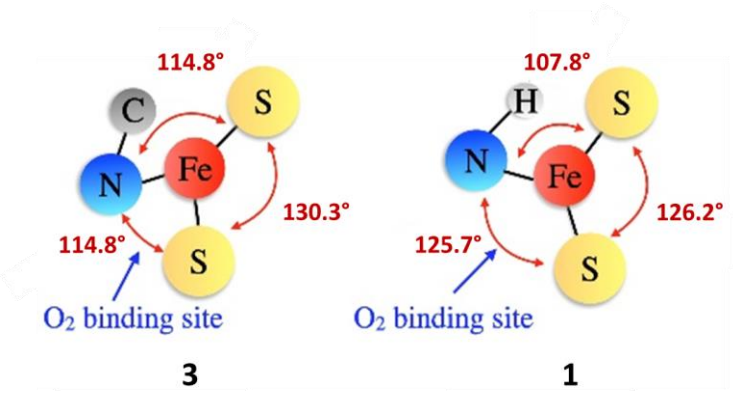

Figure 2.3 Diagram showing the change in the equatorial angles of **3** and **1** especially with regards to the O_2 binding site.

2.2.1 Structural Characterization Fe^{II} of 3 and Comparison to Other Fe^{II} Complexes

Single crystals suitable for X-ray diffraction of [Fe^{II}($S_2^{Me2}N_2N^{Me}$(Pr,Pr))] (**3**) were obtained by layering pentane onto a concentrated THF solution of the complex, yielding green needle-like crystals (***Figure 2.4*** and ***Table 2.1***). The X-ray structure showed the asymmetric unit consists of half of the molecule, with the amine backbone disordered across two positions. The complex structure was completed by a 180° rotation about the Fe—N(2) axis. The structure belonged to the C2/c space group different from the other propyl linked Fe^{II} complexes (**1** and **4**-**5**), which were all in the P 21/c space group.[4,7,8] The ethyl linked **6** also had a different space group from the majority of Fe^{II} complexes of P bca.[9] Across the series, the bond lengths were consistent with an *S* = 2 Fe^{II} complex.

The Fe—N^{im}_{avg} = 2.153(5) Å distance of **3** was within error of that for **1** (2.169(16) Å) and **5** (2.138(16) Å) (***Table 2.2***). The Fe—N^{im}_{avg} = 2.176(4) Å for **4** was longer than for **3**, (**4** included β-hydrogens that would be expected to lengthen bonds). The Fe—N^{im}_{avg} = 2.118(18) Å for **6**

demonstrated a large contraction compared to **3**, consistent with the large geometric rearrangement required from the change of the ethyl linker (**6**) to a propyl linker (**3**) along with the difference in N^{H} (**6**) to N^{Me} (**3**). The Fe—N^{amine} distances were unique for each of the Fe^{II} complexes, reflective of the different steric environments (***Table 2.2***). The tertiary amine complexes **3** (Fe—N^{amine} = 2.2204(17) Å) and **5** (Fe—N^{amine} = 2.282(7) Å) showed larger (> 0.039 Å) than the secondary amine propyl-linked complexes **1** (Fe—N^{amine} = 2.1656(16) Å), **4** (Fe—N^{amine} = 2.181(3) Å).. The Fe—S_{avg} bond distances for **3** (Fe—S_{avg} = 2.3285(5) Å) and **1** (Fe—S_{avg} = 2.3245(4) Å) were similar in distance (***Table 2.2***). Both **3** and **1** had the shortest Fe—S bond distances of the Fe^{II} series indicating a stronger covalent interaction with the thiolate arms. The steric restraints of the ethyl linker were likely responsible for the expansion observed in **6** (Fe—S_{avg} = 2.3303(6) Å), while the lack of the *gem*-dimethyl groups resulted in the expanded bond lengths of both **4** (Fe—S_{avg} = 2.853(1) Å) and **5** (Fe—S_{avg} = 2.3590(6) Å).

All of the propyl linked Fe^{II} complexes demonstrated a distorted trigonal pyramidal geometry with the τ-values in the range of 0.72-0.89, indicating that they are closer to trigonal bipyramidal (τ = 1.0) than square pyramidal geometry (τ = 0.0). (***Table 2.2***).[10] The angle of the key dioxygen binding site, N(2)—Fe—S(1)' varied depending on the steric constraints of the complex. In complex **3**, the N(2)—Fe—S(1)' = 114.846(10)° demonstrated a much smaller angle than was seen in **1** (N(2)—Fe—S(1) = 125.70(4)°), which would place the superoxo moiety in closer proximity to the thiolate arm. The S(1)—Fe—S(2) angles for all the Fe^{II} complexes were in the range of 124 – 130° (***Table 2.2***) varying by 6°.

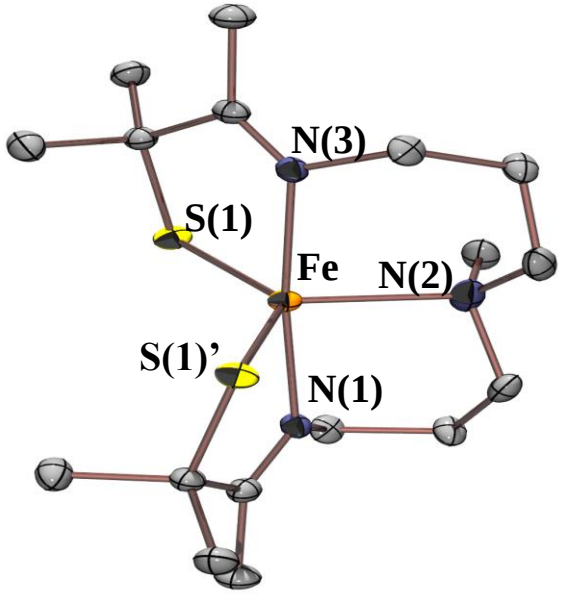

Figure 2.4 ORTEP diagram of [$Fe^{II}(S_2{}^{Me2}N_2N^{Me}(Pr,Pr))$] (**3**) with hydrogens removed, showing thermal ellipsoids at the 50% probability level.

Table 2.1 Crystal Data, Intensity Collections, and Structure Refinement Parameters for **3**.

Empirical formula	C17 H33 Fe N3 S2	
Formula weight	399.43	
Temperature	100(2) K	
Wavelength	0.71073 Å	
Crystal system	Monoclinic	
Space group	C 2/c	
Unit cell dimensions	a = 12.2134(9) Å	α= 90°.
	b = 15.9862(12) Å	β= 110.618(3)°.
	c = 11.0937(8) Å	ϒ = 90°.
Volume	2027.3(3) $Å^3$	
Z	4	
Density (calculated)	1.309 Mg/m^3	
Absorption coefficient	0.953 mm^{-1}	
F(000)	856	
Crystal size	0.160 x 0.110 x 0.090 mm^3	
Theta range for data collection	2.190 to 28.351°.	
Index ranges	-16<=h<=16, -21<=k<=21, -14<=l<=14	
Reflections collected	9917	
Independent reflections	2536 [R(int) = 0.0276]	
Completeness to theta = 25.000°	100.0%	
Absorption correction	Semi-empirical from equivalents	
Max. and min. transmission	0.746 and 0.701	
Refinement method	Full-matrix least-squares on F^2	
Data / restraints / parameters	2536 / 12 / 132	
Goodness-of-fit on F^2	1.053	
Final R indices [I>2sigma(I)]	R1 = 0.0237, wR2 = 0.0567	
R indices (all data)	R1 = 0.0288, wR2 = 0.0591	
Extinction coefficient	n/a	
Largest diff. peak and hole	0.304 and -0.258 e.$Å^{-3}$	

Table 2.2 Selected metrical parameters (Å and °) for thiolate-ligated non-heme Fe^{II} complexes: $[Fe^{II}(S_2^{Me2}N_2N^{H}(Pr,Pr))]$ (**1**); $[Fe^{II}(S_2^{Me2}N_2N^{Me}(Pr,Pr))]$ (**3**); $[Fe^{II}(S_2^{H2}N_2N^{H}(Pr,Pr))]$ (**4**); $[Fe^{II}(S_2^{H2}N_2N^{Me}(Pr,Pr))]$ (**5**); $[Fe^{II}(S_2^{Me2}N_2N^{H}(Et,Pr))]$ (**6**).

	1[4]	**3***	**4**[8]	**5**[8]	**6**[9]
Fe-N(1)	2.1556(16)	2.142(5)	2.168(3)	2.1362(16)	2.1213(18)
Fe-N(2)	2.1656(16)	2.2204(17)	2.181(3)	2.282(7)	2.206(2)
Fe-N(3)	2.1815(15)	2.164(4)	2.183(4)	2.1391(16)	2.1145(18)
Fe-S(1)	2.3306(5)	2.3245(4)	2.363(1)	2.3655(6)	2.3396(6)
Fe-S(2)	2.3263(5)	2.3245(4)	2.342(1)	2.3524(6)	2.3210(6)
N(1)-Fe-N(3)	172.81(6)	174.35(14)	167.7(1)	179.85(6)	162.39(7)
N(1)-Fe-N(2)	83.80(6)	90.2(3)	87.6(1)	86.68(11)	78.40(7)
N(1)-Fe-S(1)	97.68(5)	81.9(3)	82.9(1)	82.70(5)	81.53(5)
N(1)-Fe- S(2)	81.21(4)	102.79(10)	104.7(1)	99.17(5)	105.59(6)
N(3)-Fe-N(2)	90.96(6)	90.2(3)	80.3(1)	83.64(11)	84.35(7)
N(3)-Fe-S(1)	81.36(4)	98.60(10)	101.7(1)	104.38(5)	106.98(5)
N(3)-Fe- S(2)	105.16(4)	81.3(3)	82.3(1)	82.61(5)	82.44(5)
N(2)-Fe-S(1)	125.70(4)	114.845(10)	121.6(1)	116.77(17)	128.58(6)
N(2)-Fe- S(2)	107.79(4)	114.846(10)	114.0(1)	116.82(17)	105.81(6)
S(1)-Fe- S(2)	126.17(2)	130.31(2)	124.3(1)	126.39(2)	125.14(2)
τ	0.78	0.73	0.72	0.89	0.56
Symmetry operation	n/a	-x+2,y,-z+3/2	n/a	n/a	n/a

*For **3** N(3) = N(1)' and S(2) = S(1)'

2.2.2 Solution State Characterization of 3

The solution state behavior of **3** differentiated it from the less constrained **1**. The μ_{eff} = 4.29 B.M. was consistent with an *S* = 2 spin state in MeCN solution, while **1** demonstrated μ_{eff} = 2.63 B.M. consistent with an *S* = 1 spin state in MeCN.[4] In the electronic absorption spectrum, there was one key visible band at λ_{max} = 430 nm (ε = 800 cm^{-1} M^{-1}) in THF (***Figure 2.5***). The band was similar to the band observed for **1** which demonstrated a λ_{max} = 420 nm in THF.[4] The λ_{max} was solvent dependent, which indicated the potential of solvent bound species existing in the solution that may contribute to the spectrum, and/or to the observed reactivity. A > 5 nm shift between

solvents (λ_{max} = 418 nm (DCM), 404 nm (MeOH), 425 nm (MeCN)) (***Figure 2.5***) demonstrated dependence on solvent identity.

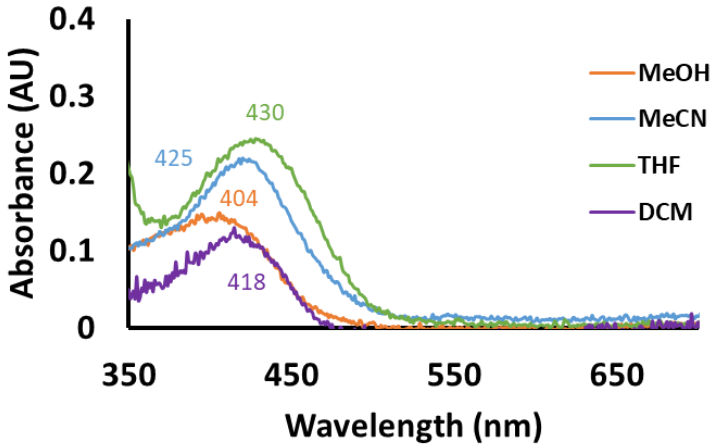

Figure 2.5 Electronic absorbance spectra for 0.230 mM solutions of **3** in various solvents illustrating the solvent dependence of the λ_{max} at room temperature.

2.2.3 DFT Modeling of Fe^{II} 3 and 1

In order to investigate the electronic structure of **3**, DFT modeling of both **3** and **1** was completed with ORCA calculations using a PBE0 functional and def2-TZVP basis set. The insights into the nature of the transition bands and the calculated Mulliken charge helped to establish whether the steric constraint of the N^{Me} of **3** resulted in electronic, steric or a combination of these effects. The optimized geometries showed the lowest error with regards to the crystallographically determined bond distances with an *S* = 2 ground state (***Table 2.3***) for both **1** and **3**. This indicated the *S* = 1 magnetic susceptibility found for **1** may be due to some interactions with the MeCN solvent. An *S* = 2 ground state was also supported by the calculation of the relative

energy for each possible spin-state (*S* = 0, 1, 2) of **3** (***Figure 2.6***) with both PBE0 and B3LYP functionals.

The TD-DFT calculated spectrum for **3** with the PBE0 functional and an *S* = 2 spin state demonstrated transitions at 372, 377, and 409 nm (***Figure 2.7***) consistent with the experimentally observed spectrum (***Figure 2.5***). The natural transition orbital analysis of these key transitions in the 300-450 nm region showed the participation of the thiolate donation of election density into the Fe and ligand orbitals (S → Fe + ligand charge transfer). The calculated Mulliken charges for both **1** and **3** are summarized in ***Table 2.4***. For both the *S* = 1 and *S* = 2 spin-states, the Mulliken charges of the Fe ions were very similar between **1** and **3**, which indicated the similar Lewis acidity for both complexes. However, there was a shift to a less positive charge (0.559 → 0.345 for **1**, and 0.559 → 0.381 for **3**) between the *S* = 2 and *S* = 1 states. If **1** and **3** exist in different spin-states in all solutions (as is the case in MeCN, **Section 2.2.2**), there would be differences in the electronic environment.

Table 2.3 Selected bond lengths (Å), percent error from crystallographically obtained distances and τ values from PBE0 DFT calculated geometry optimizations for Fe^{II} Complexes **1** and **3**.

1						
	S = 0	% error	*S* = 1	% error	*S* = 2	% error
Fe-N(1)	1.961	9.03	1.959	9.12	2.171	0.73
Fe-N(2)	2.111	2.52	2.175	0.43	2.218	2.43
Fe-N(3)	1.958	10.25	1.955	10.38	2.175	0.28
Fe-S(1)	2.226	4.49	2.242	3.80	2.295	1.53
Fe-S(2)	2.283	1.86	2.265	2.64	2.307	0.84
τ	0.68	12.82	0.64	17.95	0.58	25.64
3						
	S = 0	% error	*S* = 1	% error	*S* = 2	% error
Fe-N(1)	1.950	8.96	1.949	9.01	2.154	0.56
Fe-N(2)	2.205	0.68	2.262	1.89	2.289	3.11
Fe-N(1)'	1.953	9.75	1.948	9.98	2.138	1.20
Fe-S(1)	2.273	2.19	2.242	3.53	2.317	0.30
Fe-S(1)'	2.232	3.96	2.264	2.58	2.303	0.90
τ	0.67	8.22	0.63	13.70	0.57	21.92

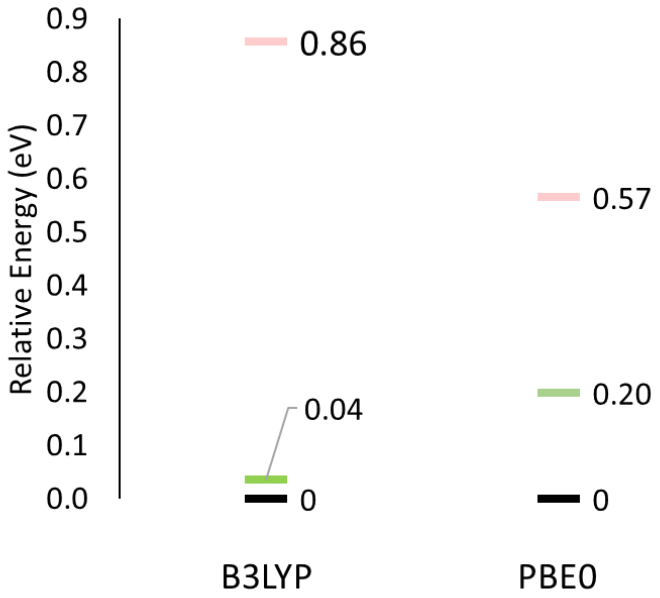

Figure 2.6 Relative energy diagram calculated for **3** with B3LYP and PBE0 *S* = 2 ground state (black), *S* = 1 (green), and *S* = 0 (peach).

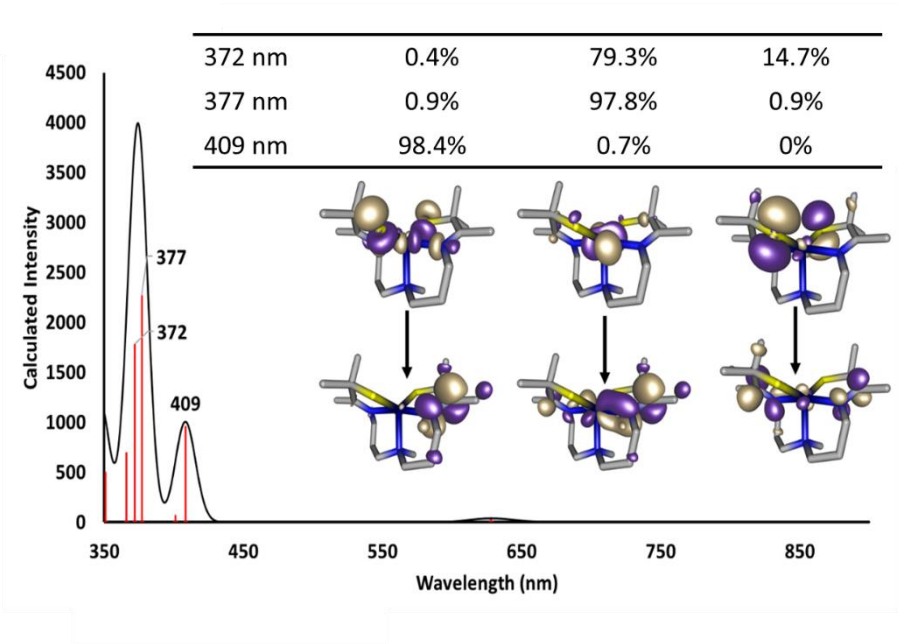

Figure 2.7 TD-DFT calculated spectrum with PBE0 functional and def2-TZVP basis set for **3** (*S* = 2) with the NTO orbitals of the major contribution to the key transitions in the 300-450 nm region.

Table 2.4 Calculated Mulliken charges for primary coordination sphere and Fe ion of **1** and **3** at for both *S* = 1 and *S* = 2 spin-states.

	1 (*S* = 2)	**3** (*S* = 2)	**1** (*S* = 1)	**3** (*S* = 1)
Fe^{II}	0.559	0.559	0.345	0.381
N(2)	-0.455	-0.828	-0.519	-0.825
S(1)	-0.542	-0.520	-0.509	-0.499
S(2)	-0.538	-0.524	-0.502	-0.501
N(1)	-0.595	-0.619	-0.503	-0.472
N(3)	-0.541	-0.543	-0.464	-0.558

2.3 Dioxygen Reactivity of 3

2.3.1 Room Temperature Dioxygen Reactivity of 3

The exposure of a THF solution of **3** to dioxygen at room temperature (via the addition of either air or dry O_2) resulted in the formation of a new dark green species at with λ_{max} = 650 nm (***Figure 2.8***). The species was relatively stable (> 1 hour lifetime) at room temperature compared to **1-O$_2$**, which rapidly converted to sulfenate **2**. The significant shift to λ_{max} = 650 nm indicated the species was likely not a sulfenate product formed from dioxygen, but another dioxygen-derived intermediate species. The characterization of the sulfenate species $[Fe^{III}(\eta^2\text{-}S^{Me2}O)(S^{Me2}N_2N^{Me}(Pr,Pr)]^+$ (**7**) will be discussed in **Chapter 3**. Sulfenate **7** demonstrated a λ_{max} = 509 nm, which eliminated it as the identity of the green species. Further characterization of the green species is discussed in **Section 2.4**.

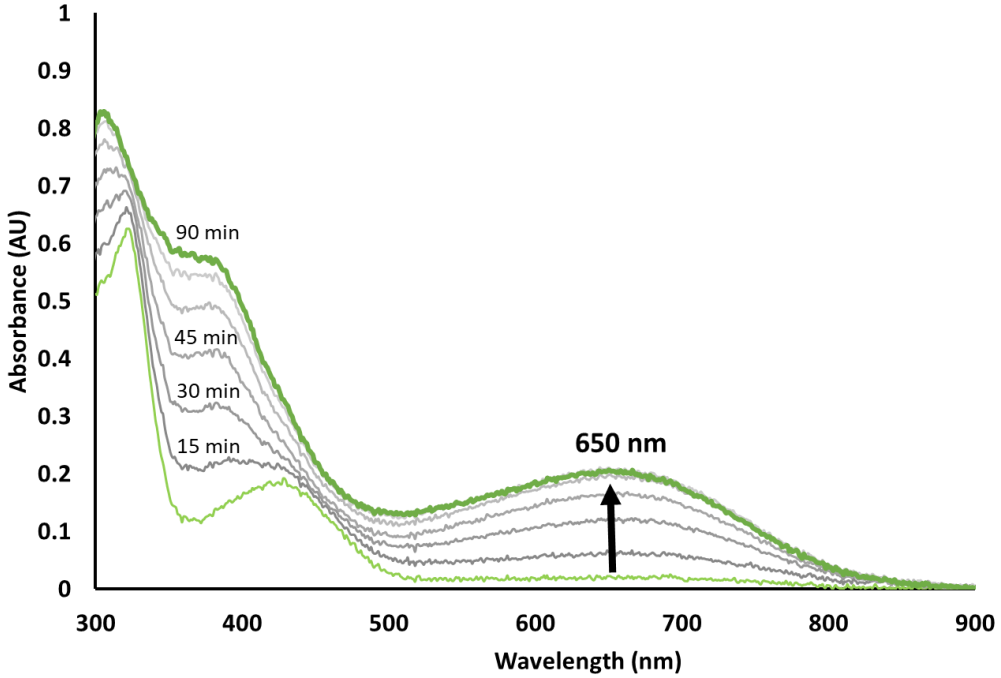

Figure 2.8 EAS monitoring the formation of the green intermediate (λ_{max} = 650 nm) from the addition of dioxygen to a THF solution of **3** (0.230 mM) at room temperature.

2.3.2 Low Temperature Dioxygen Reactivity of 3

The addition of dioxygen was also explored at low temperatures. At -73 °C, a different purple intermediate was formed with λ_{max} = 529 and 670 nm (***Figure 2.9***). The λ_{max} are similar to those found for the secondary amine (N^H) superoxo species **1-O_2** (λ_{max} = 400, 523, and 707 nm).[4] The similarities in EAS supported the purple intermediate as being a superoxo species **3-O_2,** although further characterization is necessary. Both bands appeared to grow in concurrently over the course of the reaction. At 40 °C, a broadened band centered around λ_{max} = 650 nm grew in. The broadness could have been the result of concurrent growth of both the purple and green intermediates (***Figure 2.10***). The superoxo species **1-O_2** was demonstrated to abstract H atoms from THF to form a putative hydroperoxo species **1-OOH**. In the case that **3-O_2** was also able to abstract an H-atom from THF as well, low temperature reactivity was also explored in higher BDE solvent DCM to potentially isolate the proposed superoxo species [$Fe^{III}(S_2{}^{Me2}N_2N^{Me}(Pr,Pr))(O_2)$] **3-$O_2$**. Upon exposure of **3** to dioxygen in DCM at -73 °C, bands with λ_{max} = 517 and 696 nm (***Figure 2.11***) grew in over 5.5 hours. The bands at λ_{max} = 517 and 696 nm were similar to both the bands observed from the reaction of **3** and dioxygen in THF (λ_{max} = 529 and 670 nm, ***Figure 2.10***) and **1-O_2** (λ_{max} = 400, 523, and 707 nm).[4] The bands observed in DCM were less broadened than in those observed in THF. The broadening could have been due to H-bonding from THF, or an indication that the intermediate was able to form with fewer side products in DCM.

Similarly, to the reaction demonstrated at room temperature (**Section 2.3.1**), the THF solutions of **3** converted to the green intermediate (***Figure 2.8***) and did not proceed to convert to **7**. The reaction in DCM, once warmed to room temperature, converted to a pink species with λ_{max} = 512 nm (***Figure 2.12***). The spectrum observed was consistent with the expected

absorbance for the sulfenate **7**. The differences in low-temperature reactivity indicated the solvent environment is an important factor in the reaction pathway of the thiolate-ligated Fe^{II} complexes and dioxygen. Further characterization of the low-temperature intermediates and their solvent dependence will be the focus of future studies in the Kovacs group.

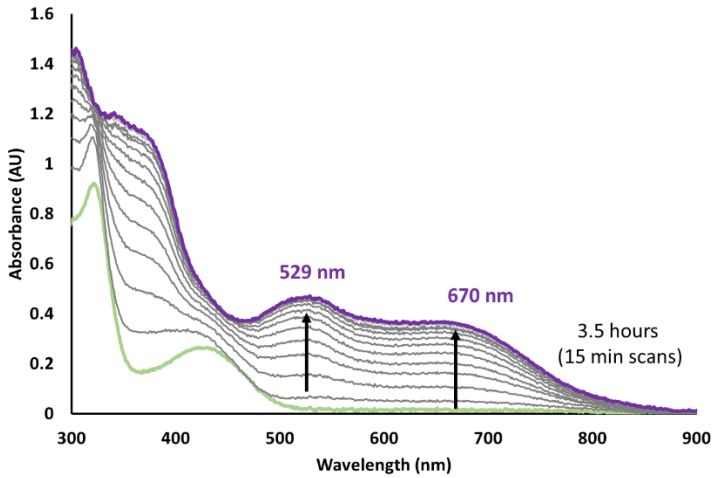

Figure 2.9 EAS monitoring the formation of a dioxygen-derived intermediate (λ_{max} = 529 and 670 nm) from the addition of dioxygen to a THF solution of **3** (0.230 mM) at -73 °C.

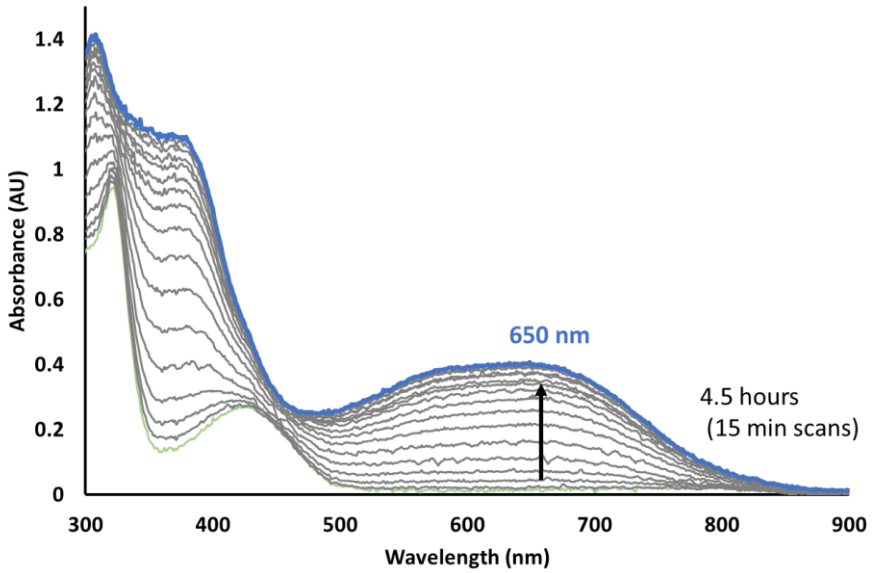

Figure 2.10 EAS monitoring the formation of a dioxygen-derived intermediate (λ_{max} = broad 650 nm) from the addition of dioxygen to a THF solution of **3** (0.230 mM) at -40 °C.

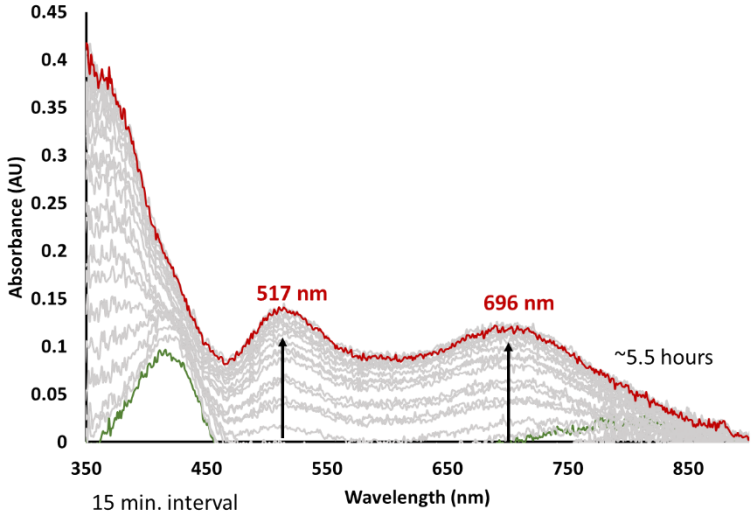

Figure 2.11 EAS monitoring the formation of a dioxygen-derived intermediate (λ_{max} = 517 and 696 nm) from the addition of dioxygen to a DCM solution of **3** (0.230 mM) at -73 °C.

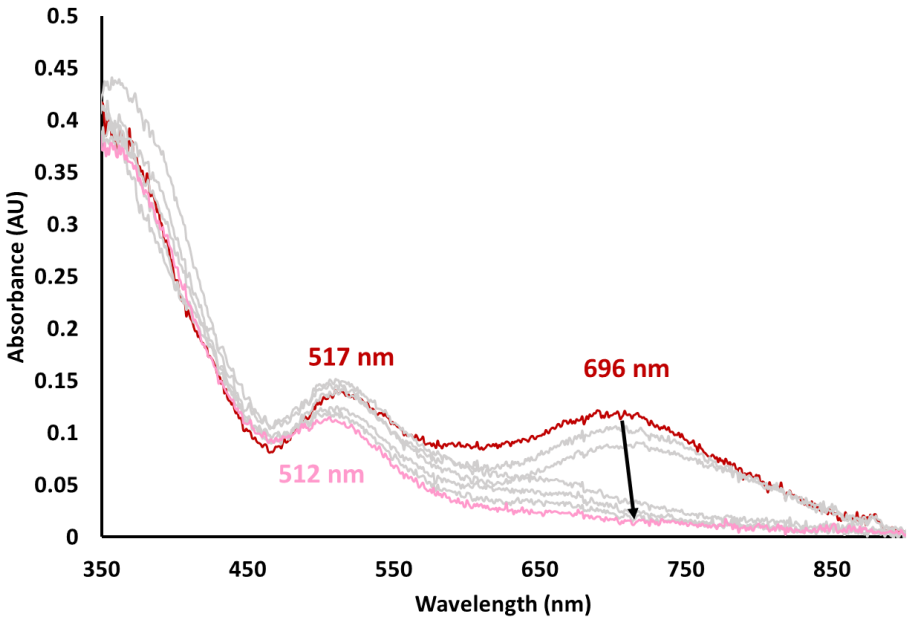

Figure 2.12 EAS monitoring the formation of a sulfenate species (λ_{max} = 512 nm) following a dioxygen-derived intermediate (λ_{max} = 517 and 696 nm) from the addition of dioxygen to a DCM solution of **3** (0.230 mM) warmed to room temperature.

2.3.3 Proposed Mechanisms for Dioxygen Activation

The dioxygen reactivity of sterically constrained **3** differed from the reactivity observed with **1** and dioxygen. The addition of steric bulk to the backbone was expected to push the superoxo species closer to one of the thiolate arms to promote the formation of the proposed peroxythiolate species of CDO (***Figure 2.2***). With these mechanistic hypotheses in mind, **Schemes 2.1**-**2.2** outline the potential intermediates that could result from dioxygen reactivity for both an IPNS-inspired mimic and a CDO-inspired mimic. Previous investigations of the electronic structure of $[Fe^{III}(S_2{}^{Me2}N_2N^H(Pr,Pr))]^+$ **1^{ox}** established that a feature in the 600-700 nm range indicated the presence of a sixth ligand coordinated in the open site of the Fe^{III} ion.[3] The λ_{max} = 650 nm of the green intermediate indicated the species is likely oxidized to an Fe^{III} and had a dioxygen-derived modality bound in the sixth coordination site. Dioxygen activation intermediates inspired by the proposed IPNS pathway (**Scheme 2.1**), would include an Fe^{III}-superoxo (**3-O$_2$**), an Fe^{III}-hydroperoxo (**3-OOH**), a high-valent Fe-oxo (**8**), or an Fe^{III} hydroxide species (**3-OH**). Dioxygen activation intermediates inspired by the proposed CDO pathway (**Scheme 2.2**), would include an Fe^{II}-peroxythiolate species (**9**) (although the Fe^{II} species would not absorb intensely in the visible region); or, following the formation of **9**, a combined sulfenate/high-valent Fe-oxo (**10**) or an Fe^{III}-hydroxy-sulfenate (**11**) following an HAT step that would be accessible by the high-valent Fe-oxo **10**. Further characterizations of the green intermediate were aided by the stability at room temperature and are described in **Section 2.4.**

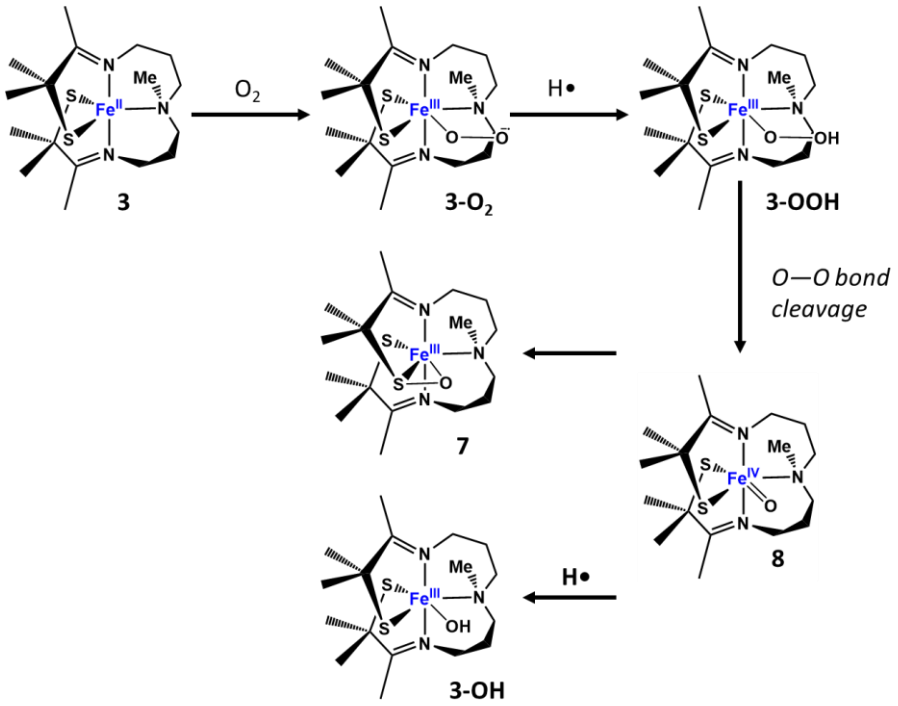

Scheme 2.1 IPNS-mimic pathway for dioxygen activation by **3**, indicating the potential intermediates that may form.

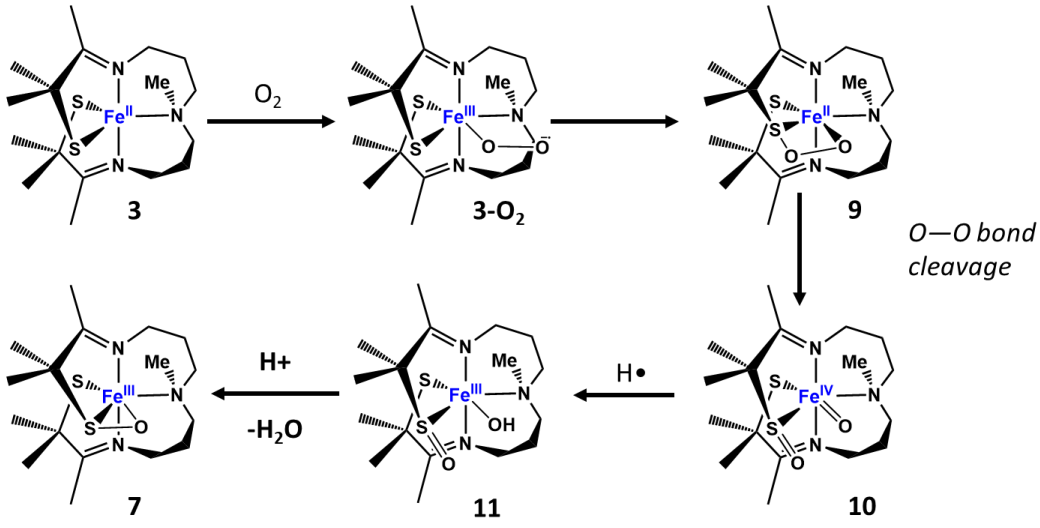

Scheme 2.2 CDO-mimic pathway for dioxygen activation by **3**, indicating the potential intermediates that may form.

2.4 Identification of Hydroxy-Sulfenate 11

2.4.1 Solution State Characterization of 11

2.4.1.1 Infrared Spectroscopy of 11

The potential intermediates outlined in **Schemes 2.1**-**2.2** included three species (**3-OOH**, **3-OH**, and **11**) that would be easily identified by the presence of a $\nu_{O\text{-}H}$ stretch with room temperature IR experiments. An ATR-IR spectrum of a highly concentrated solution (5.11 mM in THF) of **3** exposed to dioxygen through air demonstrated such a $\nu_{O\text{-}H}$ stretch at 3380 cm^{-1}, characteristic of an hydrogen bonded $\nu_{O\text{-}H}$ stretch[11] (***Figure 2.13***). The $\nu_{O\text{-}H}$ was shifted significantly from a free hydroxide ion (3700-3584 cm^{-1}) and was consistent with the OH being bound to an Fe^{III} ion. The confirmation of the $\nu_{O\text{-}H}$ stretch confirmed that the green intermediate could be **3-OOH**, **3-OH**, or **11**. All three species would demonstrate a $\nu_{Fe\text{-}O}$ identified upon isotopic labeling of the dioxygen, but only **11** should also demonstrate a sulfenate $\nu_{S\text{-}O}$ stretch.

Isotopically labeled $^{18}O_2$ was introduced to a THF solution of **3** in a similar manner mentioned above and revealed two isotopically shifted peaks, where 1019 cm^{-1} shifted to 997 cm^{-1} (22 cm^{-1}) consistent with $\nu_{S\text{-}O}$, and where 665 cm^{-1} shifted to 620 cm^{-1} (45 cm^{-1}) consistent with $\nu_{Fe\text{-}O}$ (***Figure 2.14***). The identification of these isotopically sensitive stretches confirmed that dioxygen is involved in the formation of the green intermediate. The IR spectrum was most consistent with the hydroxy-sulfenate **11** intermediate. Based on the reaction pathway outlined in ***Scheme 2.2***, two other intermediates (**9** and **10**) should form after **3-O_2** and before **11**. Therefore, the formation of hydroxy-sulfenate **11** implied the formation of reactive Fe^{II}-peroxythiolate **9** that would promote cleavage of the O—O bond to form **10**. The result confirmed the hypothesis

outlined that the addition of steric bulk on the N^{Me} promoted an interaction between **3-O_2** and one of the thiolate arms of the ligand.

The IR spectrum was reasonably reproduced with DFT calculations of a high spin (*S* = 5/2) **11** (**Figures 2.15**-**2.16**) with the PBE0 functional. Other spin-states calculated (*S* = 1/2: ν_{O-H} = 3808 cm^{-1}; and *S* = 3/2: ν_{O-H} = 3588 cm^{-1}) did not reproduce the shifted ν_{O-H}. The calculated frequency spectrum showed ν_{O-H} = 3392 cm^{-1}, ν_{S-O} = 967 cm^{-1}, and ν_{Fe-O} = 587 cm^{-1}. The calculated $^{18}O_2$ isotopically labeled frequencies shifted the ν_{S-O} to 944 cm^{-1} and ν_{Fe-O} to 565 cm^{-1}. The frequencies identified include complex modes involving both the S—O and the O—H bonds of the complex (***Figure 2.17***). The room temperature stability of **11** is likely aided by the intramolecular H-bonding interactions available between the sulfenate and hydroxide groups.

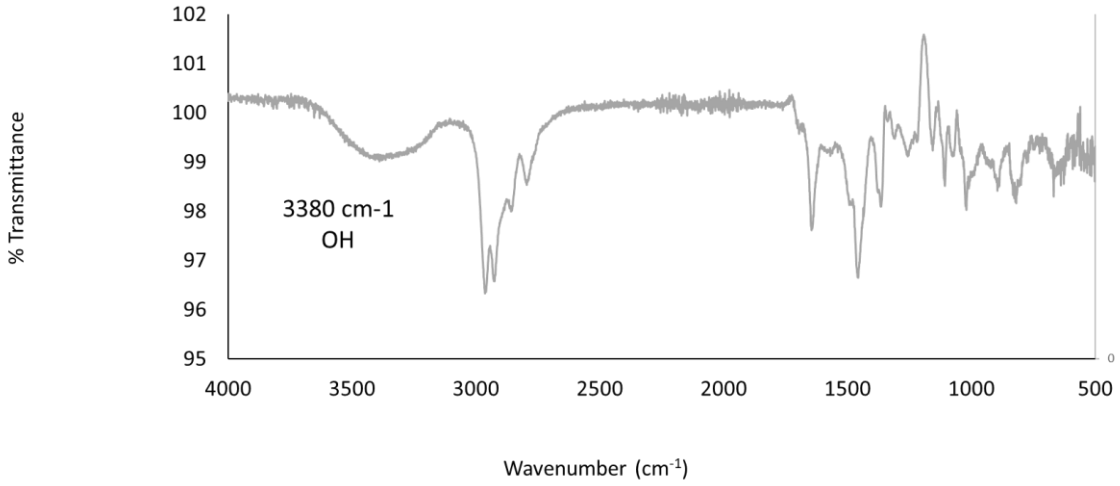

Figure 2.13 ATR-IR spectrum for hydroxy-sulfenate **11** showing characteristic O—H stretch at 3380 cm^{-1}.

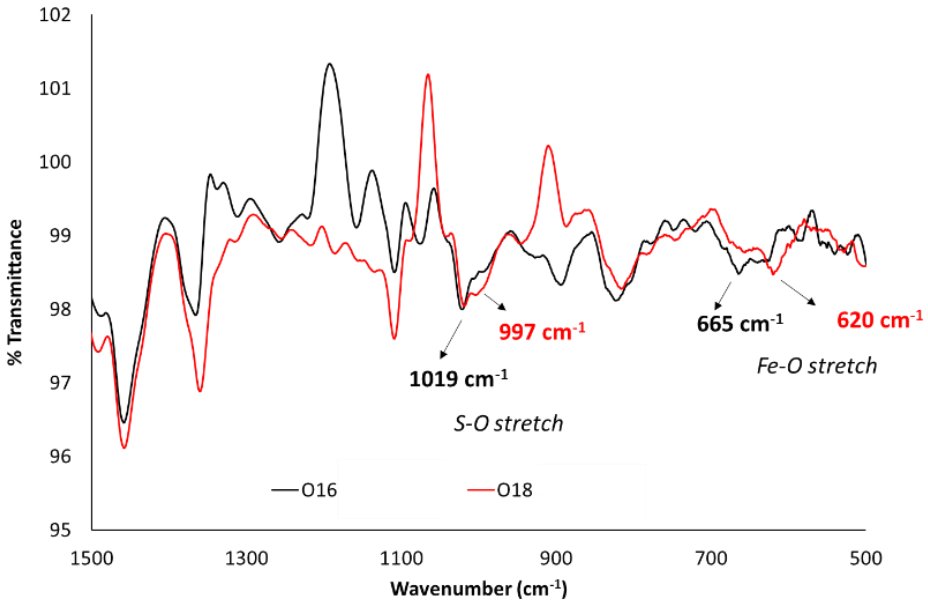

Figure 2.14 ATR-IR spectra of green intermediate species derived from **3** with $^{16}O_2$ (black) and $^{18}O_2$ (red) highlighting the shifted peaks observed indicative of an Fe—O stretch and an S—O stretch present in the spectrum.

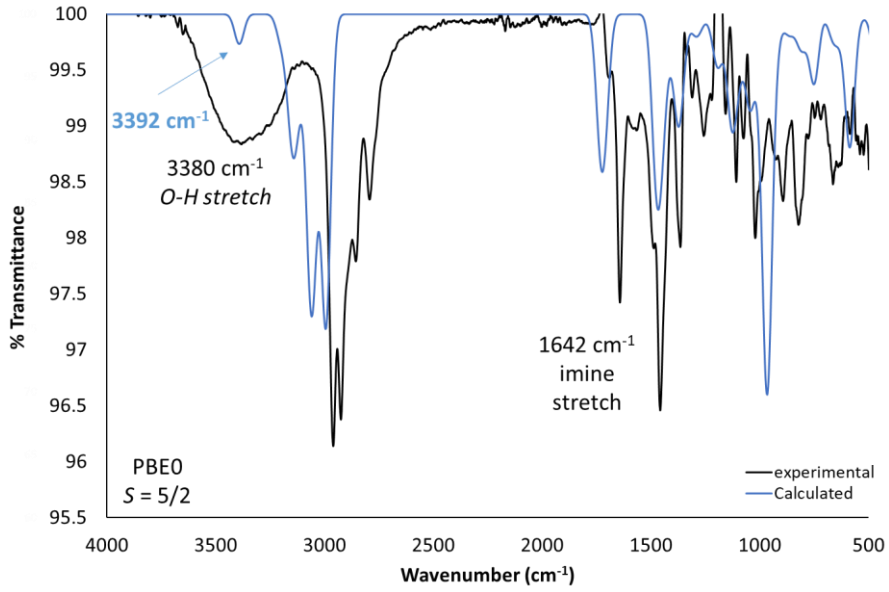

Figure 2.15 Overlay of the calculated IR spectrum for **11** with *S* = 5/2 spin-state and PBE0 functional (blue) with the experimentally determined IR spectrum (black) of the green intermediate from 4000 to 500 cm^{-1}.

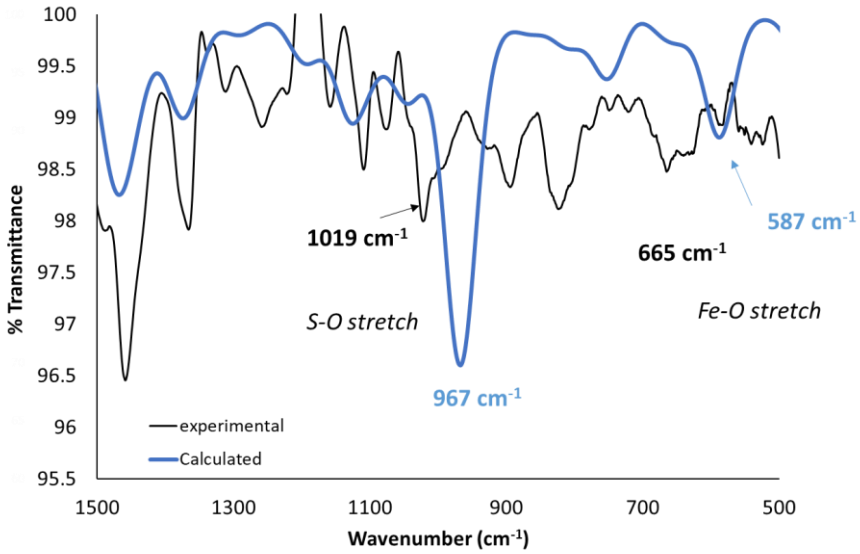

Figure 2.16 Overlay of the calculated IR spectrum for **11** with *S* = 5/2 spin-state and PBE0 functional (blue) with the experimentally determined IR spectrum (black) of the green intermediate from 1500 – 500 cm^{-1}.

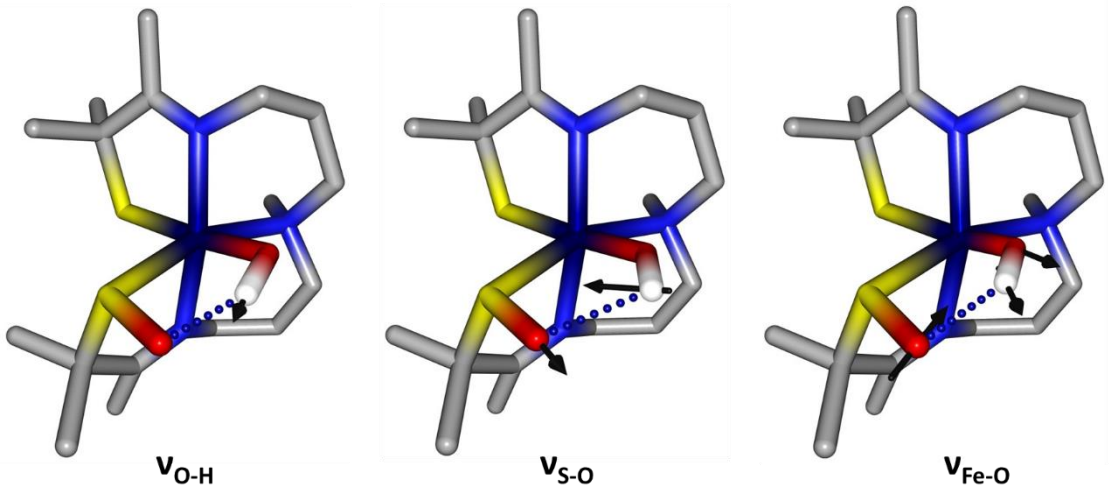

Figure 2.17 DFT calculated structure of **11** (*S* = 5/2) showing displacement arrows of the three complex key frequencies: $\nu_{O\text{-}H}$ = 3392 cm^{-1} (left), $\nu_{S\text{-}O}$ = 967 cm^{-1} (center), and $\nu_{Fe\text{-}O}$ = 587 cm^{-1} (right) (PBE0 functional).

2.4.1.2 Mass Spectrometry of 11

Examination of the mass spectrum of **11** showed signals at m/z = 399, 415, and 433 Da that corresponded, respectively, to the starting Fe^{II} complex **3**, the +16 (+O) sulfenate **7**, and +34 (+O, OH) **11**+H^+ (***Figure 2.18***). Hydroxy-sulfenate **11** should demonstrate a neutral charge, and thus the single proton is required to have both a positive charge and the m/z = 433. The m/z = 415 signal resulted from the wet atmosphere of the mass spectrometer (**Scheme 2.2**). The addition of $^{18}O_2$ resulted in the observation of m/z = 437 and 435 Da. The addition of one molecule of $^{18}O_2$ that formed both the sulfenate and hydroxide would result in and m/z = 437 Da. The m/z = 435 Da indicated that there could be scrambling of $^{18}O_2$ and $^{16}O_2$ during a reversible O—O bond cleavage/formation step along the reaction pathway.

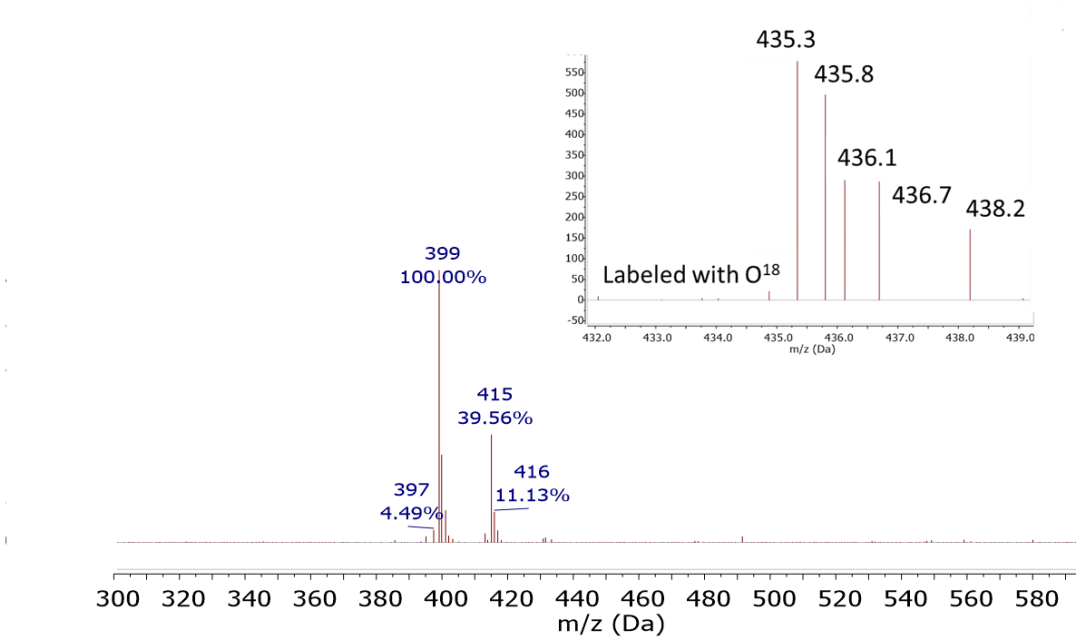

Figure 2.18 Mass spectrum of **11**, inset: the 432-439 Da range of the $^{18}O_2$ labeled experiment.

2.4.2 Kinetic Isotope Effect of Formation of 11

The formation of hydroxy-sulfenate-**11** implied that an HAT step exists along the reaction pathway after the formation of superoxo **3-O₂** (**Scheme 2.2**). The rate of the formation of the green intermediate **11** was explored in *pseudo*-first order conditions with excess dioxygen in both THF and d_8-THF. The solvent was assumed to be the source of the H-atom as was demonstrated for the HAT step of **1** and demonstrated the strong oxidative power of Fe-dioxygen species preceding the formation of **11** as the BDFE = 92 kcal, mol^{-1} for THF. The kinetic traces were fit with a single exponential function to find the value of k_{obs}. A kinetic isotope effect (KIE = 2.0) was calculated from the observed k_{obs} values, k_{obs}^{H} = 1.0 ± 0.2 x 10^{-2} s^{-1} and k_{obs}^{D} = 5.0 ± 1 x 10^{-3} s^{-1} indicating an H-atom from THF was involved in the formation of the green intermediate (***Figure 2.19***). Further investigation into the kinetics of the formation of **11** is discussed in **Section 2.5**.

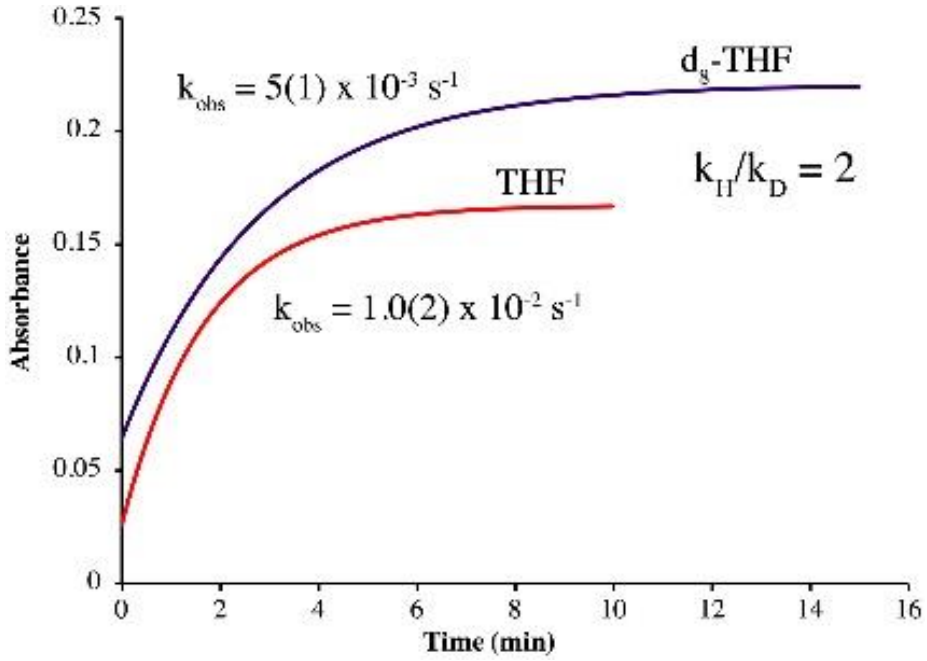

Figure 2.19 Kinetic isotope effect as formation of intermediate with exposure to O_2 is followed at 650 nm and fit with single exponential functions.

2.4.3 Reactivity of Hydroxy-Sulfenate Species 11

Another line of evidence to confirm the identity of the green intermediate as the hydroxy sulfenate was to explore the reactivity of **11** with proton sources. **Scheme 2.2** highlighted that the addition of proton sources could promote the hydroxide to leave as a water and result in trapping the sulfenate **7**. The addition of 100 µL of water to the THF solution of **3** resulted in the formation of the green intermediate **11** at λ_{max} = 650 nm, followed by the formation of a species with λ_{max} = 509 nm consistent with the formation of sulfenate **7** (***Figure 2.20***). The addition of 100 µL of MeOH to **3** also resulted in the formation of the green intermediate **11** at λ_{max} = 650 nm, followed by the formation of a band at λ_{max} = 516 nm, consistent with **7** (***Figure 2.21***). The band formed from the addition of MeOH is not as clearly isolated as in the case with the addition of water. The reactivity is not dependent on the sequence of the addition of the proton source; either before the dioxygen, or once **11** fully forms, results in the same spectrum. The proton reactivity supports the identification of the green intermediate as Fe^{III}-hydroxy-sulfenate **11** as outlined in **Scheme 2.2.** Similarly to the case of **2**, the sulfenate $[Fe^{III}(\eta^2\text{-}S^{Me2}O)(S^{Me2}N_2N^{Me}(Pr,Pr)]^+$ (**7**) was crystallographically isolated from the addition of oxo-atom donors and its characterization will be further discussed in **Chapter 3**.

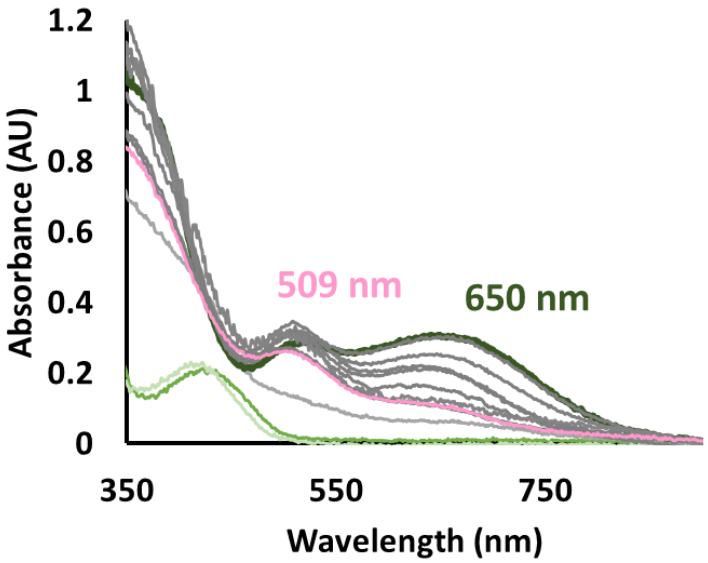

Figure 2.20 EAS monitoring the formation of green intermediate **11** (λ_{max} = 650 nm), followed by the formation of sulfenate **7** (λ_{max} = 509 nm) in the presence of water (100 µL) at room temperature ([Fe^{II}]= 0.230 mM).

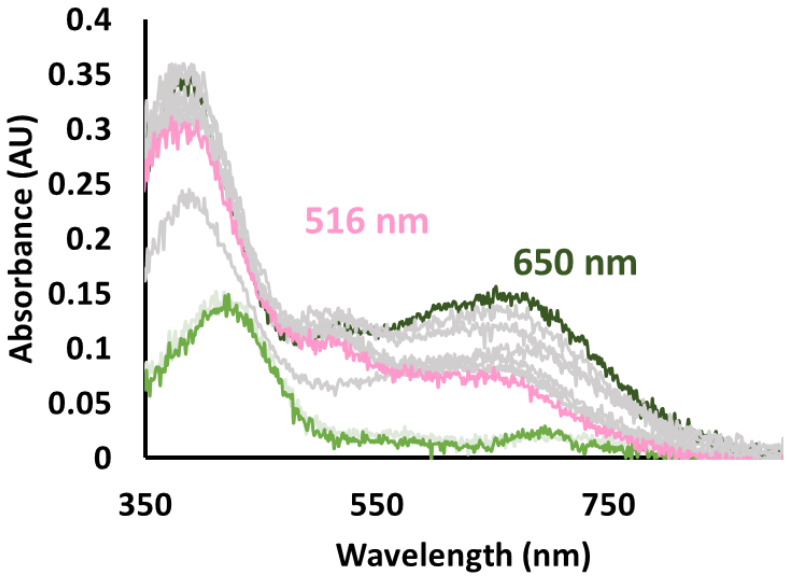

Figure 2.21 EAS monitoring the formation of green intermediate **11** (λ_{max} = 650 nm) followed by the formation of sulfenate **7** (λ_{max} = 516 nm) in the presence of MeOH (100 µL) at room temperature ([Fe^{II}]= 0.230 mM).

2.5 Stopped-Flow UV-Vis Kinetic Investigations

Stopped-flow UV-Vis spectroscopy allows for the addition of dioxygen in a closed system with no headspace in the reaction cell. The stoichiometric addition of dioxygen and exploration of the kinetics of the reaction is feasible with this experimental setup. The instrument also demonstrates a much faster temporal resolution that can identify otherwise unobserved intermediates that may only exist on millisecond time scales. The addition of dioxygen to THF solutions of **3** was explored to investigate the kinetics of the reaction, as well as to identify other short-lived intermediates. The reaction scheme and rate constants for the formation of **11** are outlined in **Scheme 2.3**. The binding of dioxygen to **3** to form superoxo **3-O_2** is assigned rate constant k_1 for the forward reaction and k_{-1} for the reverse reaction. The formation of the Fe^{II}-peroxythiolate **9** would be expected to occur rapidly as an intramolecular reaction and is assigned k_2 for the forward reaction and k_{-2} for the reverse reaction. The O—O bond cleavage to form high-valent oxo **10** is assigned k_3 for the forward reaction and k_{-3} for the reverse. The scrambling observed in the mass spectrum (***Figure 2.18***) suggested that these three steps may be reversible or an intermediate may participate in a different side reaction. Throughout the temperature range -25 °C to 20 °C, the rate-determining step was likely the binding of dioxygen to **3**, which then resulted in the rapid formation of **11** with the rate constant of k_{obs} , because no intermediates are observed past the rate-determining step of a reaction.

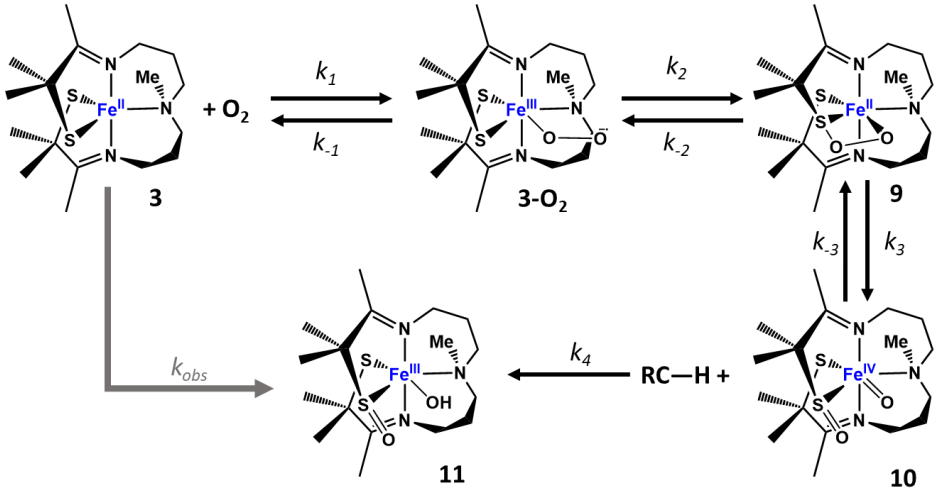

Scheme 2.3 Proposed reaction scheme for the formation of **11** with rate constants indicated for each step, from -25 °C to RT. Only **3** and **11** are spectroscopically observed.

2.5.1 Eyring Analysis and Implications

Over the temperature range (-25 °C to 5 °C), the hydroxy-sulfenate **11** formed as the first and only observed species. The dioxygen was preserved in excess (more than 10 equivalents) to ensure *pseudo*-first order conditions to explore the reaction mechanism. Eyring analysis was carried out for reactions with the addition of a 3.95 mM THF solution of dioxygen to a 0.150 mM THF solution of **3** after mixing in the stopped-flow cell (***Figure 2.22***). The activation parameters associated with the formation of **11** were determined from the Eyring plot. The positive enthalpy of activation $\Delta H^{\ddagger}$ = 34 kJ, mol^{-1} was as expected for an associative process, which would be consistent with both the H-atom abstraction step or the formation of the superoxo **3-O₂** species from dioxygen binding. The large negative value of the entropy of activation ($\Delta S^{\ddagger}$ = -151.5 J, mol^{-1}, K^{-1}) was consistent with an associative process. To summarize, either the formation of **3-O₂** or the HAT step to form **11** would be consistent with the activation parameters.

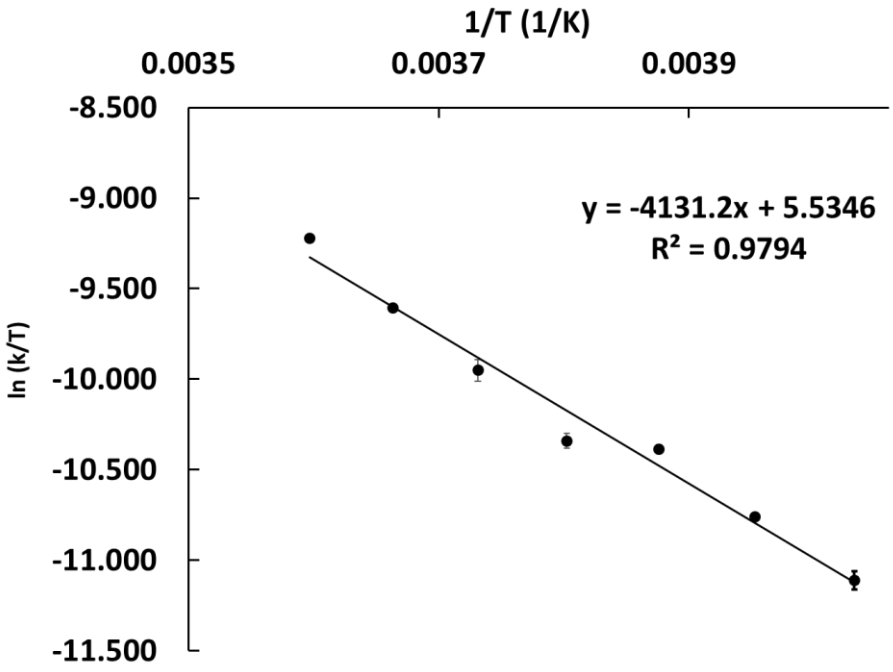

Figure 2.22 Eyring plot for the formation of **11** over the temperature range 248-278 K.

2.5.2 Preliminary Investigation of the Dependence of k_{obs} on O_2 Concentration

The investigation of the formation of **11** was continued by investigating dependence of the observed rate constant, k_{obs}, on the concentration of dioxygen. The k_{obs} appeared to demonstrate a first-order dependence on the concentration of dioxygen (***Figure 2.23***), which is consistent with the expected stoichiometry of the proposed reaction pathway (**Scheme 2.2**). However, the two most concentrated solutions of dioxygen (0.395 mM and 0.296 mM) demonstrate similar values for k_{obs}. One possible explanation is that the reaction has reached a saturation point at those higher concentrations of dioxygen. Kinetic investigations of dioxygen binding can help to determine the reversibility of the reaction. An increase in the y-intercept value, with increasing temperature would be an indication of reversibility of the dioxygen binding. The trend is roughly adhered to for the data sets shown in ***Figure 2.23***. Continued investigations altering temperature

and concentration conditions will help to establish a stronger trend and allow for more direct comparison of kinetic parameters to other thiolate-ligated Fe^{II} systems.

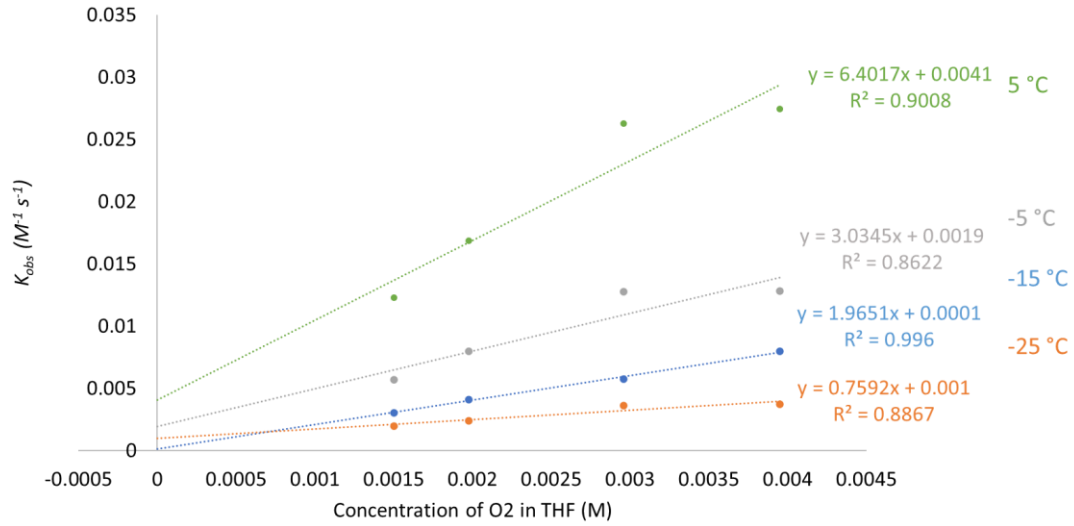

Figure 2.23 Plot of k_{obs} versus the concentration of dioxygen in THF from -25 to 5 °C, demonstrating first order dependence on dioxygen ([Fe(**3**)] = 0.150 mM).

2.6 Alternative Reaction Pathways to Observe Other Intermediates

2.6.1 The Addition of KO_2 to Oxidized 3^{ox}

Another route to form the superoxo intermediate (**3-O_2**) or any following intermediates would be through the reaction of $\mathbf{3^{ox}}$ and potassium superoxide. The energetic barrier for binding superoxide compared to binding dioxygen should be lower because the required electron transfer is already completed. By lowering the energetic barriers to the formation of **3-O_2**, intermediates of interest such as **9** and **10** could be spectroscopically observed. The addition of potassium superoxide (KO_2) to a THF solution of $\mathbf{3^{ox}}$ (the oxidized Fe^{III} version) resulted in the formation of a new intermediate with λ_{max} = 576 and 742 nm that was formed over five minutes (***Figure 2.24***). The new bands were not consistent with those found for **11** or those observed at

low temperature reactions (***Figures 2.9-2.11***). The bands associated with the new intermediate, slowly (over four hours) transformed to λ_{max} = 650 nm, which was associated with hydroxy-sulfenate **11** (***Figure 2.25***). Referencing **Scheme 2.4**, the identity of the new intermediate preceding **11** could be Fe^{III}-superoxo **3-O₂**, Fe^{II}-peroxythiolate **9**, or high-valent oxo **10**. Further investigation of this species by EPR, IR, and kinetic experiments will help to identify which species of interest has been spectroscopically observed. Once again taking into account the larger reaction pathway (**Scheme 2.4**), the addition of KO_2 represents the second pathway that implies the formation of the Fe^{II}-peroxythiolate **9.**

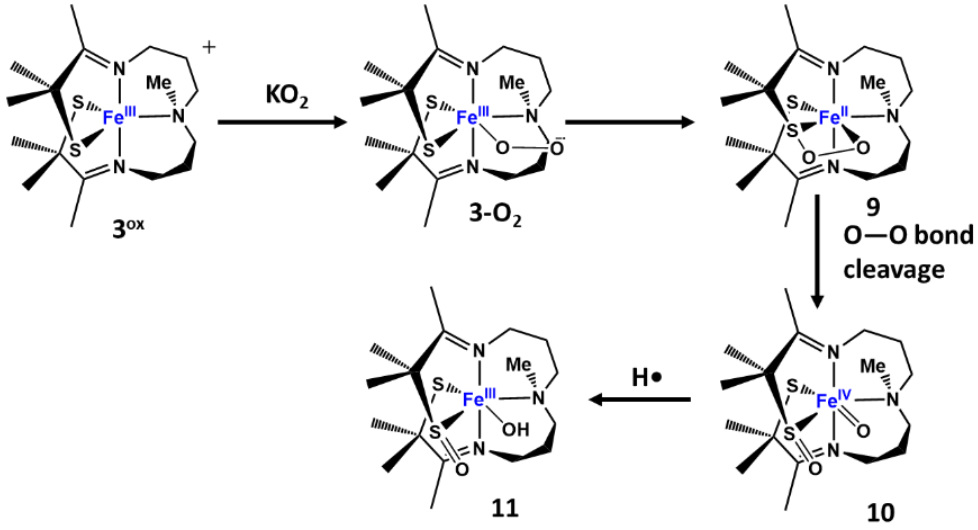

Scheme 2.4 Chemical reaction scheme for the addition of potassium superoxide to **3^{ox}**.

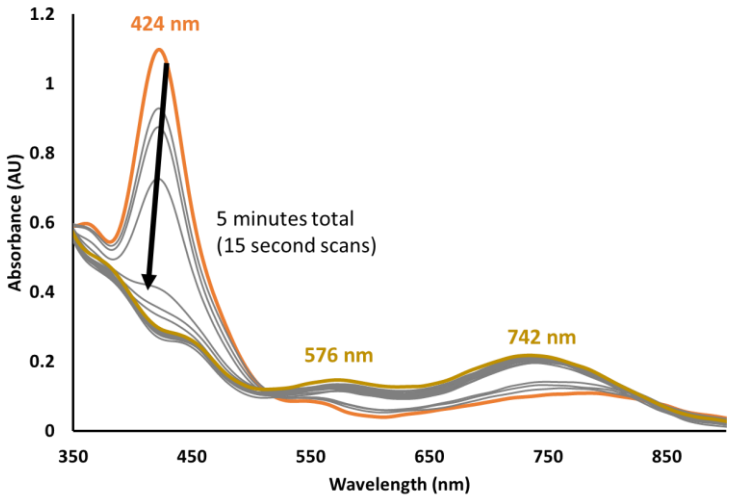

Figure 2.24 EAS monitoring the formation of a new intermediate with λ_{max} = 576 and 742 nm (yellow) from the addition of KO_2 solubilized with 18-crown-6 (18-c-6) to a solution of **3^{ox}** (orange) in THF at -73 °C ([Fe] (**3^{ox}**) = 0.230 mM).

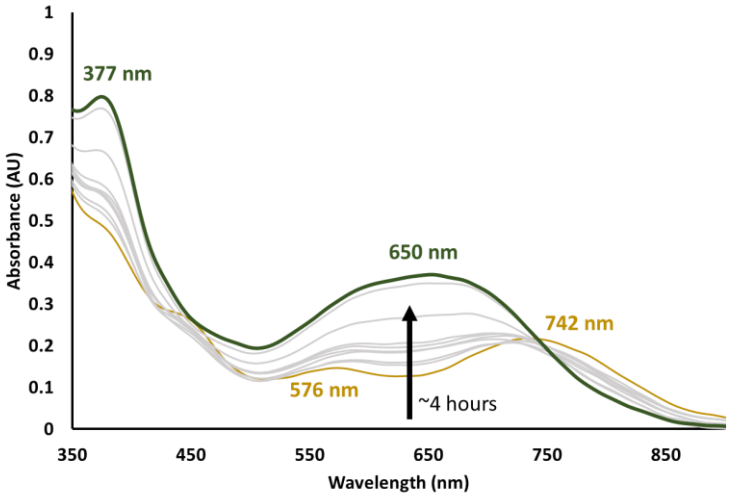

Figure 2.25 EAS monitoring the transformation of the new intermediate (orange) to **11** (green) in THF at -73 °C ([Fe] (**3^{ox}**) = 0.230 mM) over four hours.

2.6.2 Addition of Oxo-Atom Donors to 3

High-valent Fe-oxos, especially with a thiolate in the coordination sphere, are of especial interest to biomimetic modeling due to the oxidative power of these species in cleaving C—H bonds. The addition of oxo-atom donors is an established method for forming high-valent

transition metal-oxo species. The addition of oxo-atom donors PhIO, IBX-ester, and PNO to **3** was explored in order to explore the potential of forming a high-valent Fe^{IV}-oxo species **8** or **10** (***Figure 2.26***). Without a sulfenate present on the thiolate arm prior to the formation of the Fe^{IV}-oxo, the oxo will likely be rapidly intramolecularly trapped by forming an η^2-bound sulfenate moiety. This makes it less likely that CDO-mimic **10** would be formed from the addition of oxo-atom donors, however, any thiolate-ligated high-valent oxo species is of scientific interest. The reaction between **3** and PNO demonstrated no change observed by EAS. The results of the addition of PhIO or IBX-ester to **3** are discussed below.

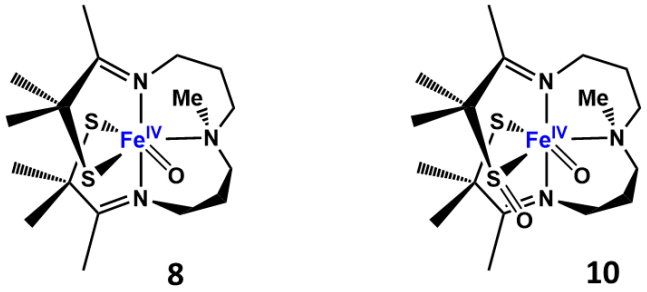

Figure 2.26 ChemDraw structures of the Fe^{IV}-oxo species that would act as an IPNS-mimic **8** (left) or a CDO-mimic **10** (right).

2.6.2.1 Addition of Iodosylbenzene to 3

The addition of PhIO to a THF solution of **3** results in the formation of $\mathbf{3^{ox}}$ at -73 °C (***Figure 2.27***), indicative of an outer-sphere one-electron oxidation. When the reaction solution is warmed to -40 °C, the $\mathbf{3^{ox}}$ forms the sulfenate product **2**. The temperature dependence of this reaction will be discussed further in **Chapter 3**. The addition of PhIO did not result in the direct spectroscopic observation of either metal-oxo species **8** or **10**.

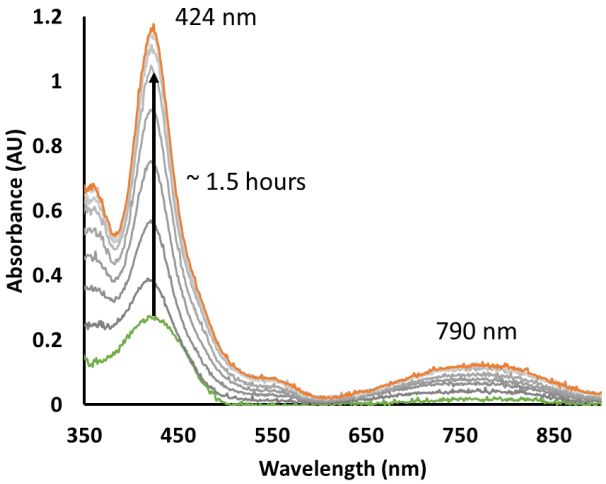

Figure 2.27 EAS monitoring the addition of PhIO to THF solution of **3** (green) resulting in the formation of **3^{ox}** (orange) at -73 °C ([Fe] = 0.230 mM).

2.6.2.2 Addition of IBX-Ester to 3

The reaction of **3** with IBX-ester at room temperature showed a new absorbing intermediate with λ_{max} = 665 nm (***Figure 2.28***). The intermediate had a similar band to hydroxy-sulfenate **11**. However, the species showed the growth of a band λ_{max} = 500 nm in the absence of an additional proton source, that would be consistent with the sulfenate product. The intermediate could be a high-valent oxo species **8** or **10**, as well as an oxo-atom donor adduct species as it demonstrated a band in the 600-700 nm region that would correspond with a six-coordinate Fe^{III} species. **Chapter 3** demonstrates reactivity between **3^{ox}** and IBX-ester (new intermediate with λ_{max} = 689 nm) that suggests the 665 nm intermediate is not an oxo-atom donor adduct. Further characterization of this new intermediate will help to elucidate the mechanism of oxo-atom donor addition and the identity of the intermediate species.

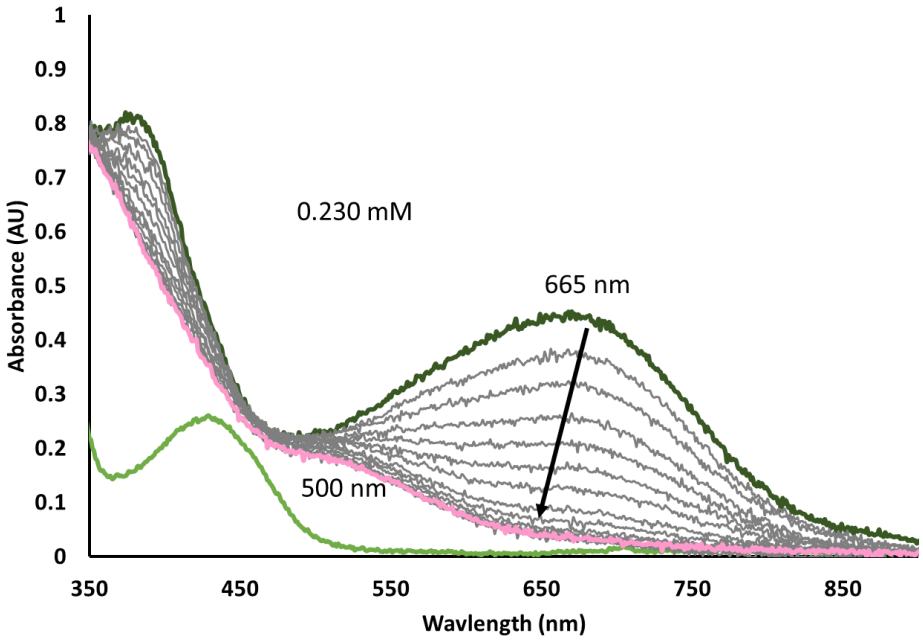

Figure 2.28 EAS monitoring the addition of IBX-ester to a THF solution of **3** (light green) resulting in the rapid formation (15 seconds) of a new intermediate λ_{max} = 665 nm (dark green), which transitions to λ_{max} = 500 nm consistent with **7** at room temperature ([Fe] = 0.230 mM).

2.6.3 Addition of H_2O_2 to 3

In the secondary amine ligated **1**, the formation of superoxo **1-O₂** preceded the formation of a hydroperoxo intermediate **1-OOH** with λ_{max} = 696 nm.[4] The addition of 1 equivalent of H_2O_2-urea to **3** was monitored with EAS at room temperature and resulted in the growth of a band at λ_{max} = 650 nm over 3.5 hours (***Figure 2.29***). The H_2O_2-urea can provide both of the oxygen atoms required to form the hydroxy-sulfenate **11**. The λ_{max} = 650 nm indicated that the species is in the Fe^{III} oxidation state with a ligand bound in the sixth coordination position. When the reaction is monitored at lower temperatures with the addition of excess H_2O_2-urea (10 equivalents), there was a dramatic increase in the absorbance of the species with λ_{max} = 650 nm (***Figure 2.30***). The increasing maximum absorbance at λ_{max} = 650 nm suggests that more of **11** is able to build up in

solution at lower temperatures and that **11** is susceptible to further oxidation with the presence of excess oxidant that may result in side reactions.

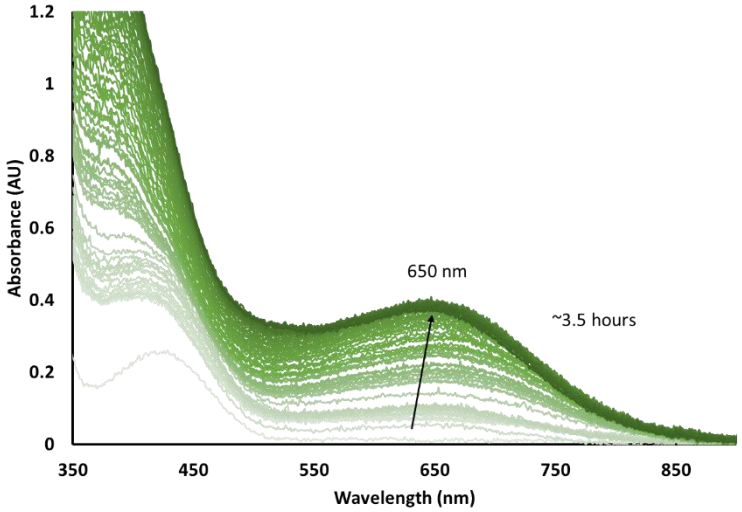

Figure 2.29 EAS monitoring the reaction of **3** with one equivalent of H_2O_2-urea at room temperature in THF ([Fe] = 0.230 mM).

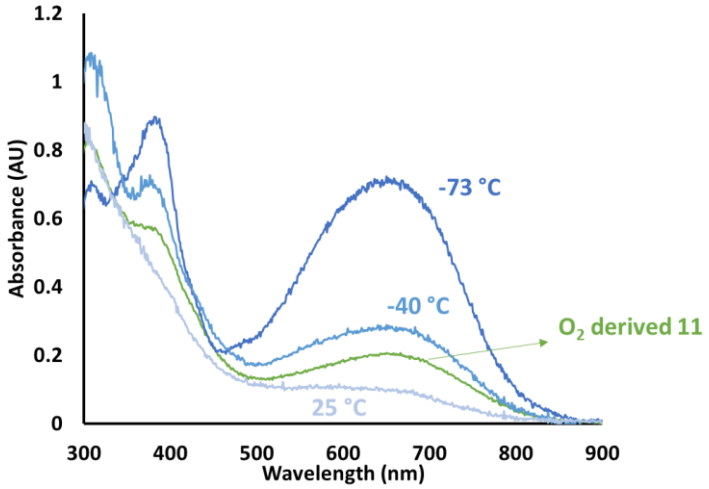

Figure 2.30 EAS of the maximum absorbance from the reaction of **3** with 10 equivalents of H_2O_2-urea at various temperatures in THF compared to the O_2 derived **11** ([Fe] = 0.230 mM).

2.6.4 Addition of Tetrabutylammonium Hydroxide to 3^{ox}

The addition of tetrabutylammonium hydroxide (TBAOH) to **3^{ox}** was investigated as an authentic path to an Fe^{III}-OH species **3-OH** (**Scheme 2.1**). The addition of TBAOH was monitored at various temperatures, the reactions proceeded rapidly. At -40 °C, a broad band centered at λ_{max} = 630 nm grew in rapidly in less than three minutes (***Figure 2.31***) and then converted to a bright aqua species with λ_{max} = 593 nm over 75 minutes (***Figure 2.32***). At room temperature, the spectrum was instantaneously converted to the bright aqua species with λ_{max} = 593 nm (***Figure 2.33***). The 593 nm species rapidly loses its spectral features when warmed to room temperature or exposed to excess OH^-, which complicated further characterization of these intermediates. Thiolate-ligated Fe^{III}-OH species are rare and relevant to studying the HAT ability of high-valent Fe-oxo species as well as the proposed rebound mechanisms found in enzymatic systems. Further investigations of hydroxide reactivity within this ligand family will be carried out in the group.

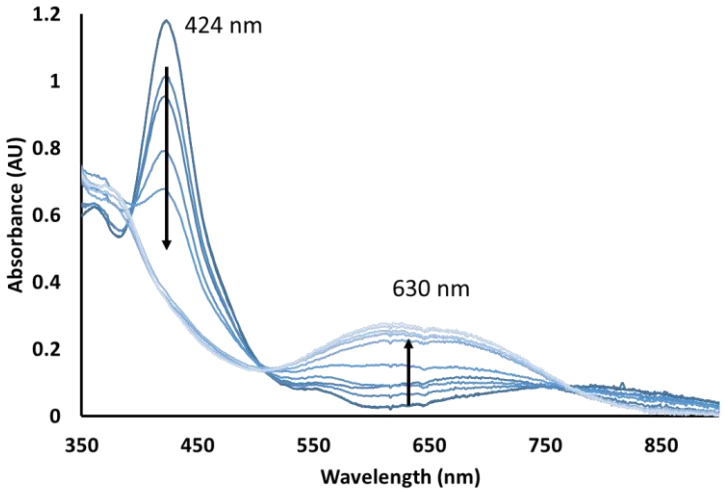

Figure 2.31 EAS monitoring the growth of λ_{max} = 630 nm species from the addition of 1 equivalent of TBAOH to **3^{ox}** in THF over 2.5 minutes at -40 °C ([Fe] = 0.230 mM).

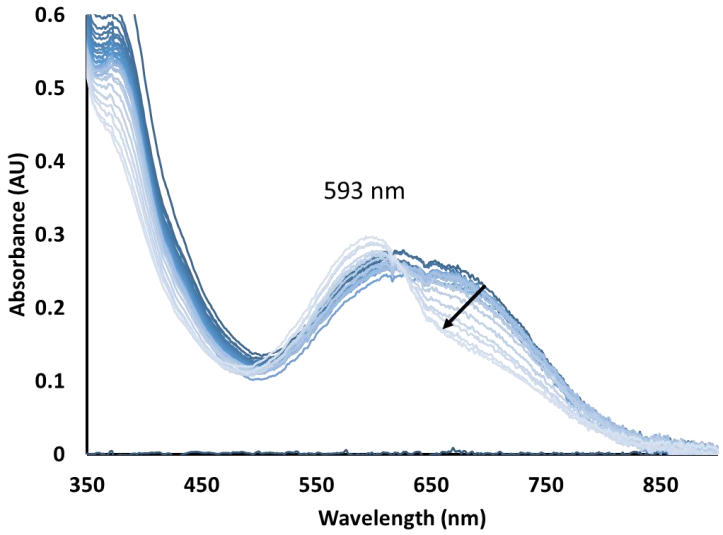

Figure 2.32 EAS monitoring the growth of λ_{max} = 593 nm species from the addition of one equivalent of TBAOH to **3^{ox}** in THF over 75 minutes at -40 °C ([Fe] = 0.230 mM).

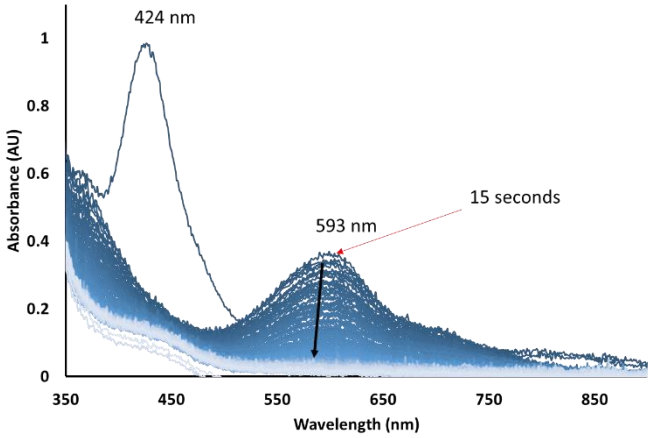

Figure 2.33 EAS monitoring the disappearance of the λ_{max} = 593 nm species, after instantaneous formation from the addition of one equivalent of TBAOH to **3^{ox}** (λ_{max} = 424 nm) in THF at room temperature ([Fe] = 0.230 mM).

2.4.3 Addition of Tetrabutylammonium Azide to 3

The addition of tetrabutylammonium azide ($TBAN_3$) to **3** was explored to investigate the ability of azide to inhibit the dioxygen reactivity. The inhibition by azide would provide more evidence that the dioxygen activation is Fe-mediated. However, upon addition of excess $TBAN_3$ (100

equivalents) to **3,** new bands with λ_{max} = 477, 538, and 771 nm were observed by EAS in THF (***Figure 2.34***). The 771 nm band was consistent with the formation of six-coordinate Fe species. The Fe^{III} azide bound derivative of $\mathbf{3^{ox}}$ [$Fe^{III}(S_2{}^{Me2}N_2N^H(Pr,Pr))(N_3)$] will be described in **Chapter 3**. The putative Fe^{III}-azide demonstrated λ_{max} = 481, 585, and 769 nm in THF. The growth of the species takes over 16 hours at -73 °C. Further investigations of this interesting reactivity between an Fe^{II} complex and azide will elucidate the different azide reactivity between **3** and other thiolate-ligated Fe complexes.

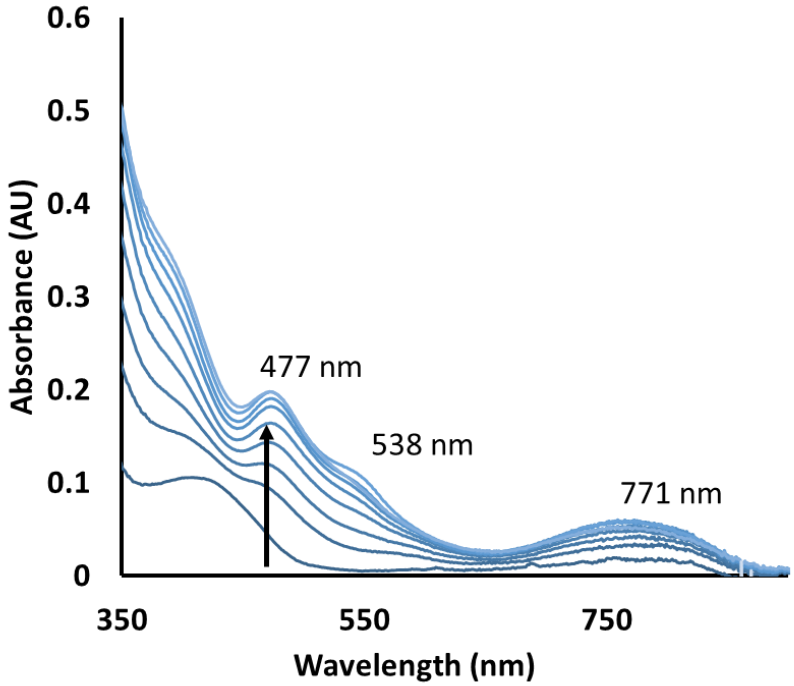

Figure 2.34 EAS monitoring the growth of a new species over 16.35 hours with λ_{max} = 477, 538, 771 nm, after the addition of 100 equivalents of $TBAN_3$ to **3** in THF at -73 °C ([Fe] = 0.230 mM).

2.4 Redox-Inactive Transition Metal Complex [$Zn^{II}(S_2^{Me2}N_2N^{Me}(Pr,Pr))$] 12

Another approach to support the dioxygen reactivity of **3** as being Fe-mediated was to replace the transition metal center with a redox inactive Zn ion. The Zn^{II} analogue of the sterically constrained ligand used in **3** was synthesized using a similar synthetic scheme to form Zn complex, [$Zn^{II}(S_2^{Me2}N_2N^{Me}(Pr,Pr))$] (**12**).[7] The Zn complex **12**, was crystallographically characterized (***Figure 2.35, Table 2.5***). The metrical parameters of **12** are summarized in ***Table 2.6***. The metrical parameters demonstrated that both metal ions were in similar coordination environments. The Zn—N^{im}_{avg} = 2.160(6) Å was within error of the Fe—N^{im}_{avg} = 2.153(5) Å found for **3**. The Zn—N(2) = 2.242(2) Å was slightly more elongated than Fe—N(2) = 2.2204(17) Å for **3**. The Zn—S = 2.3111(4) Å was contracted comparing to the Fe—S = 2.3285(5) Å found for **3**. The geometry around the transition metal ion remains in a distorted trigonal bipyramidal geometry (τ = 0.63).

Thiolate-ligands can participate in oxidation-reduction chemistry and are therefore regarded as redox non-innocent ligands, where oxidation-reduction processes can occur on the ligand instead of remaining centered on the metal ion. The CV investigation of **12** in MeCN resulted in oxidation events at E_{p1} = 0.248 V and E_{p2} = 1.042 V (***Figure 2.36***). The oxidation events are assigned to the thiolate ligands as the Zn ion (d^{10}) is redox inactive. As expected, upon exposure to dioxygen, no changes in the spectrum were observed with EAS. Further synthesis of the Zn analogues of this ligand family may elucidate the electronic differences between the thiolate arms of each ligand framework.

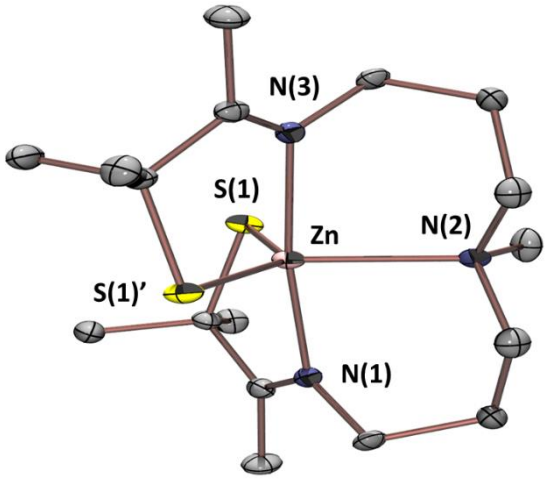

Figure 2.35 ORTEP diagram of [$Zn^{II}(S_2{}^{Me2}N_2N^{Me}(Pr,Pr))$] (**12**) with hydrogens and disorder removed showing thermal ellipsoids at the 50% probability level.

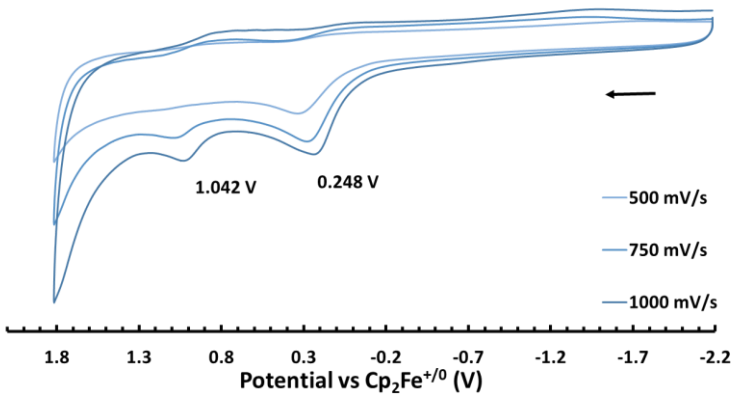

Figure 2.36 Cyclic voltammogram of MeCN solution of **12** (0.500 mM) with 0.1 M $(Bu_4N)PF_6$ supporting electrolyte, a platinum counter electrode, glassy carbon working electrode and Ag/Ag^+ reference electrode monitored with varying scan rate.

Table 2.5 Crystal data, intensity collections, and structure refinement parameters for $[Zn^{II}(S_2{}^{Me2}N_2N^{Me}(Pr,Pr))]$ (**12**)

Empirical formula	C17 H33 N3 S2 Zn	
Formula weight	408.95	
Temperature	100(2) K	
Wavelength	0.71073 Å	
Crystal system	Monoclinic	
Space group	C 2/c	
Unit cell dimensions	a = 12.2497(8) Å	α= 90°.
	b = 15.8277(8) Å	β= 109.673(3)°.
	c = 11.0721(6) Å	ϒ= 90°.
Volume	2021.4(2) $Å^3$	
Z	4	
Density (calculated)	1.344 Mg/m^3	
Absorption coefficient	1.425 mm^{-1}	
F(000)	872	
Crystal size	0.150 x 0.100 x 0.060 mm^3	
Theta range for data collection	2.185 to 28.443°.	
Index ranges	-16<=h<=16, -21<=k<=21, -14<=l<=14	
Reflections collected	9906	
Independent reflections	2546 [R(int) = 0.0348]	
Completeness to theta = 25.000°	100.0 %	
Refinement method	Full-matrix least-squares on F^2	
Data / restraints / parameters	2546 / 16 / 129	
Goodness-of-fit on F^2	1.085	
Final R indices [I>2sigma(I)]	R1 = 0.0232, wR2 = 0.0503	
R indices (all data)	R1 = 0.0303, wR2 = 0.0536	
Largest diff. peak and hole	0.366 and -0.274 $e.Å^{-3}$	

Table 2.6 Selected metrical parameters (Å and °) for thiolate-ligated [$Zn^{II}(S_2{}^{Me2}N_2N^{Me}(Pr,Pr))$] (**12**).

	12
Zn—N(1)	2.147(6)
Zn—N(2)	2.242(2)
Zn—N(3)	2.172(5)
Zn—S(1)	2.3111(4)
Zn—S(1)'	2.3111(4)
N(1)—Zn—N(3)	172.92(9)
N(1)—Zn—N(2)	86.9(4)
N(3)—Zn—N(2)	86.1(4)
N(1)—Zn—S(1)	83.2(2)
N(3)—Zn—S(1)	98.20(13)
N(2)—Zn—S(1)	110.6(4)
N(1)—Zn—S(1)'	101.44(13)
N(3)—Zn—S(1)'	82.5(2)
N(2)—Zn—S(1)'	114.4(5)
S(1)—Zn—S(1)'	134.98(2)
τ	0.63

2.9 Conclusions

The addition of a steric constraint, tertiary amine (N^{Me}), into the ligand architecture of **3** resulted in the observation of a different dioxygen activation pathway compared to that found for less sterically constrained **1.** The dioxygen reactivity of **3** led to the identification of a new dioxygen-derived intermediate the hydroxy-sulfenate-Fe^{III} **11,** characterized with IR, EAS, mass spectrometry, and supported with DFT calculations and proton reactivity. This intermediate was similar to intermediates proposed to form in the reaction pathway of CDO. A survey of dioxygen reactivity demonstrated the reaction is both solvent and temperature dependent. A survey of authentic routes to common dioxygen-derived intermediates revealed new spectroscopic data

for interesting intermediates that require further characterization. The vast changes in reactivity observed with the addition of the tertiary amine steric constraint have established the first volume of comparisons of thiolate-ligated Fe^{II} species, which will be continued with other complexes synthesized in the Kovacs group.

2.10 Experimental Details

2.10.1 General Methods

All reactions were performed under an atmosphere of nitrogen in a glovebox or using standard Schlenk techniques unless otherwise indicated. Reagents purchased from commercial vendors were of the highest purity available and used without further purification. Pentane, toluene, diethyl ether (Et_2O), tetrahydrofuran (THF), acetonitrile (MeCN), and dichloromethane (DCM) were rigorously degassed and purified using solvent purification columns housed in a custom stainless-steel cabinet, dispensed via a stainless steel Schlenk-line (Glass Contour). Methanol (MeOH) was distilled from calcium hydride and degassed prior to use. The synthesis of 3-methyl-3-mercapto-2-butanone was carried out as previously described in the literature.[12]

^{1}H-NMR spectra were recorded on Bruker AV 300 or AV 301 FT-NMR spectrometers and are referenced to a residual protio-solvent. Chemical shifts are reported in ppm and coupling constants (J) are in Hz. Electrospray ionization mass spectrometry (ESI-MS) was performed on a Bruker Esquire LC-Ion Trap. Low-temperature electronic absorption spectra were recorded using a Varian Cary 50 spectrophotometer equipped with a fiber optic cable connected to a “dip” attenuated total reflection probe (C-technologies), with a custom-built two-necked solution sample holder equipped with a threaded glass connector (sized to fit the dip probe) and purged

with argon. Cyclic voltammograms were recorded in MeCN (100 mM $^{t}Bu_4N(PF_6)$ solutions) on a PAR 273 potentiostat utilizing a glassy carbon working electrode, platinum auxiliary electrode, and an Ag/Ag^{+} reference electrode. EPR spectra were recorded on a Bruker EPX CW-EPR spectrometer operating at X-band frequency at 4 and 117 K. The EPR spectra were simulated using EasySpin (version 5.2.23), a computational package developed by Stoll and Schweiger[13] and based on Matlab (The MathWorks, Massachusetts, USA).

2.10.2 Synthesis of $[Fe^{II}(S_2^{Me2}N_2N^{Me}(Pr,Pr))]$ 3

Sodium methoxide (0.092 g, 1.7 mmol) was added to 6 mL MeOH in a 20 mL scintillation vial with a stir bar. 3-Methyl-3-mercapto-2-butanone (0.200 g, 1.69 mmol) was added to the reaction mixture and stirred at room temperature for 10 minutes. *N,N-Bis*(3-aminopropyl)methylamine (0.137 mL, 0.847 mmol) was added to the reaction mixture by syringe and stirred for 20 minutes, before the reaction mixture was cooled to -30°C for one hour. In an additional scintillation vial iron(II) chloride (0.124 g, 0.762 mmol) was dissolved in 6 mL MeOH before cooling to -30°C for one hour. The iron solution was slowly added, over thirty minutes while stirring at room temperature to afford a translucent green solution. The reaction is stirred for an additional three hours before being placed in the -30°C freezer overnight. After all MeOH is removed by vacuum, the solids are dissolved into 4 mL MeCN (with stirring to ensure all remaining particles are free flowing) and filtered over a bed of wet (MeCN) celite. The solvent is then again removed before redissolving into THF and layering with pentane to afford green crystals (0.085 g, 0.213 mmol, 28% yield). Electronic absorption (THF): λ_{max} (ε, M^{-1} cm^{-1}) = 430 (800) nm, ESI-MS calcd for $[FeC_{17}N_3S_2H_{33}]$: 399.4, found: 399.1. Evans method: μ_{eff} = 4.29 B.M. (MeCN). Anal. calcd for

$[FeC_{17}N_3S_2H_{33}]$: C, 51.12; H, 8.33; N 10.52. found: C, 50.84; H 8.04; N 10.54; Reduction potential (MeCN): $E_{1/2}$ = −0.470 V vs SCE.

2.10.3 X-ray Experimental Details for 3

A green piece, measuring 0.16 x 0.11 x 0.09 mm^3 was mounted on a loop with oil. Data was collected at -173°C on a Bruker APEX II single crystal X-ray diffractometer, Mo-radiation. Crystal-to-detector distance was 40 mm and exposure time was 10 seconds per frame for all sets. The scan width was 0.5°. Data collection was 100% complete to 25° in ϑ. A total of 9917 reflections were collected covering the indices, -16<=h<=16, -21<=k<=21, -14<=l<=14. 2536 reflections were symmetry independent and the R_{int} = 0.0276 indicated that the data was of excellent quality (0.07). Indexing and unit cell refinement indicated a C-centered monoclinic lattice. The space group was found to be C 2/c (No.15). The data was integrated and scaled using SAINT, SADABS within the APEX2 software package by Bruker.[14] Solution by direct methods (SHELXT[15] or SIR97[16]) produced a complete heavy atom phasing model consistent with the proposed structure. The structure was completed by difference Fourier synthesis with SHELXL.[17] Scattering factors are from Waasmair and Kirfel.[18] Hydrogen atoms were placed in geometrically idealized positions and constrained to ride on their parent atoms with C—H distances in the range 0.95-1.00 Angstrom. Isotropic thermal parameters U_{eq} were fixed such that they were 1.2U_{eq} of their parent atom U_{eq} for CH's and 1.5U_{eq} of their parent atom U_{eq} in case of methyl groups. All non-hydrogen atoms were refined anisotropically by full-matrix least-squares. The asymmetric unit consists of

half of the molecule, with the amine backbone disordered across two positions. The molecule is completed by a 180° rotation about the N(2)—Fe(1) axis.

2.10.4 Synthesis of [$Zn^{II}(S_2^{Me2}N_2N^{Me}(Pr,Pr))$] 12

Sodium methoxide (0.092 g, 1.7 mmol) was added to 6 mL MeOH in a 20 mL scintillation vial with a stir bar. 3-Methyl-3-mercapto-2-butanone (0.200 g, 1.69 mmol) was added to the reaction mixture and stirred at room temperature for 10 minutes. *N,N-Bis*(3-aminopropyl)methylamine (0.137 mL, 0.847 mmol) was added to the reaction mixture by syringe and stirred for 20 minutes, before the reaction mixture was cooled to -30°C for one hour. In an additional scintillation vial zinc(II) chloride (0.104 g, 0.762 mmol) was dissolved in 6 mL MeOH before cooling to -30°C for one hour. The zinc solution was slowly added, over thirty minutes while stirring at room temperature to afford a translucent solution. The reaction is stirred for an additional three hours before being placed in the -30°C freezer overnight. After all MeOH is removed by vacuum, the solids are dissolved into 4 mL MeCN (with stirring to ensure all remaining particles are free flowing) and filtered over a bed of wet (MeCN) celite. The solvent is then again removed before redissolving into THF and layering with pentane to afford colorless crystals (0.052 g, 0.127 mmol, 17% yield). ESI-MS calcd for [$ZnC_{17}N_3S_2H_{33}$] : 407.14, found: 408.2. CV (MeCN): E_{p1} = 0.248 V and E_{p2} = 1.042 V vs SCE.

2.10.5 X-ray Experimental Details for 12

A colorless piece, measuring 0.15 x 0.10 x 0.06 mm^3 was mounted on a loop with oil. Data was collected at -173°C on a Bruker APEX II single crystal X-ray diffractometer, Mo-radiation. Crystal-to-detector distance was 40 mm and exposure time was 10 seconds per frame for all sets. The scan width was 0.5°. Data collection was 100% complete to 25° in ϑ. A total of 9906 reflections were collected covering the indices, -16<=h<=16, -21<=k<=21, -14<=l<=14. 2546 reflections were symmetry independent and the R_{int} = 0. 0348 indicated that the data was excellent. Indexing and unit cell refinement indicated a C-centered monoclinic lattice. The space group was found to be C 2/c (No. 15). The data was integrated and scaled using SAINT, SADABS within the APEX2 software package by Bruker.[14] Solution by direct methods (SHELXT[15] or SIR97[16]) produced a complete heavy atom phasing model consistent with the proposed structure. The structure was completed by difference Fourier synthesis with SHELXL.[17] Scattering factors are from Waasmair and Kirfel.[18] Hydrogen atoms were placed in geometrically idealized positions and constrained to ride on their parent atoms with C—H distances in the range 0.95-1.00 Angstrom. Isotropic thermal parameters U_{eq} were fixed such that they were 1.2 U_{eq} of their parent atom U_{eq} for CH's and 1.5 U_{eq} of their parent atom U_{eq} in case of methyl groups. All non-hydrogen atoms were refined anisotropically by full-matrix least-squares. The structure exhibits disorder – and is completely through the crystallographic two-fold symmetry.

2.10.6 Electronic Absorbance Spectroscopy Measurement Example

An example of a typical EAS experiment with the addition of gas reagent is outlined herein. A 0.230 mM solution of **3** was prepared in 4 mL of THF under an inert nitrogen atmosphere in a drybox. The resulting solution was transferred via gastight syringe to a custom-made two-neck vial equipped with a septum cap and threaded dip-probe feed-through adaptor that had previously been purged with argon and contained a stir bar. To this was added a hollow needle with dioxygen gently bubbling through the solution resting at room temperature resulting in the formation of **11**.

2.10.7 Stopped Flow Solution Prep

The Fe^{II} solution was prepared at 0.300 mM for a final concentration of 0.150 mM after mixing in the stopped-flow cell. The solution was prepared under a nitrogen atmosphere and loaded onto the instrument is a gas-tight syringe with a three-way valve to maintain atmosphere free conditions.

Degassed solvent (THF) was added to a round bottom flask fitted with a septum cap under a nitrogen atmosphere in the glovebox. Dry O_2 (from a gas cylinder) was bubbled through the solvent at 1 atm for 15 min. The solution was then allowed to equilibrate over 15 minutes at 25 °C in a temperature-controlled water bath. To load the syringe, the flask was inverted and a gastight syringe equipped with a 3-way valve and needle was inserted through the septum (Position A in Figure below). The valve was turned to allow the saturated solution to flow through the open arm of the 3-way valve, leaving no headspace in the needle (Position B). The valve was

then shut and the dioxygen solution drawn into the syringe (Position C). Dilutions of the O_2-saturated solvent were performed anaerobically to obtain the desired [O_2].

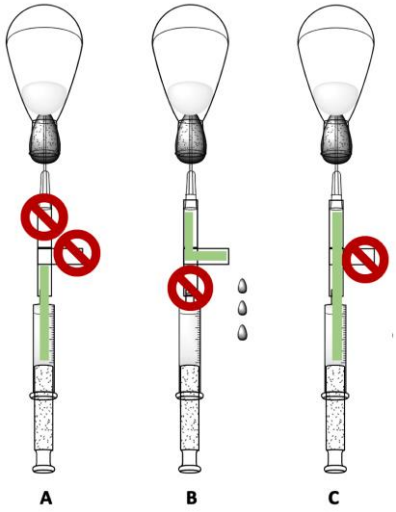

2.11 Chapter 2 References

(1) Driggers, C. M.; Kean, K. M.; Hirschberger, L. L.; Cooley, R. B.; Stipanuk, M. H.; Karplus, P. A. Structure-Based Insights into the Role of the Cys–Tyr Crosslink and Inhibitor Recognition by Mammalian Cysteine Dioxygenase. *J. Mol. Biol.* **2016**, *428* (20), 3999–4012.

(2) Kumar, D.; Thiel, W.; De Visser, S. P. Theoretical Study on the Mechanism of the Oxygen Activation Process in Cysteine Dioxygenase Enzymes. *J. Am. Chem. Soc.* **2011**, *133*, 3869–3882.

(3) Kennepohl, P.; Neese, F.; Schweitzer, D.; Jackson, H. L.; Kovacs, J. A.; Solomon, E. I. Spectroscopy of Non-Heme Iron Thiolate Complexes: Insight into the Electronic Structure of the Low-Spin Active Site of Nitrile Hydratase. *Inorg. Chem.* **2005**, *44*, 1826–1836.

(4) Blakely, M. N.; Dedushko, M. A.; Chaau, P.; Poon, Y.; Villar-Acevedo, G.; Kovacs, J. A. Formation of a Reactive, Alkyl Thiolate-Ligated Fe III-Superoxo Intermediate Derived from Dioxygen. *J. Am. Chem. Soc* **2019**, *141* (5), 1867–1870.

(5) Lugo-Mas, P.; Dey, A.; Xu, L.; Davin, S. D.; Benedict, J.; Kaminsky, W.; Hodgson, K. O.; Hedman, B.; Solomon, E. I.; Kovacs, J. A. How Does Single Oxygen Atom Addition Affect the Properties of an Fe-Nitrile Hydratase Analogue? The Compensatory Role of the Unmodified Thiolate. *J. Am. Chem. Soc.* **2006**, *128* (34), 11211–11221.

(6) Villar-Acevedo, G.; Lugo-Mas, P.; Blakely, M. N.; Rees, J. A.; Ganas, A. S.; Hanada, E. M.; Kaminsky, W.; Kovacs, J. A. Metal-Assisted Oxo Atom Addition to an Fe(III) Thiolate. *J. Am. Chem. Soc.* **2017**, *139*, 119–129.

(7) Shoner, S. C.; Nienstedt, A. M.; Ellison, J. J.; Kung, I. Y.; Barnhart, D.; Kovacs, J. A. Structural Comparison of Five-Coordinate Thiolate-Ligated MII = FeII, CoII, NiII, ZnII Ions Wrapped in a Chiral Helical Ligand. *Inorg. Chem.* **1998**, *9* (17), 5721–5726.

(8) Greiner, M.; Kaminsky, W. Crystal Structure Obtained.

(9) Rogers, D.; Kaminsky, W. Crystal Structure Obtained.

(10) Addison, A. W.; Rao, T. N.; Reedijk, J.; Van Rijn, J.; Verschoor, G. C. Synthesis, Structure, and Spectroscopic Properties of Copper(II) Compounds Containing Nitrogen-Sulphur Donor Ligands; the Crystal and Molecular Structure of Aqua[1,7-Bis(N-Methylbenzimidazol-2';-Yl)-2,6-Dithiaheptane]Copper(II) Perchlorate. *J. Chem. Soc. Dalt. Trans.* **1984**, No. 7, 1349–1356.

(11) IR Spectrum Table https://www.sigmaaldrich.com/US/en/technical-documents/technical-article/analytical-chemistry/photometry-and-reflectometry/ir-spectrum-table (accessed Sep 29, 2021).

(12) Ellison, J. J.; Nienstedt, A.; Shoner, S. C.; Barnhart, D.; Cowen, J. A.; Kovacs, J. A. Reactivity of Five-Coordinate Models for the Thiolate-Ligated Fe Site of Nitrile Hydratase. *J. Am. Chem. Soc.* **1998**, *120* (23), 5691–5700.

(13) Stoll, S.; Schweiger, A. EasySpin, a Comprehensive Software Package for Spectral Simulation and Analysis in EPR. *J. Magn. Reson.* **2006**, *178* (1), 42–55.

(14) Bruker (2007) APEX2 (Version 2.1-4), SAINT (version 7.34A), SADABS (version 2007/4), BrukerAXS Inc, Madison, Wisconsin, USA.

(15) (a) Altomare, A.; Burla, C.; Camalli, M.; Cascarano, G. L.; Giacovazzo, C.; Guagliardi, A.; Moliterni, AGG.; Polidori, G.; Spagna, R. SIR97: a new tool for crystal structure determination and refinement. *J. Appl. Crystallog*. **1999,** *32*, 115-119.

(b) Altomare, A.; Cascarano, G. L.; Giacovazzo, C.; Guagliardi, A. Completion and refinement of crystal structures with SIR 92. *J. Appl. Crystallog*. **1993,** *26*, 343-350.

(16) (a) Sheldrick, G. M. (1997) SHELXL-97, Program for the Refinement of Crystal Structures. University of Göttingen, Germany.

(b) Sheldrick, G. M. (2013) Crystal structure refinement with SHELXL. Acta Cryst. (2015). C71, 3-8.

(17) Mackay, S.; Edwards, C.; Henderson, A.; Gilmore, C.; Stewart, N.; Shankland, K.; Donald, A. *MaXus: a computer program for the solution and refinement of crystal structures from diffraction data*. **1997.** University of Glasgow, Scotland.

(18) Waasmaier, D.; Kirfel, A. New Analytical Scattering Factor Functions for Free Atoms and Ions. *Acta Crystallographica* A. **1995,** *51*, 416-430.

Chapter 3: Characterization and Kinetic Investigation of the Formation of an Fe^{III}-Sulfenate Species Derived from Oxo-Atom Donor Addition

3.1 Introduction

Previously, the Kovacs group observed that low-spin (*S* = 1/2), thiolate-ligated $[Fe^{III}(S_2{}^{Me2}N_2N^H(Pr,Pr))](PF_6)$ (**1**) reacts with oxo-atom donors (OAD), such as pentafluoroiodosylbenzene (PFIB), iodoxybenzene ($PhIO_2$), and IBX-ester, to form the Fe-sulfenate complex $[Fe^{III}(\eta^2\text{-}S^{Me2}O)(S^{Me2}N_2N^H(Pr,Pr))](PF_6)$ (**2**).[1,2] Intermediates observed with electron absorbance spectroscopy (EAS), have low energy absorbances with λ_{max} around 700 nm,[3] which shifted depending on the identity of the oxo-atom donor (including *meta*-chloroperoxybenzoic acid (^{m}CPBA), IBX-ester, $PhIO_2$, PFIB, and pyridine-*N*-oxide (PNO)). These intermediates were proposed to correspond to Fe^{III} oxo-atom donor adducts, **1-OAD**.[1] The addition of PNO to **1** resulted in an oxo-atom donor adduct $[Fe^{III}(S_2{}^{Me2}N_2N^H(Pr,Pr))(PNO)](PF_6)$ (**1-PNO**).[2] Oxo-atom donor adducts may precede the formation of high-valent Fe-oxo species that would form after the X-O bond cleavage (where X = I, N, or O depending on the oxo-atom donor). The spin-states of both the starting complex **1** and product **2** were *S* = 1/2, which indicated the reaction was spin allowed and would not need large rearrangements to access a new spin-state. The possible mechanisms for the formation of **2** are outlined in ***Scheme 3.1***.

Previous work in the group was done to investigate which of the proposed pathways resulted in the formation of **2** through analysis of the reaction kinetics. The first proposed mechanism would involve the direct oxygenation of one sulfur of **1** by the oxo-atom donor, forming Fe^{III}-sulfenate **2** (***Scheme 3.1***, **A**). The direct oxygenation was excluded by evidence that the oxo-atom

donor adducts (**1-OAD**) formed[1,2], as well as the observation that the Fe^{III} azide-bound derivative of $[Fe^{III}(S_2{}^{Me2}N_2N^H(Pr,Pr))(N_3)]$ (**3**) did not exhibit any reactivity with the addition of oxo-atom donor.[1] Inhibition of sulfenate **2** formation was observed from the addition of oxo-atom donor PFIB with the addition of excess iodopentafluorobenzene and supported the direct involvement of **1-PFIB** in the mechanism. The inhibition observed supported either (i): the reversible formation of Fe^{III}-sulfenate **2** from **1-OAD** (***Scheme 3.1***, **C**) or (ii): the reversible formation of a high-valent Fe^{V}-oxo species $[Fe^{V}(O)(S_2{}^{Me2}N_2N^H(Pr,Pr))](PF_6)$ (**4**) followed by the irreversible formation of **2** (***Scheme 3.1***, **B**). The addition of excess aryl iodide to **2** did not result in the formation of the oxo-atom donor adduct **1-OAD**. This implied the observed inhibition was likely due to the reversible formation of Fe^{V}-oxo **4**. As **4** was not observed spectroscopically, the rate-determining step of the reaction was likely the cleaving of the I—O bond in the oxo-atom donor to form **4,** which then rapidly and irreversibly formed **2** (***Scheme 3.1*****,** **B**).

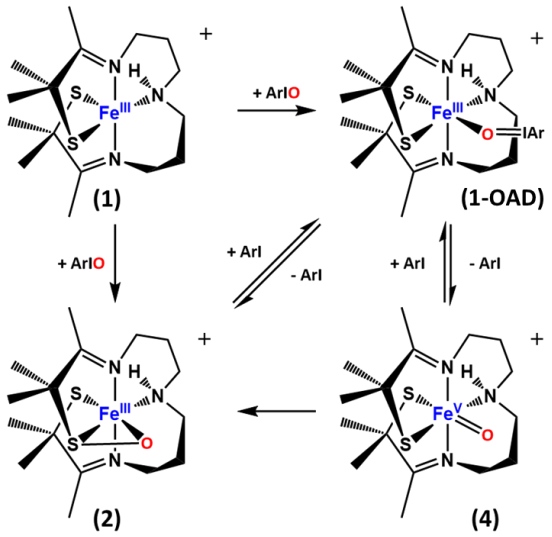

Scheme 3.1 Proposed mechanisms for the formation of the sulfenate $[Fe^{III}(\eta^2\text{-}S^{Me2}O)(S^{Me2}N_2N^H(Pr,Pr))](PF_6)$ (**2**) from $[Fe^{III}(S_2{}^{Me2}N_2N^H(Pr,Pr))](PF_6)$ (**1**), involving either: (**A**) the direct oxygenation of the thiolate from **1** → **2**; (**B**) the formation of **1-OAD** followed by cleaving the X-O bond to form **4** followed by **2**; or (**C**) the formation of **1-OAD** followed by the reversible formation of **2.**

3.2 Characterization of Sterically Constrained Fe^{III} Complex 5

3.2.1 Structural Characterization and Comparison

The addition of steric bulk in the ligand backbone was included to explore any alterations to the rate of the oxygenation reaction and to explore the potential for the observation of additional intermediates, such as a proposed rare thiolate-ligated Fe^{V}-oxo. A new sterically constrained derivative, $[Fe^{III}(S_2{}^{Me2}N^{Me}N_2(Pr,Pr))](PF_6)$ (**5**), with an additional methyl group on the amine, was synthesized following a previously reported synthesis in 38% yield[4] and previously crystallographically characterized[2] (***Figure 3.1***). The geometry of **5** ($\tau = 0.73$) is consistent with a distorted trigonal bipyramidal geometry.[5] The $Fe—N^{apical}$ bond distances were similar for both **1** ($Fe—N^{apical}{}_{avg}$ = 1.961(4) Å) and **5** (Fe—N(1) = 1.951(4) Å) indicating the steric effect of the additional methyl group is isolated to the equatorial coordinating atoms interactions. The equatorial Fe—S(1) = 2.2003(12) Å and Fe—N(2) = 2.132(5) Å bond of **5** were elongated compared to those of **1** (Fe—S(1) = 2.161(2) Å, Fe—S(2) = 2.133(2) Å and Fe—N(2) = 2.049(4) Å) (***Table 3.1***). The steric interference of the additional methyl group, located in the equatorial plane was expected to cause elongation. The elongation was consistent with a higher spin state, supporting **5** having either a $S = 3/2$ or $S = 5/2$ spin-state in the solid state.

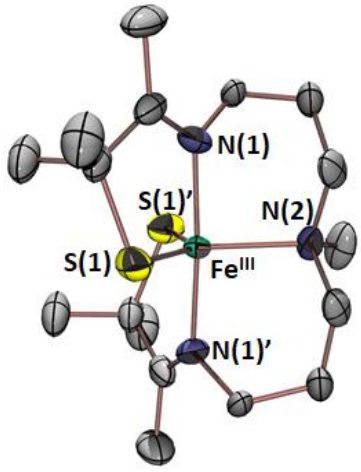

Figure 3.1 ORTEP diagram with hydrogen atoms and anion omitted for clarity showing 50% probability ellipsoids of $[Fe^{III}(S_2{}^{Me2}N_2N^{Me}(Pr,Pr))]^+$ (**5**).[2]

Table 3.1 Comparison of selected bond distances (Å) and angles (°) for thiolate-ligated Fe^{III} complexes $[Fe^{III}(S_2{}^{Me2}N_2N^{H}(Pr,Pr))]^+$ (**1**)[4] and $[Fe^{III}(S_2{}^{Me2}N_2N^{Me}(Pr,Pr))](PF_6)$ (**5**)[2].

Bond (Å), Angle (°)	**1**[4]	**5**[2*]
Fe—N(1)	1.967(4)	1.951(4)
Fe—N(2)	2.049(4)	2.132(5)
Fe—N(3)	1.954(4)	1.951(4)
Fe—S(1)	2.133(2)	2.2003(12)
Fe—S(2)	2.161(2)	2.2003(12)
N(1)—Fe—N(3)	178.1(2)	176.0 (2)
S(1)—Fe—S(2)	121.0(1)	132.11 (8)
S(1)—Fe—N(2)	132.3(1)	116.8 (4)
S(2)—Fe—N(2)	106.5(1)	111.0 (4)
N(1)—Fe—S(1)	86.7(1)	85.26 (12)
N(1)—Fe—N(2)	94.3(2)	88.5 (4)
N(1)—Fe—S(2)	95.2(1)	93.11 (11)
N(3)—Fe—S(1)	91.6(1)	93.11 (11)
N(3)—Fe—N(2)	86.2(2)	95.6 (4)
N(3)—Fe—S(2)	86.4(1)	85.26 (12)
τ	0.76	0.73

*Symmetry operations used to generate equivalent atoms: 1 -x,y,-z+1/2 where N(3) = N(1)' and S(2) = S(1)' for notation.

3.2.2 Solution State Characterization of 5

3.2.2.1 Electronic Absorption Spectroscopy of 5

The absorption band in the 400-500 nm range of **5** (λ_{max} = 424 (THF) and λ_{max} = 421 (MeOH)) were similar to those found in the EAS of **1** (λ_{max} = 415 nm in MeOH)) (***Figure 3.2***). These bands were assigned as thiolate (ligand) → metal (Fe^{III}) charge transfers. The two thiolate arms of the ligand allow for spectroscopic handles in the visible region to persist after the oxygenation of one thiolate. There was also a low intensity band with λ_{max} around 780 nm. The intensities of the bands were solvent dependent. Hydrogen bonding likely occurs between the -OH group of MeOH and the thiolate arms of the ligand, resulting in alterations to the electron donation of the thiolate to the Fe center. The solvent effect was also observed in the Co derivatives of this ligand architecture (***Chapter 4***). The oxidation of the Fe^{II} complex (**Chapter 2**) was observed with EAS by titrating ferrocenium hexafluorophosphate (Cp_2FePF_6) into the Fe^{II} solution (***Figure 3.3***), with the formation of **5** completed after the addition of 1.5 equivalents of Cp_2FePF_6.

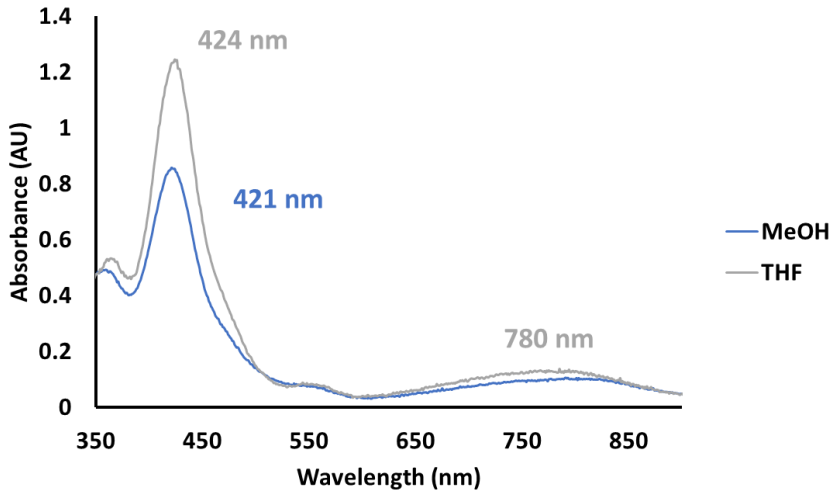

Figure 3.2 Electronic absorption spectra of **5** (0.230 mM) in THF and MeOH at room temperature.

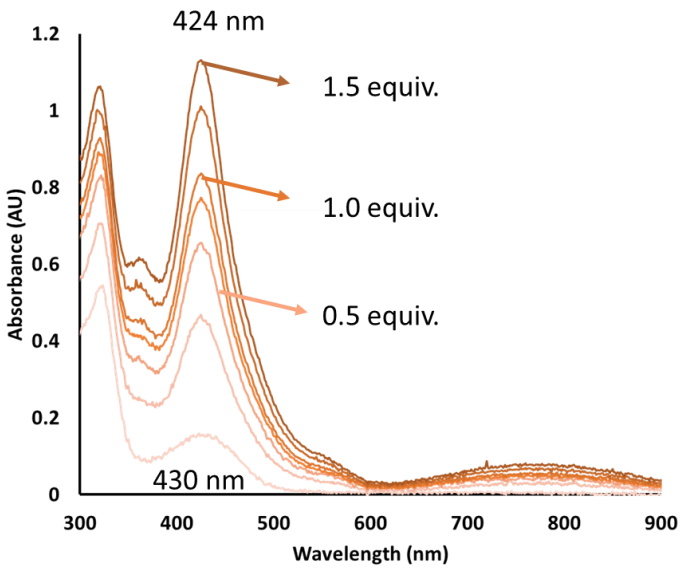

Figure 3.3 EAS observation of the oxidation of Fe^{II} complex [$Fe^{II}(S_2{}^{Me2}N_2N^{Me}(Pr,Pr))$] (0.230 mM, light orange) (**Chapter 2**) to Fe^{III}-**5** (dark orange) with ferrocenium hexafluorophosphate as the chemical oxidant in a THF solution at room temperature.

3.2.2.2 Magnetic Susceptibility

The magnetic susceptibility of a MeCN solution of **5** was measured by Evans method,[6,7] μ_{eff} = 2.84 B.M. (MeCN, 298 K). While this value would normally be assigned to a solution spin state *S* = 3/2, there is also a possibility of a mixture of a higher spin-state of S = 3/2 or *S* = 5/2 and low-spin *S* = 1/2 species in solution. Investigations into variable temperature paramagnetic NMR spectra evaluated by the Evans method (***Figure 3.4***) showed a shift towards the diamagnetic region of the spectrum as the temperature increased in five degree increments from 298 K to 323 K. The affected capillary tube chemical shift was covered up by the residual solvent chemical shift as temperature reached 308 K. However, the trend showed a movement towards a fewer number of paramagnetic electrons with increasing temperature of the solution. The correlation

with temperature and the magnetic susceptibility supported a higher spin-state of **5** is the ground state and more highly populated at lower temperatures.

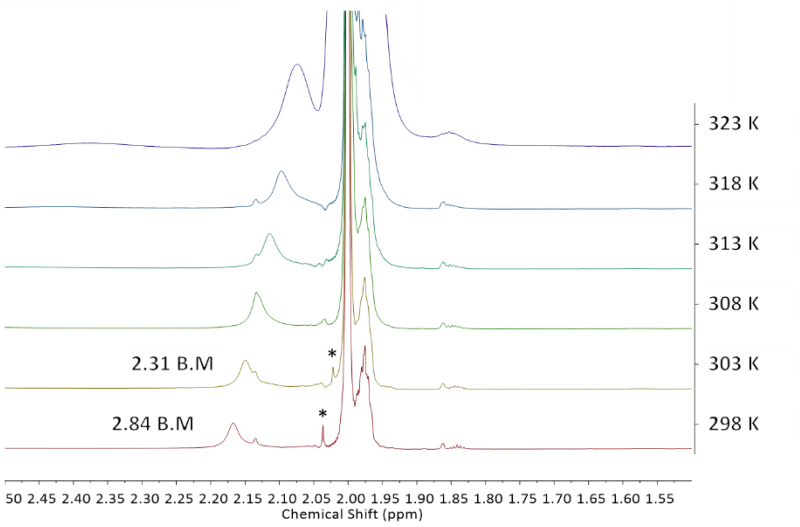

Figure 3.4 Variable temperature (298 to 323 K) ^{1}H-NMR (500 MHz) showing the temperature dependence of the paramagnetic spectrum of **5** (MeCN-d_3) and magnetic susceptibility calculated with the Evans method.

3.2.2.3 Electron Paramagnetic Resonance Studies of Solution

Another method to identify the spin-state of **5** in solution was electron paramagnetic resonance (EPR) spectroscopy as high-spin and low-spin Fe^{III} species will demonstrate unique g-values. ⊥-mode EPR experiments of **5** were carried out at liquid helium (4 K) and liquid nitrogen temperatures (117 K) (***Figure 3.5***). At 117 K, a combination of two species, a (g_{1a} = 2.19, g_{2a} = 2.14, g_{3a} = 2.03) and b (g_{1b} = 2.13, g_{2b} = 2.09, g_{3b} = 2.00); were observed and successfully simulated with EasySpin.[8] The g-values associated with species a were assigned as a low-spin S = 1/2 state of **5** as the known S = 1/2 **1** demonstrated similar g-values g_1 = 2.20, g_2 = 2.15, and g_3 = 2.00.[4] Species b may be an impurity or a solvent-bound **5** with S = 1/2 whose identity is not yet confirmed. At 4

K, the previous signals (117 K) were also observed as well as a new signal with g-values g_1 = 6.23, g_2 = 4.20, and g_3 = 2.12, consistent with the presence of a high-spin *S* = 5/2 species (***Figure 3.5***).

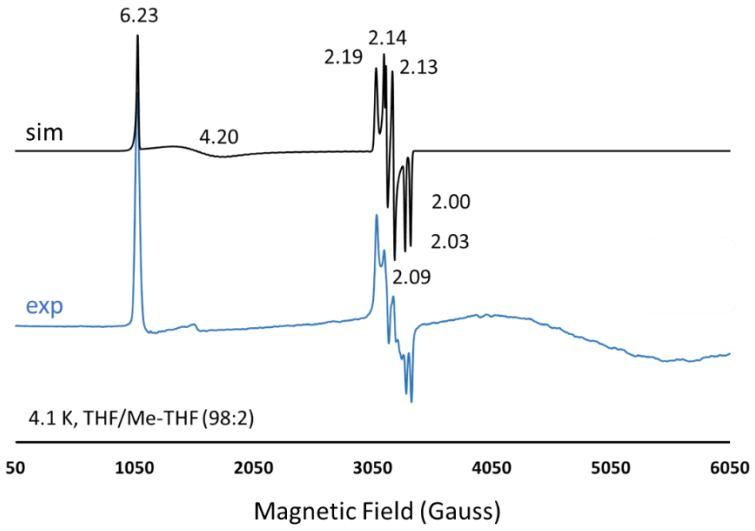

Figure 3.5 Low-temperature (4 K) X-band EPR spectrum of **5** in THF/Me-THF (98:2) glass (blue) and EasySpin simulated spectrum (black).

3.2.2.4 Cyclic Voltammetry

The reduction potential of **5** was determined in order to investigate the effect of additional steric bulk on the electronic environment of the Fe center. Cyclic voltammetry (CV) experiments revealed a reduction potential $E_{1/2}$ = -470 mV (vs SCE) for **5** (***Figure 3.6***), which was very similar to the reported reduction potential of **1** ($E_{1/2}$ = -425 mV vs SCE).[1] The difference in spin-state of the Fe^{III} complexes is not expected to greatly affect the reduction potential due to the compensating effect of the thiolate in the coordination environment.[9] The peak to peak separation of 64 mV is consistent with a reversible one-electron reduction event. The observation that the E_p value does not shift with varying the scan rate also indicate a reversible process, supporting the assignment of the wave as an $Fe^{II/III}$ couple.

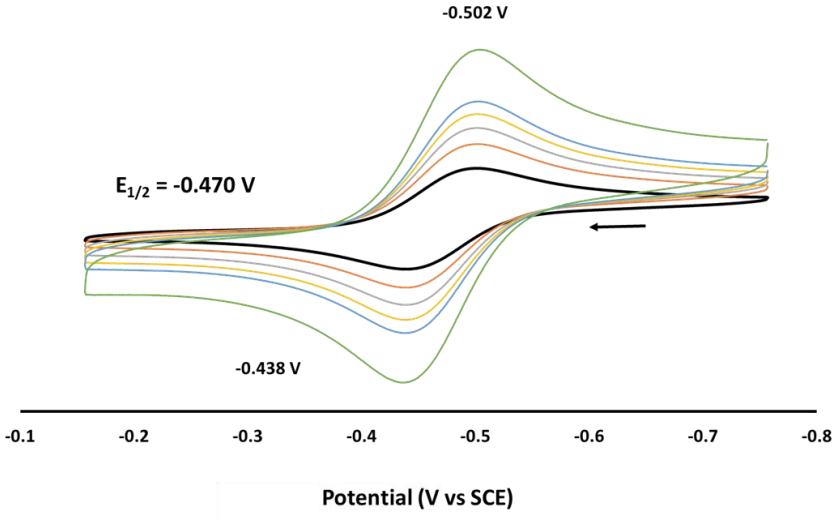

Figure 3.6 Cyclic voltammogram for **5** in MeCN with 0.1 M $(Bu_4N)PF_6$ supporting electrolyte, glassy carbon working electrode, Pt wire counter electrode and Ag/Ag^+ reference electrode with scan rates varied from 50-500 mV, s^{-1}. The peak-to-peak separation is 64 mV, consistent with a one-electron event.

3.3 Oxo-Atom Donor Reactivity

3.3.1 Reactivity of 5 with Iodosylbenzene

The addition of PhIO to sterically-hindered **5** resulted in the formation of a pink species with λ_{max} = 509 nm (***Figure 3.7***), which was similar to the characterized Fe^{III}-sulfenate λ_{max} = 510 nm found for **2**.[1] The product $[Fe^{III}((\eta^2\text{-}S^{Me2}O)S^{Me2}N^{Me}N_2(Pr,Pr))](PF_6)$ (**6**) was isolated as a single crystal from this reaction and its further characterization is discussed in **Section 3.4**. To the best of our knowledge, this was the third Fe-sulfenate to be characterized.[1,9] The formation of **6** from the addition of excess PhIO demonstrates a dependence on the reaction temperature, where the reaction only proceeds at temperatures above -60 °C. Below -60 °C, no change in the spectrum is

observed by EAS. Over the range of temperatures investigated, no intermediate species were observed before the formation of sulfur oxygenation product **6**.

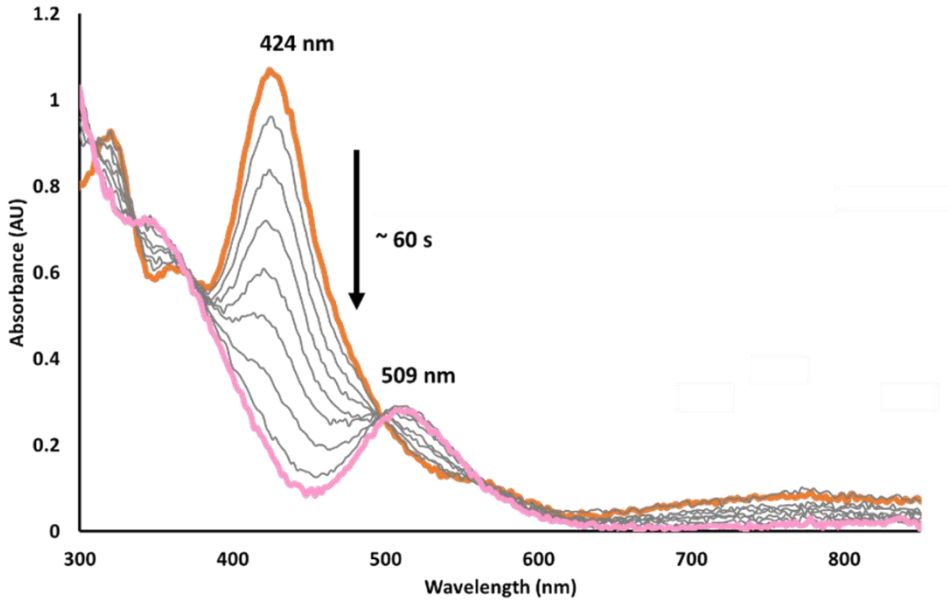

Figure 3.7 Electronic absorption spectrum for the formation of **6** (pink) over 60 seconds through the addition of 6 equivalents of PhIO (MeOH) to **5** (0.230 mM, orange) at 21 °C in THF.

3.3.2 Reactivity of 5 with IBX-Ester

The addition of IBX-ester to **5** was monitored over various temperatures with EAS and demonstrated an eventual conversion to the sulfenate species **6** in each case (***Figures 3.8***, ***3.9***, ***3.10***). A new intermediate was identified in solution as a green species with λ_{max} = 689 nm that forms prior to **6** when the reaction was conducted at low temperature. The species demonstrates a λ_{max} similar to the one found for **1-IBX-ester** (λ_{max} = 677 nm (MeOH)).[1] Following a reaction scheme similar to that found for **1** (***Scheme 3.1***), the intermediate could be either **5-IBX-ester** or a high valent oxo $[Fe^{V}(O)(S_2{}^{Me2}N_2N^{Me}(Pr,Pr))](PF_6)$ (**7**) (*vide infra,* **Scheme 3.2**). Unlike the case with **1**, the addition of other oxo-atom donors (PhIO and PNO) did not result in the growth of

bands in the 600-700 nm range. Further investigation of the species will determine whether it is **5-IBX-ester**, **7**, or another Fe^{III}- centered species.

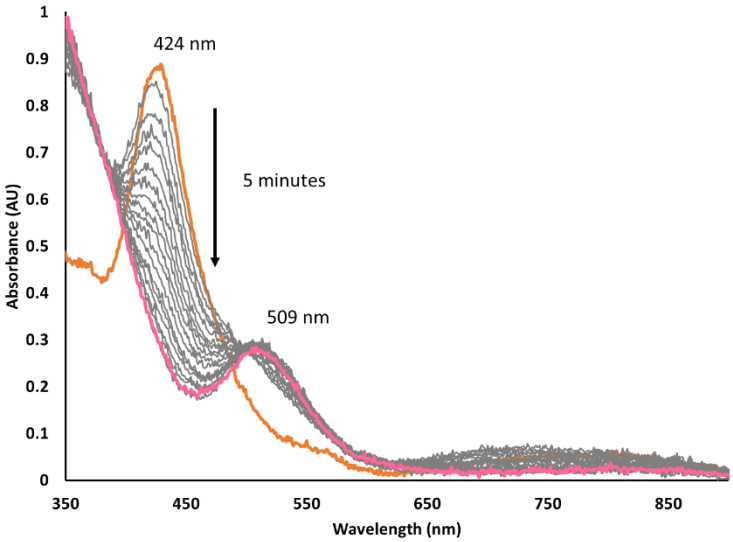

Figure 3.8 EAS monitoring the addition of 10 equivalents of IBX-ester to a solution of **5** (0.230 mM THF, orange) resulting in the formation of **6** (pink) at room temperature.

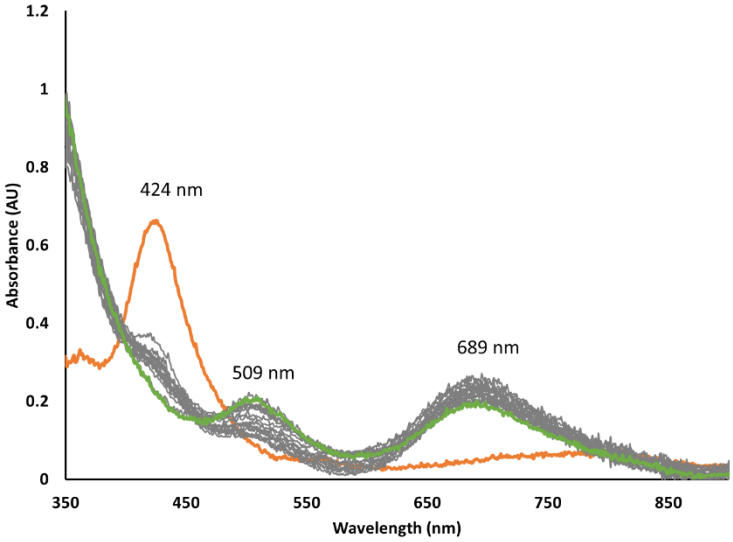

Figure 3.9 EAS monitoring the addition of 10 equivalents of IBX-ester to a solution of **5** (0.230 mM THF, orange) resulting in the concomitant formation of **6** and a new species with λ_{max} = 689 nm (green) at -40 °C.

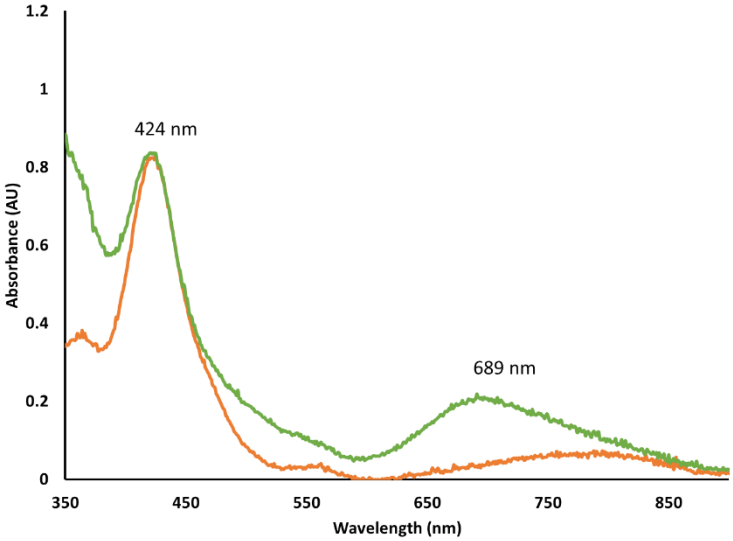

Figure 3.10 EAS monitoring the addition of 1 equivalent of IBX-ester to a solution of **5** (0.230 mM THF, orange) resulting in the formation of a species with λ_{max} = 689 nm (green) at -73 °C.

3.3.3 Reactivity of 5 with Hydrogen Peroxide

The addition of hydrogen peroxide (aqueous) to solutions of **5** resulted in the rapid formation of **6**, monitored by EAS (***Figure 3.11***). Sulfenate **6** rapidly lost its characteristic spectral features, even when cooled to -73 °C, which suggested **6** is susceptible to further oxidation in the presence of a large excess of the oxo-atom donor in solution. The addition of hydrogen peroxide urea (H_2O_2-urea) dissolved in THF to a solution of **5** did not result in the formation of **6**. However, with the addition of non-coordinating base triethylamine (TEA) along with the H_2O_2-urea, the sulfenate **6** was formed (***Figure 3.12***) even at -73 °C, compared to the temperature limitations observed during the addition of PhIO.

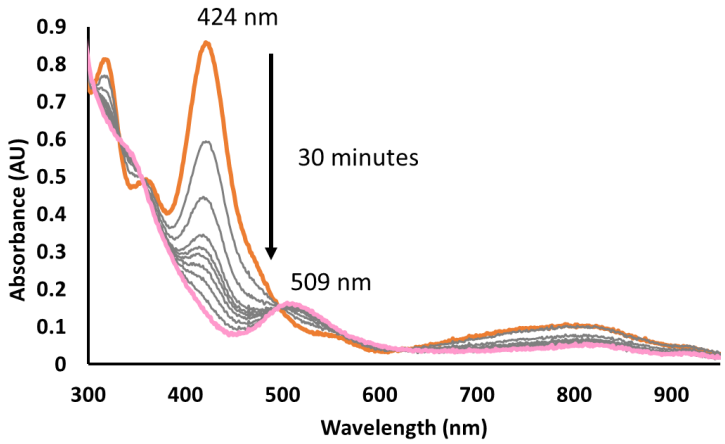

Figure 3.11 EAS monitoring the addition of 10 equivalents of aqueous H_2O_2 to a MeOH solution of **5** (0.230 mM, orange) at -73 °C, resulting in the formation of **6** (pink).

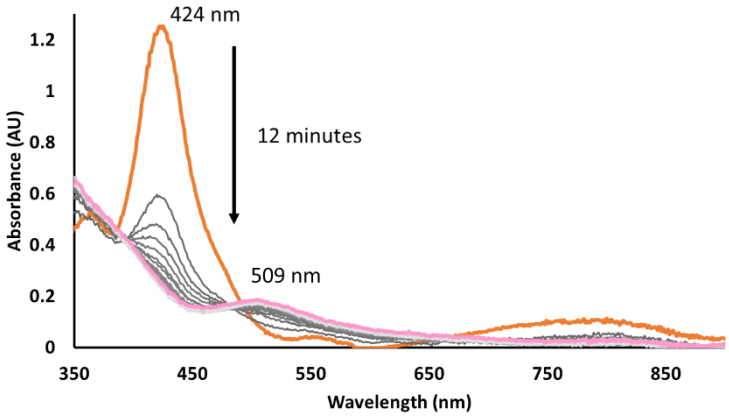

Figure 3.12 EAS monitoring the addition of 1 equivalent of H_2O_2-urea with 1 equivalent TEA to a THF solution of **5** (0.230 mM, orange) at -73 °C, resulting in the formation of **6** (pink).

3.3.4 Reactivity of 5 with Pyridine-*N*-Oxide

Two proposed mechanisms invoke an PhIO adduct intermediate (**5-PhIO**) before the formation of sulfenate **6** (*vide infra*, **Scheme 3.2**). In previous studies of **1**, a green species (λ_{max} = 702 nm (MeOH)) was observed upon the addition of oxo-atom donor pyridine-*N*-oxide (PNO). The product was crystallographically characterized as the **1-PNO** adduct.[2] The N—O bond in PNO

is stronger than the I—O bond in PhIO. The difference in strength was proposed to prevent the complete donation of the oxo-atom from PNO to the Fe^{III} complex **1**.

The reactivity of sterically hindered **5** with PNO was explored herein. Across various temperatures (-73 °C, -40 °C, and 21 °C), with an addition of excess of PNO, no change in absorbance spectrum was observed. The additional steric bulk with the methyl group of **5** likely prohibits the PNO from binding to the open site to form a similar adduct species to **1-PNO**. The difference in reactivity between N^{H}- **1** and sterically hindered N^{Me}-**5** demonstrated the presence of a new barrier to ligand binding due to the change in the steric environment. Space filling models shown in ***Figure 3.13*** were created to illustrate the additional steric interference of the methyl group in **5** compared to **1**.

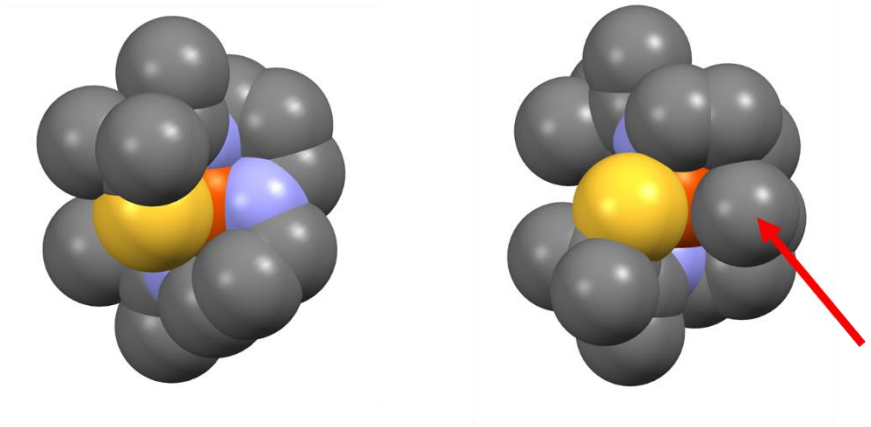

Figure 3.13 Space-filling models for **1** and **5**, showing the steric influence of the addition methyl group (red arrow) of the backbone of **5**.

3.4 Characterization of Fe^{III}-Sulfenate 6

3.4.1 Crystallographic Characterization and Comparison of 6 and 2

Crystals suitable for X-ray diffraction measurements were obtained from a MeOH/THF solution of **6** layered with pentane stored in a -80 °C freezer. The structure of $[Fe^{III}(\eta^2\text{-}S^{Me2}O)(S^{Me2}N_2N^{Me}(Pr,Pr))](PF_6)$ (**6**) was crystallographically characterized with distorted octahedral geometry (***Figure 3.14*** and ***Tables 3.2-3.3***). The equatorial bond lengths of **6** (Fe—S(1) = 2.143(3) Å, and Fe—N(2) = 2.053(12) Å) are similar to those found for **2** (Fe—S(1) = 2.1420(17) Å, Fe—S(2) = 2.1477(17) Å, and Fe—N(2) = 2.044(5) Å)[1], as was expected for similar sulfenate structures that are both low-spin (**Table 3.3**). The Fe—O = 2.165(13) Å found for **6** was elongated compared to the Fe—O = 2.115(4) Å found for **2**. The steric interference of the N^{Me} could interfere with the ability of the O-atom to move in closer to the Fe^{III} ion in **6** as compared to **2**. The angle of the sulfenate S—Fe—O = 39.4(4)° for **6** was within error of the angle found for **2** (39.72(16)°) (**Table 3.3**). To compare the *pseudo*-octahedral geometry of **2** and **6**, the variance in the octahedral angles (σ^2_{oct}) from the ideal 90° was calculated for both structures, wherein a perfect octahedral geometry would demonstrate $\sigma^2_{oct} = 0$. The geometry of **6** was much further from the ideal geometry with $\sigma^2_{oct} = 462.6$, where $\sigma^2_{oct} = 431.0$ for **2.** The steric constraint of the additional methyl group promoted the distortion of the structure and could encourage the complex to undergo further reactivity with excess oxidant.

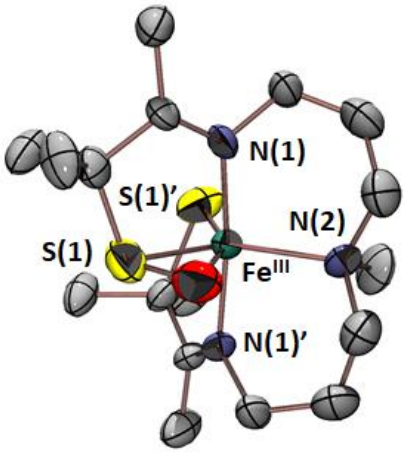

Figure 3.14 ORTEP diagram with hydrogen atoms and counterion omitted for clarity showing 50% probability ellipsoids of $[Fe^{III}(\eta^2\text{-}S^{Me2}O)(S^{Me2}N^{Me}N_2(Pr,Pr))]^+$ **6**.

Table 3.2 Crystal data, intensity collections, and structure refinement parameters for **6**.

Empirical formula	C17 H33 F6 Fe N3 O P S2	
Formula weight	560.40	
Temperature	100(2) K	
Wavelength	0.71073 Å	
Crystal system	Monoclinic	
Space group	P 2/c	
Unit cell dimensions	a = 11.349(8) Å	α= 90°.
	b = 9.077(6) Å	β= 110.88(4)°.
	c = 12.448(9) Å	ϒ = 90°.
Volume	1198.1(15) Å^3	
Z	2	
Density (calculated)	1.553 Mg/m^3	
Absorption coefficient	0.932 mm^{-1}	
F(000)	582	
Crystal size	0.15 x 0.07 x 0.07 mm^3	
Theta range for data collection	1.921 to 26.451°.	
Index ranges	-14<=h<=14, -11<=k<=11, -15<=l<=15	
Reflections collected	18732	
Independent reflections	2422 [R(int) = 0.1799]	
Completeness to theta = 25.00°	97.5%	
Max. and min. transmission	0.7454 and 0.6088	
Refinement method	Full-matrix least-squares on F^2	
Data / restraints / parameters	2422 / 83 / 213	
Goodness-of-fit on F^2	1.012	
Final R indices [I>2sigma(I)]	R1 = 0.0879, wR2 = 0.1854	
R indices (all data)	R1 = 0.1936, wR2 = 0.2363	
Largest diff. peak and hole	0.657 and -0.569 e.Å^{-3}	

Table 3.3 Comparison of selected bond distances (Å) and angles (°) for sulfenate complexes $[Fe^{III}(\eta^2\text{-}S^{Me2}O)(S^{Me2}N_2N^{H}(Pr,Pr))](PF_6)$ (**2**) and $[Fe^{III}(\eta^2\text{-}S^{Me2}O)(S^{Me2}N_2N^{Me}(Pr,Pr))](PF_6)$ (**6**).

Bond (Å), angle (°)	**2**[1]	**6**[*]
Fe—N(1)	1.976(4)	1.97(3)
Fe—N(2)	2.044(5)	2.053(12)
Fe—N(3)	1.954(4)	1.96 (3)
Fe—S(1)	2.1420(17)	2.143(3)
Fe—S(2)	2.1477(17)	2.143(3)
Fe—O(1)	2.115(4)	2.165(13)
S(1)—O(1)	1.447(6)	1.453(14)
N(1)—Fe—N(3)	178.00(19)	171.42
S(1)—Fe—S(2)	112.62(8)	113.92 (17)
S(1)—Fe—O(1)	39.72(16)	39.4 (4)
O(1)—Fe—N(2)	94.3(2)	76.1(11)
S(2)—Fe—N(2)	113.24(15)	130.6 (10)
N(1)—Fe—S(1)	86.08(15)	90.7 (8)
N(1)—Fe—N(2)	95.7(2)	89 (2)
N(1)—Fe—S(2)	91.89(14)	90.7 (19)
N(1)—Fe—O(1)	87.56(18)	89.0 (17)
N(3)—Fe—S(1)	95.37(13)	93.5 (19)
N(3)—Fe—N(2)	84.29(17)	95 (3)
N(3)—Fe—S(2)	86.28(13)	93.5 (19)
N(3)—Fe—O(1)	94.44(17)	82.1 (17)
σ^2_{oct}	341.0	462.6

*Symmetry transformations used to generate equivalent atoms: #1 -x+1,y,-z+1/2 #2 -x,y,-z+1/2. For **6** S(2) = S(1)′ and N(3) = N(1)′.

3.4.2 Solution State Characterization of 6

3.4.2.1 Magnetic Susceptibility

The similarities in bond distances and angles supported the identification of an *S* = 1/2 spin-state for **6**. To confirm the spin-state in solution, Evans method[6,7] was carried out in MeCN solution and demonstrated a magnetic susceptibility μ_{eff} = 1.70 B.M. (MeCN, 298 K). The result was consistent with the expectation for a single unpaired electron (μ_{SO} = 1.73 B.M.). The Evans

method results for Fe^{III}-**5** and sulfenate Fe^{III}-**6** indicated that a spin-state change must take place during the sulfur oxygenation reaction induced by PhIO.

3.4.2.2 Electron Paramagnetic Resonance

To further study the spin-state of **6** in solution ⊥-mode EPR experiments of PhIO derived **6** were carried out at 117 K, where an EPR spectrum with a rhombic signal was expected for **6**. At 117 K, a combination of two species with g-values g_1 = 2.18, g_2 = 2.11, g_3 = 1.98 and g-value 2.13 were observed (***Figure 3.15***). The rhombic signal likely corresponded to the *S* = 1/2 sulfenate **6**. The isotropic signal was likely due to an unidentified impurity or side-product. The g-values are different from the unidentified species present in the EPR spectrum of **5** (***Figure 3.5***). Previously characterized sulfenate-**2** demonstrated a rhombic signal composed of g_1 = 2.17, g_2 = 2.11, g_3 = 1.98, which were very similar to those identified for **6**.

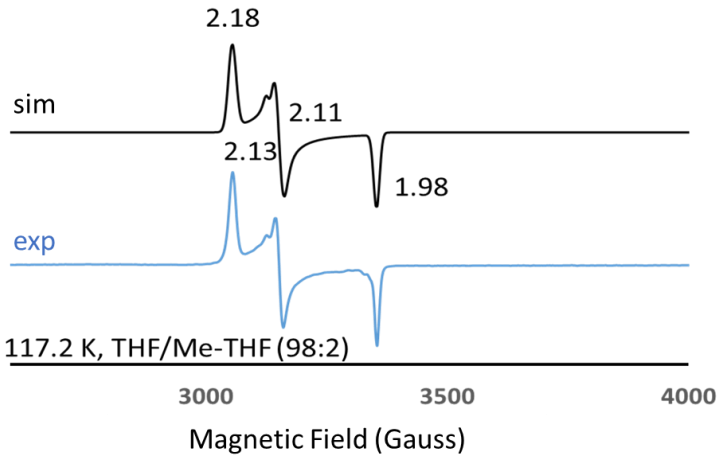

Figure 3.15 Low-temperature (117 K) X-band EPR spectrum of [Fe^{III}(η^2-$S^{Me2}O$)($S^{Me2}N_2N^{Me}$(Pr,Pr))](PF_6) **6** in THF/Me-THF (98:2) glass (blue) and spectra simulated with EasySpin (black).

3.4.2.3 Cyclic Voltammetry

The electronic environment of the Fe^{III}-sulfenate **6** in MeCN was also probed by cyclic voltammetry (CV)**.** The E_p associated with the irreversible reduction event E_{pc} = -1.117 V (vs SCE) (***Figure 3.16***) was lower than reported for **2** where E_{pc} = -0.958 V (vs SCE).[1] In both cases the observed signal was not reversible. The observed shift in reduction potential indicated **6** was more likely to be oxidized than non-methylated **2**. The increased ease of oxidation explained the tendency of **6** to further react with excess oxidant or oxo-atom donor and lose the spectral features as the thiolates of the complex are likely oxygenated and can no longer participate in the intense ligand → metal charge transfers that enable the Fe-thiolate complexes to absorb in the visible region.

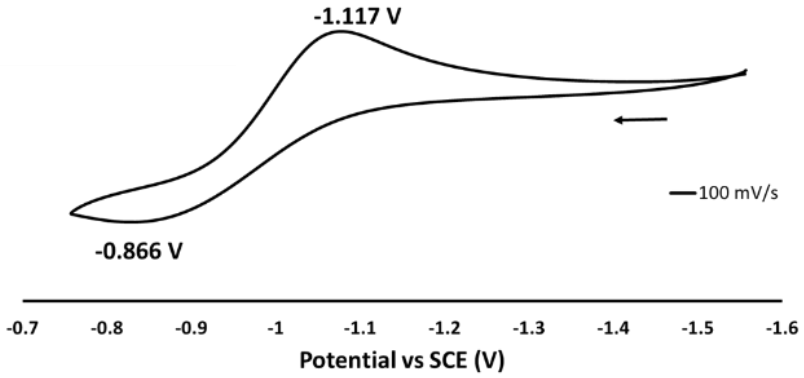

Figure 3.16 Cyclic voltammogram of **6** in MeCN with 0.1 M $Bu_4N(PF_6)$ supporting electrolyte with glassy carbon working electrode, Ag/Ag^+ reference electrode, and platinum counter electrode.

3.5 Kinetic Investigations of Sulfenate 6 Formation from PhIO

3.5.1 Proposed Mechanisms for the Formation of 6

The probable mechanisms for the formation of Fe^{III}-sulfenate **6** were similar to the formation of non-methylated **2**. However, the characterizations of these species showed some key differences from the less sterically constrained system of $[Fe^{III}(S_2{}^{Me2}N_2N^H(Pr,Pr))]^+$ **1.** The difference in spin-state between the mixture found in the starting complex **5** and the *S* = 1/2 state of **6,** supported by EPR, indicated that a spin-state change or spin crossover must occur along the reaction coordinate to the product **6**. The *S* = 1/2 spin state of Fe^{III}-sulfenate **6** supported the existence of an energetic activation cost to overcome the "spin forbiddenness" of the transformation from **5** to **6**. The high-spin **5** (**5-HS**) must undergo a spin-state change at some point along the reaction coordinate to the low spin-(**5-LS**) in order to allow the formation of **6**. In a spin crossover regime, the *S* = 5/2 state of **5** would be the ground state, with a reactive *S* = 1/2 state accessible through intersystem crossing.[10] Intersystem crossing would be consistent with the temperature dependence of the formation of **6** from PhIO.

Taking the differences in spin-state into account, the three proposed mechanisms for the formation of the sterically hindered sulfenate species **6** are illustrated in ***Scheme 3.2***. After a spin-state change from **5-HS** to **5-LS**, the sulfur oxidation resulting in complex **6** may proceed: (A) directly, through the interaction of **5-LS** with PhIO; or through the formation of an Fe^{III}-PhIO adduct (**5-PhIO**), which can then either (B) reversibly form the Fe^{III}-sulfenate **6;** or (C) reversibly form a high valent Fe^{V}-oxo intermediate (**7**), which then irreversibly forms the sulfenate **6**. The addition of small molecule probes of the open site, kinetic studies of the oxo-atom donor

addition, and potential inhibitors of sulfenate formation were investigated. Kinetic experiments also provided insight into the likely rate-determining step of the mechanism of sulfur oxygenation.

The binding of the oxo-atom donor may occur as the rate-determining step followed by processes with significantly lower activation energy barriers as no intermediates are observed upon the addition of PhIO to **5**. The identity of the rate-determining step in the formation of **6** will affect which of the proposed intermediates **5-PhIO** and **7** (***Scheme 3.2***) could be observed and will affect where reversibility of the reaction could be observed.

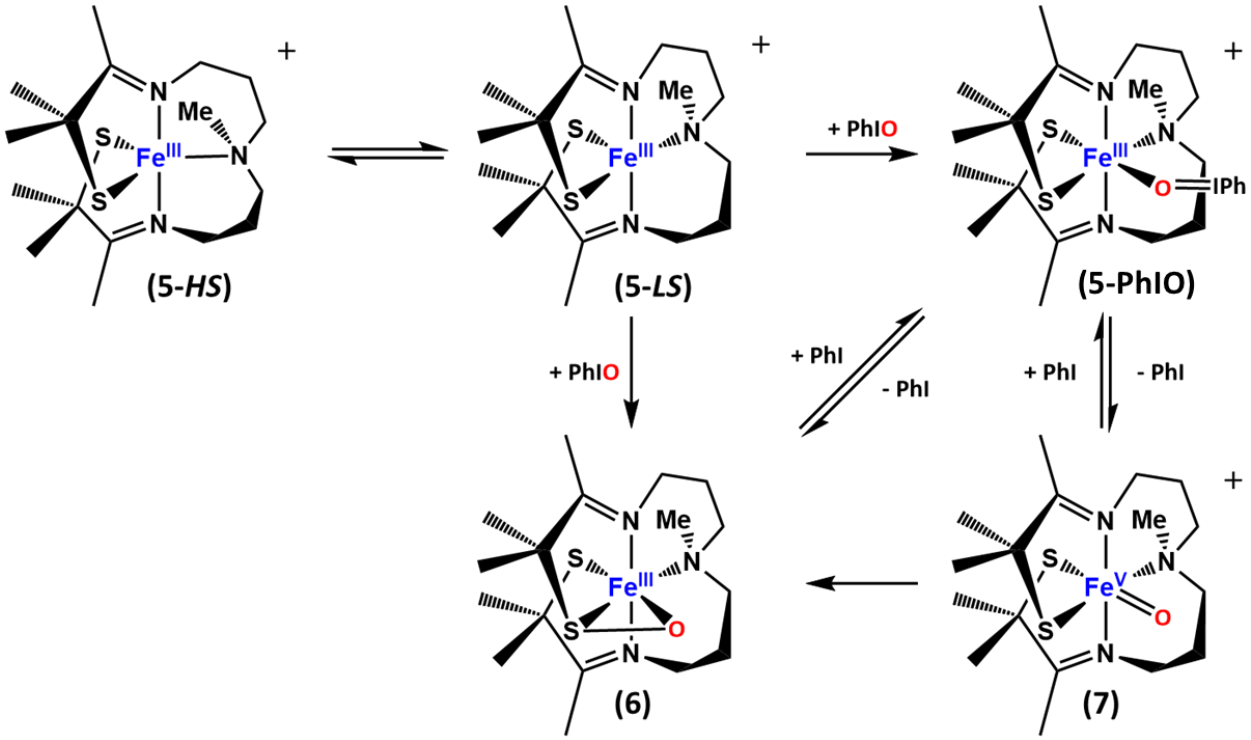

Scheme 3.2 Proposed mechanisms for the formation of the sulfenate [Fe^{III}((η^2-$S^{Me2}O$)$S^{Me2}N^{Me}N_2$(Pr,Pr))](PF_6) (**6**) from [Fe^{III}($S_2^{Me2}N^{Me}N_2$(Pr,Pr))](PF_6) (**5**). After a spin-state change from **5-HS** → **5-LS**, the PhIO can either: (A) directly add an oxo-atom to the thiolate arm (**5-LS** → **6**); (B) form an oxo-atom donor adduct (**5-PhIO**) which then reversibly forms **6**; or (C) form adduct **5-PhIO**, which then cleaves the I-O bond to form high-valent oxo **7** and irreversibly forms **6**.

3.5.2 Investigating Iodobenzene Inhibition

Observed inhibition in the formation of **6** from PhIO, due to excess iodobenzene (PhI), would support either of the reversible steps proposed following the formation of **5-PhIO** (***Scheme 3.2***). The addition of PhI to Fe^{III}-sulfenate **5** did not result in the formation of any absorbing species that would be consistent with the proposed adduct **5-PhIO**. Therefore, any observed inhibition of the reaction would support the formation of high-valent Fe^{V}-oxo **7** in the proposed mechanism, as was observed from the addition of excess pentafluoroiodobenzene to the reaction of **1** with PFIB. An excess of PhI (200 equiv.) was added to the reaction solution of excess PhIO (6 equiv.) and **5** to investigate potential inhibition. The decrease in the absorbance at 424 nm was monitored over time (s) as A_{mod}, described in **Equation 3.1**.

$$A_{mod} = \frac{A_{final} - A_{time}}{A_{final} - A_{initial}} \qquad \text{(Eq. 3.1)}$$

Surprisingly, the plot of A_{mod} vs time (s) was best modeled by a linear equation, indicating the reaction is *zero*-order with respect to **5**. The additions of excess PhI were carried out at -40 , 0 and 21 °C, so that in all cases the reaction proceeds to the sulfenate **6**. At room temperature, the average rate constant k_{obs} was found to be k_{obs} = 2.27 ± 0.6 x 10^{-2} M, s^{-1} with PhI present and k_{obs} = 1.79 ± 0.6 x 10^{-2} M, s^{-1} in the absence of PhI (***Table 3.4***). The treatment of the data sets with 2-sample t-test statistical analyses concluded that no statistically significant inhibition occurred upon the addition of PhI to the reaction mixture. The rates for k_{obs} at room temperature were also within error of each other. No observed inhibition supported the assertion that the rate-determining step for the formation of **6** involves either the spin crossover (**5-HS** → **5-LS**) or the formation of oxo-atom donor adduct **5-PhIO** (***Scheme 3.2***).

Table 3.4 Average *pseudo*-zero order rate constants for the addition of PhIO to complex **5** in both the presence and absence of iodobenzene (PhI).

Temperature (°C)	k_{obs} with PhI (M, s^{-1})	k_{obs} with no PhI (M, s^{-1})
21	$2.27 \pm 0.6 \times 10^{-2}$	$1.79 \pm 0.6 \times 10^{-2}$
0	$7.27 \pm 1 \times 10^{-3}$	$5.39 \pm 0.5 \times 10^{-3}$
-40	$4.25 \pm 0.4 \times 10^{-4}$	$4.42 \pm 1 \times 10^{-4}$

3.5.3 Dependence of Rate on the Concentration of PhIO

The addition of a reagent in a ten equivalent excess is usually referred to as *pseudo-first* order conditions. In this case, the addition of excess PhIO (6 equiv.) resulted in the observation of a *zero*-order dependence on the concentration of **5**, creating *pseudo-zero* order conditions. *Zero-order* conditions usually indicate that there is one reagent in a much larger excess compared to the other species reacting. The concentration of PhIO was varied at -40 °C (***Figure 3.17*** and ***Table 3.5***) to determine the dependence of the rate constant, k_{obs}, with respect to [PhIO]. The linear relationship between k_{obs} and [PhIO] demonstrates *first*-order dependence with respect to PhIO with a slope = 2.64, close to the expected doubling of the rate with a doubling of the concentration of PhIO. The demonstrated *first*-order dependence, indicated PhIO was involved either during or before the rate-determining step (***Scheme 3.2***). The rate-determining step was therefore likely the binding of PhIO, which also likely involves a spin-state change of the complex that accompanies the geometry change required to bind the PhIO molecule.

Two scenarios and their rate laws that would be consistent with a first order dependence on [PhIO] are outlined in ***Schemes 3.3-3.4***. The independent spin equilibrium (***Scheme 3.3***) would require **5-HS** to undergo the spin-state change to **5-LS** before interacting with the oxo-atom

donor PhIO. For the reaction to demonstrate a first-order dependence on [PhIO], the rate of the formation of the sulfenate **6** (k_2) must be much smaller than the rate of the return to **5-HS** (k_{-1}). The abundance of PhIO in the presence of a much smaller **5-LS** proportion would explain the observation of *zero-order* kinetics. A PhIO-induced spin-state change (***Scheme 3.4***) would demonstrate the **5-HS** and PhIO interacting to promote a spin-state change to **5-LS**. In order to demonstrate a first-order dependence on [PhIO], k_2 must be much larger than k_{-1}. The *zero*-order rate would be explained in this case if the rate determining step of the reaction is binding of PhIO to **5-LS**, which then rapidly forms **6**.

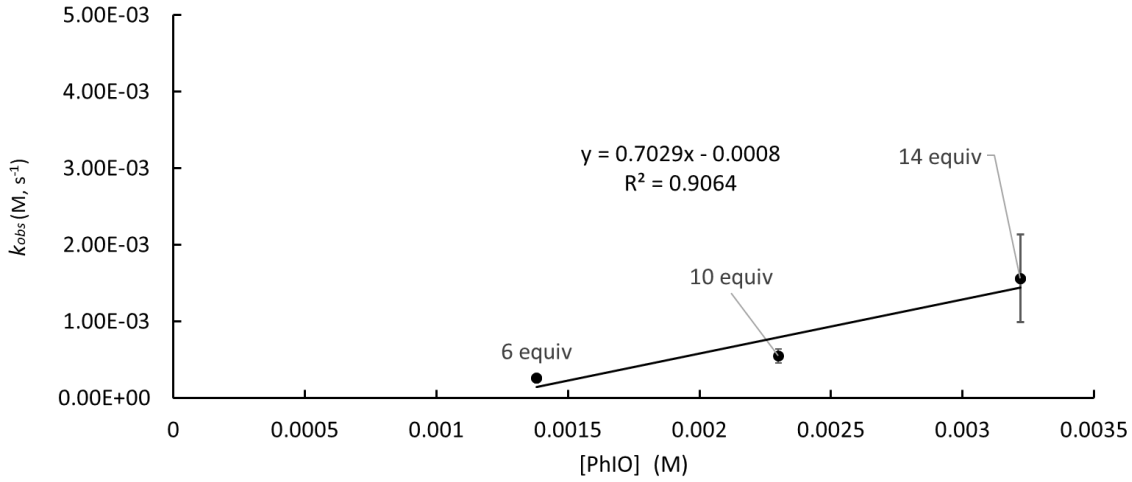

Figure 3.17 Plot of k_{obs} versus the concentration of PhIO (M) for the addition of PhIO to **5** (0.230 mM) in THF at -40°C.

$$Fe^{III}_{HS} \underset{k_{-1}}{\overset{k_1}{\rightleftharpoons}} Fe^{III}_{LS} + PhIO \xrightarrow{k_2} [Fe^{III}_{LS}{-}SO]^+$$

5-HS **5-LS** **6**

Steady-State Approximation:

$$\frac{d[Fe^{III}_{LS}]}{dt} = 0 \qquad \frac{d[Fe^{III}_{LS} - SO]^+}{dt} = \frac{k_2 k_1 [Fe^{III}_{HS}][PhIO]}{k_2[PhIO] + k_{-1}}$$

Scheme 3.3 Rate-law, rate constants, and steady-state approximation for a proposed independent spin equilibrium mechanism, where **5** must change spin-state before interacting with the oxo-atom donor to form sulfenate **6**.

$$Fe^{III}_{HS} + PhIO \underset{k_{-1}}{\overset{k_1}{\rightleftharpoons}} Fe^{III}_{LS} + PhIO \xrightarrow{k_2} [Fe^{III}_{LS}{-}SO]^+$$

5-HS **5-LS** **6**

Steady-State Approximation:

$$\frac{d[Fe^{III}_{LS}]}{dt} = 0 \qquad \frac{d[Fe^{III}_{LS} - SO]^+}{dt} = \frac{k_2 k_1 [Fe^{III}_{HS}][PhIO][PhIO]}{k_2[PhIO] + k_{-1}}$$

Scheme 3.4 Rate-law, rate constants, and steady-state approximation for a proposed PhIO-induced spin-state change mechanism, where the PhIO interacts with the high-spin **5** to form the low-spin **6**.

Table 3.5 Zero-order rate constants k_{obs} (M, s^{-1}) obtained for the formation of **6** from the addition of PhIO to **5.**

[PhIO] (x 10^{-3} M)	k_{obs} (x 10^{-4},M, s^{-1})
1.38	2.64 ± 0.2
2.30	5.51 ± 0.9
3.22	15.57 ± 5.7

3.5.4 Eyring Analysis

Eyring analysis was carried out on the formation of the sulfenate **6** from the addition of 6 equivalents of PhIO (MeOH) to **5** in THF (***Figure 3.18***). The values of $\Delta H^{\ddagger}$ = 9.15 ± 1 kcal, mol^{-1} and $\Delta S^{\ddagger}$ = -35.1 ± 0.5 cal, K^{-1}, mol^{-1} were obtained from the Eyring plot. The activation parameters support the identification of the rate-determining step of the reaction as either involving the spin-crossover of the Fe or the formation of **5-PhIO**. The value of $\Delta H^{\ddagger}$ was relatively low for involving a bond cleavage step,[11] but it would be consistent with a spin crossover in an Fe^{III} system.[12] For a strictly associative process, the value of $\Delta S^{\ddagger}$ would be expected to be about -30 cal, K^{-1}, mol^{-1}.[11] The $\Delta S^{\ddagger}$ = -35.1 ± 0.5 cal, K^{-1}, mol^{-1} was consistent with an associative mechanistic step such as the formation of **5-PhIO**, however the expected *second*-order rate law is not observed, instead, the [Fe^{III}] demonstrates a *zero*-order relationship. Spin equilibria of Fe species, ion pairing, solvent effects and vibrational entropy could also contribute to develop the high entropic cost.[13] The identification of two unique spin states by EPR and Evans method supported the presence of an Fe spin equilibria in the mechanism of the formation of sulfur oxygenation product **6**. Taken together, the results indicated that the steps of the mechanism available to study include spin-crossover and formation of an oxo-atom donor adduct. The adduct **5-PhIO** and high-valent oxo **7** were likely not observed because they occur after the rate-determining step of the formation of **6**.

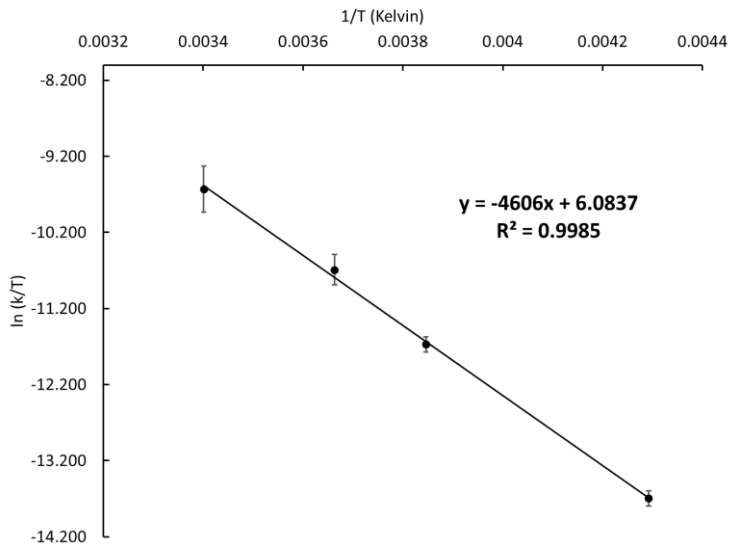

Figure 3.18 An Eyring plot for the formation of **6** from the addition of 6 equivalents of PhIO (MeOH) to **5** (0.230 mM) in THF from -40 to 21°C.

3.6 Reactivity of 5 with Azide

A sixth ligand must be able to bind to the Fe^{III} center of **5** in order to form the oxo-atom donor adduct (**5-OIPh**), which was proposed to be involved in the mechanism of the formation of **6**. Tetrabutylammonium azide ($Bu_4N(N_3)$), was added to **5** as a probe of the open site, resulting in the formation of proposed azide bound Fe^{III} species, $[Fe^{III}(S_2{}^{Me2}N^{Me}N_2(Pr,Pr)(N_3)]$ (**8, *Figure 3.19***). The six-coordinate complex **8**, has λ_{max} = 343, 481, 585, 769 nm, which was consistent with the azide-bound **3**, $[Fe^{III}(S_2{}^{Me2}N^{H}N_2(Pr,Pr)(N_3)]$ (λ_{max} = 330, 460, 708 nm).[4] Both spectra demonstrated the characteristic low energy feature in the spectrum around 700 nm, which corresponds to the presence of sixth ligand.[14] The ability of complex **5** to bind a sixth ligand supported the possibility of **5** to go through an PhIO adduct (**5-OIPh**) in the mechanism of sulfur oxygenation. The formation of the species was not dependent on the concentration of the azide in solution suggesting the azide binds irreversibly to the Fe^{III} center. Unlike **3**, the azide-bound **8** has not

been crystallographically isolated for X-ray measurements of the structure. In part, no crystal structure has been obtained due to the extremely air sensitive nature of **8** (***Figure 3.20***), which reacted with dioxygen or PhIO to form a new species with λ_{max} = 397, 485 (sh). The mechanism of the oxidatively induced reactivity of **8** and identity of the product will be the focus of future work in the group. The presence of azide in the sixth ligand coordination space supported a metal-assisted oxo-atom donor addition to **5**, as the addition of PhIO did not result in the formation of **6**. The competitive inhibition indicated the PhIO and Fe-ion must interact through the open coordination space.

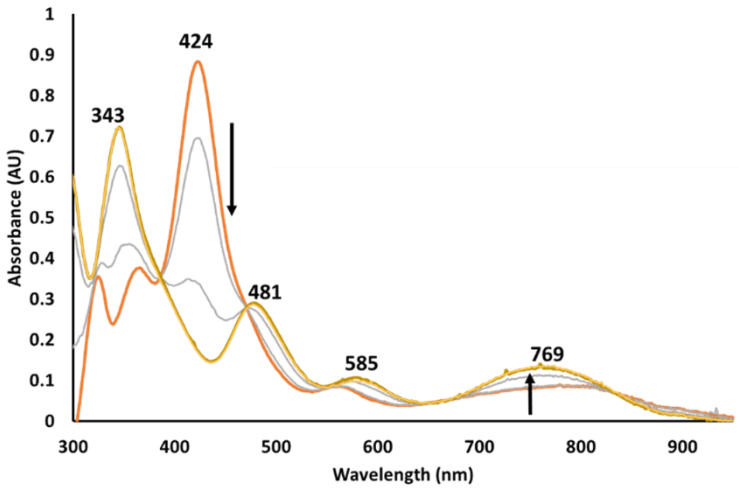

Figure 3.19 Electronic absorption spectrum for the formation of **8** (yellow) through the addition of 10 equivalents of $Bu_4N(N_3)$ to **5** (0.230 mM, orange) at -73 °C in THF over 7 minutes.

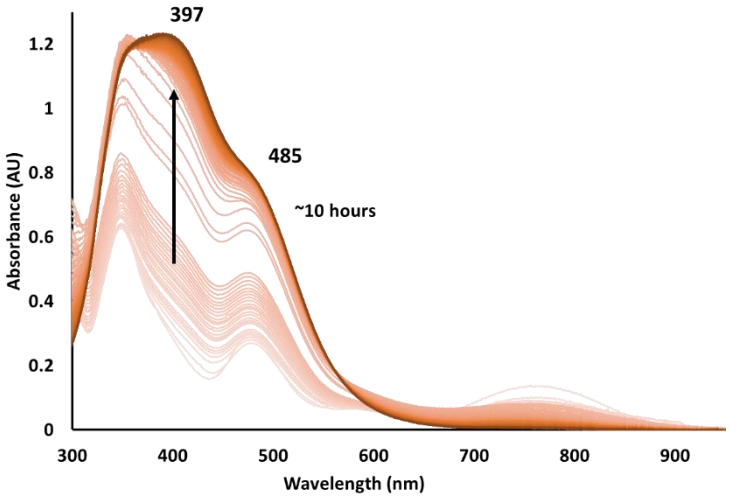

Figure 3.20 EAS monitoring the loss of features associated with **8** and the growth of an unidentified product upon exposure of **8** to dioxygen with a diffuse band λ_{max} = 397, 485 (sh) nm (monitored overnight with some loss of solvent).

3.7 DFT Modeling of the Spin-States of 5

In order to explore the spin-states of **5** and their relative energies, DFT modeling of **5** was attempted with high-spin *S* = 5/2, intermediate spin *S* = 3/2 and low-spin *S* = 1/2 versions of **5** with various functionals and basis sets with the ORCA software package (***Table 3.6***). The errors from the crystallographically obtained bond distances and the geometry optimized distances were large for all of the spin-states and functionals modeled. The low-spin cases had the lowest average errors in bond distances but demonstrated large error in modeling the τ value reflective of the geometry. However, the τ values trended to indicate a more available open site for a sixth ligand to bind for the lower spin-states (***Table 3.6***). In every high-spin model and a few intermediate-spin models the geometry optimizations showed one of the N^{imine} arms at a greater distance from the Fe^{III} than could be considered a bonding interaction, leaving a formally four-coordinate (2N-2S) complex (***Table 3.6***). The errors in modeling could be due to an odd packing

arrangement in the crystal structure perturbing the starting geometry. However, thiolate-ligated transition metal complexes are difficult to model due to the nephelauxetic effect and the changes expected to the electronic behavior. Interestingly, in all cases the comparison of the relative energies of the available spin-states (S = 1/2, S = 3/2, and S = 5/2), revealed the low-spin state was not the ground state.

Table 3.6 Relative energies and τ values calculated for S = 1/2 , S = 3/2 and S = 5/2 spin-states of **5** modeled with various functionals.

	Spin-State	Relative E (eV)	τ value
B3LYP	S = 1/2	1.01	0.62
	S = 3/2	0.25	0.78
	S = 5/2	0.00	0.78
B3LYP*	S = 1/2	1.09	0.62
	S = 3/2	0.19	0.80
	S = 5/2	0.00	0.83
BP86	S = 1/2	0.24	0.67
	S = 3/2	0.00	0.45
	S = 5/2	0.29	0.81
PBE0	S = 1/2	0.73	0.38
	S = 3/2	0.03	0.50
	S = 5/2	0.00	0.14
O3LYP	S = 1/2	41.23	0.35
	S = 3/2	0.60	0.50
	S = 5/2	0.00	0.78
O3LYP*	S = 1/2	0.45	0.35
	S = 3/2	0.38	0.40
	S = 5/2	0.00	0.83
M06	S = 1/2	0.43	0.22
	S = 3/2	0.27	0.20
	S = 5/2	0.00	0.48

Red blocks indicate the N^{imine} is outside of a formal bond distance to the Fe center. * indicates 6-31G* was basis set instead of def2-TZVP.

3.8 Conclusions

Chapter 3 discussed the characterization and reactivity of thiolate-ligated **5**. The complex was synthesized with additional steric bulk on the amine ligand arm in order to study the steric effects on the sulfur oxygenation process. The investigation of the sulfur oxygenation process resulting in rare thiolate-ligated sulfenate **6** from the addition of oxo-atom donors (PhIO, IBX-ester, and H_2O_2) to Fe^{III} **5** was described. The addition of both PhIO and H_2O_2 resulted in the formation of **6** with no intermediates. The addition of IBX-ester resulted in a new green intermediate (λ_{max} = 689 nm) that will be further studied and compared to other sterically constrained systems in the group. The sulfenate **6** was crystallographically characterized and shown to be in a more disordered *pseudo*-octahedral geometry compared to sulfenate **2**. Examples of sulfenate-Fe^{III} species are especially relevant for studying the proposed mechanisms of NHase and CDO. The kinetics of the sulfur oxygenation process from the addition of PhIO were investigated and the spin-state of **5** was determined to be a key part of the reaction pathway indicated by the *zero*-order observed reaction and activation parameters ($\Delta H^{\ddagger}$ = 9.15 ± 1 kcal, mol^{-1} and $\Delta S^{\ddagger}$ = -35.1 ± 0.5 cal, K^{-1}, mol^{-1}). The necessity of a low spin-state to form **6** was related to the rare low-spin state of the native NHase Fe cofactor.

3.9 Experimental Details

3.9.1 General Methods

All reactions were performed under an atmosphere of nitrogen in a glovebox or using standard Schlenk techniques unless otherwise indicated. Reagents purchased from commercial vendors were of the highest purity available and used without further purification. Pentane, diethyl ether

(Et_2O), tetrahydrofuran (THF), acetonitrile (MeCN), and dichloromethane (DCM) were rigorously degassed and purified using solvent purification columns housed in a custom stainless-steel cabinet, dispensed via a stainless steel Schlenk-line (Glass Contour). Methanol (MeOH) was distilled from calcium hydride and degassed prior to use. The synthesis of 3-methyl-3-mercapto-2-butanone was carried out as previously described in the literature.[4]

^{1}H-NMR spectra were recorded on Bruker AV 300, AV 301, or AV-500 FT-NMR spectrometers and are referenced to a residual protio-solvent. Chemical shifts are reported in ppm and coupling constants (J) are in Hz. Electrospray ionization mass spectrometry (ESI-MS) was performed on a Bruker Esquire LC-Ion Trap. Low-temperature electronic absorption spectra were recorded using a Varian Cary 50 spectrophotometer equipped with a fiber optic cable connected to a "dip" attenuated total reflection probe (C-technologies), with a custom-built two-necked solution sample holder equipped with a threaded glass connector (sized to fit the dip probe) and purged with argon. Cyclic voltammograms were recorded in MeCN (100 mM $Bu_4N(PF_6)$ solutions) on a PAR 273 potentiostat utilizing a glassy carbon working electrode, platinum auxiliary electrode, and a Ag/Ag^+ reference electrode. EPR spectra were recorded on a Bruker EPX CW-EPR spectrometer operating at X-band frequency at 4 and 117 K. The EPR spectra were simulated using EasySpin (version 5.2.23), a computational package developed by Stoll and Schweiger[8] and based on Matlab (The MathWorks, Massachusetts, USA). DFT calculations were completed with ORCA 4.1.[15] Visualizations of modeled geometry were completed with ChemCraft.[16]

3.9.2 Synthesis of $[Fe^{III}(S_2{}^{Me2}N^{Me}N_2(Pr,Pr))](PF_6)$ (5)

Sodium methoxide (0.13 g, 2.4 mmol) and 3-methyl-3-mercapto-2-butanone (0.28 g, 2.4 mmol) were dissolved in MeOH (8 mL) and stirred for 10 minutes. 3,3'-diamino-N-methyldipropylamine (0.19 mL, 1.2 mmol) was added to the vial by syringe and stirred for 20 minutes. In a second vial, iron(II) chloride (0.15 g, 1.2 mmol) was dissolved in MeOH (8 mL). Both solutions were cooled at -30 °C for an hour. The solutions were added together dropwise and stirred for 3 hours at room temperature. The solution was then cooled at -30 °C overnight. Ferrocenium hexafluorophosphate (0.40 g, 1.2 mmol) in MeCN (4 mL) was added to the vial and stirred for 30 minutes before returning to the -30 °C freezer overnight. The solvent was reduced to 4 mL by vacuum and filtered over celite. The remaining solution was dried completely under vacuum. The solids were recrystallized from THF/pentane layering and product obtained as a dark red solid (0.1823 g, 0.4469 mmol, 38% yield). Electronic absorption (MeCN): λ_{max} (ε, M^{-1} cm^{-1}) = 318 (4280), 364 (2570), 423 (4710), 559 (437), 768 (353) nm; (THF): λ_{max} (ε, M^{-1} cm^{-1}) = 317 (3900), 366 (2600), 424 (4600), 562 (400), 778 (360) nm. ESI-MS calcd for $[FeC_{17}N_3S_2H_{33}]^+$: 399.4, found: 399.3 m/z. μ_{eff} = 3.48 B.M. Reduction potential (MeCN): $E_{1/2}$ = −0.470 V vs SCE.

3.9.3 Synthesis of $[Fe^{III}(\eta^2\text{-}S^{Me2}O)(S^{Me2}N^{Me}N_2(Pr,Pr))](PF_6)$ (6) from PhIO

Complex **5** (0.7 mg, 1.8 μmol) was dissolved in a minimal amount of MeOH and PhIO (0.39 mg, 1.8 μmol) in MeOH was added. The solution was dissolved in THF (4 mL) and layered with pentane (16 mL) to obtain the product as a red crystalline solid. Electronic absorption (MeOH): λ_{max} (ε, M^{-1} cm^{-1}) = 509 nm (1250); (THF): λ_{max} (ε, M^{-1} cm^{-1}) = 509 nm (1200). ESI-MS calcd for

$[FeC_{17}N_3S_2OH_{33}]^+$: 415.1, found: 415.3 m/z. μ_{eff} = 1.70 B.M. Reduction potential (MeCN): $E_{p,c}$ = −1.117 V (irrev.) vs SCE.

3.9.4 X-ray Determined Structure of $[Fe^{III}(\eta^2\text{-}S^{Me2}O)(S^{Me2}N^{Me}N_2(Pr,Pr))](PF_6)$ (6)

A red prism needle, measuring 0.15 x 0.07 x 0.07 mm^3 was mounted on a loop with oil. Data was collected at -173 ^oC on a Bruker APEX II single crystal X-ray diffractometer, Mo-radiation. Crystal-to-detector distance was 40 mm and exposure time was 240 seconds per frame for all sets. The scan width was 1^o. Data collection was 97.5% complete to 25^o in ϑ. A total of 18732 reflections were collected covering the indices, -14<=h<=14, -11<=k<=11, -15<=l<=15. 2422 reflections were symmetry independent and the elevated R_{int} = 0.1799 reflects the small size of the sample. Indexing and unit cell refinement indicated a primitive monoclinic lattice. The space group was found to be P2/c (No. 13).

The data was integrated and scaled using SAINT, SADABS within the APEX2 software package by Bruker.[17] Solution by direct methods (SHELXS, SIR97[18]) produced a complete heavy atom phasing model consistent with the proposed structure. The structure was completed by difference Fourier synthesis with SHELXL97.[19-20] Scattering factors are from Waasmair and Kirfel.[21] Hydrogen atoms were placed in geometrically idealized positions and constrained to ride on their parent atoms with C—H distances in the range 0.95-1.00 Angstrom. Isotropic thermal parameters U_{eq} were fixed such that they were 1.2U_{eq} of their parent atom U_{eq} for CH's and 1.5U_{eq} of their parent atom U_{eq} in case of methyl groups. All non-hydrogen atoms were refined anisotropically by full-matrix least-squares.

3.9.5 Formation of [$Fe^{III}(S_2{}^{Me2}N^{Me}N_2(Pr,Pr))(N_3)$] (8)

A 0.230 mM solution of **5** was prepared in THF under an inert atmosphere in a drybox. The resulting solution was transferred via gastight syringe to a custom-made dip probe cell, previously purged with argon. The solution was cooled to -73 °C with an acetone and dry ice bath. A 0.92 M solution of $^{t}Bu_4N(N_3)$ was prepared in THF and 135 µL was added to the cell by gas tight syringe resulting in the formation of **8.** Electronic absorption (THF): λ_{max} = 343, 481, 585, 769 nm.

3.9.6 Addition of PNO to 5

A 0.230 mM solution of **5** was prepared in THF under an inert atmosphere in a drybox. The resulting solution was transferred via gastight syringe to a custom-made dip probe cell, previously purged with argon. The solution was cooled to -73 °C with an acetone and dry ice bath. A 0.168 M solution of PNO was prepared in THF and 200 µL was added to the cell by gas tight syringe**.**

3.9.7 Addition of PhI to 6

A 0.230 mM solution of **5** was prepared in THF under an inert atmosphere. The resulting solution was transferred via gastight syringe to a custom-made dip probe cell, previously purged with argon. Iodobenzene (20 µL, 0.184 mol, 200 equiv.) was added to the cell by gas tight syringe**.**

3.9.8 Monitoring the formation of 5 (Varying temperature)

A 0.230 mM solution of **4** was prepared in THF under an inert atmosphere in a drybox. The resulting solution was transferred via gastight syringe to a custom-made dip probe cell, previously purged with argon. The solution was held at varying temperatures of -40, -13, 0, or 21

°C with cold baths. A 55.6-167 mM solution of PhIO was prepared in MeOH and 100 µL was added to the cell by gas tight syringe resulting in the formation of **5.**

3.9.9 PhI inhibition studies

A 0.230 mM solution of **4** was prepared in THF under an inert atmosphere in a drybox. The resulting solution was transferred via gastight syringe to a custom-made dip probe cell, previously purged with argon. PhI (20 µL, 0.184 mol, 200 equiv.) was added to the cell by gas tight syringe**.** The solution was held at varying temperatures of -40, 0, or 21 °C with cold baths. A 55.6 mM solution of PhIO was prepared in MeOH and 100 µL was added to the cell by gas tight syringe resulting in the formation of **5.**

3.10 Chapter 3 References

(1) Villar-Acevedo, G.; Lugo-Mas, P.; Blakely, M. N.; Rees, J. A.; Ganas, A. S.; Hanada, E. M.; Kaminsky, W.; Kovacs, J. A. Metal-Assisted Oxo Atom Addition to an Fe(III) Thiolate. *J. Am. Chem. Soc.* **2017**, *139*, 119–129.

(2) Blakely, M. N. Insights into Dioxygen Activation by Biomimetic Alkyl Thiolate-Ligated Iron Complexes, University of Washington, 2019.

(3) Blakely, M. N.; Downing, A. N.; Kovacs, J. A. Manuscript in Preparation. **2019**.

(4) Ellison, J. J.; Nienstedt, A.; Shoner, S. C.; Barnhart, D.; Cowen, J. A.; Kovacs, J. A. Reactivity of Five-Coordinate Models for the Thiolate-Ligated Fe Site of Nitrile Hydratase. *J. Am. Chem. Soc.* **1998**, *120* (23), 5691–5700.

(5) Addison, A. W.; Nageswara Rao, T.; Reedijk, J.; van Rijn, J.; Verschoor, G. C. Synthesis, Structure, and Spectroscopic Properties of Copper(II) Compounds Containing Nitrogen-Sulphur Donor Ligands ; the Crystal and Molecular Structure of Aqua[l,7-Bis(N-Methylbenzimidazol-2'-Yl)- 2,6-Dithiaheptane]Copper(Ii) Perchlorate the Crystal A. *J. Chem. Soc. Dalt. Trans.* **1984**, No. 7, 1349–1356.

(6) Evans, D. F. The Determination of the Paramagnetic Susceptibility of Substances in Solution by Nuclear Magnetic Resonance. *J. Chem. Soc.* **1959**, No. 0, 2003–2005.

(7) Live, D. H.; Chan, S. I.; Amos, A. Bulk Susceptibility Corrections in Nuclear Magnetic Resonance Experiments Using Superconducting Solenoids. *Anal. Chem.* **1970**, *42* (7), 791–792.

(8) Stoll, S.; Schweiger, A. EasySpin, a Comprehensive Software Package for Spectral Simulation and Analysis in EPR. *J. Magn. Reson.* **2006**, *178* (1), 42–55.

(9) Lugo-Mas, P.; Dey, A.; Xu, L.; Davin, S. D.; Benedict, J.; Kaminsky, W.; Hodgson, K. O.; Hedman, B.; Solomon, E. I.; Kovacs, J. A. How Does Single Oxygen Atom Addition Affect the Properties of an Fe-Nitrile Hydratase Analogue? The Compensatory Role of the Unmodified Thiolate. *J. Am. Chem. Soc.* **2006**, *128* (34), 11211–11221.

(10) Tanabe, Y.; Sugano, S. On the Absorption Spectra of Complex Ions II. *J. Phys. Soc. Japan* **1954**, *9* (5), 766–779.

(11) Asperger, S. *Chemical Kinetics and Inorganic Reaction Mechanisms*; 2003.

(12) Nihei, M.; Shiga, T.; Maeda, Y.; Oshio, H. Spin Crossover Iron(III) Complexes. *Coord. Chem. Rev.* **2007**, *251*, 2606–2621.

(13) Mader, E. A.; Davidson, E. R.; Mayer, J. M. Large Ground-State Entropy Changes for Hydrogen Atom Transfer Reactions of Iron Complexes. *J. Am. Chem. Soc.* **2007**, *129*, 5153–5166.

(14) Kennepohl, P.; Neese, F.; Schweitzer, D.; Jackson, H. L.; Kovacs, J. A.; Solomon, E. I. Spectroscopy of Non-Heme Iron Thiolate Complexes: Insight into the Electronic Structure of the Low-Spin Active Site of Nitrile Hydratase. *Inorg. Chem.* **2005**, *44*, 1826–1836.

(15) Neese, F. The ORCA Program System. *Wiley Interdiscip. Rev. Comput. Mol. Sci.* **2012**, *2* (1), 73–78.

(16) Chemcraft - Graphical Program for Visualization of Quantum Chemistry Computations.

Ivanovo, Russia 2005.

(17) Bruker (2007) APEX2 (Version 2.1-4), SAINT (version 7.34A), SADABS (version 2007/4), BrukerAXS Inc, Madison, Wisconsin, USA.

(18) (a) Altomare, A.; Burla, C.; Camalli, M.; Cascarano, G. L.; Giacovazzo, C.; Guagliardi, A.; Moliterni, AGG.; Polidori, G.; Spagna, R. SIR97: a new tool for crystal structure determination and refinement. *J. Appl. Crystallog*. **1999,** *32*, 115-119.

(b) Altomare, A.; Cascarano, G. L.; Giacovazzo, C.; Guagliardi, A. Completion and refinement of crystal structures with SIR 92. *J. Appl. Crystallog*. **1993,** *26*, 343-350.

(19) (a) Sheldrick, G. M. (1997) SHELXL-97, Program for the Refinement of Crystal Structures. University of Göttingen, Germany.

(b) Sheldrick, G. M. (2013) Crystal structure refinement with SHELXL. Acta Cryst. (2015). C71, 3-8.

(20) Mackay, S.; Edwards, C.; Henderson, A.; Gilmore, C.; Stewart, N.; Shankland, K.; Donald, A. *MaXus: a computer program for the solution and refinement of crystal structures from diffraction data*. **1997.** University of Glasgow, Scotland.

(21) Waasmaier, D.; Kirfel, A. New Analytical Scattering Factor Functions for Free Atoms and Ions. *Acta Crystallographica* A. **1995,** *51*, 416-430.

Chapter 4: Influence of Ligand Constraints in Thiolate-Ligated Cobalt Complexes on Sulfur-Oxygenation Reactivity

4.1 Introduction

Nitrile hydratases (NHase) are non-heme Fe^{III}-containing, or non-corrinoid Co^{III}-containing, enzymes, which catalyze stereoselective hydration of nitriles to amides,[1] and are widely used in industry,[1–6] as well as for the decontamination or bioremediation of nitrile polluted sites.[7,8] The focus of **Chapter 4** concerns the cobalt-containing analogue of NHase. Structural characterization of Co-NHase using X-ray crystallography, showed that the active site consists of a six coordinate low-spin $S = 0$ Co^{III} ion[9–12] ligated by three cysteinates, two of which have been oxidized, one to a singly oxygenated sulfenic acid ($^{Cys}S–OH$)[13–15] and the other to a doubly oxygenated sulfinate ($^{Cys}S(O)_2^-$).[16] In addition, the Co^{III} ion is ligated by two amide nitrogens, and a water molecule, (***Figure 4.1***).[17] The low-spin Co^{III} environment increases metal ion Lewis acidity, relative to high-spin Co^{III}, and this facilitates the binding of nitrile substrate to the metal ion, and its subsequent hydrolysis.[18,19] The Kovacs group previously reported two Co^{III}-N≡CMe complexes that hydrolyze MeCN to form either a Co^{III}-iminol, and Co^{III}-amide intermediates.[20] The current proposed mechanism (**Chapter 1, Scheme 1.6**) for NHase implicates the $^{Cys}S–OH$ moiety in the formation of a unique, unobserved intermediate containing a five-membered ring (***Figure 4.2***), through nucleophilic attack by the $^{Cys}S–OH$ oxygen at the carbon of the bound nitrile substrate followed by proton transfer to the imine nitrogen.[21,22] NHase is inactivated when an additional oxygen atom is added to the $^{Cys}S–OH$ moiety, implying that the $^{Cys}S–OH$ plays a key role responsible for the reactivity of the enzyme.[23] Examples of singly oxygenated thiolate-ligated transition metal

complexes, and in particular examples that incorporate cobalt as the central metal ion are rare.[24–28]

The transition metal must have a sulfenate (RS–O^-) in the coordination sphere that is capable of participating in both protonation and nucleophilic attack of the nitrile substrate, in order to form biomimetic models capable of forming competent analogues of the NHase five-membered, ring-containing intermediate. However, the uniquely oxygenated cysteine residues have proven challenging to incorporate and only two Co^{III} model complexes that incorporate a sulfenate have been reported, both of which bind to the metal in an η^2-fashion, and neither of which displays further reactivity with oxidants (dioxygen or hydrogen peroxide).[24,25]

The cobalt complex $[Co^{III}(S_2{}^{Me2}N_2N^H(Pr,Pr))]^+$ (**1**) was shown to react with air to incorporate two oxygens on one of the thiolates initially to form a sulfinate complex (***Figure 4.3***), $[Co^{III}(S^{Me2}(S^{O2})N_2N^H(Pr,Pr))]^+$ (**2**). The reaction of doubly oxygenated **2** with H_2O_2, installed a single oxygen on the remaining unmodified thiolate sulfur to form an η^2-sulfenate-ligated Co complex (***Figure 4.3***), $[Co^{III}((\eta^2\text{-}S^{Me2}O)(S^{O2})N_2N^H(Pr,Pr))]^+$ (**3**).[24] Masuda and coworkers also reported several Co^{III} complexes with N_2S_3-type ligands including an η^2-bound Co^{III} sulfenate complex, which did not react further with air.[25] The following chapter demonstrates how small changes to the ligand scaffold resulted in dramatic changes to reactivity, especially concerning sulfur oxygenation.

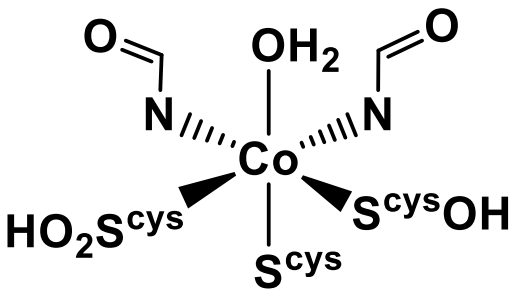

Figure 4.1 Co^{III} ion site of NHase family, with post-translationally modified cysteinate ligands.[29]

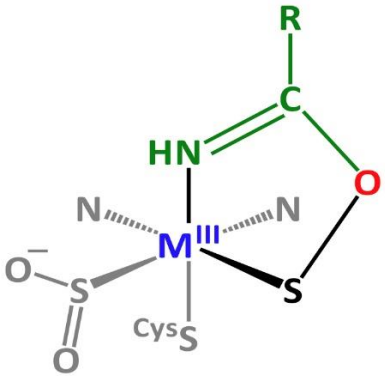

Figure 4.2 ChemDraw diagram of the proposed five-membered ring intermediate created through nucleophilic attack by the sulfenic acid.

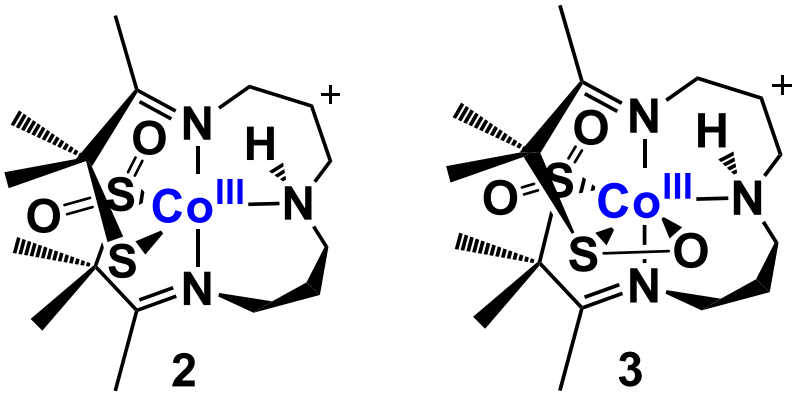

Figure 4.3 ChemDraw diagrams of the sulfinate containing cobalt complex $[Co^{III}(S^{Me2}(S^{O2})N_2N^H(Pr,Pr))]^+$ (**2**) and η^2-sulfenate-ligated complex $[Co^{III}((\eta^2\text{-}S^{Me2}O)(S^{O2})N_2N^H(Pr,Pr))]^+$ (**3**).

4.2 Cobalt(II) Thiolate Ligated Complexes with Varied Ligand Constraints

4.2.1 Sterically Constrained Co^{II} Complexes 4-6.

Changes to the ligand backbone of Co^{II} complexes explored herein involve (a) replacement of the secondary amine with a methylated tertiary amine, (b) the replacement of one of the propyl linkers with an ethyl linker and (c) the presence or absence of the *gem*-dimethyl groups on the thiolate linker, (***Figure 4.4***). Using a metal ion template,[30] a Schiff-base condensation between the modified amines and/or modified thiolate precursor resulted in the formation of three new thiolate-ligated cobalt complexes (***Figure 4.4***), $[Co^{II}(S_2{}^{Me2}N_2N^{Me}(Pr,Pr))]$ (**4**), $[Co^{II}(S_2{}^{Me2}N_2N^{H}(Et,Pr))]$ (**5**), and $[Co^{II}(S_2{}^{\beta H2}N_2N^{H}(Pr,Pr))]$ (**6**), respectively. The synthesis of **4** and **5** will be discussed in the following sections and compared to the structures of **6** and **7** obtained by other Kovacs group members.[31] New evidence to support a metal-templated mechanism for the formation of these complexes was obtained via the isolation of an intermediate, $[Co^{III}(S^{Me2}N_2N^{Me}(Pr,Pr)(TK))]^+$ (**8**), and its structure was determined via X-ray crystallography (***Figure 4.5***, ***Table 4.1***). Complex **8** (***Figure 4.5***) contained an uncondensed 3-methyl-3-mercapto-2-butanone (thioketone, TK) coordinated to the metal ion, in addition to a condensed imine/thiolate arm. The ketone of this intermediate would be more activated than a free ketone, making it easier for the second condensation reaction to take place via decoordination of primary amine nitrogen N(2).

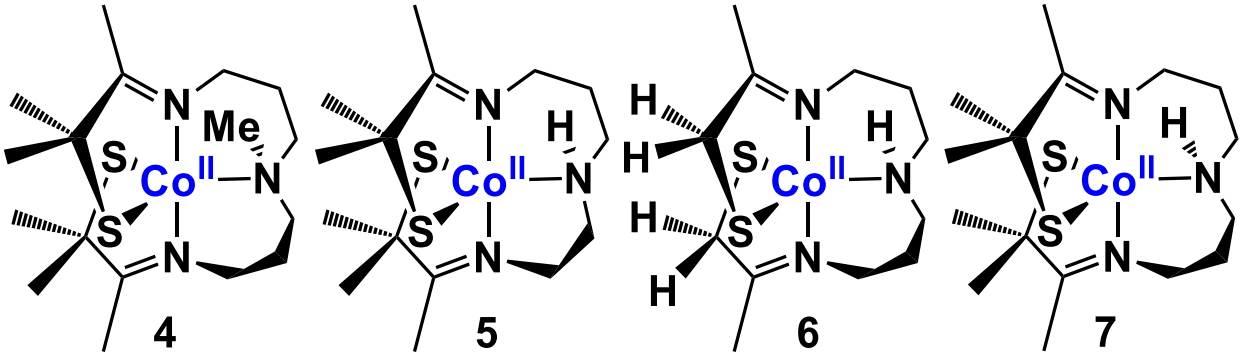

Figure 4.4 ChemDraw structures of the thiolate-ligated Co^{II} series: [$Co^{II}(S_2^{Me2}N_2N^{Me}(Pr,Pr))$] (**4**); [$Co^{II}(S_2^{Me2}N_2N^{H}(Et,Pr))$] (**5**); [$Co^{II}(S_2^{\beta H2}N_2N^{H}(Pr,Pr))$] (**6**); and [$Co^{II}(S_2^{Me2}N_2N^{H}(Pr,Pr))$] (**7**).

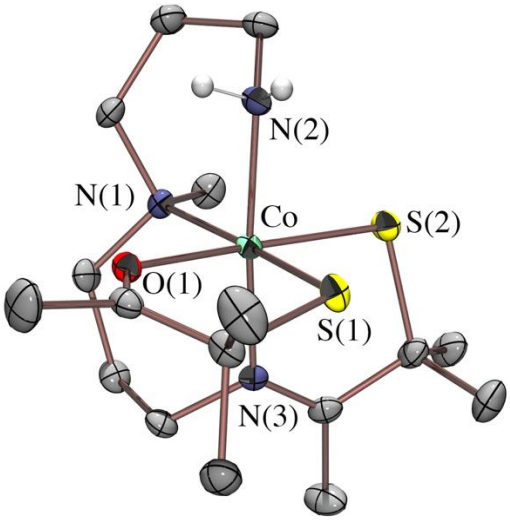

Figure 4.5 ORTEP figure of majority cation (79%) of [$Co^{III}(S^{Me2}N_2N^{Me}(Pr,Pr)(TK))]^+$ (**8**). showing 50% probability ellipsoids. With the exception of the primary amine hydrogens, hydrogen atoms and counterion have been omitted for clarity.

Table 4.1 Crystal data, intensity collections, and structure refinement parameters for $[Co^{III}(S^{Me2}N^{Me}N_2(Pr,Pr)(TK))]^+$ (**8**).

formula	$C_{17}H_{35}B_{0.20}CoF_{5.59}N_3OP_{0.79}S_2$	
MW	553.58	
T, K	100(2)	
Wavelength	0.71073 Å	
Crystal system	Monoclinic	
Space group	P 2_1/n	
Unit cell dimensions	a = 9.5131(12) Å	α= 90°.
	b = 21.165(3) Å	β= 109.214(4)°.
	c = 12.6076(17) Å	ϒ = 90°.
Volume	2397.1(5) $Å^3$	
Z	4	
Density (calculated)	1.534 Mg/m^3	
Absorption coefficient	1.001 mm^{-1}	
F(000)	1153	
Crystal size	0.300 x 0.300 x 0.150 mm^3	
Theta range for data collection	1.924 to 28.492°.	
Index ranges	-12<=h<=12, -28<=k<=28, -16<=l<=16	
Reflections collected	59457	
Independent reflections	6036 [R(int) = 0.0563]	
Completeness to theta = 25.000°	100.0 %	
Refinement method	Full-matrix least-squares on F^2	
Data / restraints / parameters	6036 / 58 / 376	
Goodness-of-fit on F^2	1.032	
Final R indices [I>2sigma(I)]	R1 = 0.0317, wR2 = 0.0712	
R indices (all data)	R1 = 0.0446, wR2 = 0.0771	
Largest diff. peak and hole	0.519 and -0.285 e– $Å^{-3}$	

4.2.2 Structural Comparison of Five-Coordinate Co^{II} Complexes 4-7.

The constraints placed on the ligand backbone of the series of complexes discussed herein (***Figure 4.4***) influenced the metrical parameters, as well as the electronic structures and reactivity. The ethyl linker of **5** reduced the flexibility of the carbon chain, relative to the propyl linker of **4** and **6**. The tertiary amine (N^{Me}) of **4** increased the steric bulk of the complex compared to the secondary amine (N^{H}) of **5**-**7**, which will place restrictions on the ability of small molecules

to coordinate to the Co^{II} ion to form a six-coordinate structure. The *gem*-dimethyl groups of **4**-**5** and **7** created steric bulk that can prevent the formation of dimeric species in solution, while the *β*-hydrogen-derivative, **6**, was less effective at preventing intermolecular interactions. Five-coordinate thiolate-ligated complexes, **4**-**7**, all maintained an open site for ligand binding (***Figure 4.4***). The complex with a bulkier tertiary amine ligand was isolated in two forms—either free from coordination of additional solvent, **4a** (***Figure 4.6***), or with a MeCN solvent of crystallization, **4b**, depending on the crystallization conditions. The difference was only relevant in the solid state. In the absence of a co-crystallized solvent, the space group of **4a** (C 2/c) contained a crystallographic symmetry element making it unique amongst the structurally related Co^{II} complexes, **1**-**6**, reported herein. Consequently, the amine backbone of **4a** was disordered across two positions. The symmetry-related half of the molecule was completed by a 180° rotation about the N(2)-Co axis. The thiolate sulfur S(1') was crystallographically equivalent to S(1). In contrast, there were two symmetry independent sulfurs in complexes **4b, 5, 6,** and **7**.

ORTEP diagrams are shown for **4** (***Figure 4.6***) and **5** (***Figure 4.7***) and the associated crystal structure details in ***Table 4.2***. Metrical parameters for **4-6** are compared with previously reported **7** in ***Table 4.3***. The mean Co–S bond distances of tertiary amine-ligated **4a** (2.2814(3) Å) and **4b** (2.2854(13) Å) were within error of the corresponding distance in secondary amine-ligated **7** (2.285(2) Å).[31] The average Co–N_{apical} (N_{apical}= N(1), N(3)) distances in **4a** (2.1045(15) Å) and **4b** (2.0875(4) Å) were contracted relative to **7** (2.118(4) Å), whereas the Co–N(2) bonds of **4a** (2.1762(13) Å) and **4b** (2.226(4) Å) were longer than that of **7** (2.141(4) Å), as was expected with a sterically encumbering methyl group on N(2).

Replacement of the *gem*-dimethyl groups adjacent to the sulfurs of [$Co^{II}(S_2^{Me2}N_2N^H(Pr,Pr))$] (**7**)[24,31] with β-hydrogens in [$Co^{II}(S_2^{\beta H2}N_2N^H(Pr,Pr))$] (**6**), while maintaining a secondary amine at N(2), resulted in a very slight elongation of the Co—S_{avg} bond length from 2.285(2) Å in **7** to 2.3001(6) Å in **6**.[31] The average Co–N^{apical}(N(1),N(3)) distance was identical in **6** (2.1183(16) Å) and **7** (2.118(4) Å). The Co—N(2) bond in **6** (2.115(2) Å) was slightly contracted relative to **7** (2.141(4) Å). The shorter ligand backbone of [$Co^{II}(S_2^{Me2}N_2N^H(Et,Pr))$] (**5, *Figure 4.7***), which contained one propyl and one ethyl linker, did not appear to affect the average Co—S bond distance (2.2805(5) Å), relative to the complexes containing two propyl linkers, **4a**, **4b**, **6**, and **7** (***Table 4.3***). The average Co–N^{apical} distance of **5** (of 2.0940(15) Å) was contracted relative to previously reported **7** (Co–N^{apical} = 2.118(4) Å). The secondary amine Co–N(2) bond distance of **5** (2.119(2) Å) was within error of that of **7** (2.141(4) Å).

Even with the additional steric influence of the tertiary amine methyl group, the geometry around the Co^{II} ion of all complexes with *gem*-dimethyl, **4a**, **4b**, **5**, and **7**, remained similar: τ ~ 0.7 (***Table 4.3***), indicating that they are closer to trigonal bipyramidal (τ = 1.0) than square pyramidal geometry (τ = 0.0).[32] The equatorial angles reflected the relative availability of the open site to bind a small molecule. The key angles in the equatorial plane of tertiary amine ligated **4a** (N(2)–Co–S(2) = 115.099(8)˚ and S(1)–Co–S(2) = 129.802(16)°) were slightly larger than those of secondary amine-ligated **7** (N(2)–Co–S(2) = 112.6(1)˚ and S(1)–Co–S(2) = 126.6(1)°). The expansion reflected the steric bulk introduced by the methyl group on N(2). Key angles for ethyl-linked **5** (N(1)–Co–N(3) = 168.73(6)° and S(1)-Co-S(2) = 121.36(2)°) were smaller than propyl-linked **7** (N(1)–Co–N(3) = 170.3(1)° and S(1)-Co-S(2) 126.6(1)°), reflecting the constraints of the ethyl-linker of **5**. The τ-value for **6** (0.84) indicated that the Co^{II} ion exists in a slightly less distorted

trigonal bipyramidal geometry relative to **4** and **5**, likely due to the reduction in steric bulk caused by the replacement of the *gem*-dimethyl groups in **7** with β-hydrogen groups (***Figure 4.4***). The key angles for β-hydrogen **6** (N(1)–Co–N(3)= 172.86(6))° and S(1)—Co—S(2) 122.66(2)°) showed that the environment around the Co^{II} remains similar to that of **7**.

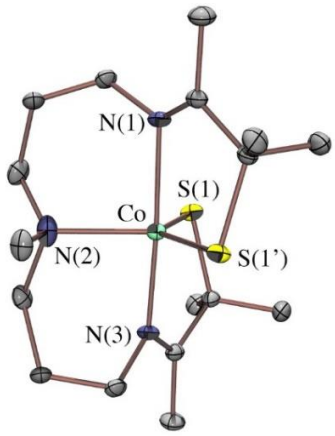

Figure 4.6 ORTEP diagram of tertiary amine-ligated [$Co^{II}(S_2{}^{Me2}N_2N^{Me}$(Pr,Pr))] (**4a**) showing 50% probability ellipsoids. Hydrogen atoms have been omitted for clarity.

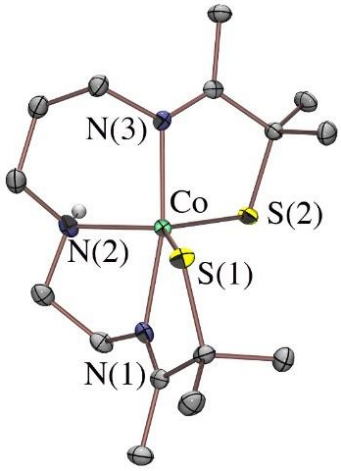

Figure 4.7 ORTEP diagram of [$Co^{II}(S_2{}^{Me2}N_2N^{H}$(Et,Pr))] (**5**) with hydrogen atoms, except for N(2)-H omitted for clarity showing 50% probability ellipsoids.

Table 4.2 Crystal data and structure refinement for [$Co^{II}(S_2^{Me2}N_2N^{Me}(Pr,Pr))$] (**4a**) and [$Co^{II}(S_2^{Me2}N_2N^{H}(Et,Pr))$] (**5**).

	4a	**5**
Empirical formula	C17 H33 Co N3 S2	C19 H37 Co N3 O S2
Formula weight	402.51	446.56
Temperature	100(2) K	100(2) K
Wavelength	0.71073 Å	0.71073 Å
Crystal system	Monoclinic	Monoclinic
Space group	C 2/c	P 21/c
Unit cell dimensions	a = 12.1928(7) Å b = 15.8279(9) Å c = 11.0690(6) Å	a = 12.2688(14) Å b = 20.042(2) Å c = 9.0039(9) Å
Volume	2013.5(2) $Å^3$	2213.2(4) $Å^3$
Z	4	4
Density (calculated)	1.328 Mg/m^3	1.340 Mg/m^3
Absorption coefficient	1.063 mm^{-1}	0.977 mm^{-1}
F(000)	860	956
Crystal size	0.270 x 0.220 x 0.180 mm^3	0.150 x 0.060 x 0.050 mm^3
Theta range for data collection	2.190 to 28.325°.	1.660 to 28.323°.
Index ranges	-16<=h<=16, -21<=k<=21, -14<=l<=14	-16<=h<=16, -26<=k<=26, -11<=l<=11
Reflections collected	4929	10671
Independent reflections	2510 [R(int) = 0.0098]	5471 [R(int) = 0.0254]
Completeness to theta = 25.000°	100.0 %	100.0 %
Absorption correction	Semi-empirical from equivalents	
Max. and min. transmission	0.746 and 0.694	
Refinement method	Full-matrix least-squares on F^2	Full-matrix least-squares on F^2
Data / restraints / parameters	2510 / 12 / 132	5471 / 0 / 245
Goodness-of-fit on F^2	1.057	1.026
Final R indices [I>2sigma(I)]	R1 = 0.0184, wR2 = 0.0468	R1 = 0.0307, wR2 = 0.0666
R indices (all data)	R1 = 0.0192, wR2 = 0.0474	R1 = 0.0501, wR2 = 0.0752
Largest diff. peak and hole	0.431 and -0.213 $e.Å^{-3}$	0.454 and -0.290 $e.Å^{-3}$

Table 4.3 Comparison of selected bond distances (Å) and angles (°) for thiolate-ligated Co^{II} complexes **4-7.**

	4a*	4b	5	6	7[31]
Co—N(1)	2.045(15)	2.094(4)	2.0940(15)	2.1152(15)	2.127(4)
Co—N(2)	2.1762(13)	2.227(4)	2.1189(15)	2.1154(17)	2.141(4)
Co—N(3)	2.164(14)	2.079(4)	2.0940(15)	2.1213(16)	2.109(4)
Co—S(1)	2.2814(3)	2.2902(12)	2.2884(5)	2.2949(5)	2.293(1)
Co—S(2)	2.2814(3)	2.2803(13)	2.2725(5)	2.3064(6)	2.278(2)
N(1)-Co-N(3)	176.9(2)	172.78(16)	168.73(6)	172.86(6)	170.3(1)
S(1)-Co-S(2)	129.80(2)	128.75(5)	121.36(2)	122.66(2)	126.6(1)
S(1)-Co-N(2)	115.099(8)	116.09(11)	125.63(4)	120.02(5)	120.2(1)
S(2)-Co-N(2)	115.099(8)	115.15(11)	112.35(5)	117.05(5)	112.6(1)
N(1)-Co-S(1)	82.9(3)	82.71(11)	82.51(4)	84.44(5)	83.0(1)
N(1)-Co-N(2)	87.7(2)	86.17(16)	80.03(6)	89.79(6)	89.7(1)
N(1)-Co-S(2)	99.1(2)	100.14(11)	100.63(4)	101.10(4)	105.6(1)
N(3)-Co-S(1	97.2(2)	99.85(11)	104.03(4)	97.22(5)	96.3(1)
N(3)-Co-N(2)	89.5(2)	86.65(16)	88.71(6)	83.37(6)	82.2(1)
N(3)-Co-S(2)	83.2(3)	83.58(11)	83.95(4)	83.90(5)	82.6(1)
τ	0.79	0.73	0.72	0.84	0.73

*Symmetry transformations used to generate equivalent atom S2 derived from S1: #1 -x+2,y,-z+3/2

4.2.3 Spin-State Characterization of Co^{II} Complexes 4-6.

The solution magnetic moment of **4** (μ_{eff} = 3.15 μ_β), determined using the Evans method[33,34] in MeCN, was consistent with a mixture of two spin-states, *S* = 3/2 (μ_{eff} = 3.87 μ_β) and *S* = 1/2 (μ_{eff} = 1.73 μ_β), with the highest population in the *S* = 3/2 state (***Table 4.4***). This was supported by the DFT calculations discussed in **Section 4.2.3** , as well as the crystallographically-determined bond lengths. The spin-orbit coupling contribution to the magnetic moment of **4** was larger in MeOH (μ_{eff} = 4.60 μ_β) relative to MeCN (μ_{eff} = 3.15 μ_β). H-bonding between the solvent and the thiolate arms of the ligand and/or some proportion of the solvent occupying the available open site could

alter the electronics of the Co^{II} to activate more spin orbit coupling in the molecule as has been shown by calculating enhanced SOC terms at minimum energy crossing points of spin surfaces for a Pd^{II} complex.[35] Complex **5** consisted of a mixture of spin states with a μ_{eff} = 2.67 μ_β found in MeCN and μ_{eff} = 1.55 μ_β in MeOH. These values were consistent with the majority of the complex being *S* = 1/2 (μ_{eff} = 1.73 μ_β), in contrast to **4**, which was predominantly *S* = 3/2. The least sterically encumbered complex, **6**, which contains β-hydrogens in place of the *gem*-dimethyl groups of **7** displayed an even higher population of low-spin *S* = 1/2 (μ_{eff} = 1.73 μ_β) in solution with μ_{eff} = 1.80 μ_β in MeCN and μ_{eff} = 2.12 μ_β in MeOH. These differences in spin-state in solution could reflect a greater propensity for solvent molecules, MeOH and MeCN, to bind to the available open site of **5** and **6**.

The proportion of each spin-state was calculated according to the method outlined in **Equations 4.1-4.4**. Assuming that the concentration of the high-spin species, denoted as *HS*, and the low-spin species, denoted as *LS* are in an equilibrium, the magnetic susceptibility of the solution should be proportional to the temperature and the μ_{eff}^2(**Eq. 4.1**). The magnetic susceptibility of the solution ($\chi_{(T)}$) can therefore be expressed as proportions (ϒ) of the high-spin and low-spin species and their individual magnetic susceptibilities (χ) as shown in **Eq. 4.2**. For two spin-states in equilibrium, the proportion of each can be found by using **Eq. 4.3** and **Eq. 4.4**. Due to spin-orbit coupling effects found in high-spin Co^{II}, which can result in μ_{eff} values larger than the spin-only values of μ_{SO}, the theoretical μ_{eff} values can lead to an overestimation of the proportion of high-spin species. However, more in depth studies of the magnetic moment must be done to explore the amount of spin-orbit coupling.

$$\chi_{(T)} = \frac{(\frac{u_{eff}}{2.84})^2}{T} \quad \text{Eq. 4.1}$$

$$\chi_{(T)} = \gamma_{HS} \times \chi_{HS} + (1 - \gamma_{HS}) \times \chi_{LS} \quad \text{Eq. 4.2}$$

$$\left(\mu_{eff}(obs)\right)^2 = \gamma_{HS} \times \mu_{eff}(HS\ theoretical)^2 + \gamma_{LS} \times \mu_{eff}(LS\ theoretical)^2 \quad \text{Eq. 4.3}$$

$$\gamma_{HS} + \gamma_{LS} = 1 \quad \text{Eq. 4.4}$$

Table 4.4 Solvent-dependent spin-state, redox properties, and electronic absorption for Co^{II} complexes **4**-**7.**

	4	**5**	**6**	**7**[31]
μ_{eff} (μ_B) (MeCN)	3.15	2.67	1.80	4.32
μ_{eff} (μ_B) (MeOH)	4.60	1.55	2.12	N/A
Majority Spin-state (MeCN)	*S* = 3/2 58%	*S* = 1/2 65%	*S* =1/2 98%	*S* = 3/2 131%
Majority Spin-state (MeOH)	*S* = 3/2 152%	*S* = 1/2 105%	*S* =1/2 87%	N/A
$E_{p,a}$ (mV vs SCE)	–444 +927	+523 +1027	-542	-405
λ_{max} (nm)	370 (MeCN) 356 (MeOH)	379 (MeCN) 365(MeOH)	358 (MeCN) 348 (MeOH)	362 (MeCN) 350 (MeOH)

4.2.4 DFT Calculations of Co^{II} Complexes 4-7

4.2.4.1 Geometry Optimizations of Co^{II} Complexes 4-7

Density function theory (DFT) calculations were completed using the PBE0 and B3LYP functionals and either a 6-31G* or def2-TZVP basis set, starting from the X-ray crystallographic coordinates for [Co^{II}($S_2^{Me2}N_2N^{Me}$(Pr,Pr))] (**4a**) for both high-spin (*S* = 3/2) and low-spin (*S* = 1/2)

states. In both cases, the minimized structures were found to possess an *S* = 3/2 ground state (***Figure 4.8***), which was consistent with the observed bond lengths, as well as the experimentally measured magnetic moments. The geometry optimizations for *S* = 3/2 showed a τ-value of 0.73 using the PBE0 functional, and 0.78 using the B3LYP functional, which was in good agreement with the X-ray determined value of τ = 0.79, and consistent with a distorted trigonal bipyramidal geometry. The open site would be less accessible in this geometry relative to a square pyramidal arrangement. The low-spin *S* = 1/2 geometry optimizations suggested that in order to undergo a spin-state change, a geometric rearrangement must also take place. Calculated τ-values of low-spin tertiary amine ligated **4** (τ= 0.49) and low-spin secondary amine ligated **7** (τ = 0.60) indicated that a movement towards a square pyramidal geometry would take place if a spin-state change (*S* = 3/2 → *S* = 1/2) were to occur. Along the same vein, the structural rearrangement and angle changes (~120˚ → ~90˚) associated with ligand binding would require an energetically uphill spin-state change. Similar patterns correlating structural rearrangement and spin-state changes were observed for β-hydrogen **6** (***Figure 4.9, Table 4.5-4.6***), while the structural constraint of the ethyl-linked **5** restricted this ligand set from following the pattern found in the propyl-linked complexes. The calculated relative energies of the *S* = 1/2 and *S* = 3/2 states offered an explanation for why **4** undergoes outer-sphere oxidation with dioxygen as opposed to an inner sphere mechanism involving O_2 binding, as the more open spin-state, that would facilitate dioxygen binding, is higher in energy. In contrast, the reaction between oxidized $[Co^{III}(S_2{}^{Me2}N_2N^{Me}(Pr,Pr))]^+$ (**4^{ox}**) and dioxygen or iodosylbenzene (PhIO), involved an inner-sphere mechanism with O_2 or PhIO binding (***Sections 4.4-4.5***).

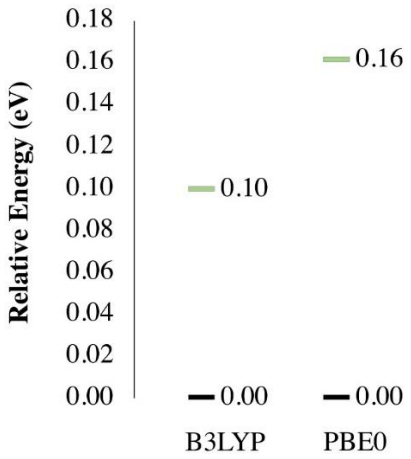

Figure 4.8 Relative energy diagram from density functional theory calculations with ORCA software package for [$Co^{II}(S_2{}^{Me2}N_2N^{Me}(Pr,Pr))$] (**4**). High-spin (*S* = 3/2) is shown in black at 0 eV and low-spin (*S* = 1/2) is shown in green.

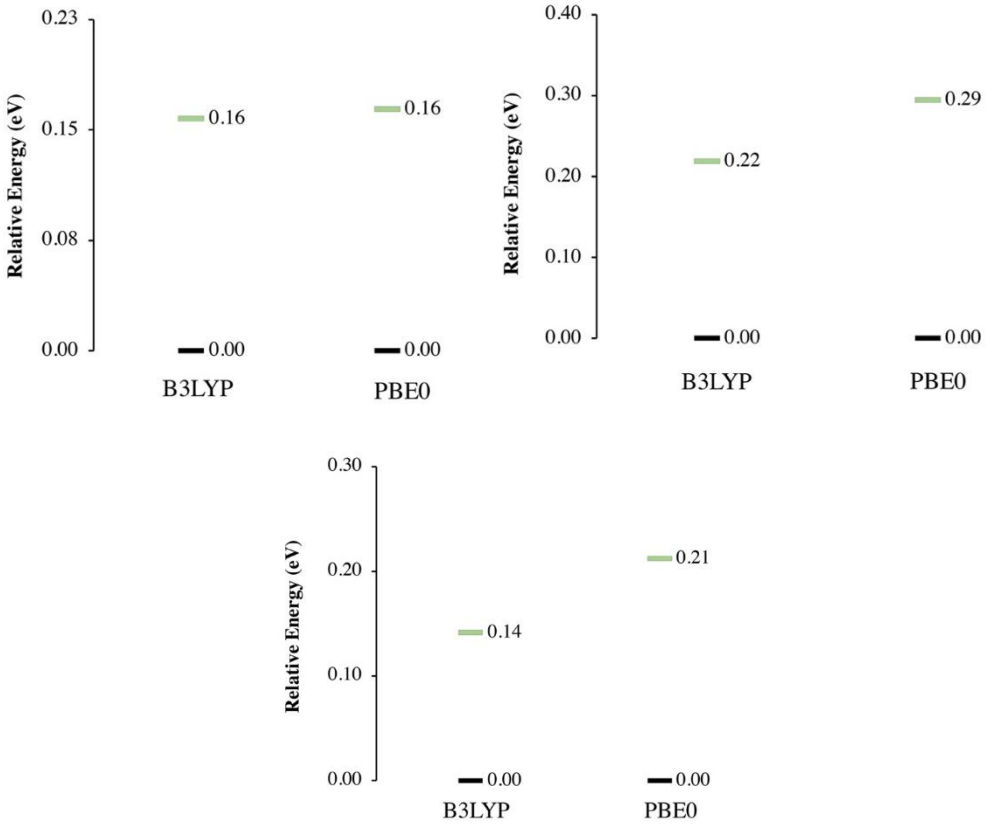

Figure 4.9 Relative energy diagrams calculated for Co^{II} complexes 5 (top left), 6 (top right), and **7** (bottom). All three compounds have a ground state of *S* = 3/2 (black) with a higher energy *S* = 1/2 state (green).

Table 4.5 Selected bond lengths (Å), percent error from crystallographically obtained distances and τ values from B3LYP DFT calculated geometry optimizations for Co^{II} Complexes **4-7.**

	4				**5**			
	S = 1/2	% error	*S* = 3/2	% error	*S* = 1/2	% error	*S* = 3/2	% error
Co-N(1)	1.916	6.3	2.080	1.7	1.896	9.5	2.089	1.4
Co-N(2)	2.197	1.0	2.178	0.1	2.110	0.4	2.236	5.7
Co-N(3)	1.916	11.5	2.074	4.2	1.903	9.2	2.110	0.9
Co-S(1)	2.252	1.3	2.304	1.0	2.323	2.2	2.271	1.0
Co-S(2)	2.328	2.0	2.315	1.5	2.265	1.0	2.266	0.4
τ	0.6	24.1	0.78	1.6	0.58	19.4	0.53	26.4
	6				**7**			
	S = 1/2	% error	*S* = 3/2	% error	*S* = 1/2	% error	*S* = 3/2	% error
Co-N(1)	1.922	9.1	2.123	0.4	1.924	9.5	2.112	0.7
Co-N(2)	2.101	0.7	2.135	0.9	2.109	1.5	2.135	0.3
Co-N(3)	1.923	9.3	2.078	2.0	1.918	9.1	2.090	0.9
Co-S(1)	2.366	2.6	2.323	0.7	2.335	1.8	2.302	0.4
Co-S(2)	2.271	1.1	2.320	1.1	2.253	1.1	2.294	0.7
τ	0.63	28.4	0.70	20.5	0.60	17.8	0.75	2.7

Table 4.6 Selected bond lengths (Å), % error from crystallographically obtained distances and τ values from PBE0 DFT calculated geometry optimizations for Co^{II} Complexes **4-7.**

	4				**5**			
	S = 1/2	% error	*S* = 3/2	% error	*S* = 1/2	% error	*S* = 3/2	% error
Co-N(1)	1.931	5.6	2.109	3.1	1.909	8.8	2.089	0.2
Co-N(2)	2.237	2.8	2.203	1.2	2.130	0.5	2.236	5.5
Co-N(3)	1.929	10.9	2.093	3.3	1.919	8.4	2.110	0.7
Co-S(1)	2.231	2.2	2.275	0.3	2.244	1.3	2.271	0.1
Co-S(2)	2.280	0.1	2.287	0.2	2.287	0.0	2.266	1.0
τ	0.49	38.0	0.73	7.6	0.72	31.9	0.53	26.4
	6				**7**			
	S = 1/2	% error	*S* = 3/2	% error	*S* = 1/2	% error	*S* = 3/2	% error
Co-N(1)	1.938	8.4	2.110	0.3	1.938	8.9	2.138	0.5
Co-N(2)	2.147	1.5	2.158	2.0	2.147	0.3	2.153	0.6
Co-N(3)	1.940	8.5	2.147	1.2	1.932	8.4	2.115	0.3
Co-S(1)	2.289	0.7	2.287	0.8	2.27	1.0	2.277	0.7
Co-S(2)	2.257	1.6	2.288	0.3	2.24	1.7	2.267	0.5
τ	0.44	50.0	0.65	26.4	0.41	43.8	0.7	4.1

4.2.4.2 TD-DFT Calculated Spectra for Co^{II} Complexes 4, 5 and 7

The time-dependent DFT (TD-DFT) calculated electronic absorption spectra (***Figures 4.10***, ***4.11***, ***4.12***) were in good agreement with the experimentally measured spectra (***Figures 4.13-4.14***). Whereas [$Co^{II}(S_2{}^{Me2}N_2N^{Me}(Pr,Pr))$] (**4**) and [$Co^{II}(S_2{}^{Me2}N_2N^{H}(Pr,Pr))$] (**7**) displayed a single band in both the experimental and calculated spectra, [$Co^{II}(S_2{}^{Me2}N_2N^{H}(Et,Pr))$] (**5**) displayed additional, less intense bands at lower energies. These differences were explained by the population of thermally accessible spin-states in solution with the latter. As shown in the calculated spectra of ***Figures 4.10***, ***4.11***, ***4.12***, the intensity of transitions associated with a low-spin configuration was 22-57% of the high-spin configuration.

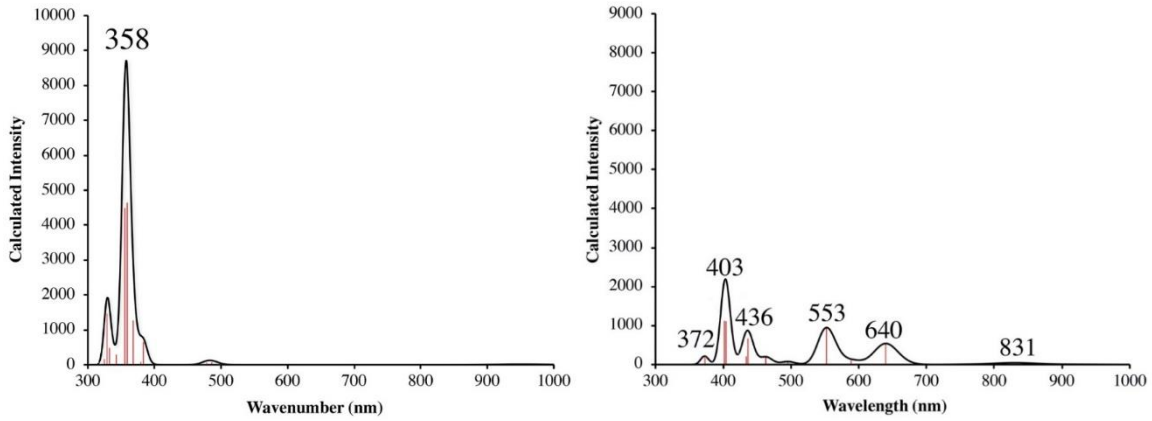

Figure 4.10 TD-DFT calculated spectra for *S* = 3/2 (left) and *S* = 1/2 (right) [$Co^{II}(S_2{}^{Me2}N_2N^{Me}(Pr,Pr))$] (**4**) with PBE0 functional.

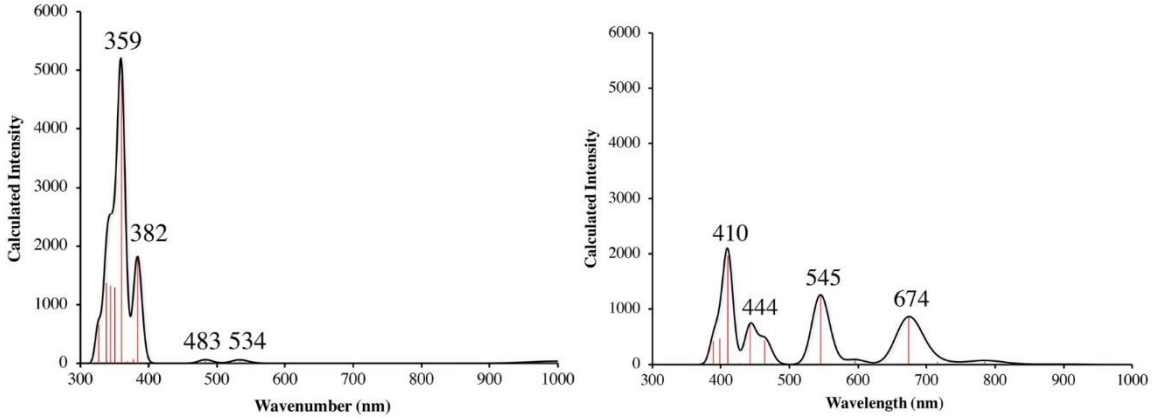

Figure 4.11 TD-DFT calculated spectra with PBE0 functional for [$Co^{II}(S_2{}^{Me2}N_2N^H(Et,Pr))$] (**5**) (S = 3/2) (left) and **5** (S = 1/2) (right).

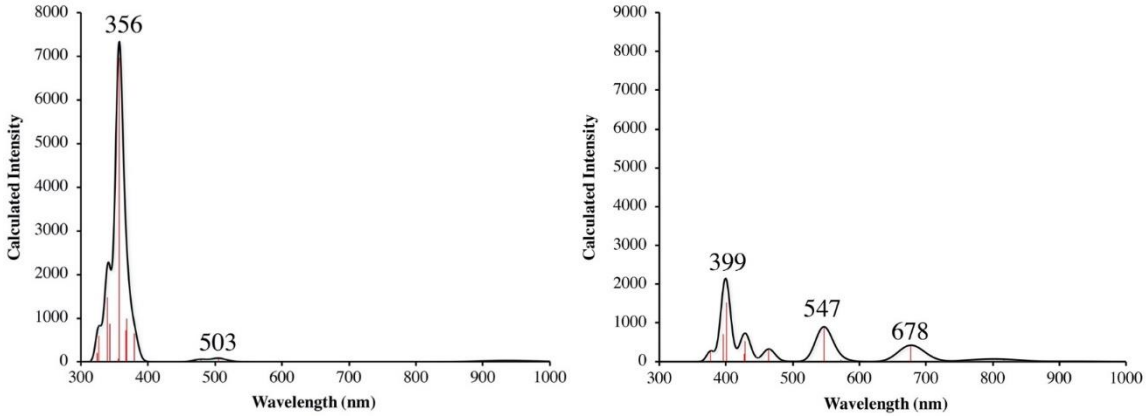

Figure 4.12 TD-DFT calculated spectra with the PBE0 functional for [$Co^{II}(S_2{}^{Me2}N_2N^H(Pr,Pr))$] (**7**) (S = 3/2) (left) and **7** (S = 1/2) (right).

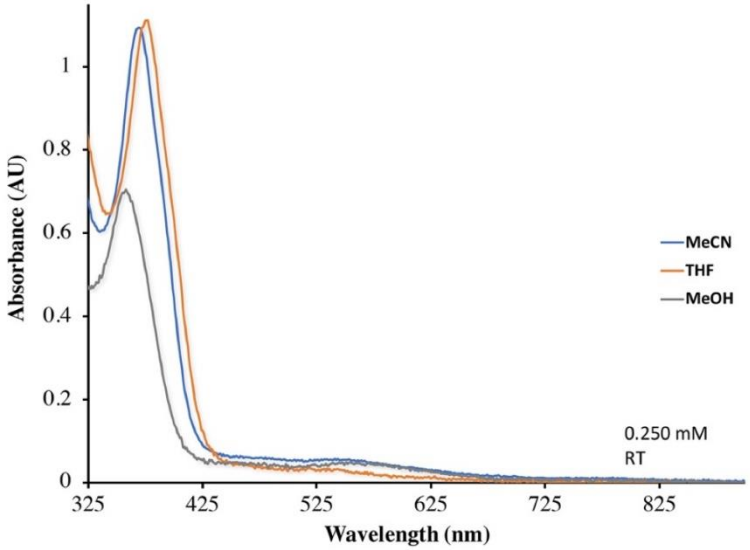

Figure 4.13 Electronic absorption spectra of 0.250 mM solutions of [$Co^{II}(S_2{}^{Me2}N_2N^{Me}(Pr,Pr))$] (**4**) in MeCN (**blue**), THF (**orange**), and MeOH (**grey**) at room temperature.

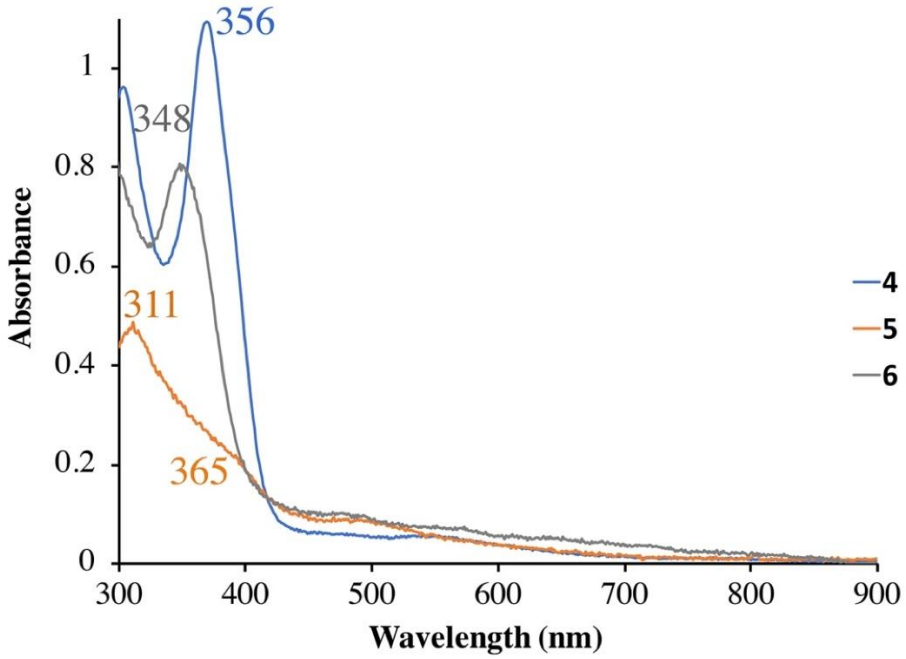

Figure 4.14 Electronic absorption spectra of Co^{II} complexes **4** (blue), **5** (orange), and **6** (grey) in MeOH, (0.250 mM **4,** 0.500 mM **5**, and 0.500 mM **6**)**.**

4.2.4.3 Natural Transition Orbital Analysis for Co^{II} Complexes 4-7.

Natural transition orbital (NTO) analysis revealed the main character of the band at λ_{max} = 358 nm for **4** to be from the promotion of an electron from an orbital with π(Co(d)+S(p)) character to π(Co(d) +N(p)) character (***Figure 4.15***) at 91.3% and 63.8% contributions for the two main contributing states of the 358 nm band. The orbitals of the thiolate ligands illustrated the delocalization of electrons onto the thiolate arms of the ligand framework due to the nephelauxetic effect. The slightly shifted, less intense band in MeOH likely reflects hydrogen bonding interaction between the thiolate sulfurs and the protic solvent (***Figure 4.13***).[36,37] The other TD-DFT calculated spectra for complexes **4-7** for both high spin and low spin states identified similar key transitions across the series of Co^{II} complexes (***Figure 4.16, 4.17***, ***4.18***). In

the low spin case, the major contribution to the bands includes a similar donating orbital, π(Co(d)+S(p)), being promoted to a non-bonding-(Co(d)+ π*(C(p)/N(p))) (***Figure 4.16-4.17***).

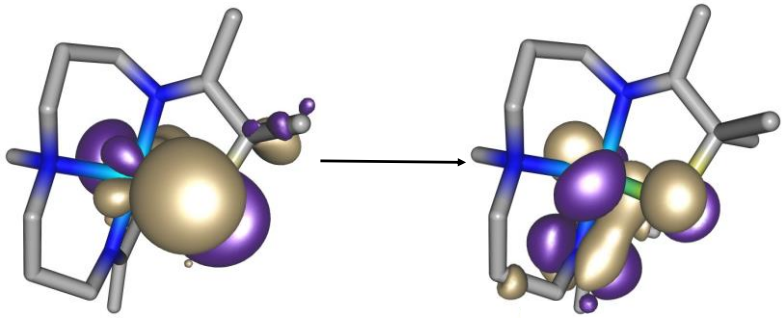

Figure 4.15 Major transition identified from NTO analysis of the TD-DFT spectrum of **4** of π(Co(d)+S(p)) → π(Co(d) +N(p)).

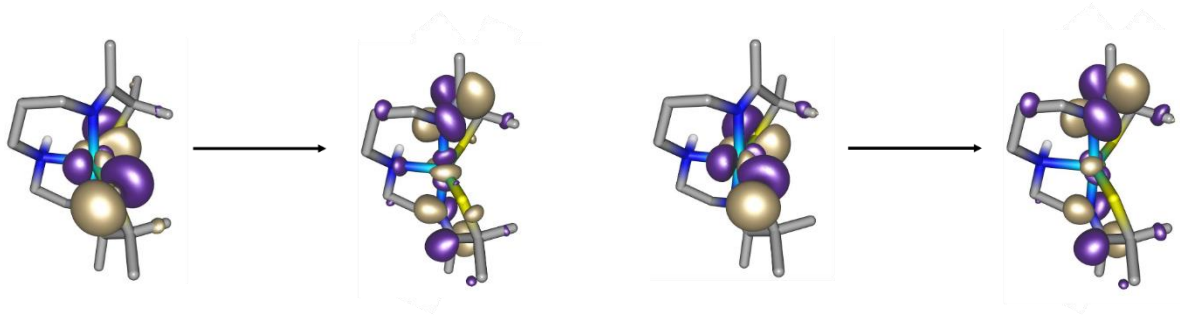

Figure 4.16 Major transitions identified from NTO analysis of the TD-DFT spectrum of **5** for *S* = 1/2 (α-left; β-right)**.**

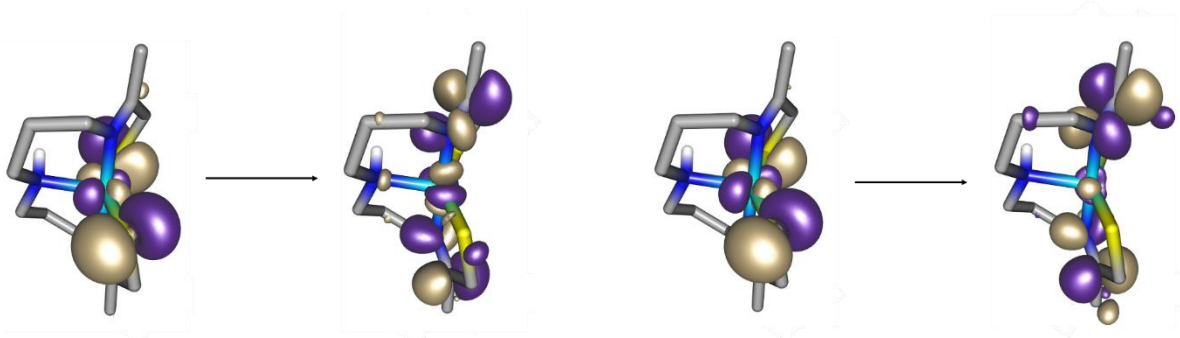

Figure 4.17 Major transition identified from NTO analysis of the TD-DFT spectrum of **6** for *S* = 1/2 (α-left; β-right)**.**

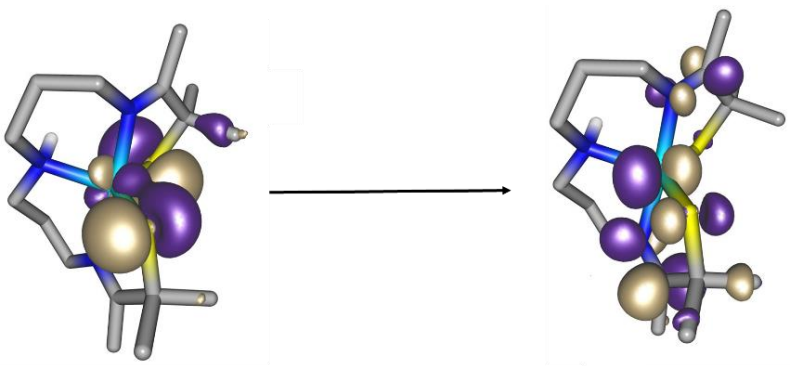

Figure 4.18 Major transition (54.3%) identified from NTO analysis of the TD-DFT spectrum of **7.**

4.2.6 Correlations with Metrical Parameters and λ_{max} for the Co^{II} Series

A correlation between the electronic absorption band energy, λ_{max}, and the mean Co-N^{apical} distance was observed, whereby the transition energy increases as the mean distance was increased (***Figure 4.19***), regardless of solvent (***Figure 4.20***). The correlation provided additional support that changes to the ligand scaffold are reflected in the N^{apical} distances of these complexes. The electronic absorption band energy, λ_{max}, also correlated with the Co—$N(2)^{amine}$ distance but shifted in the opposite direction– as the Co—$N(2)^{amine}$ distance increased, the energy of λ_{max} decreased. In this case, the trend only held for complexes containing a propyl-linked ligand scaffold (**4**, **6**, and **7**) (***Figures 4.21-4.22***), indicating the ethyl-linker perturbs the equatorial plane.

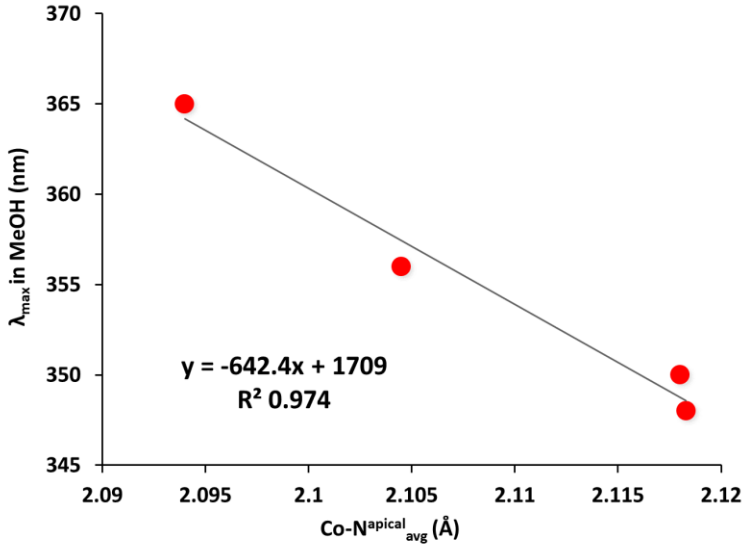

Figure 4.19 Correlation between λ_{max} in MeOH and Co-N^{apical} distance for the Co^{II} complexes **4**-**7**.

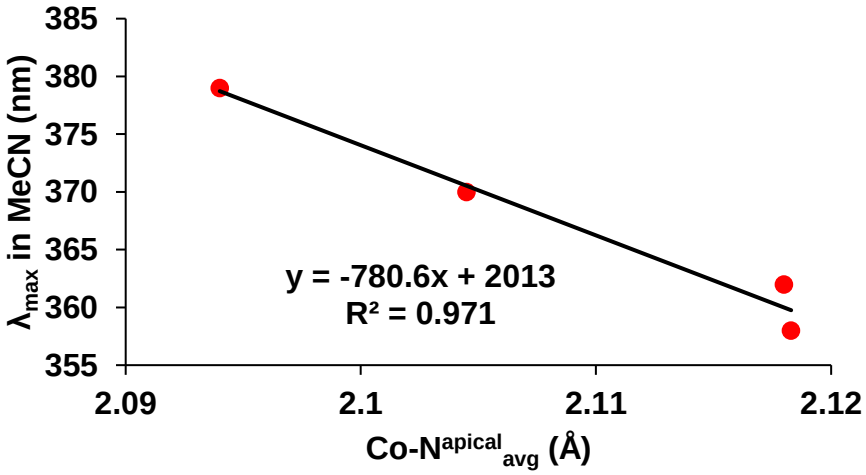

Figure 4.20 Correlation between λ_{max} in MeCN vs. Co-N^{apical}_{avg} distance for the Co^{II} complexes **4**-**7.**

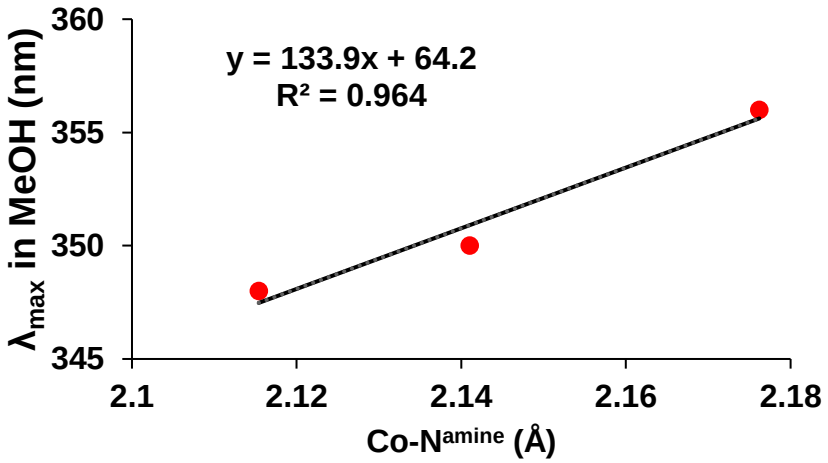

Figure 4.21 Correlation between λ_{max} in MeOH vs. Co-N^{amine} distance for the Pr,Pr ligand scaffold series of Co^{II} complexes **4**, **6** and **7**.

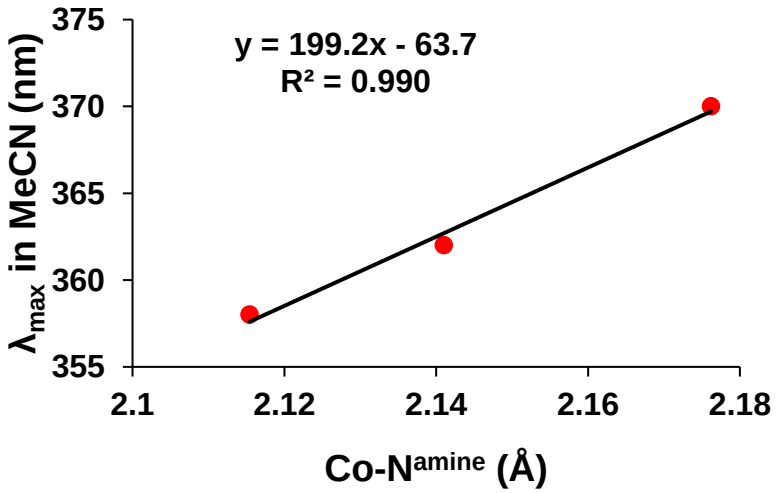

Figure 4.22 Correlation between λ_{max} in MeCN vs. Co-N^{amine} distance for the Pr,Pr ligand scaffold series of Co^{II} complexes **4**, **6** and **7**.

4.3 Oxidation-Reduction Behavior.

4.3.1 Cyclic Voltammetry Characterizations

Cyclic voltammetry (CV) experiments were carried out in both MeCN and MeOH, and were referenced to the $Cp_2Fe^{+/0}$ couple. In MeOH, the potential of **4** was -733 mV vs $Cp_2Fe^{+/0}$ (***Figure 4.23***), while the potential measured in MeCN was -858 mV vs $Cp_2Fe^{+/0}$ (***Figure 4.24***), a full 125 mV less negative reduction potential in protic solvent. Depending on the solvent, the presence of hydrogen bonding in the protic MeOH could lower the energy of the thiolate orbitals causing the complex to demonstrate higher stability of the reduced Co^{II} state of **4**.

The reduction potential of $Co^{II}(PrPr)N^{H}$ (**1**) was obtained in MeCN previously and can be compared with the other potentials reported vs SCE (***Table 4.4***). The tertiary vs secondary amine did not greatly affect the reduction potentials of the $Co^{II/III}$ couple of complexes **1** (-405 mV vs SCE) and **4** (-444 mV vs SCE). The oxidized $\mathbf{4^{ox}}$ also showed a quasi-reversible wave most consistent with a $Co^{III/IV}$ couple, which was not seen in the case of the less restrained ligand system of **7** (only one wave). The assignment of the $Co^{II/III}$ and $Co^{III/IV}$ couples was supported by no observed change in EAS with the addition of a reductant, cobaltocene, to **4** (***Figure 4.25***). Upon addition of strong oxidant, cerium ammonium nitrate (CAN), to $\mathbf{4^{ox}}$ an abrupt change in EAS was observed (***Figure 4.26***). An exploration of the formation of the Co^{IV} species will be explored in the group with future experiments. The CV of ethyl-linked **5** (***Figure 4.27***) shows two irreversible reduction events, which may indicate the presence of a solvent bound species.

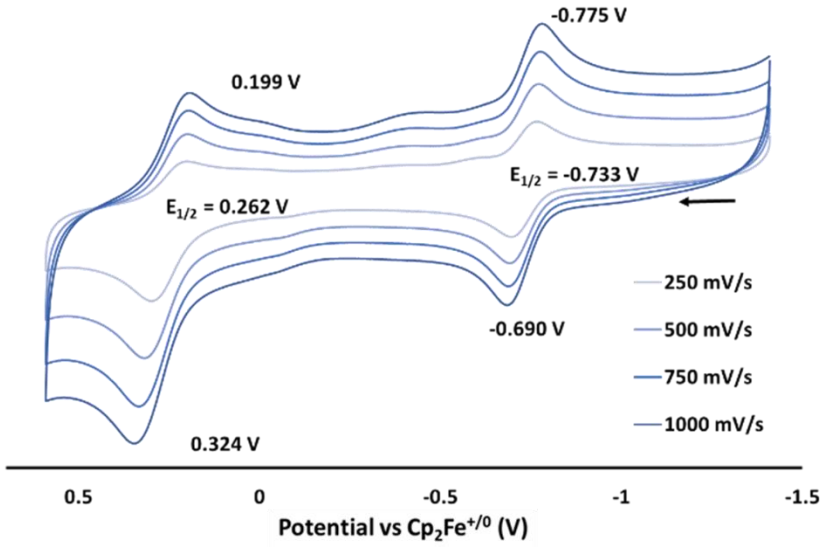

Figure 4.23 Cyclic voltammogram of **4** in MeOH vs $Cp_2Fe^{+/0}$.

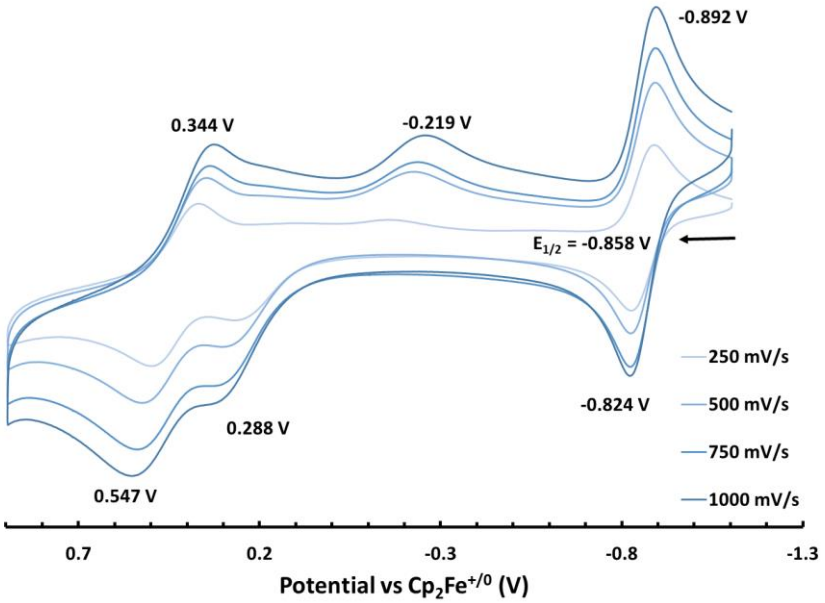

Figure 4.24 Cyclic voltammogram of **4** in MeCN vs $Cp_2Fe^{+/0}$.

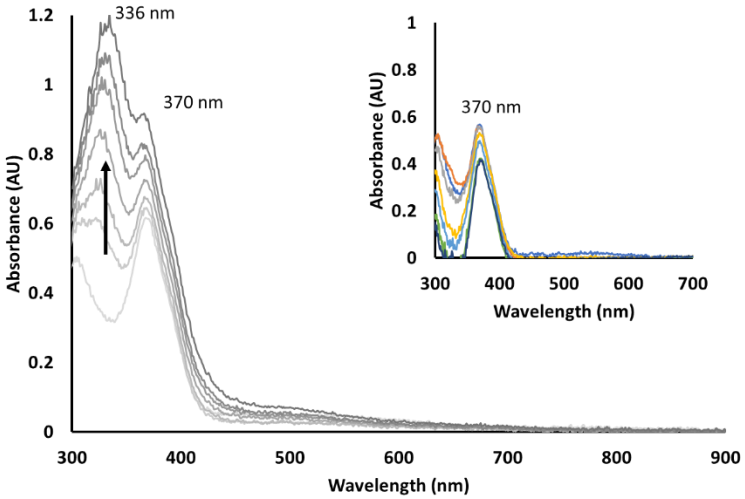

Figure 4.25 EAS monitoring no change to the spectrum of 4 from the addition of 1.5 equiv. cobaltocene in 25 µL aliquots to a 0.225 mM solution of 4 in MeCN at room temperature. (Insert shows the difference spectrum with cobaltocene spectrum removed).

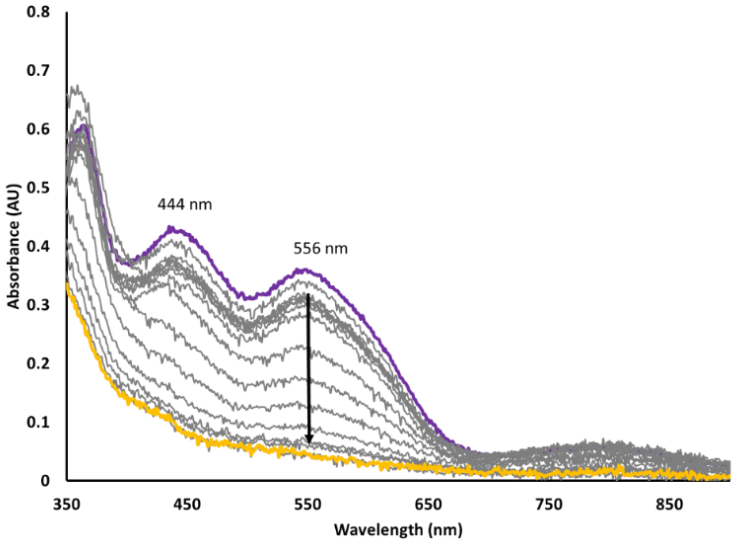

Figure 4.26 EAS monitoring of the addition of 1 equiv. CAN (H_2O) to a 0.250 mM solution of **4^{ox}** in MeOH at 0°C over 1 hour.

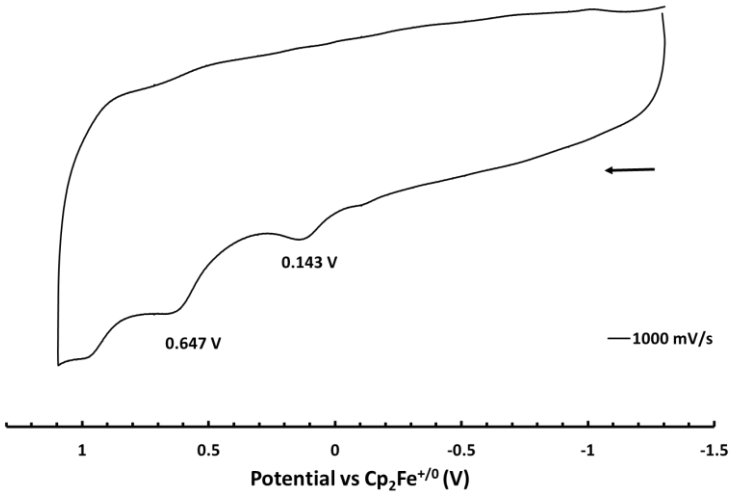

Figure 4.27 Cyclic voltammogram for [$Co^{II}(S_2{}^{Me2}N_2N^H(Et,Pr))$] **5** in MeCN referenced to $Cp_2Fe^{+/0}$**.**

4.3.2 Outer-Sphere Oxidation of 4 to 4a^{ox}

The oxidation of **4** via the addition of ferrocenium hexafluorophosphate to form [$Co^{III}(S_2{}^{Me2}N_2N^{Me}(Pr,Pr))]^+$ (**4^{ox}**) was monitored using electronic absorption spectroscopy (EAS) at 25 ˚C (***Figure 4.28***). The solution darkens in color from colorless to deep maroon, and bands grew in at 444 nm, 556 nm, and 790 nm. The presence of a small excess of the oxidant did not cause a further increase or decrease in the absorption of **4^{ox}**. The $\boldsymbol{\lambda}_{max}$ of the bands were identical in MeOH, THF and MeCN with small shifts in intensity depending on the solvent (***Figure 4.29***).

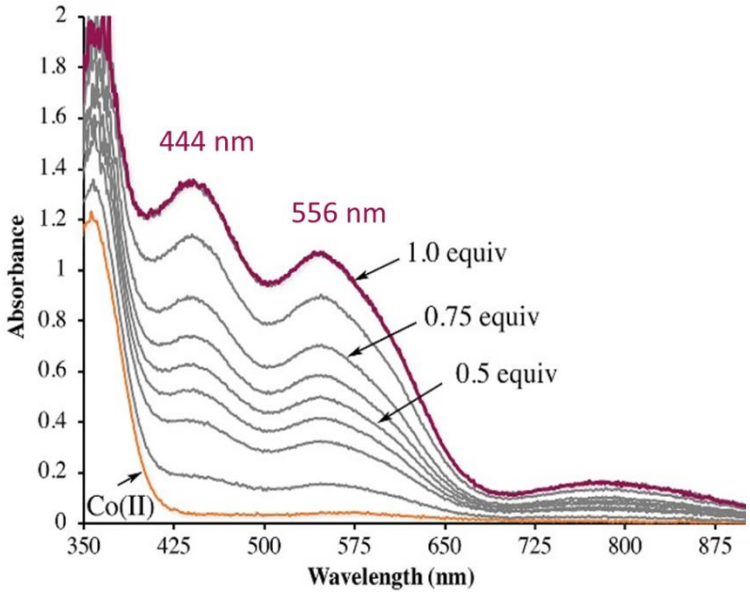

Figure 4.28 Monitoring the oxidation of $Co^{II}(S_2{}^{Me2}N_2N^{Me}(Pr,Pr))$ (**4**) via the addition of 1.25 equiv. of $Cp_2Fe(PF_6)$ in 0.125 equiv. aliquots in MeOH at 25 ˚C to afford $[Co^{III}(S_2{}^{Me2}N_2N^{Me}(Pr,Pr))](PF_6)$ (**4^{ox}**).

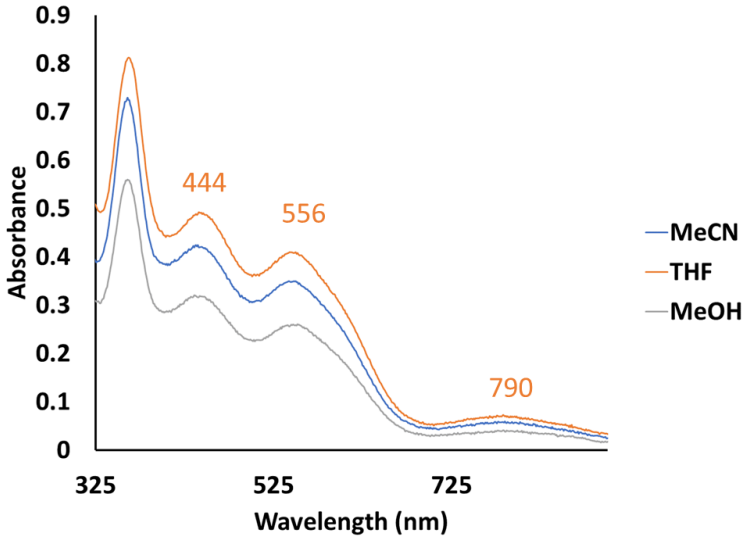

Figure 4.29 Electronic absorption spectra of 0.125 mM solutions $[Co^{III}(S_2{}^{Me2}N_2N^{Me}(Pr,Pr))]^+$ (**4^{ox}**) in MeCN (blue), THF (orange), and MeOH (grey) at room temperature.

4.3.3 Characterization of 4^{ox}

The synthesis of oxidized $[Co^{III}(S_2{}^{Me2}N^{Me}N_2(Pr,Pr))](PF_6)$ (**4^{ox}**) was carried out on a larger scale using previously reported methods.[38,39] The electronic absorption spectrum of the isolated complex showed absorption bands at λ_{max} = 356 (4210), 444 (2280), 556 (1840), and 790 (282) nm in MeOH. As shown in the ORTEP diagram of ***Figure 4.30*** and ***Table 4.7***, and the metrical parameters of ***Table 4.8***, **4^{ox}** contained Co^{III} in a five-coordinate distorted trigonal bipyramidal geometry (τ = 0.83) with compressed bond lengths relative to reduced **4**. The compressed bonds in **4^{ox}** were consistent with the metal ion having a higher Lewis acidity. The mean Co^{III}—N^{im}(1,3) distance in **4^{ox}** was 0.18 Å shorter than the corresponding distance in **4** (***Table 4.8***). The Co^{III}—N(2) distance was 0.085 Å shorter in **4^{ox}** relative to reduced **4**, and the mean Co^{III}—S distance in **4^{ox}** was 0.11 Å shorter than the corresponding distance in **4** (***Table 4.8***). These distances are virtually identical in tertiary amine-ligated **4^{ox}** versus secondary amine-ligated **1**, with the exception of the Co—S(2) distance. The latter was 0.052 Å longer in tertiary amine ligated **4^{ox}**, likely reflecting the added steric bulk of the methyl group, which points towards S(2). The Co—S(2) distance in **4^{ox}** was 0.79 Å longer than the Co—S(1) distance, reflecting the fact that the methyl group points towards S(2), and not S(1). The τ-values (0.83(**4^{ox}**) and 0.87(**1**)), and bond angles were virtually identical in oxidized **1** and **4^{ox}**, indicating that the methyl group does not distort the angles in the equatorial plane. The bond distances of **4^{ox}** are consistent with an intermediate spin-state, S = 1.[24] The solution magnetic moment of **4^{ox}** (μ_{eff} = 2.85 μ_β) in MeCN determined using the Evans method[33,34] was indicative of an S = 1 spin-state (spin-only μ_{eff} = 2.83 μ_β S = 1). In MeOH, the magnetic moment (μ_{eff} = 2.23 μ_β) was consistent with a mixture of S = 0 (μ_{eff} = 0.0 μ_β) and S = 1 (μ_{eff} = 2.83 μ_β) spin-states, with a larger proportion in the S = 1 state (62%).

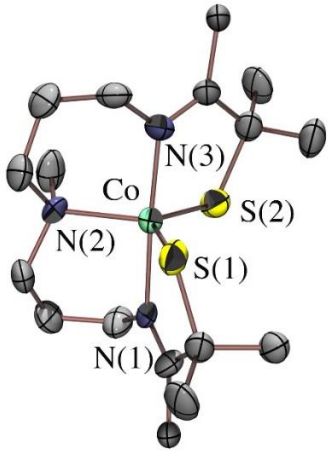

Figure 4.30 ORTEP diagram of the cation of oxidized $[Co^{III}(S_2{}^{Me2}N_2N^{Me}(Pr,Pr))](PF_6)$ (**4^{ox}**) showing 50% probability ellipsoids. Hydrogen atoms and the counterion have been omitted for clarity.

Table 4.7 Crystal data and structure refinement for $[Co^{III}(S_2{}^{Me2}N_2N^{Me}(Pr,Pr))]^+$ (**4^{ox}**).

Empirical formula	C17 H33 Co F6 N3 P S2	
Formula weight	547.48	
Temperature	100(2) K	
Wavelength	0.71073 Å	
Crystal system	Monoclinic	
Space group	P 2/c	
Unit cell dimensions	a = 11.361(3) Å	α= 90°.
	b = 9.002(2) Å	β= 111.787(10)°.
	c = 12.500(3) Å	ϒ = 90°.
Volume	1187.1(5) $Å^3$	
Z	2	
Density (calculated)	1.532 Mg/m^3	
Absorption coefficient	1.022 mm^{-1}	
F(000)	568	
Crystal size	0.050 x 0.030 x 0.020 mm^3	
Theta range for data collection	1.930 to 26.021°.	
Index ranges	-14<=h<=13, -11<=k<=11, -15<=l<=15	
Reflections collected	4508	
Independent reflections	2333 [R(int) = 0.1791]	
Completeness to theta = 25.242°	99.8 %	
Refinement method	Full-matrix least-squares on F^2	
Data / restraints / parameters	2333 / 244 / 289	
Goodness-of-fit on F^2	0.965	
Final R indices [I>2sigma(I)]	R1 = 0.0679, wR2 = 0.1098	
R indices (all data)	R1 = 0.2065, wR2 = 0.1473	
Largest diff. peak and hole	0.405 and -0.536 e.$Å^{-3}$	

Table 4.8 Comparison of selected bond distances (Å) and angles (°) for five-coordinate Co^{III} complexes **4^{ox}**, and previously reported **1** and **2.**[24]

	4^{ox}	**1**	**2**
Co–N(1)	1.895(17)	1.923(4)	1.938(3)
Co–N(2)	2.091(9)	2.060(5)	2.026(3)
Co–N(3)	1.949(15)	1.923(4)	1.913(3)
Co–S(1)	2.131(9)	2.162(22)	2.121(1)
Co–S(2)	2.210(9)	2.158(2)	2.116(1)
N(1)–Co–N(3)	175.8(7)	179.2(2)	174.82 (15)
S(1)–Co–S(2)	125.75(18)	126.80(7)	110.89 (5)
S(1)–Co–N(2)	120.1(6)	117.3(1)	145.68(11)
S(2)–Co–N(2)	114.1(6)	115.8(1)	102.82(11)
N(1)–Co–S(1)	88.0(5)	86.99(14)	87.45 (11)
N(1)–Co–N(2)	93.1(6)	92.6(2)	95.73(13)
N(1)–Co–S(2)	92.2(8)	92.77(14)	95.49 (11)
N(3)–Co–S(1)	91.6(7)	92.25(14)	88.40(1)
N(3)–Co–N(2)	90.8(5)	88.0(2)	89.44 (13)
N(3)–Co–S(2)	84.6(5)	87.38(14)	83.12 (11)
τ	0.83	0.87	0.49

4.3.4 DFT Optimized Geometries for Five-Coordinate Co^{III} Species

4.3.4.1 DFT Optimized Geometries and TDDFT Spectra for *S* = 0, 1, and 2 of 4^{ox} and 1

As shown in ***Figure 4.31***, the calculated relative energies for *S* = 0, 1, 2 spin-states indicated that the intermediate-spin *S* = 1 state was the ground state for **4^{ox}**, which explained the similarities in bond lengths between this and **1** and was consistent with the magnetic moments in MeCN and MeOH. Similar to the case of the Co^{II} complexes, the calculations demonstrated a pattern wherein the Co^{III} complexes were more responsive to changes in their angles than in the Co—N_{axial} and Co—S_{avg} bond lengths. The calculated τ-value (0.40) for the low-spin *S* = 0 system indicated that the geometry was closer to square pyramidal with a more open coordination site,

whereas the calculated geometry (τ = 0.9) associated with an *S* = 1 system was closer to a trigonal pyramidal geometry with a less accessible open coordination site. DFT calculations were also performed on **1** to provide a comparison (***Figure 4.32*** and ***Tables 4.9-4.10*****)**. The same pattern was observed for both the tertiary (**4^{ox}**) and secondary amine-containing ligand systems (**1**) with Co^{III} metal ions, suggesting that the observed differences in reactivity may be attributed to the flexibility in the equatorial plane of the complexes as the first intermediate formed from the reaction with O_2 involves a large geometry rearrangement and a spin state change to *S* = 0.[24]

The mixture of spin states in solution was also supported by the calculated TD-DFT spectra (***Figures 4.33-4.34*****).** In the case of **4^{ox}**, the spectrum was best recreated as a compilation of the calculated spectra for the *S* = 0 and *S* = 1 spin states (***Figure 4.33***). The compilation of *S* = 0 and *S* = 1 calculated spectra for **1**, also recreated the various bands reported in the 200-600 nm range (***Figure 4.34***).[24]

The major contribution to the visible bands of the calculated spectra for **4^{ox}** were best described as β-π(Co(d)+S(p)) → β-π*(Co(d)+S(p)) and α-π*(Co(d)+S(p)) → α-σ*(Co(d_{z2})+S(p)) for the *S* = 1 case, where both α- and β-electrons were available (***Figure 4.35***, top). Both of the NTOs demonstrate a large participation of the thiolate p orbitals in the transition. The *S* = 0 case for **4^{ox}**, showed a NTO with character described as α-π*(Co(d)+S(p)) → α-σ*(Co(d)+S(p)) as the majority transition for the bands observed (***Figure 4.35***, bottom). The orbital was similar to the β orbital observed for the *S* = 1 case, however the geometric arrangement of the thiolate arms had changed so that one is in a σ*-arrangement and the other in a π*-arrangement with the Co(d) orbital, instead of both thiolates having the same interaction. The presence of the σ* interaction helped to explain why the *S* = 0 state was not the ground state for these Co^{III} systems as the

antibonding interaction would be destabilizing. The NTO analysis of **1** revealed similar donor and acceptor orbitals responsible for the transitions (***Figure 4.36***), highlighting the electronic similarities between the N^{H} and N^{Me} systems.

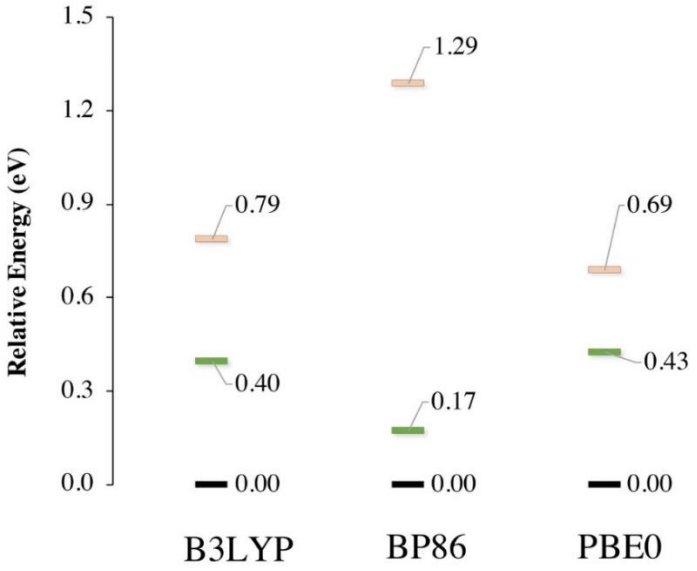

Figure 4.31 Relative energy diagram calculated for **4^{ox}** with B3LYP, BP86, and PBE0 *S* = 1 ground state (black), *S* = 0 (green), and *S* = 2 (peach).

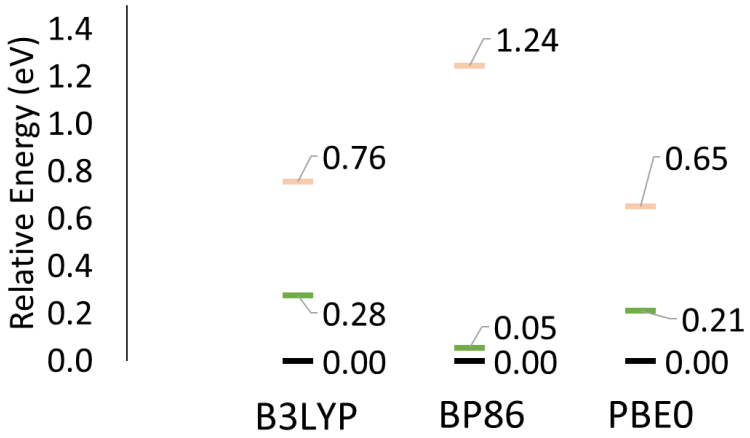

Figure 4.32 Relative energy diagram for **1** with B3LYP, BP86, and PBE0 *S* = 1 ground state (black), *S* = 0 (green), and *S* = 2 (peach).

Table 4.9 Selected bond lengths (Å), percent error from crystallographically obtained metrical parameters and τ values from DFT calculated geometry optimizations for **4^{ox}**.

B3LYP						
	S = 0	% error	*S* = 1	% error	*S* = 2	% error
Co—N(1)	1.933	2.01	1.926	1.64	2.065	8.97
Co—N(2)	2.026	3.11	2.12	1.39	2.124	1.58
Co—N(3)	1.922	1.39	1.918	1.59	2.077	6.57
Co—S(1)	2.132	0.05	2.179	2.25	2.216	3.99
Co—S(2)	2.205	0.23	2.182	1.27	2.241	1.40
τ	0.58	30.12	0.87	4.82	0.96	15.66
BP86						
	S = 0	% error	*S* = 1	% error	*S* = 2	% error
Co—N(1)	1.926	1.64	1.923	1.48	2.076	9.55
Co—N(2)	2.07	1.00	2.15	2.82	2.164	3.49
Co—N(3)	1.922	1.39	1.916	1.69	2.087	7.08
Co—S(1)	2.100	1.45	2.152	0.99	2.198	3.14
Co—S(2)	2.184	1.18	2.154	2.53	2.199	0.50
τ	0.51	38.55	0.86	3.61	0.97	16.87
PBE0						
	S = 0	% error	*S* = 1	% error	*S* = 2	% error
Co—N(1)	1.931	1.90	1.925	1.58	2.072	9.34
Co—N(2)	2.06	1.48	2.152	2.92	2.147	2.68
Co—N(3)	1.919	1.54	1.919	1.54	2.083	6.88
Co—S(1)	2.104	1.27	2.153	1.03	2.199	3.19
Co—S(2)	2.166	1.99	2.158	2.35	2.220	0.45
τ	0.48	42.17	0.81	2.41	0.98	18.07

Table 4.10 Selected bond lengths (Å), percent error from crystallographically obtained metrical parameters and τ values from DFT calculated geometry optimizations for **1**.

B3LYP						
	S = 0	% error	*S* = 1	% error	*S* = 2	% error
Co—N(1)	1.938	0.78	1.924	0.05	2.102	1.938
Co—N(2)	1.99	3.40	2.072	0.58	2.093	1.99
Co—N(3)	1.925	0.10	1.928	0.26	2.075	1.925
Co—S(1)	2.131	1.43	2.177	0.69	2.227	2.131
Co—S(2)	2.199	1.90	2.181	1.07	2.214	2.199
τ	0.46	47.13	0.88	0.80	0.85	0.46
BP86						
	S = 0	% error	*S* = 1	% error	*S* = 2	% error
Co—N(1)	1.922	0.05	1.921	0.10	2.105	9.46
Co—N(2)	2.036	1.17	2.094	1.65	2.13	3.40
Co—N(3)	1.932	0.47	1.925	0.10	2.079	8.11
Co—S(1)	2.182	0.93	2.153	0.42	2.189	1.25
Co—S(2)	2.102	2.59	2.154	0.19	2.194	1.67
τ	0.36	58.62	0.89	2.30	0.84	3.45
PBE0						
	S = 0	% error	*S* = 1	% error	*S* = 2	% error
Co—N(1)	1.919	0.21	1.924	0.05	2.100	9.20
Co—N(2)	2.053	0.34	2.094	1.65	2.110	2.43
Co—N(3)	1.936	0.68	1.93	0.36	2.087	8.53
Co—S(1)	2.176	0.65	2.152	0.46	2.211	2.27
Co—S(2)	2.118	1.85	2.153	0.23	2.196	1.76
τ	0.50	42.53	0.83	4.60	0.84	3.45

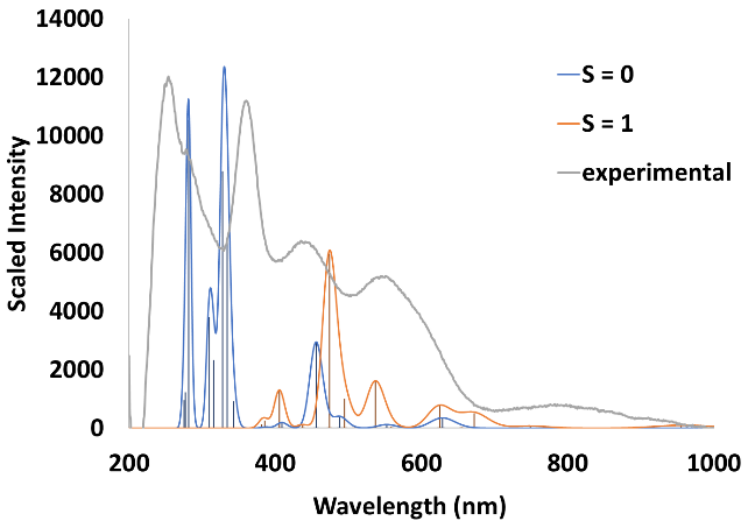

Figure 4.33 EAS and calculated TD-DFT PBE0 spectra for **4^{ox},** the three key features of the spectrum are in agreement with the present of a mix of spin-states (*S* = 0 blue and *S* = 1 orange) in solution to create the key features.

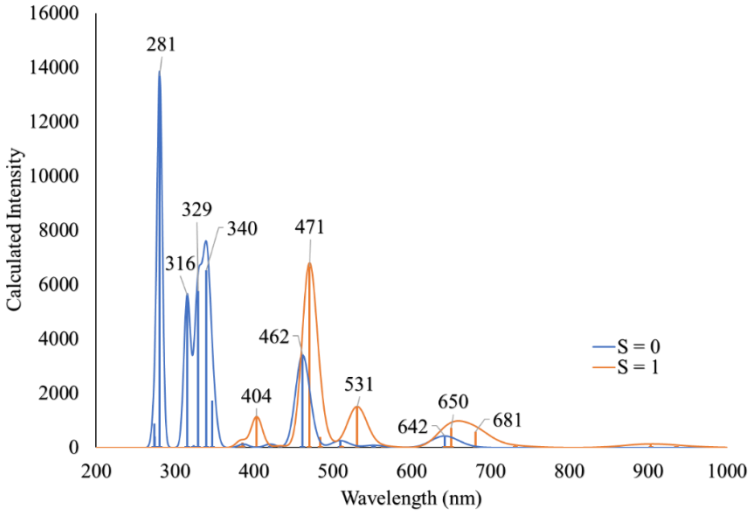

Figure 4.34 Calculated TD-DFT PBE0 spectra for **1,** the three key features of the spectrum are in agreement with the present of a mix of spin-states (*S* = 0 blue and *S* = 1 orange) in solution to create the key features (λ_{max} (ε_M) = 239 (7600), 317(3600), 358 (5200), 445 (2200), 522 (2100) and 797 (50) nm in MeCN).[24]

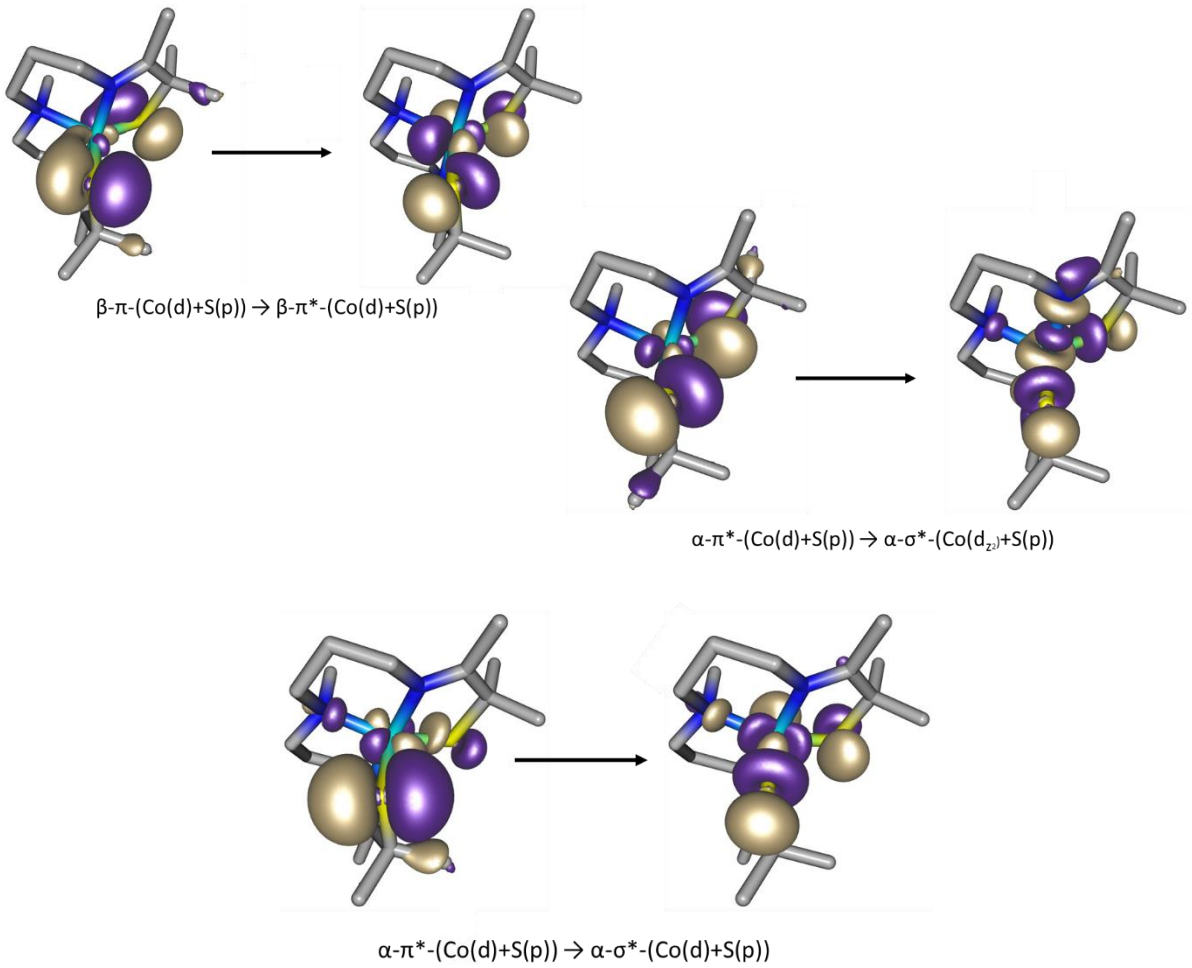

Figure 4.35 Major contributions of the NTOs for *S* = 1 (top, includes β and α) and *S* = 0 (bottom) for the major bands of the TD-DFT calculated spectra of **4^{ox}**.

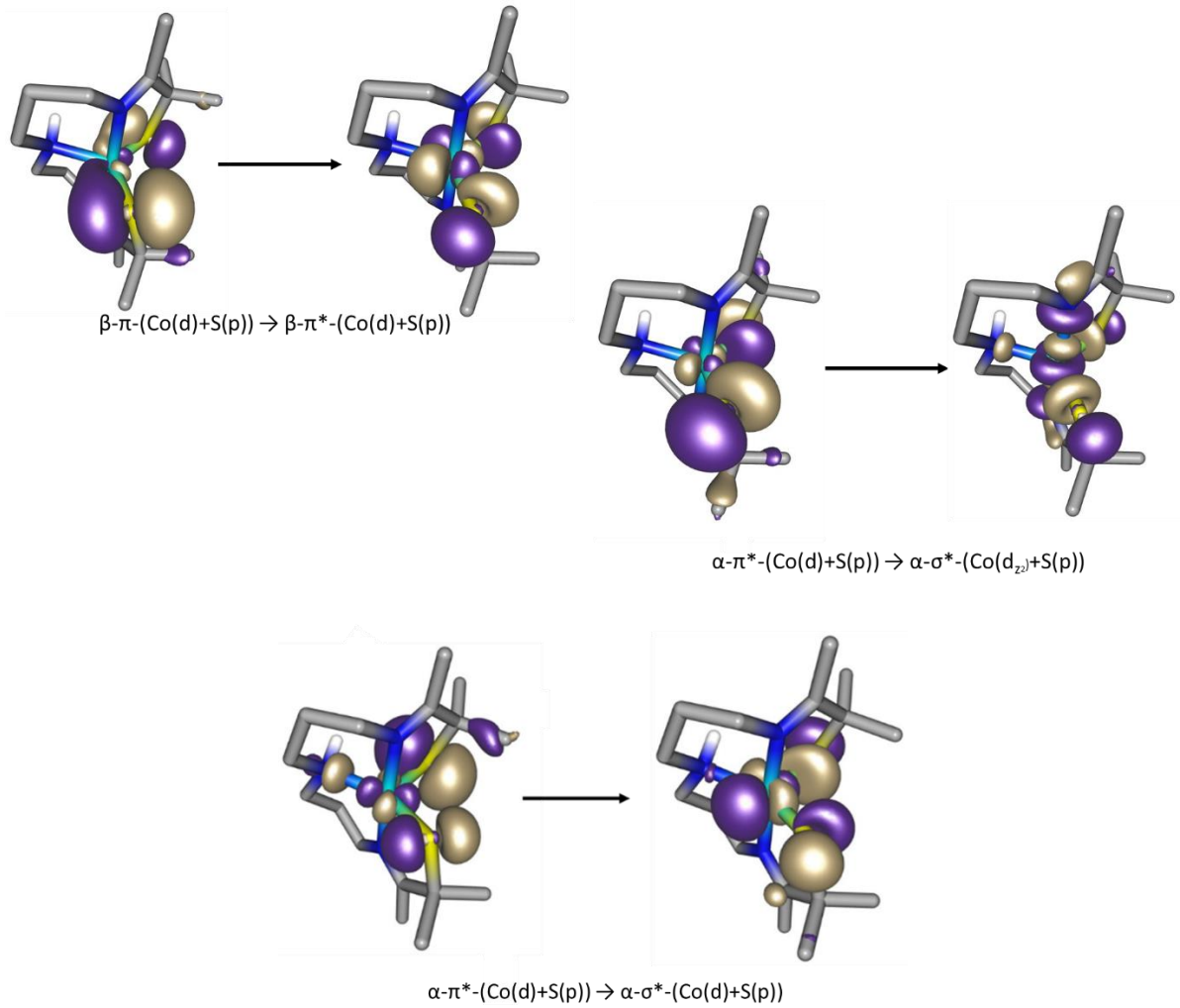

Figure 4.36 Major contributions of the NTOs for *S* = 1 (top, includes β and α) and *S* = 0 (bottom) for the major bands of the TD-DFT calculated spectra of **1**.

4.3.4.2 DFT Optimized Geometries and TDDFT Spectra of 2 (*S* = 0, 1, and 2).

To further explore the results of sulfur oxygenation on these Co^{III} species the previously characterized, doubly oxygenated $[Co^{III}(S^{Me2}(S^{O2})N_2N^{H}(Pr,Pr))]^{+}$ (**2**) was also modeled with DFT calculations in a similar manner to the other cobalt complexes. Geometry optimizations (***Table 4.11***) with the B3LYP, BP86, and PBE0 functionals were completed as well as TD-DFT calculations. As was shown previously, the sulfur oxygenation results in a significant change in geometry from

0.87 → 0.48 for **2** as well as a change in spin-state to *S* = 0. The calculated relative energy diagram (***Figure 4.37***) showed that the *S* = 0 state was the ground state, differing from the order calculated for **1** and **4^{ox}**. The relative energy was consistent with the observation of a diamagnetic species for **2**.

The TD-DFT calculated spectrum from the PBE0 functional and *S* = 0 spin-state (***Figure 4.38***) showed bands shifted ~75 nm from the experimentally reported peaks. The relative intensities of the bands were similar, wherein the 200-400 nm bands were much more intense than in the lower energy 500-800 nm region of the spectrum. The major NTO contribution to the bands (***Figure 4.39***) was a complicated interaction between orbitals of the cobalt, thiolate and oxygen atoms, which highlighted how sulfur oxygenation alters the electronics of the complex. The donor orbital included bonding interactions between the thiolate and Co(d) orbitals and nonbonding interactions between the oxygen and thiolate p orbitals of the sulfinate arm. The acceptor orbital included both a π* interaction with the unmodified thiolate arm and a σ* interaction with the sulfinate arm, marking a clear difference from the unmodified Co^{III} systems of **1** and **4^{ox}** (***Figures 4.35-4.36***).

Table 4.11 Selected bond lengths (Å), percent error from crystallographically obtained metrical parameters and τ-values from DFT calculated geometry optimizations for **2**.

B3LYP						
	S = 0	% error	*S* = 1	% error	*S* = 2	% error
Co—N(1)	1.938	0.00	1.941	0.15	2.084	7.53
Co—N(2)	1.995	4.29	1.925	0.63	2.086	9.04
Co—N(3)	1.944	4.05	2.046	0.99	2.120	4.64
Co—S(1)	2.128	0.33	2.164	2.03	2.410	13.63
Co—S(2)	2.125	0.43	2.226	5.20	2.241	5.91
τ	0.41	14.58	0.76	58.33	0.77	60.42
BP86						
	S = 0	% error	*S* = 1	% error	*S* = 2	% error
Co—N(1)	1.935	0.15	1.936	0.10	2.089	7.79
Co—N(2)	1.941	1.46	1.930	0.89	2.107	10.14
Co—N(3)	2.031	0.25	2.062	1.78	2.119	4.59
Co—S(1)	2.108	0.61	2.144	1.08	2.193	3.39
Co—S(2)	2.114	0.09	2.183	3.17	2.319	9.59
τ	0.38	20.21	0.80	66.67	0.78	62.50
PBE0						
	S = 0	% error	*S* = 1	% error	*S* = 2	% error
Co—N(1)	1.935	0.15	1.951	0.67	2.111	8.93
Co—N(2)	1.944	1.62	1.925	0.63	2.100	9.78
Co—N(3)	2.011	0.74	2.079	2.62	2.118	4.54
Co—S(1)	2.110	0.52	2.147	1.23	2.266	6.84
Co—S(2)	2.115	0.05	2.231	5.43	2.546	20.32
τ	0.36	25.00	0.70	45.83	0.71	47.92

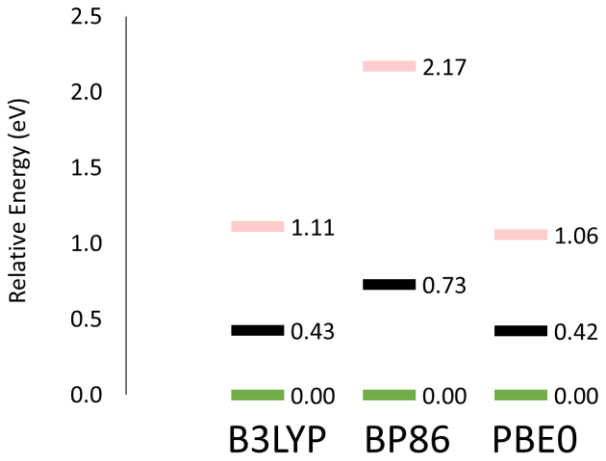

Figure 4.37 Relative energy diagram calculated for **2** with B3LYP, BP86 and PBE0 *S* = 0 ground state (green), *S* = 1 (black), and *S* = 2 (peach).

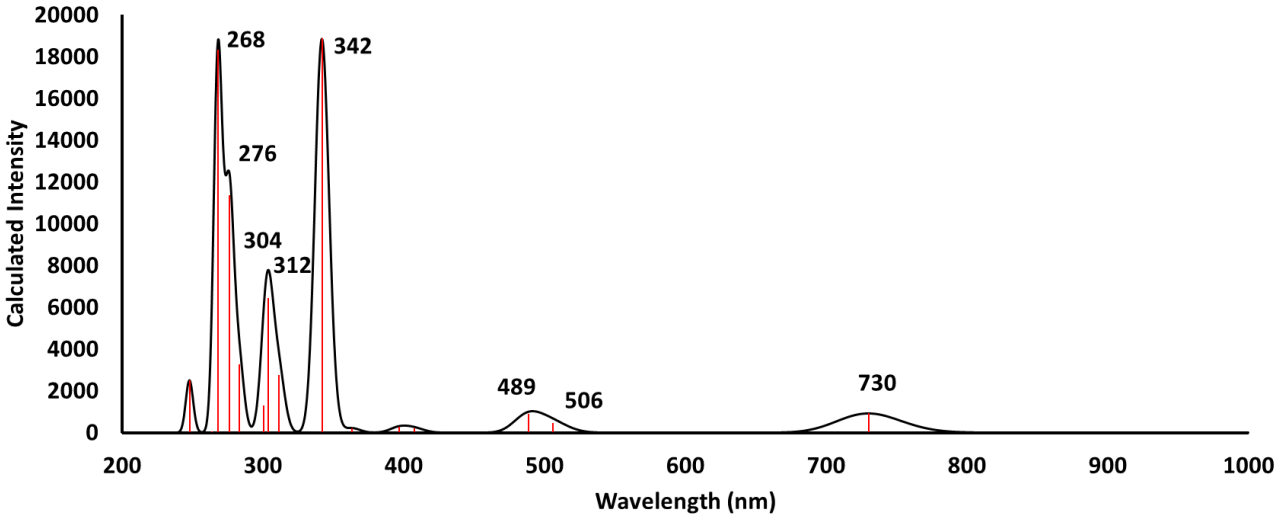

Figure 4.38 Calculated TD-DFT PBE0 spectra for **2**, the three key features of the spectrum are in agreement with the present of a mix of spin states in solution to create the key features (blue-shifted ~75 nm) (λ_{max} (ε_M) = 319(7900), 414(2700), and 805(290) nm in MeCN).[24]

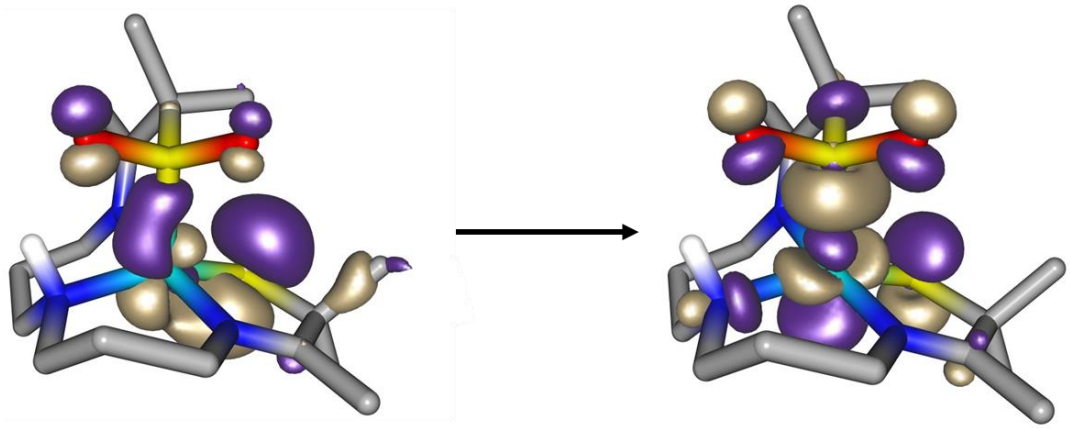

Figure 4.39 Major contribution of the NTOs for $S = 0$ for the major bands of the TD-DFT calculated spectra of **2**.

4.3.5 Correlations with Metrical Parameters in the Five-Coordinate Co^{III} Series

Once the complexes were oxidized the λ_{max} demonstrate da correlation with the Co—S_{avg} bond distance instead of with the Co—N bond distances (***Figure 4.40***). The change reflected the compensatory effect of the thiolate ligands on managing changes to the electronics of the complex once oxidized.[40] As the electronic density was reduced on the Co^{III} ion, the thiolates became more donating to the Co^{III} center and therein reflective of the electronic behavior. The correlation was also observed through with the reduction potential of the three five-coordinate species **1**, **2** and $\mathbf{4^{ox}}$ (***Figure 4.41***).

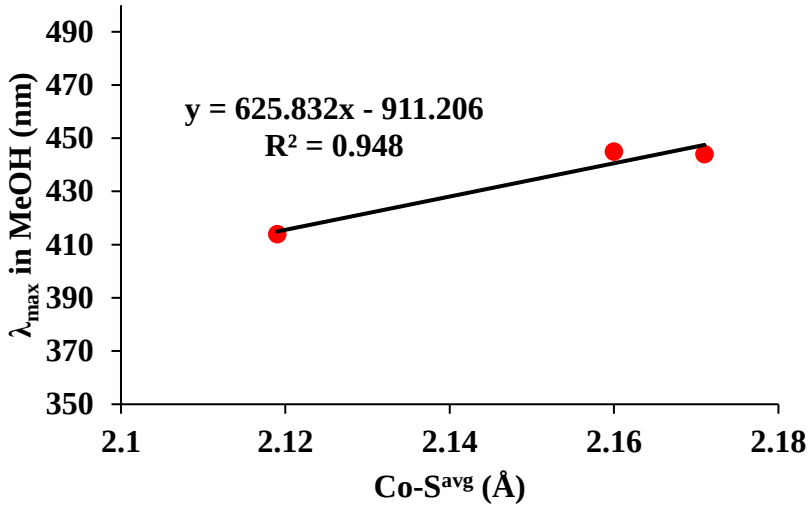

Figure 4.40 Correlation between λ_{max} (MeOH) and Co—S distance for five-coordinate Co^{III} species **1**, **2**, and **4^{ox}**.

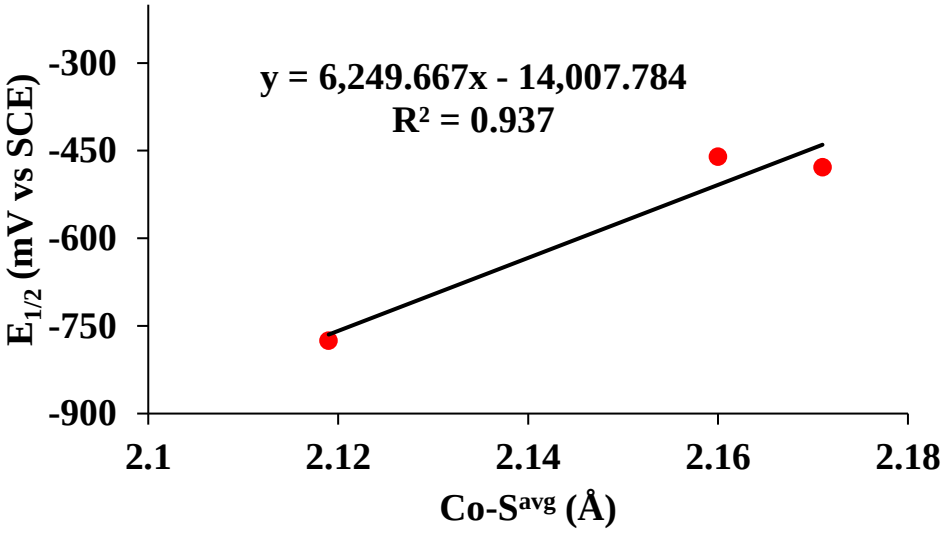

Figure 4.41 Correlation plot of $E_{1/2}$ and Co—S bond length for five-coordinate Co^{III} species **1**, **2** and **4^{ox}**.

4.3.6 Oxidation of a More Constrained Complex with Et,Pr-linker, 5

The oxidation of **5** with Cp_2Fe^+ resulted in the formation of a persulfide complex $[Co^{III}(S^{Me2}N_2N^H(Et,Pr)(\eta^2\text{-}S_2)](PF_6)$ (**5^{ox}**, ***Figure 4.42***, ***Table 4.12***) as was isolated by previous members of the group. This was dramatically different from the behavior of **4**, but consistent with the behavior of the corresponding Fe derivative.[41] The mechanism of sulfur extrusion will be the subject of future investigations and requires the cleavage of a C—S bond derived from a sacrificial complex. The C–S bond strength is ~72-75 kcal mol^{-1},[42] demonstrating the formidable bond cleaving capabilities of **5^{ox}**. There are only a handful of crystallographically characterized transition-metal persulfide complexes.[41,43,44] The structure was similar to the persulfide bound Fe species $[Fe^{III}(S^{Me2}N_2N^H(Et,Pr)(\eta^2\text{-}S_2)](PF_6)$ and the metrical parameters are summarized in ***Table 4.12***. The average metal-ligand bond distances in **5^{ox}** (Co—S_{avg} = 2.2037(16) Å and Co—N_{avg} = 1.9403(4) Å) were comparable to other cobalt complexes containing ligands similar that described herein. The persulfide S—S bond distance (2.0114(19) Å) was in the range of other crystallographically characterized persulfide complexes (S—S distances = 2.011(1) Å[41], 2.015(8) Å[43], 2.027(4) Å[44]). The angle of the persulfide (52.69(5)°) was also very similar to that found for the Fe-derivative of 51.85(3)° indicating a similar binding mode of the persulfide. The *pseudo*-octahedral environment was probed by calculating the variance (σ^2_{oct}) from the ideal 90°, where σ^2_{oct} = 0 would be ideal octahedral geometry. The cobalt derivative **5^{ox}** was closer to an ideal octahedral environment showing σ^2_{oct} = 186.8 while the iron version was more distorted with σ^2_{oct} = 200.4

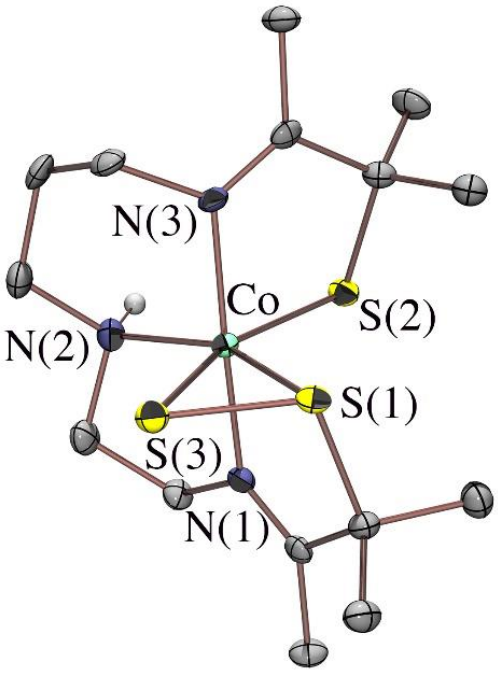

Figure 4.42 ORTEP diagram of $[Co^{III}(S^{Me2}N_2N^H(Et,Pr)(\eta^2\text{-}S_2)](PF_6)$ (**5^{ox}**) showing 50% probability ellipsoids. Hydrogen atoms, with the exception of N(2)-H, and the counterion have been omitted for clarity (structure obtained by Dr. Dirk Schweitzer).

Table 4.12 Comparison of selected bond distances (Å) and angles (°) for persulfide Co^{III} complexes **5^{ox}**, and previously reported $[Fe^{III}(S^{Me2}N_2N^H(Et,Pr)(\eta^2\text{-}S_2)]$.[41]

	5^{ox}	**$[Fe^{III}(S^{Me2}N_2N^H(Et,Pr)(\eta^2\text{-}S_2)]$**
M—N(1)	1.912(4)	1.944(2)
M—N(2)	1.972(5)	1.993(3)
M—N(3)	1.937(4)	1.971(2)
M—S(1)	2.1923(17)	2.2209(9)
M—S(2)	2.2150(15)	2.1694(8)
M—S(3)	2.3313(16)	2.3687(9)
S(1)—S(3)	2.0114(19)	2.011(1)
N(1)—M—N(3)	174.2 (2)	175.6(1)
S(1)—M—S(2)	103.53 (6)	100.57(3)
S(1)—M—S(3)	52.69(5)	51.85(3)
S(3)—M—N(2)	104.57(15)	99.23(9)
S(2)—M—N(2)	99.10 (15)	108.25(9)
N(1)—M—S(1)	85.96 (15)	84.99(8)
N(1)—M—N(2)	86.7 (2)	85.2(1)
N(1)—M—S(2)	90.73 (14)	92.35(8)
N(1)—M—S(3)	88.35(14)	87.13(8)
N(3)—M—S(1)	97.91 (16)	99.07(8)
N(3)—M—N(2)	91.4 (2)	92.1(1)
N(3)—M—S(2)	84.16(16)	85.13(8)
N(3)—M—S(3)	97.45(16)	96.80(8)
σ^2_{oct}	186.8	200.4

M = Co or Fe

4.4 Dioxygen Reactivity with Thiolate-Ligated Cobalt Complexes

4.4.1 Reactivity of 4 with Dioxygen

In a MeOH solution, **4** reacted with dioxygen to form the oxidized complex $\mathbf{4^{ox}}$ at low temperatures**,** consistent with outer-sphere oxidation (***Figure 4.43***). The electronic absorption spectrum did not indicate the addition of any solvent binding as a sixth ligand on the metal center in the open site of five-coordinate **4**, which would have resulted in a change in the EAS features observed thus the reactivity can be classified as a likely outer-sphere oxidation. The solution reached 100% of the expected absorbance for complex $\mathbf{4^{ox}}$ with characteristic peaks at λ_{max} = 444, 556 and 790 nm, which grew into the spectrum over an hour at -73 °C.

The oxidative activity was solvent dependent, MeCN and THF solutions did not undergo full oxidative conversion to complex $\mathbf{4^{ox}}$ (***Figures 4.44-4.45***). Further investigations of the MeCN solution reaction would be valuable to see if the presence of nitrile substrates (relevant to the mechanism of NHase) affected the pathway of sulfur oxygenation. A small band with λ_{max} = 500 nm grew in after dioxygen exposure in THF solution (***Figure 4.45***). The species did not show a high absorbance as expected for the $\mathbf{4^{ox}}$ species formed in MeOH. The species could be either a small amount of the oxidized product forming or another unidentified species. The original study of **1** and **7** was carried out in MeCN for the most part. These results indicated the solvent can have large effects on reactivity and further investigations into solvent dependency may lead to new avenues of research.

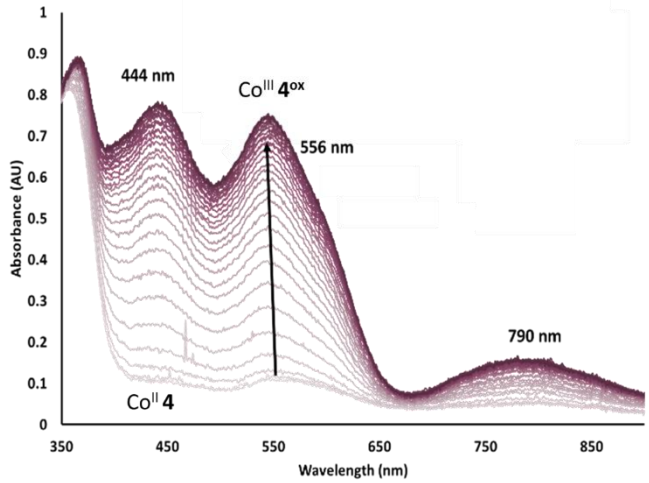

Figure 4.43 EAS monitoring the oxidation of $Co^{II}(S_2{}^{Me2}N_2N^{Me}(Pr,Pr))$ (**4**) with excess dioxygen, in MeOH at -73 °C to $[Co^{III}(S_2{}^{Me2}N_2N^{M}e(Pr,Pr))](PF_6)$ (**4**^{ox}) over one hour. [Co] = 0.450 mM.

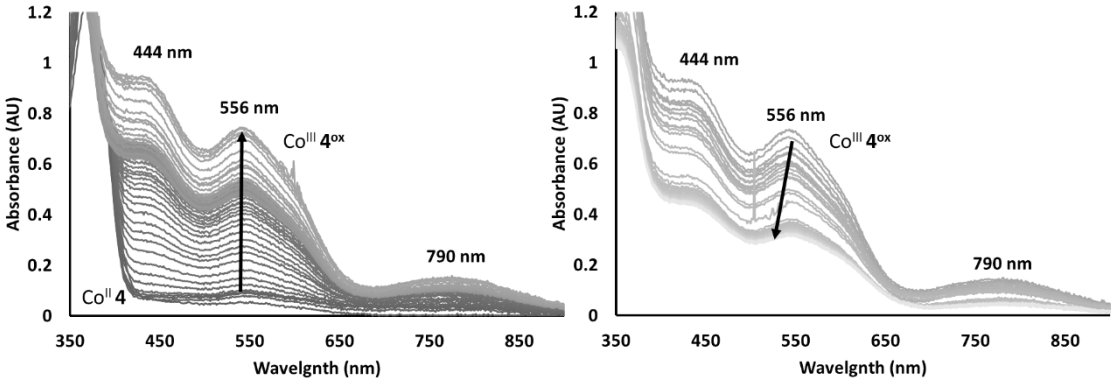

Figure 4.44 EAS monitoring the incomplete oxidation (1.5 hours) of $Co^{II}(S_2{}^{Me2}N_2N^{Me}(Pr,Pr))$ (**4**, left) with excess dioxygen, in MeCN at -40 °C to $[Co^{III}(S_2{}^{Me2}N_2N^{M}e(Pr,Pr))](PF_6)$ (**4**^{ox}) followed by a loss of intensity in the spectral features over 1.5 hours. [Co] = 0.450 mM.

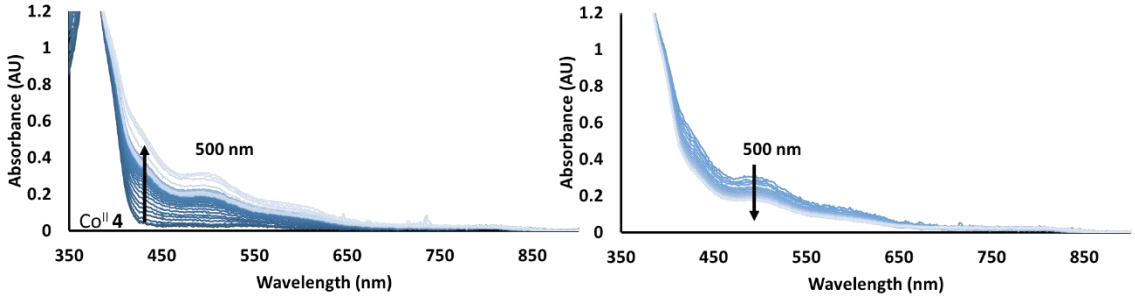

Figure 4.45 EAS monitoring the reaction of $Co^{II}(S_2{}^{Me2}N_2N^{Me}(Pr,Pr))$ (**4**) with excess dioxygen, in THF at -73 °C showing the growth of a band at λ_{max} = 500 nm (left) over one hour followed by a loss of intensity of the species over another hour (right). [Co] = 0.450 mM.

4.4.2 Reactivity of 4^{ox} with Dioxygen

In a similar manner to previously reported **1**, the complex $\mathbf{4^{ox}}$ was left to stir open to air and monitored by EAS. Over a period of days, the spectrum shifted to show the conversion to two species with new bands at λ_{max} = 530 and λ_{max} = 411 nm respectively (***Figure 4.46***). The absence of clear isosbestic points indicated the first intermediate (λ_{max} = 530 nm) continued to form the second product (λ_{max} = 411 nm) before $\mathbf{4^{ox}}$ had fully reacted. This indicated the first intermediate was a dioxygen reactive species that may be difficult to isolate in the presence of excess dioxygen.

Mass spectrometry (MS) analysis of the solutions at consecutive timepoints in the reaction demonstrated sequential m/z signals at $[M^+]$+16, $[M^+]$+32, and $[M^+]$+48 Da (***Figure 4.47***, left). When the λ_{max} = 530 nm band was dominant in the solution the $[M^+]$+16 peak was present at a higher intensity in the mass spectrum, which indicated this species was likely a singly oxygenated cobalt complex, $[Co^{III}(\eta^2\text{-}S^{Me2}O)((S^{Me2}N_2N^{Me}(Pr,Pr))]^+$ (**9**), (**Section 4.5**). The formation of a sulfenate ($RS—O^-$) species preceding a sulfinate ($RS(=O)_2$) product was different than the reactivity observed with **1** and dioxygen. When the λ_{max} = 411 nm band was dominant in the EAS, there were a multitude of signals with higher m/z = $[M^+]$+32 and $[M^+]$+48 Da gaining in intensity

(***Figure 4.47***, right). The serial addition of oxygen atoms demonstrated for the first time, a Co-sulfenate species has continued to react with dioxygen and undergo further sulfur oxygenation.

The second product was crystallographically characterized as $[Co^{III}((\eta^2\text{-}S^{Me2}O)(S^{O2})N_2N^{Me}(Pr,Pr))]^+$ (**10**) (**Section 4.4.3**) from a MeOH solution resting open to air. The addition of three oxygen atoms to the thiolate arms from air demonstrated **4^{ox}** is capable of cleaving a stronger O=O bond (dioxygen) than the secondary amine system **1,** which forms the sulfenate product only from a weaker O—O bond delivered by the addition of H_2O_2.[24]

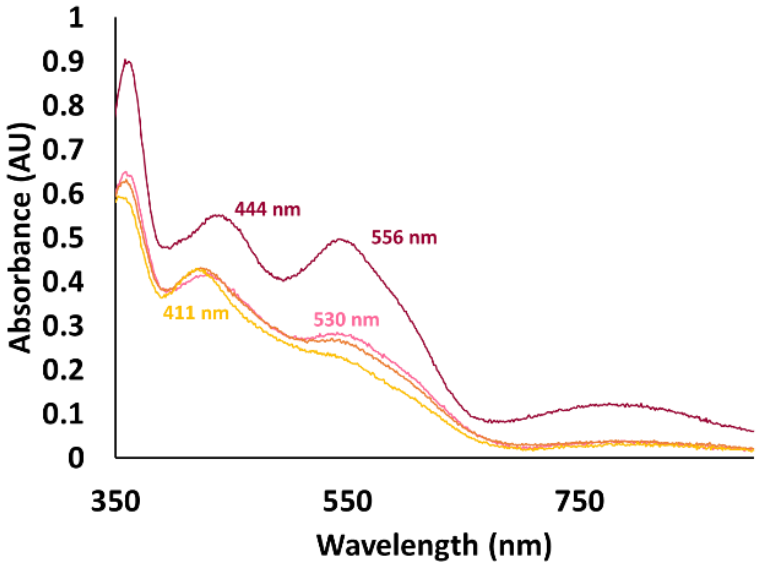

Figure 4.46 EAS monitoring the reaction of $[Co^{III}(S_2^{Me2}N_2N^{Me}(Pr,Pr))](PF_6)$ (**4^{ox}**, maroon) with excess dioxygen from air, in MeOH at room temperature to $[Co^{III}(\eta^2\text{-}S^{Me2}O)((S^{Me2}N_2N^{Me}(Pr,Pr))]^+$ (**9**, pink) and $[Co^{III}((\eta^2\text{-}S^{Me2}O)(S^{O2})N_2N^{Me}(Pr,Pr))]^+$ (**10**, yellow) respectively monitored over 12 days.

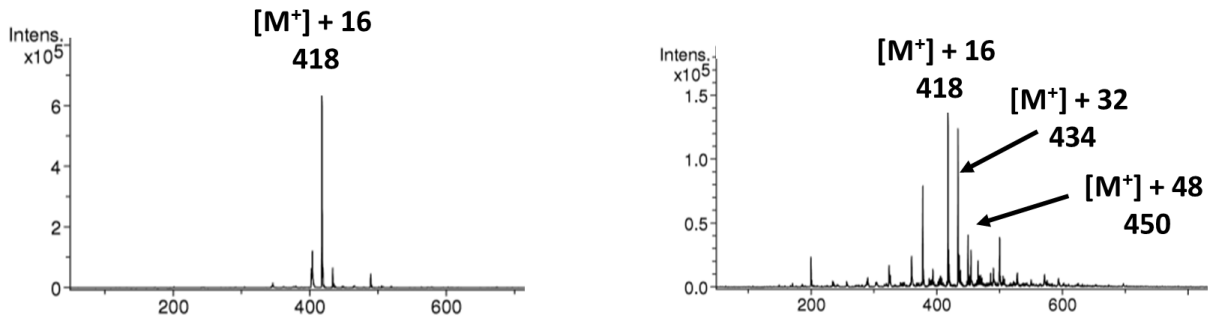

Figure 4.47 Mass spectrum of MeOH solution of **4^{ox}** exposed to dioxygen at sequential time points where the majority absorbances were λ_{max} = 530 nm corresponding to **9** (left) and λ_{max} = 411 nm corresponding to **10** (right).

4.4.3 Triply Oxygenated Thiolate-Ligated Cobalt Complex 10

A concentrated MeOH solution of **4^{ox}** was left open to air for several weeks. Red, needlelike crystals developed from slow evaporation of the solvent while exposed to air to yield single crystals of **10** (***Figure 4.48***, ***Table 4.13***). There was a small amount of disorder in the propyl connector between N(2) and N(3). The d^6 electron configuration of Co^{III} species renders them substitutionally inert. If the spin-state change observed from **1** → **2** also takes place in the transition from **4^{ox}** → **10**, then **10** is likely also diamagnetic. Combined, these factors are likely responsible for the sluggish rate of sulfur oxidation that results in **10**. The sequential sulfur oxygenation process observed in the transformation of **4^{ox}** → **9** → **10** was similar to the oxygenation process observed with an Fe-peptide model of NHase through EPR studies.[46]

The metrical parameters of this species are summarized in ***Table 4.14*** and compared to the other known triply oxygenated Co^{III} model complexes **3** and the Masuda group's $PPh_4[Co(L\text{-}O_3)]$**[25]**. The Co—$S^{thiolate}$ bond distances were all very similar (~2.13 Å) between the three species, while the one Co—$S^{thioether}$ bond was expanded at 2.565 Å, as was expected. The Co—O distances

(2.031-2.045 Å) and S—O (1.548-1.573 Å) of the η^2-bound sulfenate species were also all very similar. The σ^2_{oct} revealed a difference for the more sterically bulky **10** as was expected with the addition of the methyl group on the amine nitrogen. The σ^2_{oct} = 452.6 represented significantly more distortion from the ideal octahedral geometry than for **3** (σ^2_{oct} = 280.4) or $PPh_4[Co(L\text{-}O_3)]$[25] (σ^2_{oct} = 276.5) (***Table 4.14***).

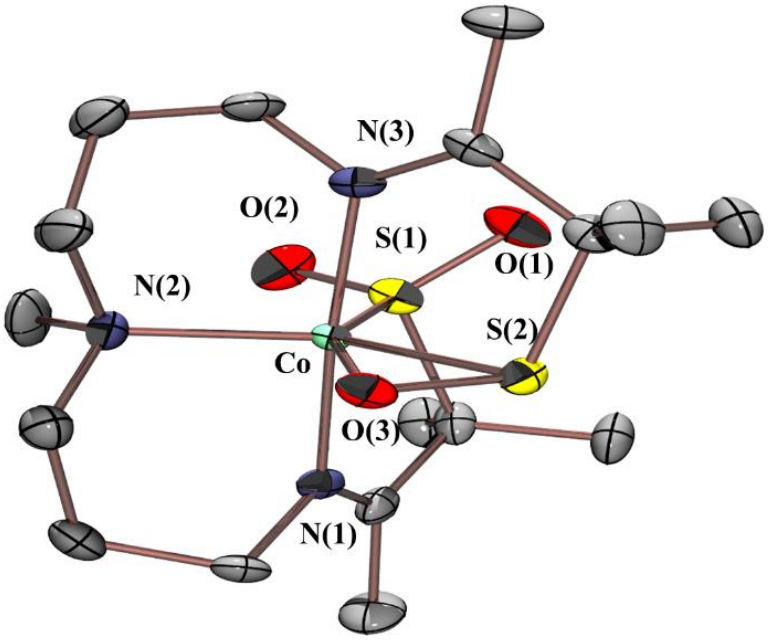

Figure 4.48 ORTEP diagram of $[Co^{III}((\eta^2\text{-}S^{Me2}O)(S^{O2})N_2N^{Me}(Pr,Pr))]^+$ (**10**) showing 50% probability ellipsoids. Hydrogen atoms, disorder in the amine arms, and the anion have been omitted for clarity.

Table 4.13 Crystal data, intensity collections, and structure refinement parameters for $[Co^{III}((\eta^2\text{-}S^{Me2}O)(S^{O2})N_2N^{Me}(Pr,Pr))]^+$ (**10**).

Empirical formula	C17 H33 Co F6 N3 O3 P S2	
Formula weight	595.48	
Temperature	296(2) K	
Wavelength	0.71073 Å	
Crystal system	Monoclinic	
Space group	P c	
Unit cell dimensions	a = 11.2247(8) Å	α= 90°.
	b = 9.0526(7) Å	β= 111.447(2)°.
	c = 12.8170(10) Å	ϒ= 90°.
Volume	1212.19(16) $Å^3$	
Z	2	
Density (calculated)	1.631 Mg/m^3	
Absorption coefficient	1.017 mm^{-1}	
F(000)	616	
Crystal size	0.170 x 0.140 x 0.100 mm^3	
Theta range for data collection	1.949 to 28.365°.	
Index ranges	-14<=h<=14, -12<=k<=12, -17<=l<=17	
Reflections collected	11319	
Independent reflections	6011 [R(int) = 0.0319]	
Completeness to theta = 25.000°	100.0 %	
Refinement method	Full-matrix least-squares on F^2	
Data / restraints / parameters	6011 / 17 / 318	
Goodness-of-fit on F^2	1.032	
Final R indices [I>2sigma(I)]	R1 = 0.0425, wR2 = 0.1012	
R indices (all data)	R1 = 0.0509, wR2 = 0.1055	
Absolute structure parameter	0.13(2)	
Largest diff. peak and hole	0.851 and -0.590 $e.Å^{-3}$	

Table 4.14 Comparison of selected bond distances (Å) and octahedral variance for triply oxygenated Co^{III} complexes **10, 3** and $PPh_4[Co(L\text{-}O_3)]$**[25]**.

	10	**3**[24]	**$PPh_4[Co(L\text{-}O_3)]$**[25]
Co—N(1)	1.952(5)	1.957(3)	1.942(2)
Co—N(2)	2.031(5)	1.943(3)	1.928(2)
Co—N(3)	1.944(5)	1.993(3)	n/a
Co—S(1)	2.1399(15)	2.132(1)	2.2565(6)
Co—S(2)	2.1368(15)	2.118(1)	2.1329(6)
Co—S(3)	n/a	n/a	2.1332(7)
$Co—O^{sulfenate}$	2.031(4)	2.042(2)	2.044(2)
$^{sulfenate}S—O$	1.549(4)	1.548(3)	1.573(2)
σ^2_{oct}	452.6	280.4	276.5

4.5 Oxo-Atom Donor Reactivity to Isolate 9

4.5.1 Reactivity of PhIO with 4^{ox} Monitored with EAS

An alternative approach for oxygenation of transition metal complexes involved utilizing oxo-atom donors, which donate a single oxo-atom at a time. We previously demonstrated this approach was viable for isolating transition metal sulfenate species.[47] The addition of oxo-atom donor PhIO monitored by EAS (***Figure 4.49***), followed the same changes observed during addition of dioxygen at a much more rapid rate. The addition of isotopically labeled $PhI^{18/16}O$ was conducted to ensure the oxygen atom was derived from the PhIO reagent. The mass spectrum of this experiment showed a signal for **9** at $[M^+]+18$ = 420 m/z which is consistent with the labeled ^{18}O being the source of the sulfenate oxo-atom.

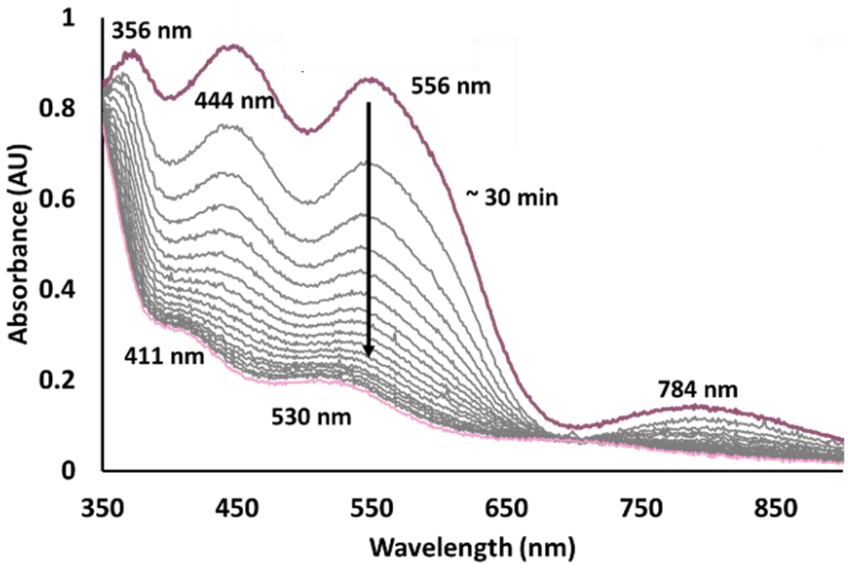

Figure 4.49 EAS monitoring the reaction of $[Co^{III}(S_2{}^{Me2}N^{Me}N_2(Pr,Pr))](PF_6)$ (**4^{ox}**) with 10 equiv. PhIO in MeOH, at room temperature to $[Co^{III}(\eta^2\text{-}S^{Me2}O)((S^{Me2}N_2N^{Me}(Pr,Pr))]^+$ (**9**).[Co] = 0.450 mM.

4.5.2 Characterization of Isolated Singly Oxygenated Thiolate-Ligated Cobalt Complex 9

The use of PhIO allowed for the equivalent stoichiometric addition of reagent to the complex compared to the excess of oxidant present from dioxygen exposure. In turn, this facilitated the isolation of a single crystal suitable for X-ray crystallography of the reactive intermediate species **9** (***Figure 4.50*** and ***Table 4.15***). The crystal obtained was chemically disordered with the Co^{III} complex **4^{ox}**. The site occupancy fitting suggested the oxygen-containing species (54.8(8)%) is the major component with metrical parameters described in ***Table 4.16***. The singly oxygenated Co-sulfenate species **9** was the only one with an isolated sulfenate present with no other modified thiolates in the coordination sphere.

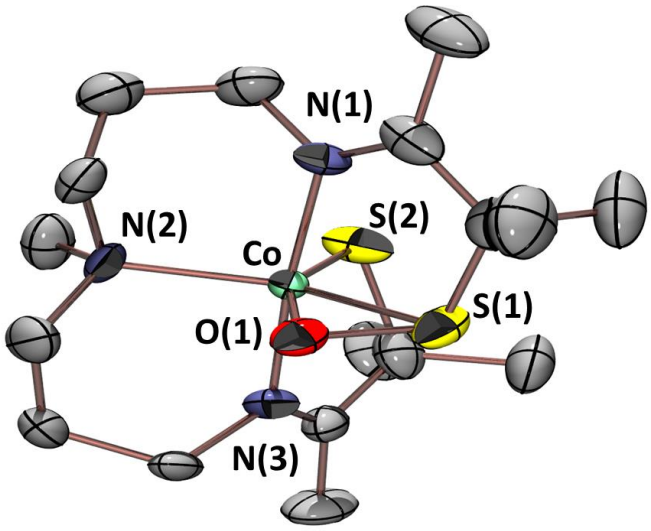

Figure 4.50 ORTEP diagram of $[Co^{III}(\eta^2\text{-}S^{Me2}O)(S^{Me2}N_2N^{Me}(Pr,Pr))]^+$ (**9**) showing 30% probability ellipsoids. Hydrogen atoms and the anion have been omitted for clarity.

Table 4.15 Crystal data, intensity collections, and structure refinement parameters for $[Co^{III}(\eta^2\text{-}S^{Me2}O)(S^{Me2}N_2N^{Me}(Pr,Pr))]^+$ (**9**).

Empirical formula	C17 H33 Co F6 N3 O0.54 P S2	
Formula weight	556.12	
Temperature	100(2) K	
Wavelength	0.71073 Å	
Crystal system	Monoclinic	
Space group	P c	
Unit cell dimensions	a = 11.2653(7) Å	α= 90°.
	b = 9.0804(6) Å	β= 110.872(3)°.
	c = 12.3712(8) Å	ϒ= 90°.
Volume	1182.45(13) $Å^3$	
Z	2	
Density (calculated)	1.562 Mg/m^3	
Absorption coefficient	1.029 mm^{-1}	
F(000)	577	
Crystal size	0.200 x 0.120 x 0.080 mm^3	
Theta range for data collection	1.935 to 28.462°.	
Index ranges	-15<=h<=15, -12<=k<=12, -16<=l<=16	
Reflections collected	11251	
Independent reflections	5912 [R(int) = 0.0724]	
Completeness to theta = 25.000°	100.0 %	
Refinement method	Full-matrix least-squares on F^2	
Data / restraints / parameters	5912 / 304 / 360	
Goodness-of-fit on F^2	1.033	
Final R indices [I>2sigma(I)]	R1 = 0.0590, wR2 = 0.1234	
R indices (all data)	R1 = 0.0858, wR2 = 0.1374	
Absolute structure parameter	0.25(4)	
Largest diff. peak and hole	0.772 and -0.461 $e.Å^{-3}$	

Table 4.16 Selected Bond Distances (Å) and Angles (°) for $[Co^{III}(\eta^2\text{-}S^{Me2}O)(S^{Me2}N_2N^{Me}(Pr,Pr))]^+$ (**9**).

	9
Co—N(1)	1.945(9)
Co—N(2)	2.001(18)
Co—N(3)	1.914(10)
Co—S(1)	2.204(8)
Co—S(2)	2.145(4)
Co—O(1)	2.220(9)
S(1)—O(1)	1.624(12)
N(1)—Co—N(3)	174.9(2)
S(1)—Co—S(2)	112.5(2)
S(1)—Co—O(1)	43.1(3)
O(1)—Co—N(2)	92.3(6)
S(2)—Co—N(2)	111.9(5)
N(1)—Co—S(1)	83.0(4)
N(1)—Co—N(2)	91.2(5)
N(1)—Co—S(2)	90.0(4)
N(1)—Co—O(1)	86.8(4)
N(3)—Co—S(1)	94.0(4)
N(3)—Co—N(2)	93.8(5)
N(3)—Co—S(2)	87.3(3)
N(3)—Co—O(1)	93.9(4)
σ^2_{oct}	300.4

4.6 *Pseudo*-Octahedral Co^{III} Products

4.6.1 Comparison of the Metrical Parameters of η^2-bound-sulfenate Cobalt Complexes 9, 10, and 3 and η^2-bound-persulfide Complex 5^{ox}

The average Co—S bond was shorter in the sulfenate-containing structures **9** (Co—S_{avg} = 2.1745(6) Å), **10** (Co—S_{avg} = 2.1384 Å), and **3** (Co—S_{avg} = 2.125 Å) compared to the persulfide-containing $\mathbf{5^{ox}}$ (Co—S_{avg} = 2.246 Å). This was consistent with the additional sulfur being a larger atom than the oxygen of the various sulfenate species. Complex **9** was found to have a longer S—O bond length at 1.624(12) Å over 1.548(3) Å for **3** and 1.549(4) Å for **10**. The Co—O bond lengths demonstrated a similar trend where **9** had a longer bond at 2.220(9) Å over 2.042(2) Å in **3** and 2.031(4) Å in **10**.

The η^2-bond angle S(1)—Co—O(1) = 43.49(8)° in **3** was within error of the angle for **9** and **10** at 43.1(3)° and 3.56(12)°. The angle that included the newly bound O- or S-atom was largely distorted from the ideal octahedral angle. To compare the degree of the distortion, the octahedral variance (σ^2_{oct}) in the distorted octahedral bonds was calculated and complex **10** was found to have the highest degree of variance in octahedral angle (***Table 4.17***). The steric bulk of the methyl group could cause the higher angular variance. The high level of distortion in the octahedral angles helped to explain why **9** continued to be less reactive compared to the other species, which did not proceed to undergo further chemistry with dioxygen or in the case of **3** excess H_2O_2.

Table 4.17 Comparison of selected bond distances (Å) and angles (°) for η^2-bound-sulfenate cobalt complexes **9**, **10**, **3**, and η^2-bound-persulfide complex $\mathbf{5^{ox}}$.

	9	**10**	**3**[24]	$\mathbf{5^{ox}}$
Co—N(1)	1.945(9)	1.952(5)	1.957(3)	1.912(4)
Co—N(2)	2.001(18)	2.031(5)	1.943(3)	1.972(5)
Co—N(3)	1.914(10)	1.944(5)	1.993(3)	1.937(4)
Co—S(1)	2.204(8)	2.1399(15)	2.132(1)	2.1923(17)
Co—S(2)	2.145(4)	2.1368(15)	2.118(1)	2.2150 (15)
Co—X	2.220(9)	2.031(4)	2.042(2)	2.3313 (16)
$^{\text{sulfenate}}$**S—**X	1.624(12)	1.549(4)	1.548(3)	2.0114(19)
N(1)—Co—N(3)	174.9(2)	173.4(2)	95.19 (13)	174.2 (2)
S(1)—Co—S(2)	112.5(2)	110.85(5)	114.38 (5)	103.53 (6)
S(1)—Co—O(1)	43.1(3)	43.56(12)	43.49(8)	n/a
S(1)—Co—S(3)	n/a	n/a	n/a	52.69(5)
S(3)—Co—N(2)	n/a	n/a	n/a	104.57(15)
O(1)—Co—N(2)	92.3(6)	94.31(18)	94.50 (12)	n/a
S(2)—Co—N(2)	111.9(5)	137.85(14)	83.50 (10)	99.10 (15)
N(1)—Co—S(1)	83.0(4)	84.25(15)	87.02 (10)	85.96 (15)
N(1)—Co—N(2)	91.2(5)	91.10(19)	173.57 (14)	86.7 (2)
N(1)—Co—S(2)	90.0(4)	92.85(14)	90.81 (10)	90.73 (14)
N(1)—Co—O(1)	86.8(4)	94.03(18)	89.65 (12)	n/a
N(1)—Co—S(3)	n/a	n/a	n/a	88.35(14)
N(3)—Co—S(1)	94.0(4)	89.63(15)	143.21 (10)	97.91 (16)
N(3)—Co—N(2)	93.8(5)	93.4(2)	88.96 (13)	91.4 (2)
N(3)—Co—S(2)	87.3(3)	87.05(16)	102.34 (10)	84.16(16)
N(3)—Co—O(1)	93.9(4)	90.44(18)	99.73 (13)	n/a
N(3)—Co—S(3)	n/a	n/a	n/a	97.45(16)
$\mathbf{\sigma^2_{oct}}$	300.4	452.6	280.4	186.8

X = S(3) for $\mathbf{5^{ox}}$, O(3) for **10**, and O(1) for **3** and **9**.

4.6.2 DFT Modeling of *Pseudo*-Octahedral Products

The *pseudo*-octahedral products **9**, **10**, **5^{ox}** and **3** were modeled with DFT calculations using B3LYP, BP86, and PBE0 functionals similar to the modeling performed for the five-coordinate **4^{ox}, 1,** and **2**. In all cases, geometry optimizations, frequency calculations, and time-dependent DFT calculations were carried out. The calculations were started with **3** to establish that the methods were good models for these systems as the tertiary amine oxygenation products **9** and **10** reacted more sluggishly and were more challenging to isolate from each other to form more in depth characterizations. The calculations were then continued to the crystallographically isolated *pseudo*-octahedral products **5^{ox}**, **9** and **10** to compare calculated properties of the Co-sulfenate species.

4.6.2.1 Geometry Optimizations, Time-Dependent DFT, and Frequency Calculations for 3

As was expected, the *S* = 0 state resulted in the lowest error for all three functionals (***Table 4.18***), which was consistent with the established findings of the spin-state from previous work. The *S* = 0 state was also consistent with the expectation of a Co^{III} ion in a *psuedo*-octahedral ligand field. The relative energy diagram also supported this by demonstrating the *S* = 0 state was the ground state across all three functionals (***Figure 4.51***). The experimentally obtained IR spectrum did not include an assignment of the $\nu_{S\text{-}O}$ frequency due to the overlapping signal from the PF_6 counterion in the range the $\nu_{S\text{-}O}$ signal would be expected. DFT calculations therefore offer a useful tool to compare the expected sulfenate $\nu_{S\text{-}O}$ from the various species obtained. The $\nu_{S\text{-}O}$ stretch calculated with 868 cm^{-1} (B3LYP) and 954 cm^{-1} (PBE0). The calculated TD-DFT spectra with the PBE0 functional and *S* = 0 spin state (***Figure 4.52***) showed bands at λ_{max} = 353 and 463 nm that were in agreement with the absorption bands observed from 300-1000 nm in the

experimental spectrum (λ_{max} = 338 (9800) and 480 (450) nm).[24] The NTO analysis of the bands showeds the participation of the oxygenated thiolate ligands in both the donor and acceptor orbitals of the transitions.

Table 4.18 Selected bond lengths (Å) and percent error from crystallographically obtained metrical parameters from DFT calculated geometry optimizations for *S* = 0, 1, and 2 of **3**.

			B3LYP			
	S = 0	% error	*S* = 1	% error	*S* = 2	% error
Co—N(1)	1.953	0.20	2.076	6.08	2.130	8.84
Co—N(2)	1.976	1.70	2.037	4.84	2.069	6.48
Co—N(3)	1.961	1.61	2.047	2.71	2.098	5.27
Co—S(1)	2.182	2.35	2.360	10.69	2.451	14.96
Co—S(2)	2.153	1.65	2.241	5.81	2.391	12.89
Co—O	1.958	4.11	1.889	7.49	1.893	7.30
^{sulfenate}S—O	1.607	3.81	1.628	5.17	1.639	5.88
			BP86			
	S = 0	% error	*S* = 1	% error	*S* = 2	% error
Co—N(1)	1.949	0.41	2.082	6.39	2.119	8.28
Co—N(2)	2.018	3.86	2.056	5.82	2.09	7.57
Co—N(3)	1.962	1.56	2.068	3.76	2.104	5.57
Co—S(1)	2.133	0.05	2.273	6.61	2.428	13.88
Co—S(2)	2.126	0.38	2.225	5.05	2.404	13.50
Co—O	2.095	2.60	1.932	5.39	1.909	6.51
^{sulfenate}S—O	1.573	1.61	1.606	3.75	1.620	4.65
			PBE0			
	S = 0	% error	*S* = 1	% error	*S* = 2	% error
Co—N(1)	1.950	0.36	2.111	7.87	2.127	8.69
Co—N(2)	1.993	2.57	2.045	5.25	2.099	8.03
Co—N(3)	1.964	1.46	2.087	4.72	2.094	5.07
Co—S(1)	2.133	0.05	2.265	6.24	2.382	11.73
Co—S(2)	2.137	0.90	2.251	6.28	2.375	12.13
Co—O	2.001	2.01	1.936	5.19	2.051	0.44
^{sulfenate}S—O	1.556	0.52	1.571	1.49	1.565	1.10

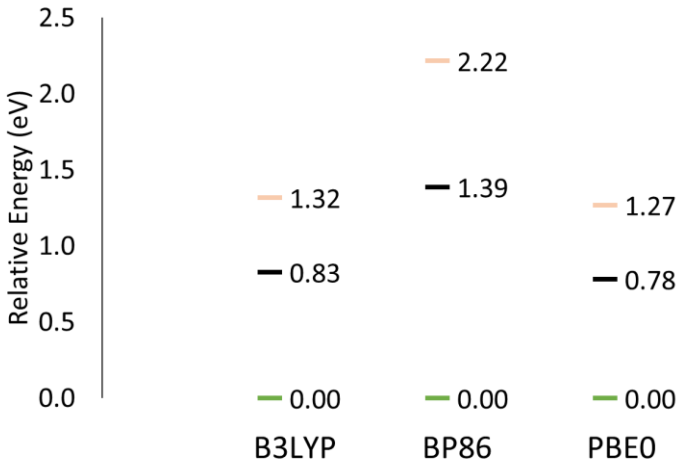

Figure 4.51 Relative energy diagram calculated for **3** with B3LYP, BP86, and PBE0 *S* = 0 ground state (green), *S* = 1 (black), and *S* = 2 (peach).

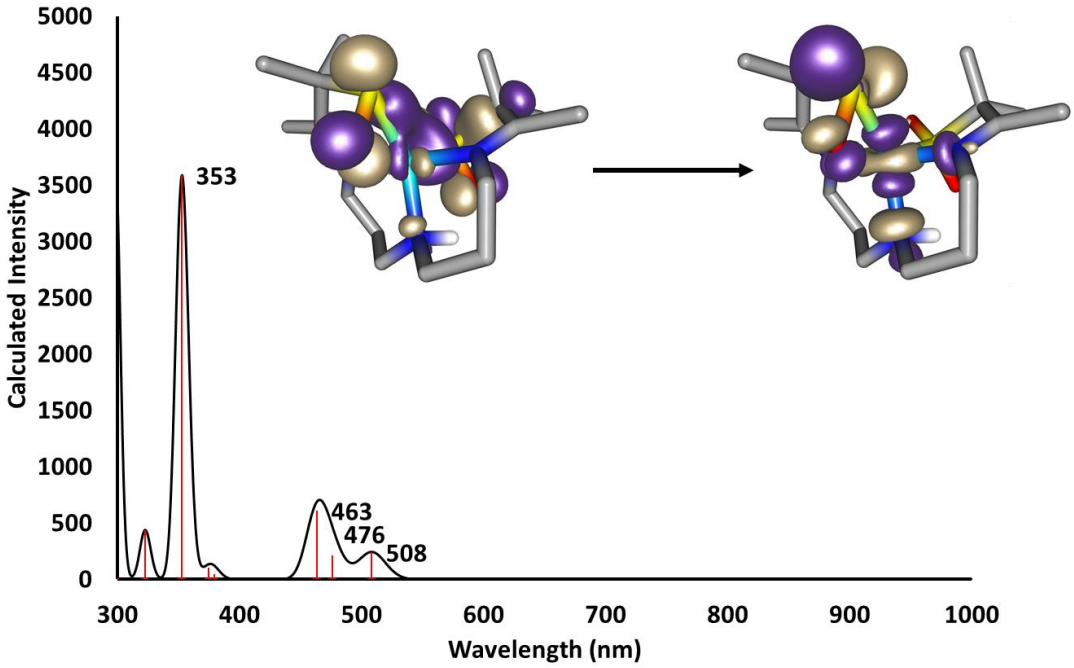

Figure 4.52 TD-DFT calculated spectrum for **3** with PBE0 functional. NTO analysis showing the major contribution to the bands includes the participation of the sulfenate S- and O- π* orbitals.

4.6.2.2 Geometry Optimizations and Time-Dependent DFT Calculations for 5^{ox}

As was expected, the *S* = 0 state resulted in the lowest error for all three functionals (***Table 4.19***). The *S* = 0 state was also consistent with the expectation of a Co^{III} ion in a *pseudo*-octahedral ligand field. The relative energy diagram also supported this by demonstrating the *S* = 0 state was the ground state across all three functionals (***Figure 4.53***). The calculated TD-DFT spectra with the PBE0 functional and *S* = 0 spin state (***Figure 4.54***) shows a series of bands at λ = 200-400 nm that were in agreement with the broad absorption band observed around 315 nm in the experimental spectrum. The NTO analysis of the bands showed the participation of the unmodified thiolate in the donor orbital and the participation of the π*-persulfide orbital in the acceptor orbital of the transitions.

Table 4.19 Selected bond lengths (Å) and percent error from crystallographically obtained metrical parameters from DFT calculated geometry optimizations for *S* = 0, 1, and 2 of **5^{ox}**.

			B3LYP			
	S = 0	% error	*S* = 1	% error	*S* = 2	% error
Co—N(1)	1.908	0.21	1.947	1.83	2.079	8.73
Co—N(2)	1.956	0.81	2.127	7.86	2.122	7.61
Co—N(3)	1.937	0.00	1.950	0.67	2.085	7.64
Co—S(1)	2.237	2.04	2.467	12.53	2.426	10.66
Co—S(2)	2.226	0.50	2.156	2.66	2.262	2.12
Co—S(3)	2.342	0.46	2.362	1.32	2.463	5.65
S(1)—S(3)	2.057	2.27	2.070	2.91	2.079	8.73
			BP86			
	S = 0	% error	*S* = 1	% error	*S* = 2	% error
Co—N(1)	1.889	1.20	1.931	0.99	2.093	9.47
Co—N(2)	1.968	0.20	2.145	8.77	2.179	10.50
Co—N(3)	1.927	0.52	1.941	0.21	2.104	8.62
Co—S(1)	2.162	1.38	2.373	8.24	2.384	8.74
Co—S(2)	2.199	0.72	2.107	4.88	2.225	0.45
Co—S(3)	2.325	0.27	2.329	0.10	2.297	1.47
S(1)—S(3)	2.025	0.68	2.039	1.37	2.093	9.47
			PBE0			
	S = 0	% error	*S* = 1	% error	*S* = 2	% error
Co—N(1)	1.909	0.16	1.996	4.39	2.094	9.52
Co—N(2)	1.967	0.25	2.158	9.43	2.137	8.37
Co—N(3)	1.941	0.21	1.984	2.43	2.095	8.16
Co—S(1)	2.190	0.10	2.373	8.24	2.375	8.33
Co—S(2)	2.203	0.54	2.132	3.75	2.247	1.44
Co—S(3)	2.306	1.09	2.305	1.13	2.445	4.88
S(1)—S(3)	2.004	0.37	2.008	0.17	2.094	9.52

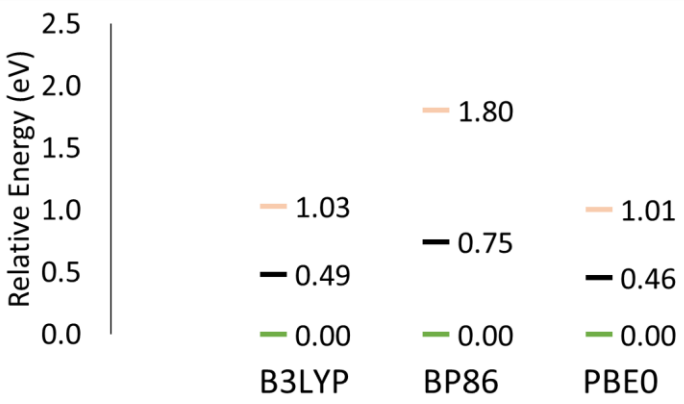

Figure 4.53 Relative energy diagram calculated for **5^{ox}** with B3LYP, BP86, and PBE0 *S* = 0 ground state (green), *S* = 1 (black), and *S* = 2 (peach).

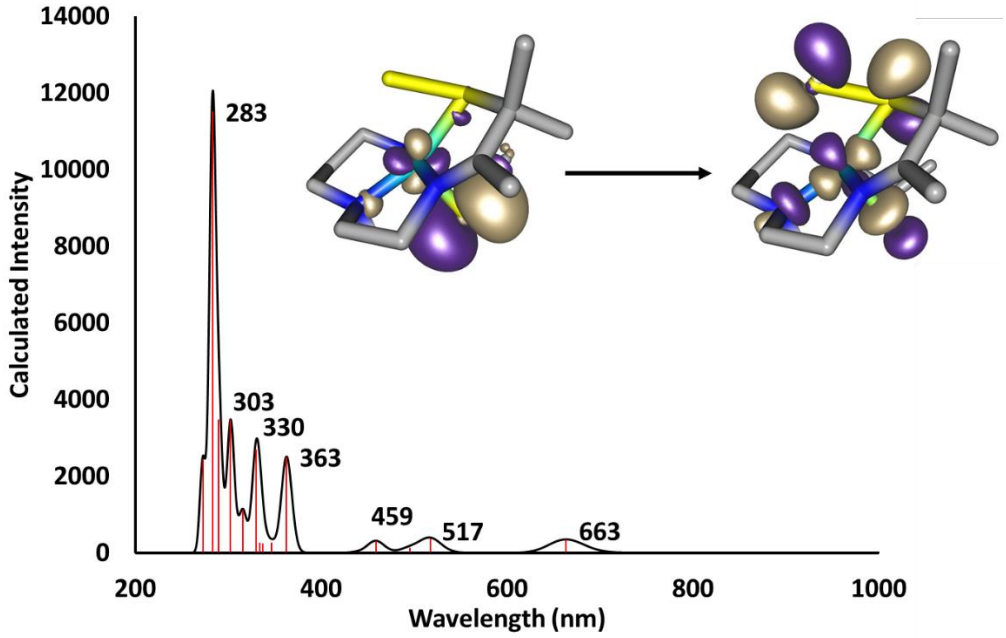

Figure 4.54 TD-DFT calculated spectrum for **5^{ox}** with PBE0 functional. NTO analysis showing the major contribution to the bands includes the participation of the thiolate and persulfide.

4.6.2.3 Geometry Optimizations, Time-Dependent DFT, and Frequency Calculations for 9

The DFT geometry optimizations show the most consistency with an *S* = 0 spin-state (***Table 4.20***). The largest error in the geometry optimizations existed for the Co—O bond distance, where it is at 12.34% (PBE0) and 10.32% (B3LYP). The S—O bond distance was accurately modeled with each functional and did not depend on the spin-state of the complex. The relative energy diagram (***Figure 4.55***) calculated for **9** showed that the low-spin (*S* = 0) were the lowest in energy as was expected for a *pseudo*-octahedral Co^{III} complex. The TD-DFT calculated spectrum of **9** shows bands in the 400-800 nm region at λ_{max} = 480, 556, and 745 nm (***Figure 4.56***). The absorbances were consistent with the feature observed at λ_{max} = 530 nm that was observed when $\mathbf{4^{ox}}$ was reacted with dioxygen (***Figure 4.46***) or PhIO (***Figure 4.49***). The λ_{max} = 745 nm feature was observed in the EAS from the reaction of $\mathbf{4^{ox}}$ and PhIO, whereas on exposure to dioxygen, this feature was not clear due to the mixture of $\mathbf{4^{ox}}$, **9**, and **10** in solution.

Table 4.20 Selected bond lengths (Å) and percent error from crystallographically obtained metrical parameters from DFT calculated geometry optimizations for *S* = 0, 1, and 2 of **9**.

B3LYP						
	S = 0	% error	*S* = 1	% error	*S* = 2	% error
Co—N(1)	1.958	0.67	1.989	2.26	2.095	7.71
Co—N(2)	2.021	1.00	2.291	14.49	2.151	7.50
Co—N(3)	1.936	1.15	1.958	2.30	2.102	9.82
Co—S(1)	2.214	0.45	2.448	11.07	2.414	9.53
Co—S(2)	2.230	3.96	2.154	0.42	2.267	5.69
Co—O	1.946	12.34	1.934	12.88	1.955	11.94
^{sulfenate}S—O	1.605	1.17	1.628	0.25	1.631	0.43
BP86						
	S = 0	% error	*S* = 1	% error	*S* = 2	% error
Co—N(1)	1.957	0.62	1.977	1.65	2.075	6.68
Co—N(2)	2.163	8.10	2.300	14.94	2.176	8.75
Co—N(3)	1.935	1.10	1.951	1.93	2.146	12.12
Co—S(1)	2.125	3.58	2.349	6.58	2.434	10.44
Co—S(2)	2.183	1.77	2.108	1.72	2.214	3.22
Co—O	2.224	0.18	2.023	8.87	2.011	9.41
^{sulfenate}S—O	1.561	0.62	1.594	1.85	1.603	1.29
PBE0						
	S = 0	% error	*S* = 1	% error	*S* = 2	% error
Co—N(1)	1.956	0.57	2.001	2.88	2.093	7.61
Co—N(2)	2.053	2.60	2.314	15.64	2.168	8.35
Co—N(3)	1.932	0.94	1.972	3.03	2.088	9.09
Co—S(1)	2.146	2.63	2.342	6.26	2.345	6.40
Co—S(2)	2.194	2.28	2.123	1.03	2.251	4.94
Co—O	1.991	10.32	1.962	11.62	2.041	8.06
^{sulfenate}S—O	1.554	0.57	1.573	3.14	1.568	3.45

Figure 4.55 Relative energy diagram for $[Co^{III}((\eta^2\text{-}S^{Me2}O)(S^{O2})N_2N^H(Pr,Pr))]^+$ (**9**) calculated with B3LYP, BP86, and PBE0 functionals. Ground state is S = 0 (green), followed by S = 1 (black) and S = 2 (peach).

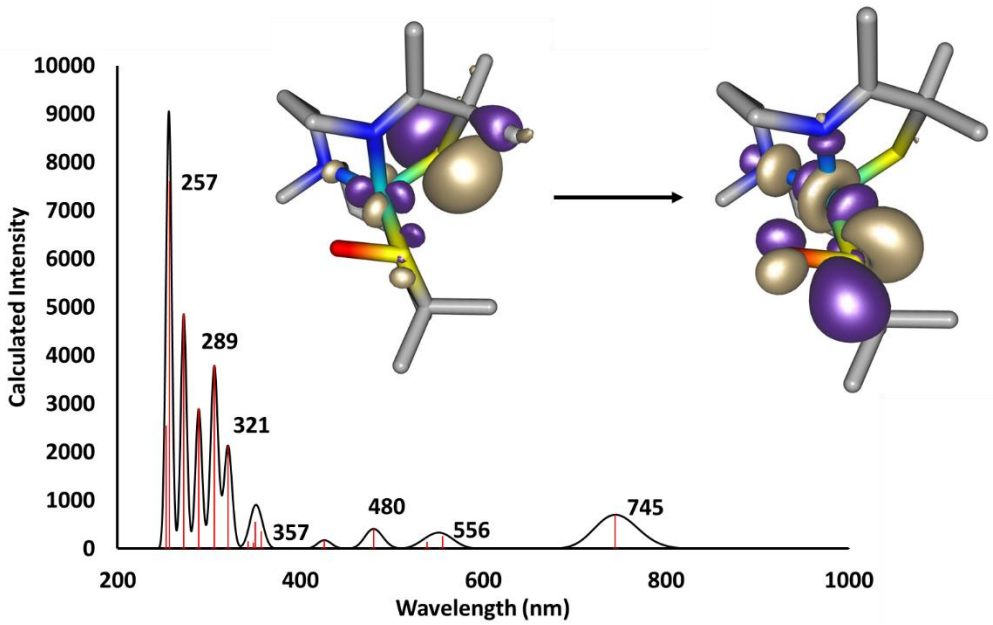

Figure 4.56 TD-DFT calculated spectrum for **9** with PBE0 functional and S = 0 spin-state. NTO analysis showing the major contribution to the bands includes the participation of the unmodified thiolate and the π* of the sulfenate.

4.6.2.4 Geometry Optimizations, Time-Dependent DFT, and Frequency Calculations for 10

The geometry optimizations of **10** were in good agreement with the crystallographic parameters with all functionals at *S* = 0 spin state (***Table 4.21***). This was once again consistent with the expectation for a six-coordinate Co^{III} species. The S—O bond distances of the sulfenate and sulfinate modified thiolate arms, did not change very much with the spin-state of the complex. The relative energy diagram for **10** (***Figure 4.57***) showed an *S* = 0 ground state for all of the functionals used. The TD-DFT calculated spectrum of **10** (***Figure 4.58***, left) did not reproduce the characteristic λ_{max} = 411 nm that was observed through EAS. However, previously, solvent has been shown to affect the spin-state of the cobalt complexes in solution. On the other hand, the spectrum calculated for the *S* = 1 state (***Figure 4.58***, right) showed an intense band at 416 nm that was consistent with the experimental value. The NTO analysis in both cases demonstrated the participation of the oxygenated thiolates ligands in the key transition orbitals.

Table 4.21 Selected bond lengths (Å) and percent error from crystallographically obtained metrical parameters from DFT calculated geometry optimizations for *S* = 0, 1, and 2 of **10**.

B3LYP						
	S = 0	% error	*S* = 1	% error	*S* = 2	% error
Co—N (1)	1.951	0.05	1.956	0.20	2.121	8.66
Co—N(2)	2.044	0.64	2.154	6.06	2.148	5.76
Co—N(3)	1.941	0.15	1.973	1.49	2.095	7.77
Co—S(1)	2.173	1.55	2.428	13.46	2.454	14.68
Co—S(2)	2.177	1.88	2.172	1.65	2.410	12.79
Co—O	1.967	3.15	1.928	5.07	2.016	0.74
$^{\text{sulfenate}}$S—O	1.604	3.55	1.626	4.97	1.618	4.45
BP86						
	S = 0	% error	*S* = 1	% error	*S* = 2	% error
Co—N (1)	1.946	0.31	1.977	1.28	2.094	7.27
Co—N(2)	2.103	3.55	2.253	10.93	2.145	5.61
Co—N(3)	1.936	0.41	1.970	1.34	2.078	6.89
Co—S(1)	2.126	0.65	2.416	12.90	2.437	13.88
Co—S(2)	2.138	0.06	2.131	0.27	2.394	12.04
Co—O	2.127	4.73	2.056	1.23	1.927	5.12
$^{\text{sulfenate}}$S—O	1.567	1.16	1.592	2.78	1.623	4.78
PBE0						
	S = 0	% error	*S* = 1	% error	*S* = 2	% error
Co—N (1)	1.948	0.20	1.990	1.95	2.096	7.38
Co—N(2)	2.060	1.43	2.198	8.22	2.142	5.47
Co—N(3)	1.939	0.26	1.977	1.70	2.090	7.51
Co—S(1)	2.130	0.46	2.352	9.91	2.438	13.93
Co—S(2)	2.152	0.71	2.167	1.41	2.411	12.83
Co—O	2.021	0.49	1.969	3.05	2.095	3.15
$^{\text{sulfenate}}$S—O	1.551	0.13	1.571	1.42	1.553	0.26

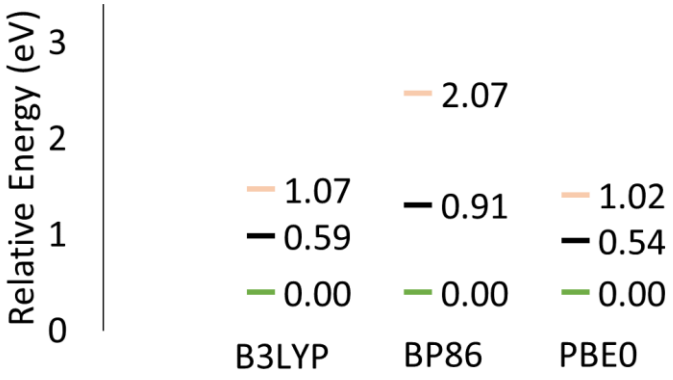

Figure 4.57 Relative energy diagram for **10** calculated with B3LYP, BP86, and PBE0 functionals. Ground state is *S* = 0 (green), followed by *S* = 1 (black) and *S* = 2 (peach).

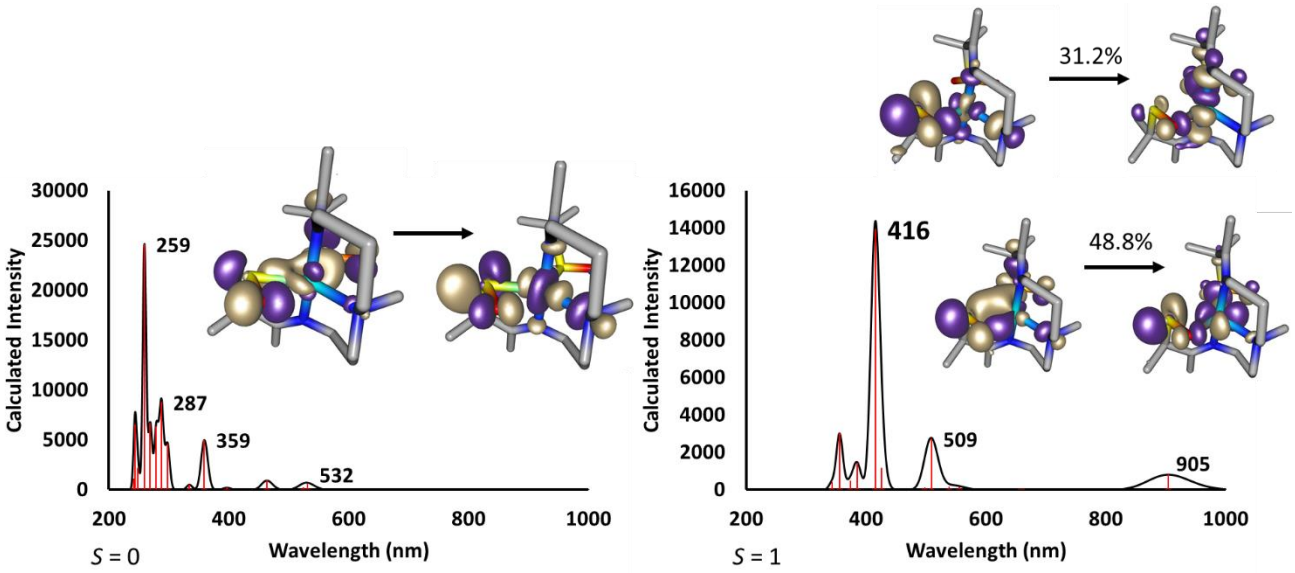

Figure 4.58 TD-DFT calculated spectrum for **10** with PBE0 functional for *S* = 0 (left) and *S* = 1 (right) spin-state. NTO analysis showing the major contribution to the bands for *S* = 0 includes the participation of the modified thiolates. Right: NTO analysis of the 416 band shows two major contributions from the α-HOMO-LUMO transition (insert top, 31.2%) and from the β-HOMO-LUMO transition (insert bottom, 48.8%).

4.6.3 Correlation Between Metrical Parameters of Six-Coordinate Species

Similar to the correlations observed for the five-coordinate Co^{III} species, the Co—S average bond distances were correlated with the Lewis acidity of the Co^{III} ions as represented by the calculated Mulliken charges of each species in the *S* = 0 ground state (***Figure 4.59***). The pattern held for all six-coordinate complexes **3**, $\mathbf{5^{ox}}$, **9**, and **10**, despite the differences in the ligand backbone and levels of oxygenation.

A correlation also existed between the Mulliken charge of the Co^{III} ion in the *S* = 0 state and the S—O bond length of the sulfenate moiety of **3**, **9**, and **10** (***Figure 4.60***). The small changes to the ligand backbones allow for the analysis of these rare species with regards to the electronic environment on the Co^{III} ion and the thiolate arms due to the cooperation of the nephelauxetic effect.

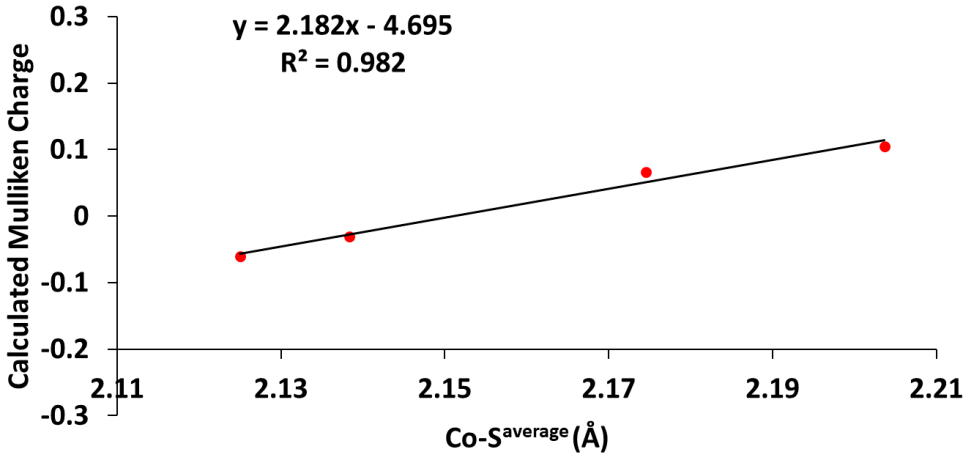

Figure 4.59 Correlation between the Mulliken charge of the Co^{III} ion in the *S* = 0 ground state and the Co—$S^{average}$ bond distance for **3**, $\mathbf{5^{ox}}$, **9**, and **10**.

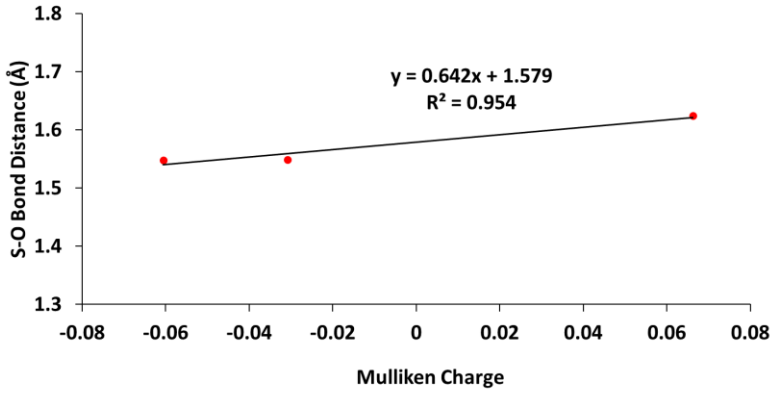

Figure 4.60 Correlation between the S—O bond distance and the Mulliken charge of the Co^{III} ion in the *S* = 0 ground state for **3**, **9**, and **10**.

4.7 Other Reactivity Explored with Co Complexes

4.7.1 Addition of PhIO to 4

The addition of PhIO to $\mathbf{4^{ox}}$ was discussed in **Section 4.5.2** and resulted in the formation of **9** and **10**. In order to explore the potential formation of a high valent Co oxo/oxyl species, the addition of PhIO to **4** was monitored with EAS (***Figure 4.61***). After 2.5 minutes, the spectrum had shifted to a new species with λ_{max} = 434 nm. The reactivity was originally explored at room temperature, further studies using cryogenic conditions will help to identify the new 434 nm intermediate.

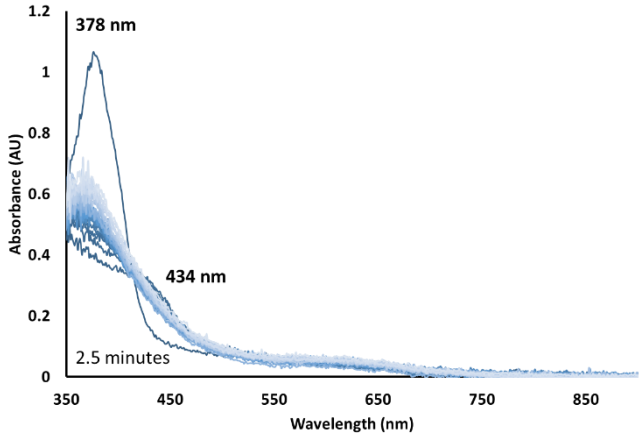

Figure 4.61 EAS monitoring the addition of 10 equiv. of PhIO (MeOH) to a THF solution of **4** 0.250 mM at room temperature. A new species with λ_{max} = 434 nm appears within 2.5 minutes**.**

4.7.2 Addition of Pyridine-N-oxide (PNO)

The addition of another oxo-atom donor, with a stronger X—O bond compared to PhIO, was also conducted. The stronger X—O bond could result in the stabilization of an oxo-atom donor adduct[47] or slow the formation of the high valent metal oxo species to facilitate its observation by EAS. The addition of PNO to **4^{ox}** was explored (***Figure 4.62***) with the addition of 10 equivalents of PNO to a MeOH solution at room temperature. Over 4 hours the absorbance of the λ_{max} = 444 and 556 nm bands increased likely due to solvent evaporation from the solution cell. Further investigations at low temperatures may assist the observation of any spectral changes as the formation of an oxo-atom donor adduct would be an entropically disfavored process.

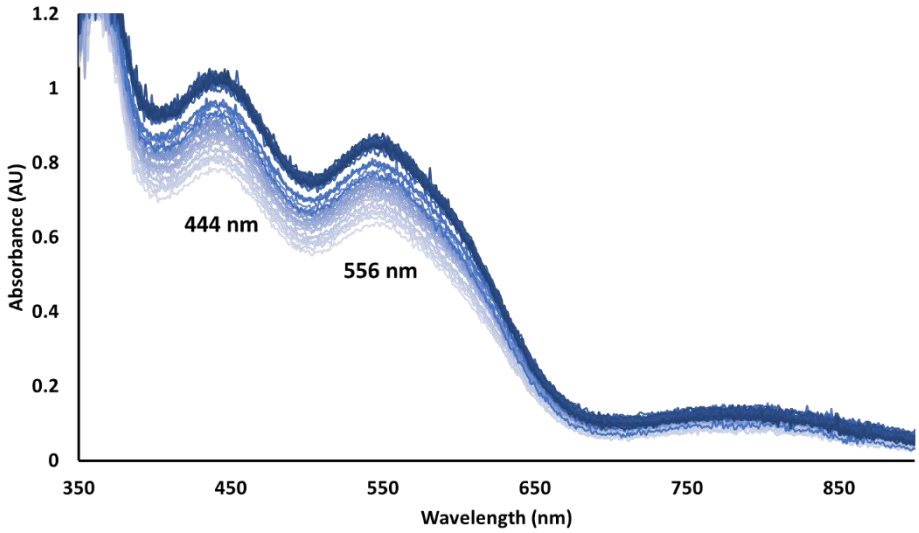

Figure 4.62 EAS monitoring of the addition of 10 equiv. PNO to **4^{ox}** (0.230 mM) in MeOH at room temperature over 4 hours.

4.7.3 Addition of Hydrogen Peroxide

As discussed in **Chapter 3**, the addition of hydrogen peroxide urea resulted in the formation of the Fe-sulfenate species. The addition of hydrogen peroxide urea to **4^{ox}** in MeOH was monitored by EAS (***Figure 4.63***). The hydrogen peroxide urea was added at -73 °C , however no change to the spectrum was observed until the solution was warmed to room temperature. The bands at λ_{max} = 444 and 556 nm only decreased in absorbance instead of shifting to the λ_{max} = 530 nm that would indicate conversion to **9** in a manner analogous to the Fe system**.**

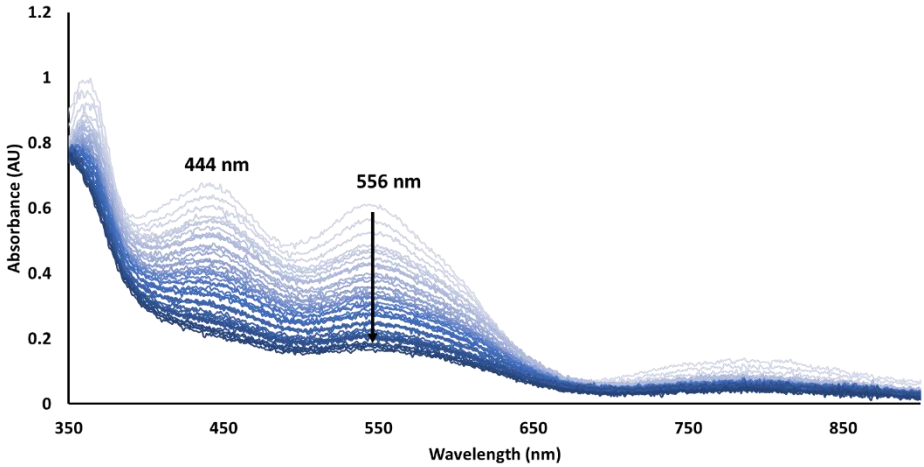

Figure 4.63 EAS monitoring of the addition of 10 equiv. H_2O_2-urea to **4^{ox}** (0.225 mM) in MeOH while warming to room temperature from -73 °C.

4.8 Conclusions

Small alterations in ligand backbone and structure changed the spin environment of the cobalt ions. The spin-state differences correlated with solvent dependent reactivity and altered the reaction paths available resulting in the formation of rare sulfur-containing products on the transition metal complexes, including persulfide and sulfenate species. The η^2-bound persulfide **5^{ox}** is only among a handful of metal-persulfide species characterized. The electronic and geometric properties created by the ligand and coordination sphere likely help to direct, the sulfur oxygenation pathways that are available to enzymatic systems. The systematic alteration of the ligand backbone allowed for the isolation and crystallographic characterization of two new sulfenate-containing cobalt complexes **9** and **10**.

4.9 Experimental Details

4.9.1 General Methods

All reactions were performed under an atmosphere of nitrogen in a glovebox or using standard Schlenk techniques unless otherwise indicated. Reagents purchased from commercial vendors were of the highest purity available and used without further purification. Pentane, toluene, diethyl ether (Et_2O), tetrahydrofuran (THF), acetonitrile (MeCN), and dichloromethane (DCM) were rigorously degassed and purified using solvent purification columns housed in a custom stainless-steel cabinet, dispensed via a stainless steel Schlenk-line (Glass Contour). Methanol (MeOH) was distilled from calcium hydride and degassed prior to use. The synthesis of 3-methyl-3-mercapto-2-butanone was carried out as previously described in the literature.[30]

^{1}H-NMR spectra were recorded on Bruker AV 300 or AV 301 FT-NMR spectrometers and are referenced to a residual protio-solvent. Chemical shifts are reported in ppm and coupling constants (J) are in Hz. Electrospray ionization mass spectrometry (ESI-MS) was performed on a Bruker Esquire LC-Ion Trap. Low-temperature electronic absorption spectra were recorded using a Varian Cary 50 spectrophotometer equipped with a fiber optic cable connected to a “dip” attenuated total reflection probe (C-technologies), with a custom-built two-necked solution sample holder equipped with a threaded glass connector (sized to fit the dip probe) and purged with argon. Cyclic voltammograms were recorded in MeCN or MeOH (100 mM $Bu_4N(PF_6)$ solutions) on a PAR 273 potentiostat utilizing a glassy carbon working electrode, platinum auxiliary electrode, and a Ag/Ag^+ (MeCN) or a Ag/AgCl (MeOH) reference electrode.

4.9.2 DFT Calculation Details

All calculations were performed using the ORCA v. 4.1.1. quantum chemistry package developed by Neese and coworkers[48] and employed a 6-31G* or def2-SVP basis sets, atom-pairwise dispersion correction of Grimme(D3BJ).[49] Single point calculation was performed using tight convergence criteria were required for self-consistent field (SCF) solutions. The Grid3 (Grid3) integration grid size, slow convergence (SlowConv), as well as B3LYP, BP86 and PBE0 functionals initiated from the crystallographic coordinates were used for geometry optimizations. Chemcraft was used to visualize TD-DFT calculated spectra, frequency spectra, and natural transition orbitals.[50]

4.9.3 Electronic Absorbance Spectroscopy

An example of a typical EAS experiment with the addition of reagent is outlined herein. A 0.450 mM solution of **4** was prepared in 4 mL of MeOH under an inert nitrogen atmosphere in a drybox. The resulting solution was transferred via gastight syringe to a custom-made two-neck vial equipped with a septum cap and threaded dip-probe feed-through adaptor that had previously been purged with argon and contained a stir bar. To this was added 1.25 equiv. of Cp_2FePF_6 (250 µL of 9.2 mM solution of Cp_2FePF_6 in MeCN), resulting in the formation of $\mathbf{4^{ox}}$.

An example of a typical EAS experiment with the addition of gas reagent is outlined herein. A 0.450 mM solution of **4** was prepared in 4 mL of MeOH under an inert nitrogen atmosphere in a drybox. The resulting solution was transferred via gastight syringe to a custom-made two-neck vial equipped with a septum cap and threaded dip-probe feed-through adaptor that had previously been purged with argon and contained a stir bar. To this was added a hollow needle

with dioxygen gently bubbling through the solution previously cooled to -73 C, resulting in the formation of **4^{ox}**.

4.9.4 Synthesis of [Co^{II}($S_2^{Me2}N_2N^{Me}$(Pr,Pr))] 4

Sodium methoxide (0.092 g, 1.7 mmol) was added to 6 mL MeOH in a 20 mL scintillation vial with a stir bar. 3-Methyl-3-mercapto-2-butanone (0.200 g, 1.69 mmol) was added to the reaction mixture and stirred at room temperature for 10 minutes. *N,N-Bis*(3-aminopropyl)methylamine (0.137 mL, 0.847 mmol) was added to the reaction mixture by syringe and stirred for 20 minutes, before the reaction mixture was cooled to -30 °C for one hour. In an additional scintillation vial cobalt(II) chloride (0.099 g, 0.76 mmol) was dissolved in 6 mL MeOH before cooling to -30 °C for one hour. The cobalt solution was added over thirty minutes while stirring at room temperature to afford a dark red solution. The reaction was stirred at room temperature for an additional five hours before being placed in the -30 °C freezer overnight. Solvent was removed by vacuum, and the solids were dissolved into 4 mL MeCN (stirred to ensure all remaining particles were free flowing) and filtered over a bed of wet (MeCN) celite. Solvent was again removed, before the solids were dissolved in THF and layered with pentane to afford purple crystals (0.100 g, 0.248 mmol, 33% yield). Electronic absorption (CH_3CN): λ_{max} (ε, M^{-1}, cm^{-1}) = 370 (4150), 534 (100) nm; (MeOH): λ_{max} (ε, M^{-1}, cm^{-1}) = 356 (3080), 577 (73) nm (THF): λ_{max} (ε, M^{-1} cm^{-1}) 375 (4920) (Figure S3) ESI-MS calc'd for [$CoC_{17}N_3S_2H_{33}$]: 402.1, found: 402.1. ^{1}H-NMR(MeCN, 301 MHz): δ 97.54, 51.05, 40.66, 34.93, 30.99, 19.66, 18.76, -1.36, -4.75, -5.53, -8.94, -11.25, -16.98, -17.21, -74.76 ppm. Evans method (MeCN): μ_{eff} = 3.15 μ_β. Anal. calc'd for [$CoC_{17}N_3S_2H_{33}$] : C, 50.73; H, 8.26; N, 10.44. found: C, 50.84; H, 8.04; N, 10.36.

4.9.5 X-ray Measurement Details of 4a

A green piece, measuring 0.27 x 0.22 x 0.18 mm^3 was mounted on a loop with oil. Data was collected at -173 ^oC on a Bruker APEX II single crystal X-ray diffractometer, Mo-radiation. Crystal-to-detector distance was 40 mm and exposure time was 10 seconds per frame for all sets. The scan width was 0.5^o. Data collection was 100% complete to 25^o in ϑ. A total of 4929 reflections were collected covering the indices, -16<=h<=16, -21<=k<=21, -14<=l<=14. 2510 reflections were symmetry independent and the R_{int} = 0.0098 indicated that the data was of excellent quality (0.07). Indexing and unit cell refinement indicated a C-centered monoclinic lattice. The space group was found to be C 2/c (No.15). The data was integrated and scaled using SAINT, SADABS within the APEX2 software package by Bruker.[51] Solution by direct methods (SHELXT[52] or SIR97[53]) produced a complete heavy atom phasing model consistent with the proposed structure. The structure was completed by difference Fourier synthesis with SHELXL.[54-55] Scattering factors are from Waasmair and Kirfel.[56] Hydrogen atoms were placed in geometrically idealized positions and constrained to ride on their parent atoms with C—H distances in the range 0.95-1.00 Angstrom. Isotropic thermal parameters U_{eq} were fixed such that they were 1.2U_{eq} of their parent atom U_{eq} for CH's and 1.5U_{eq} of their parent atom U_{eq} in case of methyl groups. All non-hydrogen atoms were refined anisotropically by full-matrix least-squares.

4.9.6 Synthesis of $Co^{II}(S_2^{Me2}N_2N^H(Et,Pr))]$•THF (5)

Sodium methoxide (0.092 g, 1.694 mmol) was dissolved in 6 mL MeOH in a 20 mL vial and stirred before 3-methyl-3-mercapto-2-butanone (0.200 g, 1.694 mmol) was added and stirred at room temperature for 10 mins. *N*-(2-Aminoethyl)-1,3-propanediamine (0.106 mL, 0.847 mmol)

was added and stirred for 20 minutes and then cooled in -30 °C freezer for one hour. In another vial, cobalt(II)chloride (0.099 g, 0.762 mmol) was dissolved in 6 mL MeOH and cooled for an hour in -30 °C freezer. The cobalt solution was added slowly to the organic solution over 25 minutes and left to stir at room temperature for 5 hours and placed in freezer overnight. The solvent was removed by vacuum and solids are redissolved in 4 mL MeCN and filtered through celite before the solvent is again removed by vacuum. The solids were then redissolved in 2 mL THF and layered with pentane to afford **5** as a dark red powder (30 mg). The solvent layering is repeated as necessary for purity. Electronic absorption (MeOH): λ_{max} (ε, M^{-1}, cm^{-1}) = 311 (2780), 365 (1470), 491 (349) nm; ESI-MS calcd for $[CoC_{15}N_3S_2H_{29}]^+$: 374.1, found: 308.0 m/z. Evans method (MeCN): μ_{eff} = 2.67 μ_β. Evans method (MeOH): μ_{eff} = 1.55 μ_β Anal. calc'd for $[CoC_{15}N_3S_2H_{29}]$: C, 48.11; H, 7.81; N, 11.22. found: C, 46.38; H, 7.80; N, 11.33.

4.9.7 X-ray Details of 5

A red needle, measuring 0.15 x 0.06 x 0.05 mm^3 was mounted on a loop with oil. Data was collected at -173 °C on a Nonius Kappa CCD FR590 single crystal X-ray diffractometer, Mo-radiation. Crystal-to-detector distance was 44.1 mm and exposure time was 40 seconds per degree for all sets. The scan width was 1°. Data collection was 100% complete to 25° in ϑ. A total of 10671 merged reflections were collected covering the indices, -16<=h<=16, -26<=k<=26, -11<=l<=11. A total of 5471 symmetry independent reflections with R_{int} = 0.0254 were collected. Indexing and unit cell refinement indicated a primitive monoclinic lattice. The space group was found to be P 2_1/c (No.14). The data was integrated and scaled using SAINT, SADABS within the

APEX2 software package by Bruker.[51] Solution by direct methods (SHELXT[52] or SIR97[53]) produced a complete heavy atom phasing model consistent with the proposed structure. The structure was completed by difference Fourier synthesis with SHELXL.[54-55] Scattering factors are from Waasmair and Kirfel.[56] Hydrogen atoms were placed in geometrically idealized positions and constrained to ride on their parent atoms with C—H distances in the range 0.95-1.00 Angstrom. Isotropic thermal parameters U_{eq} were fixed such that they were $1.2U_{eq}$ of their parent atom U_{eq} for CH's and $1.5U_{eq}$ of their parent atom U_{eq} in case of methyl groups. All non-hydrogen atoms were refined anisotropically by full-matrix least-squares.

4.9.8 Synthetic details of 8

The synthesis of **8** followed the same procedure as for **4^{ox}** described below (**Section 4.9.10**), except the reaction stirred for a limited 3 hours. A single-crystal suitable for X-ray measurements was obtained.

4.9.9 X-ray Details of $[Co^{III}(S^{Me2}N_2N^{Me}(Pr,Pr)(TK))]^+$ (**8**)

A purple prism, measuring 0.30 x 0.30 x 0.15 mm^3 was mounted on a loop with oil. Data was collected at -173 ^oC on a Bruker APEX II single crystal X-ray diffractometer, Mo-radiation. Crystal-to-detector distance was 40 mm and exposure time was 10 seconds per frame for all sets. The scan width was 0.5^o. Data collection was 100% complete to 25^o in ϑ. A total of 59457 reflections were collected covering the indices, -12<=h<=12, -28<=k<=28, -16<=l<=16. 6036 reflections were symmetry independent and the R_{int} = 0.0563 indicated that the data was of better than average quality (0.07). Indexing and unit cell refinement indicated a monoclinic lattice. The space group

was found to be P 2_1/n (No.14). The data was integrated and scaled using SAINT, SADABS within the APEX2 software package by Bruker.[51] Solution by direct methods (SHELXS,[52] SIR97[53]) produced a complete heavy atom phasing model consistent with the proposed structure. The structure was completed by difference Fourier synthesis with SHELXL97.[54-55] Scattering factors are from Waasmair and Kirfel.[56] Hydrogen atoms were placed in geometrically idealized positions and constrained to ride on their parent atoms with C—H distances in the range 0.95-1.00 Angstrom. Isotropic thermal parameters U_{eq} were fixed such that they were $1.2U_{eq}$ of their parent atom U_{eq} for CH's and $1.5U_{eq}$ of their parent atom U_{eq} in case of methyl groups. All non-hydrogen atoms were refined anisotropically by full-matrix least-squares.

4.9.10 Synthesis of $[Co^{III}(S_2^{Me2}N_2N^{Me}(Pr,Pr))]^+$ (4^{ox})

To a stirred solution of **4** (0.574 g, 1.429 mmol) in 6 mL of MeCN was added ferroceniumPF_6 (0.526 g, 1.588 mmol) stirred at room temperature for 30 min, before the solution was left in the -35 °C freezer overnight. The solvent was then removed by vacuum and the solids redissolved in 4 mL THF layered with pentane. The product was isolated as a dark purple powder (200 mg, 0.365 mmol, 26 % yield.) Electronic absorption (CH_3CN): λ_{max} (ε, M^{-1}, cm^{-1}) = 363 (5200), 442 (3110), 547 (2580), 780 (291) nm; (MeOH): λ_{max} (ε, M^{-1}, cm^{-1}) = 362 (4210), 444 (2280), 556 (1840), 790 (282) nm; (THF): λ_{max} (ε, M^{-1}, cm^{-1}) 363 (5390), 442 (3570), 550 (3010), 783 (388) nm. $E_{1/2}$ (MeCN) = -478 mV vs SCE. $E_{1/2}$ (MeOH) = -733 mV vs Fc/Fc+. ESI-MS calcd for $[CoC_{17}N_3S_2H_{33}]$: 402.1, found: 402.1. ^{1}H-NMR (MeCN-d_3, 301 MHz) δ (ppm) 96.19, 51.29, 40.64, 34.31, 31.02, 20.12, 18.95, 1.31, -1.36, -5.53, -11.11, -17.31, -73.82, -91.87. Evans method (MeCN): μ_{eff} = 3.85 μ_β,; (MeOH): μ_{eff} =

3.23 μ_β. Anal. calc'd for $[CoC_{17}N_3S_2H_{33}PF_6]$: C, 37.30; H, 6.08; N, 7.68. found: C, 37.51; H, 5.43; N, 7.68.

4.9.11 X-ray Details for $[Co^{III}(S_2^{Me2}N_2N^{Me}(Pr,Pr))]^+$ (4^{ox})

A brown prism, measuring 0.05 x 0.03 x 0.02 mm^3 was mounted on a loop with oil. Data was collected at -173 ^oC on a Bruker APEX II single crystal X-ray diffractometer, Mo-radiation. Crystal-to-detector distance was 40 mm and exposure time was 240 seconds per frame for all sets. The scan width was 1.0^o. Data collection was 99.8% complete to 25^o in ϑ. A total of 4508 reflections were collected covering the indices, -14<=h<=13, -11<=k<=11, -15<=l<=15. 2333 reflections were symmetry independent and the R_{int} = 0.1791 indicated that the data was of less than average quality (0.07). Indexing and unit cell refinement indicated a primitive monoclinic lattice. The space group was found to be P2/c (No.13). The data was integrated and scaled using SAINT, SADABS within the APEX2 software package by Bruker.[51] Solution by direct methods (SHELXT[52] or SIR97[53]) produced a complete heavy atom phasing model consistent with the proposed structure. The structure was completed by difference Fourier synthesis with SHELXL.[54-55] Scattering factors are from Waasmair and Kirfel.[56] Hydrogen atoms were placed in geometrically idealized positions and constrained to ride on their parent atoms with C—H distances in the range 0.95-1.00 Angstrom. Isotropic thermal parameters U_{eq} were fixed such that they were 1.2U_{eq} of their parent atom U_{eq} for CH's and 1.5U_{eq} of their parent atom U_{eq} in case of methyl groups. All non-hydrogen atoms were refined anisotropically by full-matrix least-squares.

4.9.12 Synthesis of $[Co^{III}(\eta^2\text{-}S^{Me2}O)(S^{Me2}N_2N^{Me}(Pr,Pr))]^+$ (9)

A small amount of **4^{ox}** (~20 mg) was dissolved in 1 mL MeOH to which 1 equivalent of PhIO dissolved in MeOH was added and allowed to react at room temperature for 5 minutes before the addition of 4 mL of THF and layering with 16 mL pentane to afford dark crystals suitable for X-ray diffraction. Electronic absorption (MeOH): λ_{max} = 530 nm. ESI-MS calcd for $[CoC_{17}N_3S_2OH_{33}]$: 418, found: 418.

4.9.13 X-Ray Details of $[Co^{III}(\eta^2\text{-}S^{Me2}O)(S^{Me2}N_2N^{Me}(Pr,Pr))]^+$ (9)

A black piece, measuring 0.20 x 0.12 x 0.08 mm^3 was mounted on a loop with oil. Data was collected at -173 ^{o}C on a Bruker APEX II single crystal X-ray diffractometer, Mo-radiation. Crystal-to-detector distance was 40 mm and exposure time was 30 seconds per frame for all sets. The scan width was 0.5^o. A total of 11251 reflections were collected covering the indices, -15<=h<=15, -12<=k<=12, -16<=l<=16. 5912 reflections were symmetry independent and the R_{int} = 0.0724 indicated that the data was of average quality (0.07). Indexing and unit cell refinement indicated a primitive monoclinic lattice. The space group was found to be P c (No. 7). The data was integrated and scaled using SAINT, SADABS within the APEX2 software package by Bruker.[51] Solution by direct methods (SHELXT[52] or SIR97[53]) produced a complete heavy atom phasing model consistent with the proposed structure. The structure was completed by difference Fourier synthesis with SHELXL.[54-55] Scattering factors are from Waasmair and Kirfel.[56] Hydrogen atoms were placed in geometrically idealized positions and constrained to ride on their parent atoms with C—H distances in the range 0.95-1.00 Angstrom. Isotropic thermal parameters U_{eq} were fixed such that they were 1.2U_{eq} of their parent atom U_{eq} for CH's and 1.5U_{eq} of their parent

atom U_{eq} in case of methyl groups. All non-hydrogen atoms were refined anisotropically by full-matrix least-squares. The compound is chemically disordered and site occupancy fitting suggests that one species (54.8(8)%) contains an oxygen with the methyl group C12 pointing away from that oxygen, and another minor component with the methyl (C12b) on the site of the cobalt that is occupied in the major species by oxygen.

4.9.14 Synthesis of $[Co^{III}((\eta^2\text{-}S^{Me2}O)(S^{O2})N_2N^{Me}(Pr,Pr))]^+$ (10)

A 4 mL 0.450 mM solution of **4^{ox}** (MeOH) was left in a 20 mL scintillation vial under atmospheric conditions for a couple of weeks. The solvent slowly evaporated to leave behind minimal orange-red crystals suitable for X-ray diffraction. Electronic absorption (MeOH): λ_{max} = 411 nm. ESI-MS calcd for $[CoC_{17}N_3S_2O_3H_{33}]$: 450, found: 418, 434, 450.

4.9.15 X-Ray Details of 10

A red piece, measuring 0.10 x 0.14 x 0.17 mm^3 was mounted on a loop with oil. Data was collected at -173 ^oC on a Bruker APEX II single crystal X-ray diffractometer, Mo-radiation. Crystal-to-detector distance was 40 mm. The scan width was 0.5^o. Data collection was 100% complete to 25^o in ϑ. A total of 11319 reflections were collected covering the indices, -14<=h<=14, -12<=k<=12, -17<=l<=17. 6011 reflections were symmetry independent and the R_{int} = 0.0319 indicated that the data was of good quality (0.07). Indexing and unit cell refinement indicated a monoclinic C lattice. The space group was found to be P c (No.7). The data was integrated and scaled using SAINT, SADABS within the APEX2 software package by Bruker.[51] Solution by direct methods (SHELXT[52] or SIR97[53]) produced a complete heavy atom phasing model consistent with

the proposed structure. The structure was completed by difference Fourier synthesis with SHELXL.[54-55] Scattering factors are from Waasmair and Kirfel.[56] Hydrogen atoms were placed in geometrically idealized positions and constrained to ride on their parent atoms with C—H distances in the range 0.95-1.00 Angstrom. Isotropic thermal parameters U_{eq} were fixed such that they were $1.2U_{eq}$ of their parent atom U_{eq} for CH's and $1.5U_{eq}$ of their parent atom U_{eq} in case of methyl groups. All non-hydrogen atoms were refined anisotropically by full-matrix least-squares. There is a small amount of disorder between N2 and N3 in the connecting propyl group.

4.10 Chapter 4 References

(1) Kobayashi, M.; Shimizu, S. Metalloenzyine Nitrile Hydratase: Structure, Regulation, and Application to Biotechnology. *Nat. Biotechnol.* **1998**, *16*, 733–736.

(2) Mitra, S.; Holz, R. C. Unraveling the Catalytic Mechanism of Nitrile Hydratases. *J. Biol. Chem.* **2007**, *282* (10), 7397–7404.

(3) Sugiura, Y.; Kuwahara, J. Nitrile Hydratase: The First Non-Heme Iron Enzyme with a Typical Low-Spin Fe(III)-Active Center. *J. Am. Chem. Soc.* **1987**, *109*, 5848–5850.

(4) Stolz, A.; Trott, S.; Binder, M.; Bauer, R.; Hirrlinger, B.; Layh, N.; Knackmuss, H.-J. Enantioselective Nitrile Hydratases and Amidases from Different Bacterial Isolates. *J. Mol. Catal. B Enzym.* **1998**, *5*, 137–141.

(5) Prasad, S.; Chand Bhalla, T. Nitrile Hydratases (NHases): At the Interface of Academia and Industry. *Biotechnol. Adv.* **2010**, *28*, 725–741.

(6) Petrillo, K. L.; Wu, S.; Hann, E. C.; Cooling, F. B.; Ben-Bassat, A.; Gavagan, J. E.; DiCosimo, R.; Payne, M. S. Over-Expression in Escherichia Coli of a Thermally Stable and Regio-Selective Nitrile Hydratase from Comamonas Testosteroni 5-MGAM-4D. *Appl. Microbiol. Biotechnol.* **2005**, *67* (5), 664–670.

(7) Kohyama, E.; Yoshimura, A.; Aoshima, D.; Yoshida, T.; Kawamoto, H.; Nagasawa, T. Convenient Treatment of Acetonitrile-Containing Wastes Using the Tandem Combination of Nitrile Hydratase and Amidase-Producing Microorganisms. *Appl. Microbiol. Biotechnol.* **2006**, *72*, 600–606.

(8) Baxter, J.; Cummings, S. P. The Current and Future Applications of Microorganism in the Bioremediation of Cyanide Contamination. *Antonie Van Leeuwenhoek* **2006**, *90*, 1–17.

(9) Brennan, B. A.; Alms, G.; Nelson, M. J.; Durney, L. T.; Scarrow, R. C. Nitrile Hydratase from Rhodococcus Rhodochrous J1 Contains a Non-Corrin Cobalt Ion with Two Sulfur Ligands. *J. Am. Chem. Soc.* **1996**, *118* (38), 9194–9195.

(10) Nagasawa, T.; Takeuchi, K.; Yamada, H. Characterization of a New Cobalt-Containing Nitrile Hydratase Purified from Urea-Induced Cells of Rhodococcus Rhodochrous J1. *Eur. J. Biochem.* **1991**, *196* (3), 581–589.

(11) Nojiri, M.; Nakayama, H.; Odaka, M.; Yohda, M.; Takio, K.; Endo, I. Cobalt-Substituted Fe-Type Nitrile Hydratase of Rhodococcus Sp. N-771. *FEBS Lett.* **2000**, *465* (2–3), 173–177.

(12) Payne, M. S.; Wu, S.; Fallon, R. D.; Tudor, G.; Stieglitz, B.; Turner, I. M.; Nelson, M. J. A Stereoselective Cobalt-Containing Nitrile Hydratase. *Biochemistry* **1997**, *36* (18), 5447–5454.

(13) Martinez, S.; Wu, R.; Sanishvili, R.; Liu, D.; Holz, R. The Active Site Sulfenic Acid Ligand in Nitrile Hydratases Can Function as a Nucleophile. *J. Am. Chem. Soc.* **2014**, *136* (4), 1186–1189.

(14) Dey, A.; Chow, M.; Taniguchi, K.; Lugo-Mas, P.; Davin, S.; Maeda, M.; Kovacs, J. A.; Odaka, M.; Hodgson, K. O.; Hedman, B.; et al. Sulfur K-Edge XAS and DFT Calculations on Nitrile Hydratase: Geometric and Electronic Structure of the Non-Heme Iron Active Site. *J. Am. Chem. Soc.* **2006**, *128*, 533–541.

(15) Song, L.; Wang, M.; Shi, J.; Xue, Z.; Wang, M.-X.; Qian, S. High Resolution X-Ray Molecular Structure of the Nitrile Hydratase from Rhodococcus Erythropolis AJ270 Reveals Posttranslational Oxidation of Two Cysteines into Sulfinic Acids and a Novel Biocatalytic Nitrile Hydration Mechanism. *Biochem. Biophys. Res. Commun.* **2007**, *362*, 319–324.

(16) Nagashima, S.; Nakasako, M.; Dohmae, N.; Tsujimura, M.; Takio, K.; Odaka, M.; Yohda, M.; Kamiya, N.; Endo, L. Novel Non-Heme Iron Center of Nirtile Hydratase with a Claw Setting of Oxygen Atoms. *Nat. Struct. Biol.* **1998**, *5* (5), 347–351.

(17) Miyanaga, A.; Fushinobu, S.; Ito, K.; Wakagi, T. Crystal Structure of Cobalt-Containing Nitrile Hydratase. *Biochem. Biophys. Res. Commun.* **2001**, *288* (5), 1169–1174.

(18) Light, K. M.; Yamanaka, Y.; Odaka, M.; Solomon, E. I. Spectroscopic and Computational Studies of Nitrile Hydratase: Insights into Geometric and Electronic Structure and the Mechanism of Amide Synthesis. *Chem. Sci.* **2015**, *6*, 6280–6294.

(19) Kovacs, J. A. Synthetic Analogues of Cysteinate-Ligated Non-Heme Iron and Non-Corrinoid Cobalt Enzymes. *Chem. Rev.* **2004**, *104* (2), 825–848.

(20) Swartz, R. D.; Coggins, M. K.; Kaminsky, W.; Kovacs, J. A. Nitrile Hydration by Thiolate- and Alkoxide-Ligated Co-NHase Analogues. Isolation of Co(III)-Amidate and Co(III)-Iminol Intermediates. *J. Am. Chem. Soc.* **2011**, *133* (11), 3954–3963.

(21) Yamanaka, Y.; Kato, Y.; Hashimoto, K.; Iida, K.; Nagasawa, K.; Nakayama, H.; Dohmae, N.; Noguchi, K.; Noguchi, T.; Yohda, M.; et al. Time-Resolved Crystallography of the Reaction Intermediate of Nitrile Hydratase: Revealing a Role for the Cysteinesulfenic Acid Ligand as

a Catalytic Nucleophile. *Angew. Chemie Int. Ed.* **2015**, *54* (37), 10763–10767.

(22) Martinez, S.; Wu, R.; Sanishvili, R.; Liu, D.; Holz, R. The Active Site Sulfenic Acid Ligand in Nitrile Hydratases Can Function as a Nucleophile. *J. Am. Chem. Soc.* **2014**, *136* (4), 1186–1189.

(23) Tsujimura, M.; Odaka, M.; Nakayama, H.; Dohmae, N.; Koshino, H.; Asami, T.; Hoshino, M.; Takio, K.; Yoshida, S.; Maeda, M.; et al. A Novel Inhibitor for Fe-Type Nitrile Hydratase: 2-Cyano-2-Propyl Hydroperoxide. *J. Am. Chem. Soc.* **2003**, *125*, 11532–11538.

(24) Kung, I.; Schweitzer, D.; Shearer, J.; Taylor, W. D.; Jackson, H. L.; Lovell, S.; Kovacs, J. A. How Do Oxidized Thiolate Ligands Affect the Electronic and Reactivity Properties of a Nitrile Hydratase Model Compound? *J. Am. Chem. Soc.* **2000**, *122*, 8299–8300.

(25) Yano, T.; Wasada-Tsutsui, Y.; Ikeda, T.; Shibayama, T.; Kajita, Y.; Inomata, T.; Funahashi, Y.; Ozawa, T.; Masuda, H. Co(III) Complexes with N 2 S 3 -Type Ligands as Structural/Functional Models for the Isocyanide Hydrolysis Reaction Catalyzed by Nitrile Hydratase. *Inorg. Chem.* **2018**, *57* (8), 4277–4290.

(26) Heinrich, L. .; Mary-Verla, A. .; Li, Y. .; Vaissermann, J. .; Chottard, J.-C. Cobalt(III) Complexes with Carboxamido-N and Sulfenato-S or Sulfinato-S Ligands Suggest That a Coordinated Sulfenate-S Is Essential for the Catalytic Activity of Nitrile Hydratases. *Eur. J. Inorg. Chem.* **2001**, *2001* (9), 2203–2206.

(27) Lydon, J. D.; Deutsch, E. Chemistry and Reactivity of S-Bonded Sulfenato-Cobalt(III) Complexes. *Inorg. Chem* **1982**, *21*, 3180–3185.

(28) Adzamli, I. K.; Libson, K.; Lydon, J. D.; Elder, R. C.; Deutsch, E. Synthesis, Characterization, and Reactivity of Coordinated Sulfenic Acids. *Inorg. Chem.* **1979**, *18* (2), 303–311.

(29) Murakami, T.; Nojiri, M.; Nakayama, H.; Odaka, M.; Yohda, M.; Dohmae, N.; Takio, K.; Nagamune, T.; Endo, I. Post-Translational Modification Is Essential for Catalytic Activity of Nitrile Hydratase. *Protein Sci.* **2000**, *9*, 1024–1030.

(30) Ellison, J. J.; Nienstedt, A.; Shoner, S. C.; Barnhart, D.; Cowen, J. A.; Kovacs, J. A. Reactivity of Five-Coordinate Models for the Thiolate-Ligated Fe Site of Nitrile Hydratase. *J. Am. Chem. Soc.* **1998**, *120* (23), 5691–5700.

(31) Shoner, S. C.; Nienstedt, A. M.; Ellison, J. J.; Kung, I. Y.; Barnhart, D.; Kovacs, J. A. Structural Comparison of Five-Coordinate Thiolate-Ligated MII = FeII, CoII, NiII, ZnII Ions Wrapped in a Chiral Helical Ligand. *Inorg. Chem.* **1998**, *9* (17), 5721–5726.

(32) Addison, A. W.; Nageswara Rao, T.; Reedijk, J.; van Rijn, J.; Verschoor, G. C. Synthesis, Structure, and Spectroscopic Properties of Copper(II) Compounds Containing Nitrogen-Sulphur Donor Ligands ; the Crystal and Molecular Structure of Aqua[l,7-Bis(N-Methylbenzimidazol-2'-Yl)- 2,6-Dithiaheptane]Copper(Ii) Perchlorate the Crystal A. *J. Chem. Soc. Dalt. Trans.* **1984**, No. 7, 1349–1356.

(33) Evans, D. F. The Determination of the Paramagnetic Susceptibility of Substances in Solution by Nuclear Magnetic Resonance. *J. Chem. Soc.* **1959**, No. 0, 2003–2005.

(34) Live, D. H.; Chan, S. I.; Amos, A. Bulk Susceptibility Corrections in Nuclear Magnetic Resonance Experiments Using Superconducting Solenoids. *Anal. Chem.* **1970**, *42* (7), 791–

792.

(35) Ghosh, B.; Banerjee, A.; Paul, A. Understanding the Role of Solvents and Spin–Orbit Coupling in an Oxygen-Assisted SN2-Type Oxidative Transmetalation Reaction. *Chem. - A Eur. J.* **2019**, *25* (72), 16606–16616.

(36) Shoner, S. C.; Nienstedt, A. M.; Ellison, J. J.; Kung, I. Y.; Barnhart, D.; Kovacs, J. A. Articles Structural Comparison of Five-Coordinate Thiolate-Ligated M II) Fe II , Co II , Ni II , and Zn II Ions Wrapped in a Chiral Helical Ligand. **1998**.

(37) Kennepohl, P.; Neese, F.; Schweitzer, D.; Jackson, H. L.; Kovacs, J. A.; Solomon, E. I. Spectroscopy of Non-Heme Iron Thiolate Complexes: Insight into the Electronic Structure of the Low-Spin Active Site of Nitrile Hydratase. *Inorg. Chem.* **2005**, *44*, 1826–1836.

(38) Shearer, J.; Jackson, H. L.; Schweitzer, D.; Rittenberg, D. K.; Leavy, T. M.; Kaminsky, W.; Scarrow, R. C.; Kovacs, J. A. The First Example of a Nitrile Hydratase Model Complex That Reversibly Binds Nitriles. *J. Am. Chem. Soc.* **2002**, *124* (38), 11417–11428.

(39) Shearer, J.; Kung, I. Y.; Lovell, S.; Kaminsky, W.; Kovacs, J. A. Why Is There an " Inert " Metal Center in the Active Site of Nitrile Hydratase? Reactivity and Ligand Dissociation from a Five-Coordinate Co(III) Nitrile Hydratase Model. *J. Am. Chem. Soc.* **2001**, *16* (35), 733–736.

(40) Shearer, J.; Kung, I. Y.; Lovell, S.; Kovacs, J. A. A Co(III) Complex in a Mixed Sulfur/Nitrogen Ligand Environment: Modeling the Substrate-and Product-Bound Forms of the Metalloenzyme Thiocyanate Hydrolase HHS Public Access. *Inorg Chem* **2000**, *39* (22),

4998–4999.

(41) Lugo-Mas, P.; Dey, A.; Xu, L.; Davin, S. D.; Benedict, J.; Kaminsky, W.; Hodgson, K. O.; Hedman, B.; Solomon, E. I.; Kovacs, J. A. How Does Single Oxygen Atom Addition Affect the Properties of an Fe-Nitrile Hydratase Analogue? The Compensatory Role of the Unmodified Thiolate. *J. Am. Chem. Soc.* **2006**, *128* (34), 11211–11221.

(42) Schweitzer, D.; Shearer, J.; Rittenberg, D. K.; Shoner, S. C.; Ellison, J. J.; Loloee, R.; Lovell, S.; Barnhart, D.; Kovacs, J. A. Enhancing Reactivity via Structural Distortion. *Inorg. Chem.* **2002**, *41* (12), 3128–3136.

(43) Luo, Y.-R. *Comprehensive Handbook of Chemical Bond Energies*.

(44) Song, L.; Hu, Q.; Qin, X. Synthesis of ("S_R1CsH4)(CO)2Mo(,,2_S2R). **1999**, *2*, 84–85.

(45) Evans, S. V.; Legzdins, P.; Rettig, S. J.; Sanchez, L.; Trotter, J. Crystal Structures of Organotungsten Complexes Formed by Sequential Insertion of Elemental Sulfur into Tungsten—Carbon Bonds. *Organometallics* **1987**, *6* (1), 7–9.

(46) Ogutu, I. R. A. M.; Holz, R. C.; Bennett, B. Insight into the Maturation Process of the Nitrile Hydratase Active Site. *Inorg. Chem.* **2021**, *60* (8), 5432–5435.

(47) Villar-Acevedo, G.; Lugo-Mas, P.; Blakely, M. N.; Rees, J. A.; Ganas, A. S.; Hanada, E. M.; Kaminsky, W.; Kovacs, J. A. Metal-Assisted Oxo Atom Addition to an Fe(III) Thiolate. *J. Am. Chem. Soc.* **2017**, *139*, 119–129.

(48) Neese, F. The ORCA Program System. *Wiley Interdiscip. Rev. Comput. Mol. Sci.* **2012**, *2* (1), 73–78.

(49) Grimme, S.; Ehrlich, S.; Goerigk, L. Effect of the Damping Function in Dispersion Corrected Density Functional Theory. *J. Comput. Chem.* **2011**, *32* (7), 1456–1465.

(50) Chemcraft - Graphical Program for Visualization of Quantum Chemistry Computations. Ivanovo, Russia 2005.

(51) Bruker (2007) APEX2 (Version 2.1-4), SAINT (version 7.34A), SADABS (version 2007/4), BrukerAXS Inc, Madison, Wisconsin, USA.

(52) Sheldrick GM. (2015) SHELXT - Integrated space-group and crystal-structure determination. Acta Cryst. A71, 3-8.

(53) (a) Altomare, A.; Burla, C.; Camalli, M.; Cascarano, G. L.; Giacovazzo, C.; Guagliardi, A.; Moliterni, AGG.; Polidori, G.; Spagna, R. SIR97: a new tool for crystal structure determination and refinement. *J. Appl. Crystallog*. **1999,** *32*, 115-119.

(b) Altomare, A.; Cascarano, G. L.; Giacovazzo, C.; Guagliardi, A. Completion and refinement of crystal structures with SIR 92. *J. Appl. Crystallog*. **1993,** *26*, 343-350.

(54) (a) Sheldrick, G. M. (1997) SHELXL-97, Program for the Refinement of Crystal Structures. University of Göttingen, Germany.

(b) Sheldrick, G. M. (2013) Crystal structure refinement with SHELXL. Acta Cryst. (2015). C71, 3-8.

(55) Mackay, S.; Edwards, C.; Henderson, A.; Gilmore, C.; Stewart, N.; Shankland, K.; Donald, A. *MaXus: a computer program for the solution and refinement of crystal structures from diffraction data*. **[1997].** University of Glasgow, Scotland.

(56) Waasmaier, D.; Kirfel, A. New Analytical Scattering Factor Functions for Free Atoms and Ions. *Acta Crystallographica* A. **1995,** *51*, 416-430

Chapter 5: Influence of Thiolate versus Alkoxide Ligands on the Stability of Crystallographically Characterized Mn^{III}-Alkylperoxo Complexes

Portions of this chapter have been republished or adapted with permission of the Journal of the American Chemical Society from "*Influence of Thiolate versus Alkoxide Ligands on the Stability of Crystallographically Characterized Mn(III)-Alkylperoxo Complexes",* Downing, Alexandra N.; Coggins, Michael K.; Poon, Penny Chaau Yan; Kovacs, Julie A. *J. Am. Chem. Soc.* **2021,** *143*, 16, 6104-6113.; Copyright 2021 American Chemical Society.

As well as from, "*Comparison of two $Mn^{IV}Mn^{IV}$-bis-μ-oxo complexes $\{[Mn^{IV}(N_4(6\text{-Me-DPEN}))]_2(\mu\text{-}O)_2\}^{2+}$ and $\{[Mn^{IV}(N_4(6\text{-Me-DPPN}))]_2(\mu\text{-}O)_2\}^{2+}$"*, Coggins, Michael K.; Downing, Alexandra N.; Kaminsky, Werner; Kovacs, Julie A. *Acta Cryst.* **2020**, *E76*, 1042-1046.

5.1 Introduction

As discussed in **Chapter 1**, Nature utilizes manganese ions to promote a wide variety of oxidative transformations, many of which involve metastable Mn-peroxo species as key intermediates.[1–18] The majority of which have yet to be spectroscopically characterized. The catalyst involved in these enzymatic reactions contain oxygen/nitrogen ligands in the manganese ion's primary coordination sphere. Why cysteinates are not incorporated in these manganese enzyme active sites has yet to be investigated. The inherent instability of metastable transition-metal peroxo intermediates precludes their structural characterization in most cases, and despite their significant role, very few well-characterized Mn-peroxo compounds have been reported,[8,19–30] and how the primary coordination affects reactivity properties has yet to be investigated. Previously, the Kovacs group reported the first crystallographically characterized examples of Mn^{III}-alkylperoxo compounds, Mn^{III}-OOR (R = ^{t}Bu, Cm),[19,23] and showed that there

are distinct correlations between their geometric and electronic structures and the kinetic barrier to peroxo O—O bond cleavage.[19]

Ligand substituents and the carbon backbone were varied, while maintaining a constant N_4S^- inner coordination sphere (***Figure 5.1***). The alkoxide derivative, $[Mn^{III}(O^{Me2}N_4$(6-Me-DPEN)$(OO^tBu))]^+$ (**1**) of a previously reported alkylperoxo compound, $[Mn^{III}(S^{Me2}N_4$(6-Me-DPEN)$(OO^tBu))]^+$ (**2**),[19] was also crystallographically characterized (***Figure 5.2***). Replacement of the monoanionic thiolate with a monoanionic alkoxide (RS^- → RO^-) allows for a meaningful comparison of their structures and reactivity.

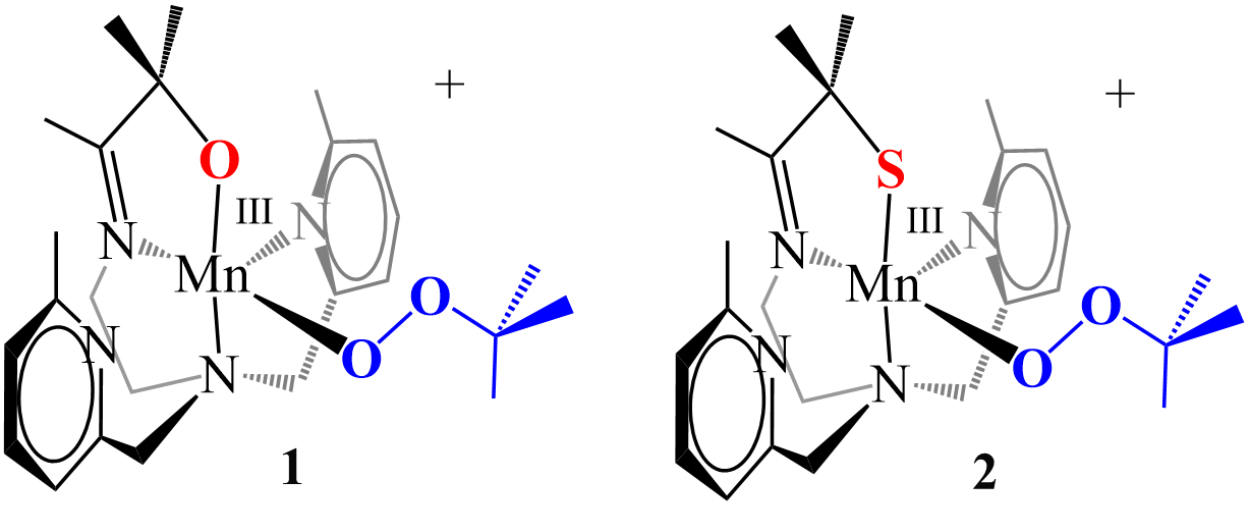

Figure 5.1 ChemDraw representations of $[Mn^{III}(O^{Me2}N_4$(6-Me-DPEN))$(OO^tBu)]^+$ (**1**) and $[Mn^{III}(O^{Me2}N_4$(6-Me-DPEN))$(OO^tBu)]^+$ (**2**).

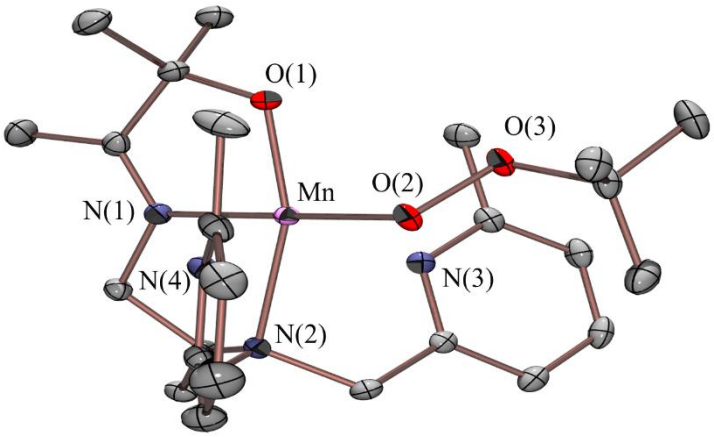

Figure 5.2 ORTEP diagram of $[Mn^{III}(O^{Me2}N_4(6\text{-Me-DPEN}))(OO^tBu)](BPh_4)\bullet Et_2O$ (**1**). Hydrogen atoms, counterion, and solvent of crystallization have been omitted for clarity.[31]

5.2 Previous Characterization and Reactivity for Complexes 1 and 2

5.2.1. Synthesis and Structure of Mn^{II} Alkoxide Starting Complexes

In order to determine how the primary coordination sphere influences the electronic, redox, and reactivity properties of previously reported $[Mn^{II}(S^{Me2}N_4(6\text{-Me-DPEN}))]^+$ (**3**) and $Mn^{II}(S^{Me2}N_4(6\text{-MeDPPN}))]^+$ (**4**, ***Figure 5.2***)[32], the alkoxide derivatives of these complexes were synthesized and characterized. Thiolate-ligated **3** and **4** are precursors to rare examples of structurally characterized alkylperoxo complexes $[Mn^{III}(S^{Me2}N_4(6\text{-Me-DPEN})(OO^tBu))^+$ (**2**, ***Figure 5.1***) and $[Mn^{III}(S^{Me2}N_4(6\text{-Me-DPPN})(OO^tBu))^+$ (**5**).[19] The corresponding alkoxide or alcohol-ligated derivatives **6-8** (***Figure 5.3***) were synthesized using a strategy identical to that used to prepare **3** and **4**,[32] except that 3-hydroxy-3-methyl-2-butanone was used in place of 3-mercapto-3-methyl-2-butanone, and in the case of **8** (***Figure 5.3***), manganese(II) bis-formate, $Mn^{II}(OC(H)O)_2$, was used in place of $[Mn^{II}(H_2O)_6](SO_4)$. The yield of MeCN-ligated **7** (***Figure 5.3***) was low (7%), making it inconvenient to interrogate its spectroscopic properties or explore its reactivity. Thus, the

remainder of the discussion, with the exception of crystallographic characterization, will focus on complexes **6** and **8** (***Figures 5.3***-**5.4**).

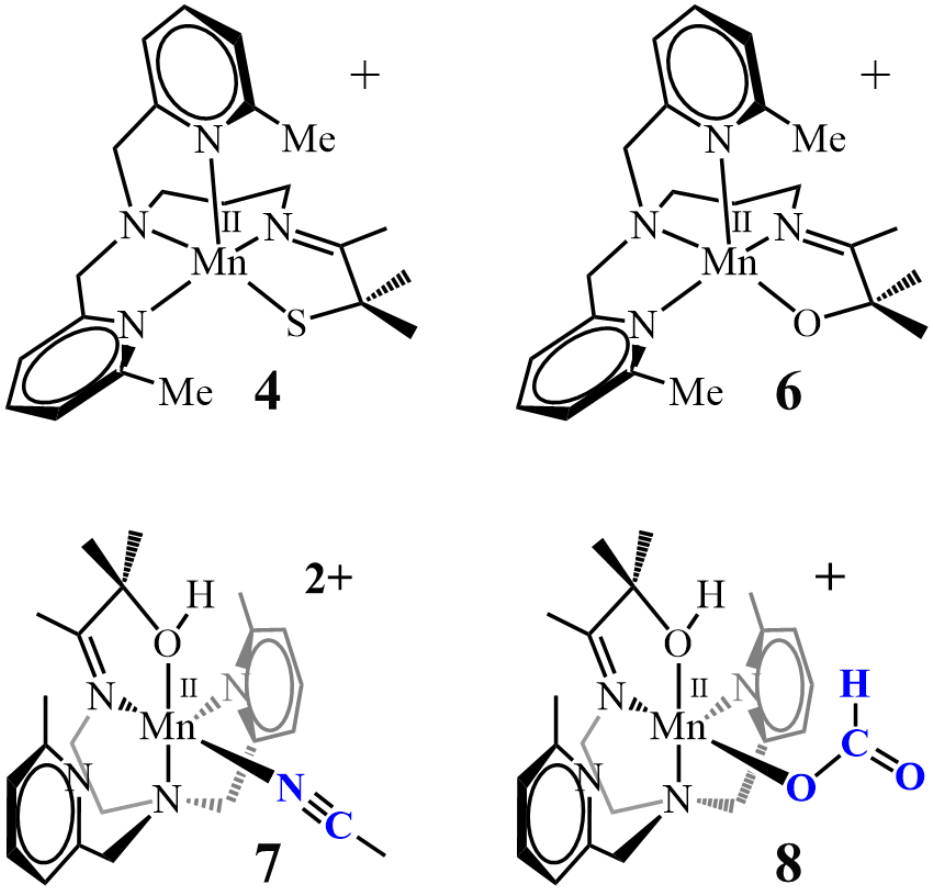

Figure 5.3 ChemDraw representations of $[Mn^{II}(S^{Me2}N_4(6\text{-Me-DPPN}))]^+$ (**4**), $[Mn^{II}(O^{Me2}N_4(6\text{-Me-DPPN}))]^+$ (**6**), $[Mn^{II}(HO^{Me2}N_4(6\text{-Me-DPEN})(MeCN))]^{2+}$ (**7**), and $[Mn^{II}(HO^{Me2}N_4(6\text{-Me-DPEN})(CHO_2))]^+$ (**8**).

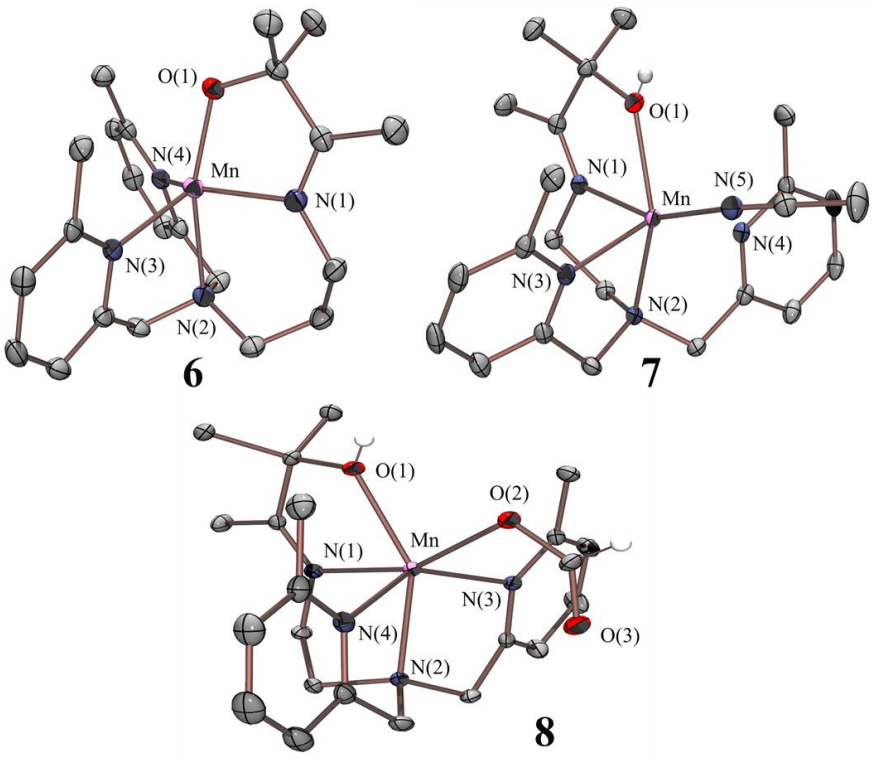

Figure 5.4 ORTEP diagram of $[Mn^{II}(O^{Me2}N_4(6\text{-Me-DPPN}))]^{+}$ (**6**)[33], $[Mn^{II}(HO^{Me2}N_4(6\text{-Me-DPEN})(MeCN))]^{2+}$ (**7**)[33], and $[Mn^{II}(HO^{Me2}N_4(6\text{-Me-DPEN})(CHO_2))]^{+}$ (**8**), 50% probability ellipsoids, with hydrogen atoms, with the exception of alcohol protons, counterions, and solvents of crystallization omitted for clarity.

Single crystals of **6-8** suitable were grown by layering Et_2O onto a concentrated MeCN solution of the corresponding Mn^{II} complex. As shown in the ORTEP diagrams of ***Figure 5.4***, $[Mn^{II}(O^{Me2}N_4(6\text{-Me-DPPN}))](BPh_4)$ (**6**) was five-coordinate and contained an alkoxide in place of the thiolate of **4**. The carbon backbone and ligand scaffold were identical. Selected metrical parameters and crystal data for **6-8** are compiled in ***Table 5.1***. Complexes **7** and **8** were shown to reproducibly contain a proton on the alkoxide oxygen (***Figure 5.4***). Evidence to support this is based on their relative Mn-O bond distances, the number of associated counterions, and observed H-bonding network. The presence of the alcohol was also supported by comparison of DFT calculations on the Mn^{II} complex. By replacing the BPh_4^{-} with a PF_6^{-} counterion, a higher

resolution structure of **8** (R = 2.0% for **8-PF_6** versus R = 6.8% for **8-BPh_4**) was obtained and was also shown to contain a proton on the alkoxide oxygen, O(1). The Mn—O(1) bonds of five-coordinate alkoxide-ligated **6** were 0.24 Å, and 0.21 Å shorter than the corresponding distance in six-coordinate alcohol-ligated **7** and **8**, respectively (***Table 5.1***, ***Figure 5.4***), where each contained a protonated alkoxide. The hydrogen bonded network shown in the packing diagram of **8** (***Figure 5.5***) provided additional evidence to indicate that a proton resides on O(1). Bond distances for all three structures (***Table 5.1***) were more consistent with Mn^{II} than Mn^{III}, ruling this out as an explanation for the extra counterion of **7** and **8**. The Mn^{II} ions of **7** and **8** are each six-coordinate, with either MeCN (**7**) or formate (**8**) coordinated *trans* to the imine nitrogen. Alkoxide-ligated **6** and thiolate-ligated **4** are both mononuclear, monocationic five-coordinate Mn^{II} complexes and constructed from an identical ligand scaffold, therefore a comparison of their metrical parameters (***Table 5.1***) should provide the best insight into the structural influence of the thiolate versus alkoxide. Three of the four Mn—N bond lengths (Mn—N(1), Mn—N(2), and Mn—N(3)) in alkoxide-ligated **6** were noticeably longer than the corresponding distances in thiolate-ligated **4** (***Table 5.1***). This in part reflected the more distorted square pyramidal geometry (τ = 0.47) of alkoxide-ligated **6** relative to thiolate-ligated **4** (τ = 0.22), a geometry which provides optimum orbital overlap is favored by the highly covalent M—SR bonds.[34,35]

Table 5.1 Selected bond distances (Å) and angles (deg) for thiolate-ligated [$Mn^{II}(S^{Me2}N_4$(6-Me-DPPN))](BPh_4) (**3**)[32], alkoxide-ligated [$Mn^{II}(O^{Me2}N_4$(6-Me-DPPN))](BPh_4) (**6**)[33], alkoxide-ligated [$Mn^{II}(HO^{Me2}N_4$(6-Me-DPEN)(MeCN))](BPh_4)$_2$ (**7**)[33], [$Mn^{II}(HO^{Me2}N_4$(6-Me-DPEN)(CHO_2))](BPh_4)•MeCN•Et_2O (**8-BPh_4**)[33], and [$Mn^{II}(HO^{Me2}N_4$(6-Me-DPEN)(CHO_2))](PF_6)•MeCN (**8-PF_6**).

	4	**6**	**7**	**8-BPh_4**	**8-PF_6**
Mn-X	2.3742(3)[b]	1.9585(14)[a]	2.203(10)[c]	2.172(4)[c]	2.233(1)[c]
Mn-N(1)	2.1909(10)	2.2184(19)	2.2027(9)	2.248(3)	2.246(1)
Mn-N(2)	2.2476(10)	2.2962(17)	2.2798(9)	2.329(3)	2.308(2)
Mn-N(3)	2.1830(10)	2.2293(18)	2.3157(10)	2.267(3)	2.306(2)
Mn-N(4)	2.2787(10)	2.1931(18)	2.2784(10)	2.275(3)	2.291(2)
Mn-N(5)	N/A	N/A	2.2254(10)	N/A	N/A
Mn-O(2)	N/A	N/A	N/A	2.118(3)	2.120(1)
X-Mn-N(1)	82.03(3)	77.95(6)	69.95(3)	69.68(9)	68.65(5)
X-Mn-N(2)	154.06(3)	162.39(7)	147.53(3)	144.13(9)	144.03(9)
X-Mn-N(3)	127.47(3)	118.62(6)	105.39(3)	109.39(9)	106.10(5)
X-Mn-N(4)	93.97(3)	105.96(6)	108.30(4)	113.6(1)	110.51(5)
X-Mn-O(2)	N/A	N/A	N/A	84.0(1)	87.12(5)
N(1)-Mn-N(3)	114.15(4)	112.41(7)	102.24(3)	100.8(1)	86.63(5)
N(1)-Mn-N(4)	140.58(4)	133.98(7)	86.94(3)	99.0(1)	106.37(5)
N(3)-Mn-N(4)	99.40(4)	105.51(6)	146.22(3)	136.6(1)	143.38(5)
O(2)-Mn-N(1)	N/A	N/A	N/A	158.6(1)	154.53(5)
O(2)-Mn-N(2)	N/A	N/A	N/A	126.6(1)	128.85(5)
O(2)-Mn-N(3)	N/A	N/A	N/A	89.22(11)	92.98(5)
O(2)-Mn-N(4)	N/A	N/A	N/A	85.98(11)	88.98(5)
τ	0.22	0.47	N/A	N/A	N/A

Note: [a]X = O, [b]X = S, [c]X = OH.

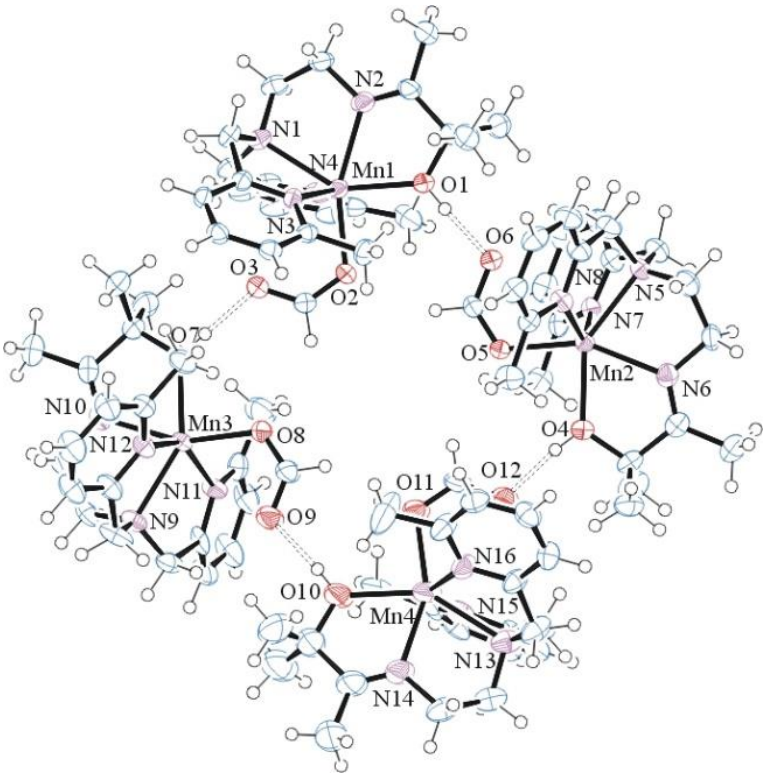

Figure 5.5 Packing diagram of **8**, which shows a hydrogen bonded tetramer involving the coordinated alcohol proton and the distal formate oxygen.

5.2.2 X-ray Structure of Alkoxide-Ligated Alkylperoxo 1

Dark blue single crystals of $[Mn^{III}(O^{Me2}N_4(6\text{-Me-DPEN}))(OO^tBu)](BPh_4)$ (**1**) were previously obtained[33] and the ORTEP diagram is shown in ***Figure 5.2***. Selected metrical parameters for alkoxide-ligated **1** are compared with those of thiolate-ligated $[Mn^{III}(S^{Me2}N_4(6\text{-Me-DPEN}))(OO^tBu)]^+$ (**2**) in ***Table 5.2.*** As shown in ***Figure 5.2***, ^{t}BuOO$^-$ was bound *cis* to the alkoxide oxygen, and *trans* to the imine nitrogen and was coordinated in an end-on η^1-OOR fashion. A similar *cis*-orientation of the alkylperoxo was seen with thiolate-ligated **2**, as well as all of our previously reported thiolate-ligated RS-Mn-OOR complexes.[19,36] The separation between the Mn^{III} ion and the distal oxygen, O(2), in **1** (2.743 Å) was significantly longer than the sum of the covalent radii (2.01 Å),[37] and approximately the same (***Figure 5.2***) as that of **2**,[19] ruling out a side-

on η^2-OO(R) binding mode. The peroxo O—O bond of **1** was significantly longer than reported side-on η^2-coordinated Mn^{III}-peroxo compounds (O—O bond range = 1.403(4)-1.428(7) Å).[19,36,38–41] The presence of a single BPh_4^- counterion (per Mn) confirmed that the manganese ion is in the Mn^{III} oxidation state. The distance between the Mn ion of **1**, and each of the pyridine nitrogens, N(3) and N(4) (***Table 5.2***), was significantly longer than the sum of the covalent radii (2.10 Å). The expansion was also the case with thiolate-ligated **2** (***Table 5.2***), as well as the other three crystallographically characterized thiolate-ligated Mn^{III}-OOR complexes reported by our group.[19,36] The average Mn•••N^{Ar} distance (2.39(4) Å) in **1** was within error of that (2.41(6) Å) of **2**. The peroxo O—O and Mn—O bond lengths in **1** (1.473(1) Å and 1.856(1) Å, respectively) were also within error of the corresponding bond lengths in **2** (1.468(7) Å and 1.853(6) Å, respectively).

Table 5.2 Comparison of Selected Bond Distances (Å) and Angles (deg) for Alkoxide-Ligated ^{t}Butyl Peroxo Compound $[Mn^{III}(O^{Me2}N_4(6\text{-Me-DPEN}))(OO^tBu)]^+$ (**1**)[33] and Thiolate-Ligated ^{t}Butyl Peroxo Compound $[Mn^{III}(S^{Me2}N_4(6\text{-Me-DPEN}))(OO^tBu)]^+$ (**2**).[19]

	1	**2**
Mn—X	1.8535(9)[b])	2.241(3)[a]
Mn—N(1)	2.004(1)	2.015(8)
Mn—N(2)	2.161(1)	2.163(7)
Mn—N(3)	2.355(1)	2.354(8)
Mn—N(4)	2.431(1)	2.471(7)
Mn—O^{peroxo}	1.856(1)	1.853(6)
O—O^{peroxo}	1.473(1)	1.468(7)
Mn•••O^{peroxo}	2.743	2.769
Mn—O(2)—O(3)	110.41(7)	112.4(4)
O(2)—Mn—X	98.26(4)[b]	94.9(2)[a]
O(2)—Mn—N(1)	176.10(5)	175.7(3)
X—Mn—N(2)	159.67(4)[b]	162.6(2)[a]
X—Mn—N(3)	113.08(4)[b]	112.4(2)[a]
X—Mn—N(4)	107.98(4)[b]	109.13(18)[a]
N(3)—Mn—N(4)	134.84(4)	133.3(3)

Note: [a]X = S(1), [b]X = O(1)

5.2.3 Electronic Absorbance Spectroscopy Characterization of 1

The addition of *tert*-butyl hydroperoxide (^{t}BuOOH) to **6** and **8** in the presence of Et_3N caused a color change from colorless to blue accompanied by the growth of an intense absorption band at λ_{max} = 650 nm (ε = 1010 $M^{-1}cm^{-1}$) (**Figures 5.6** and **5.7**). The band was noticeably red-shifted relative to thiolate-ligated Mn^{III}-OOR (**2**, λ_{max} = 603(600) nm).[19] The band was also lower in energy than all of our other thiolate-ligated Mn^{III}-OO^{t}Bu compounds (λ_{max} = 585-600 nm, ***Table 5.3***),[19,36] but closer in energy to that of carboxamide-ligated $[Mn^{III}(dpaq^{2Me})(OO^tBu)]^+$ (**9**, λ_{max} = 690(115) nm).[30] The latter contains Mn^{III} in an N_5^- coordination sphere.[30] The intensity of the 650 nm band associated with metastable, alkoxide-ligated **1** maximizes once 1.6 equivalents of ^{t}BuOOH had been added Mn^{II}-**8** (***Figure 5.6***), a stoichiometry that was consistent with a mechanism involving the initial oxidation of Mn^{II}, to afford an unobserved Mn^{III} intermediate, possibly a Mn^{III}-OH (**Eq. 5.1**),[30,42] followed by proton-induced release of H_2O (**Eq. 5.2**), or ROH (**Eq. 5.3**) and binding of ^{t}BuOO$^-$ Support for this mechanism was provided previously via a titration between $[Mn^{II}(dpaq^{2Me})]^+$ and 0-1.0 equiv. of ^{t}BuOOH to initially afford $[Mn^{III}(dpaq^{2Me})(OH)]^+$, followed by the addition of 50 equiv. of ^{t}BuOOH to afford $[Mn^{III}(dpaq^{2Me})(OO^tBu)]^+$ (**9**).[30]

In contrast to the reaction observed with **8**, no intermediates were observed in the reaction between ^{t}BuOOH and five-coordinate **6**. Instead, direct conversion to a stable, crystallographically characterized bis-oxo $Mn^{IV}Mn^{IV}$ dimer, $\{[Mn^{IV}(N_4(6\text{-Me-DPPN}))]_2(\mu\text{-}O)_2\}^{2+}$, was observed (***Figure 5.8*****,** right),[43] implying that the rate-determining step involves ^{t}BuOOH binding with **6**. The final product in the reaction between **8** and ^{t}BuOOH was also a bis-oxo $\{[Mn^{IV}(N_4(6\text{-Me-DPEN}))]_2(\mu\text{-}O)_2\}^{2+}$ (***Figure 5.8***, left). Although the rate at which metastable **1**

forms (***Figure 5.9***) was slow (k_{obs}^{298K} = 4.4 x 10^{-4} s^{-1}, ***Figure 5.10***), it decayed four times more slowly (*vide infra*) under the same conditions, thereby facilitating its observation. The slow rate at which **1** formed likely reflects the fact that formic acid must dissociate in order for the reaction to occur.

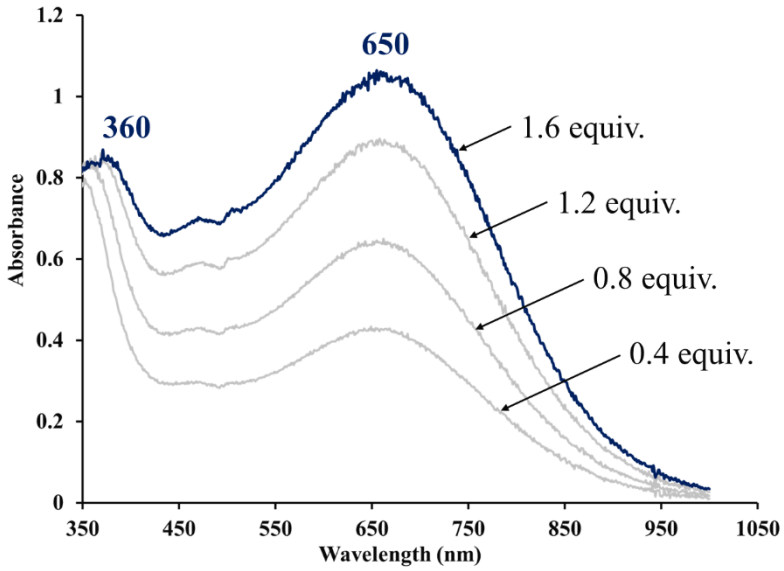

Figure 5.6 EAS spectrum of monitoring the titration of 1.6 equiv. ^{t}BuOOH to Mn^{II} **8** in DCM at -40 °C.[33]

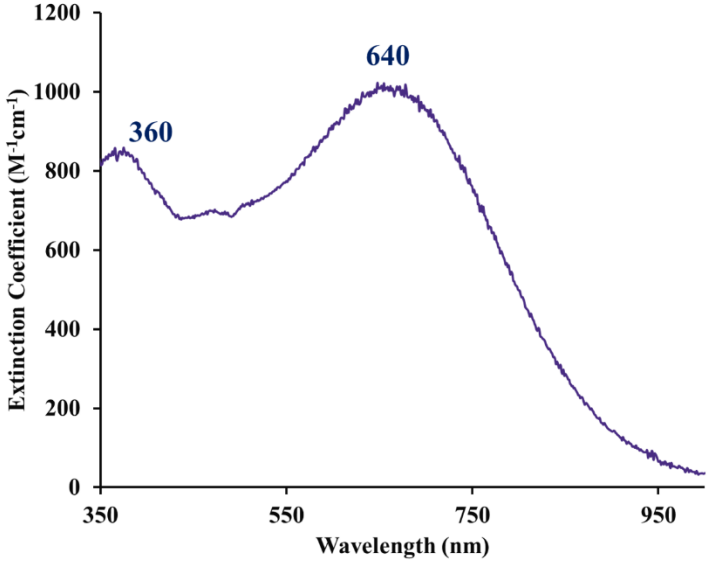

Figure 5.7 Quantitative electronic absorption spectrum of $[Mn^{III}(O^{Me2}N_4(6\text{-Me-DPEN}))(OO^{t}Bu)]]^{+}$ (**1**) in DCM at ambient temperature.

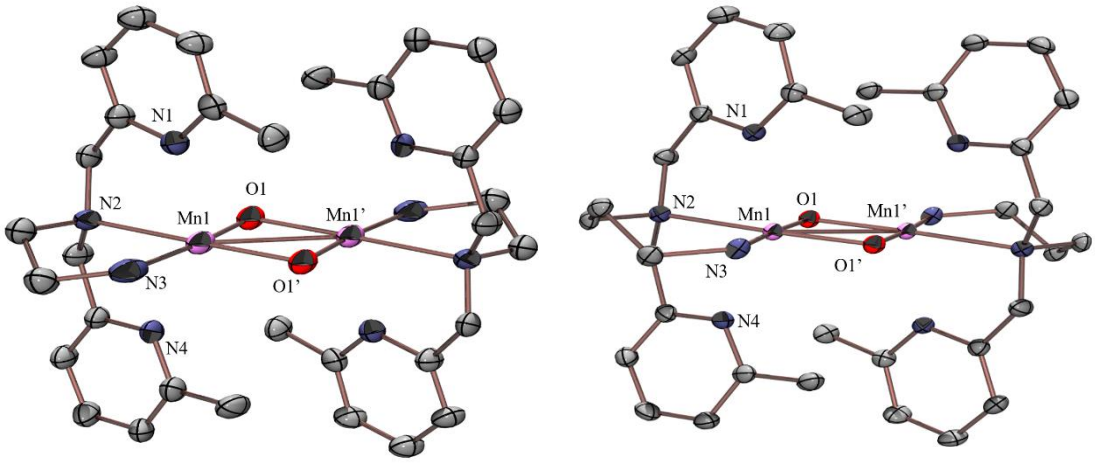

Figure 5.8 ORTEP diagrams of $\{[Mn^{IV}(N_4(6\text{-Me-DPEN}))]_2(\mu\text{-}O)_2\}^{2+}$ (left) and $\{[Mn^{IV}(N_4(6\text{-Me-DPPN}))]_2(\mu\text{-}O)_2\}^{2+}$ (right) showing the atom labeling scheme. The anions, all hydrogen atoms, solvent, and disorder have been removed for clarity. Thermal ellipsoids are drawn at the 50% probability level.[44]

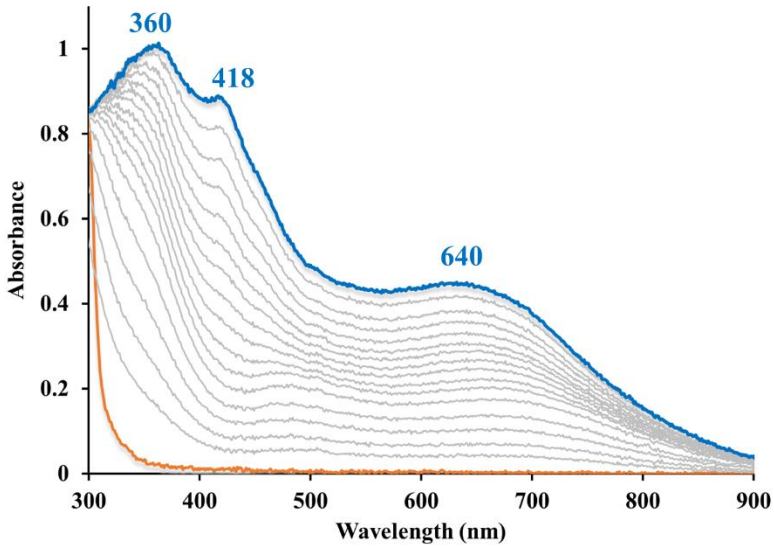

Figure 5.9 EAS spectrum monitoring the formation of alkoxide-ligated Mn^{III}-OO^tBu (**1**, blue trace) by addition of 2.5 equiv. ^{t}BuOOH and 2.5 equiv. TEA to DCM solution of Mn^{II} (**8**, orange trace) at 298 K. Spectrum recorded in 13.8 minutes interval. Growth was monitored over 3.23 hours. [Mn^{II} (**8**)] = 1.0 mM.

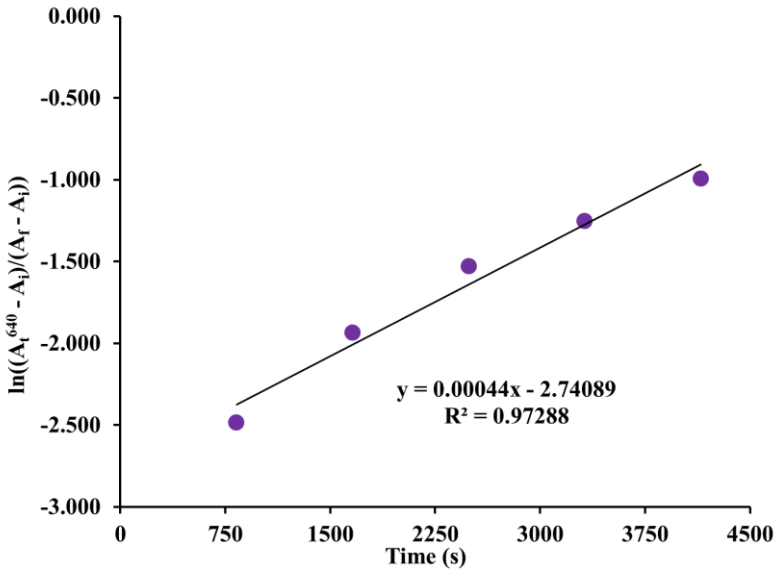

Figure 5.10 First order kinetics plot for the growth of alkoxide-ligated Mn^{III}-$OO^{t}Bu$ (**1**) in DCM at 298 K. [Mn^{II} (**8**)] = 1 mM, [^{t}BuOOH] = 3 mM, [Et_3N] = 3 mM.

$$2Mn^{II} + ROOH \rightarrow Mn^{III}\text{-}OH + Mn^{III}\text{-}OR \qquad \textbf{(Eq. 5.1)}$$

$$Mn^{III}\text{-}OH + ROOH \rightarrow Mn^{III}\text{-}OOR + H_2O \qquad \textbf{(Eq. 5.2)}$$

$$Mn^{III}\text{-}OR + ROOH \rightarrow Mn^{III}\text{-}OOR + ROH \qquad \textbf{(Eq. 5.3)}$$

5.2.4 Vibrational Characterization of 1

The FT-IR spectrum of **1** displayed an isotopically sensitive stretch at 850 cm^{-1}, which shifted to 816 cm^{-1} when $^{t}Bu^{18}O^{18}OH$ was used in place of $^{t}Bu^{16}O^{16}OH$. (***Figure 5.11***) Both the $\nu_{O\text{-}O}$ stretching frequency and isotopic shifts (34 cm^{-1}), provided evidence to support the formation of an alkylperoxo intermediate **1**. The isotopic shift was close to that predicted (44 cm^{-1}) based on a harmonic oscillator and Hooke's law. The $\nu(^{16}O—^{16}O)$ stretching frequency of **1** was close to that of **2** (875 cm^{-1}), both of which were the lowest reported stretches for any vibrationally characterized Mn^{III}-alkylperoxo compounds (range: 875-896 cm^{-1}),[29,40,41] including our previously

reported thiolate-ligated peroxo compounds,[19,36] complexes **2**, **5**, $[Mn^{III}(S^{Me2}N_4(quinoEN))(OO^tBu)]^+$ (**10**), and $[Mn^{III}(S^{Me2N}{}_4(quinoPN))(OO^tBu)]^+$ (**11**), but was closer to that of carboxamide-ligated **9** (872 cm^{-1})[30] (***Table 5.3***). The only reported Mn^{III}-peroxo with a lower $\nu(^{16}O—^{16}O)$ stretching frequency ($\nu_{O\text{-}O}$ = 819 cm^{-1}), $[Mn^{III}(S^{Me2}N_4(6\text{-Me-DPEN}))]_2$(*trans*-μ-1,2-$O_2$)$(BPh_4)_2$, contains a bridging peroxo.[45] Badger's rule[46,47] was roughly adhered to for alkoxide-ligated **1** as well as thiolate-ligated **2**, **5**, **10**, and **11** (***Figure 5.12***). Deviations from linearity (R^2 = 0.71) likely reflected perturbations introduced by altering the ligand scaffold, replacing the thiolate with an alkoxide, and more likely, were a result of a more complex vibration mode that involves other portions of the molecule (**Section 5.6**). The $\nu_{O\text{-}O}$ stretching frequency for our previously reported thiolate-ligated complexes **2**, **5**, **10**, and **11**,[19] decreased as the O—O bond length increased (***Figure 5.13***). The data point for alkoxide-ligated **1** fell off the trendline (***Figure 5.10***), however, indicating that the $\nu_{O\text{-}O}$ vibrational mode involved the alkoxide and other portions of the molecule. The variation was supported by density functional theory (DFT) calculations (**Section 5.6**).

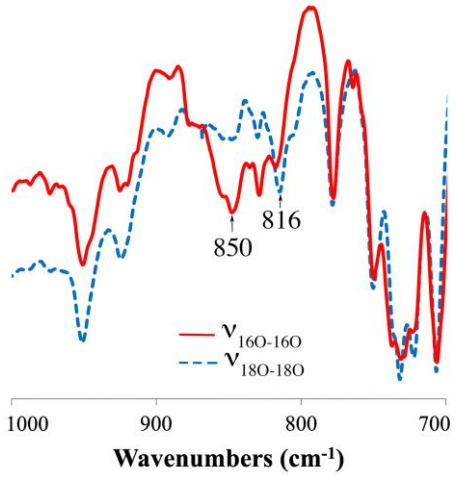

Figure 5.11 FT-IR spectrum of alkoxide-ligated ^{t}butyl peroxo compound **1**.[33]

Table 5.3 Comparison of Vibrational and Electronic Absorption Parameters, and Half-life of Thiolate- (**2**, **5**, **10**, and **11**), Alkoxide- (**1**), and carboxamide- (**9**) Ligated Alkylperoxo Compounds.

Peroxo Compound	**O—O (Å)**	$\nu_{16O\text{-}16O}$ (cm^{-1})	$\nu_{18O\text{-}18O}$ (cm^{-1})	λ_{max} (nm)	λ_{max} (nm)	**Mn●●●N^{Ar}_{avg} (Å)**	**$t_{1/2}$ (T, K) (sec)**
1	1.473(1)	850	816	360	650	2.39	6730(298)
9	1.48[a]	872	N/A	~475	690	N/A	3200(253)[b]
2	1.468(7)	875	816	355	600	2.41	249(293)
10	1.457(7)	888	831	385	590	2.44	367(293)
5	1.431(5)	893	835	420	585	2.510	147(293)
11	1.438(5)	895	831	415	590	2.48	136(293)

Note: [a]DFT calculated distance. [b] Parham, J. D.; Wijeratne, G. B.; Rice, D. B.; Jackson, T. A. *Inorg. Chem.* **2018**, *57*, 2489–2502.[30]

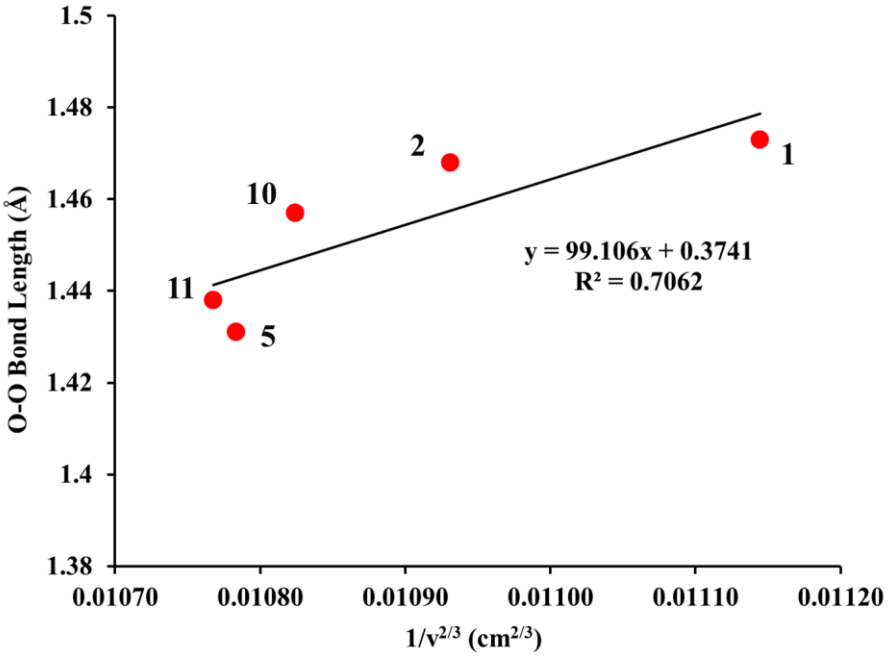

Figure 5.12 Badger's rule[46,47] plot.

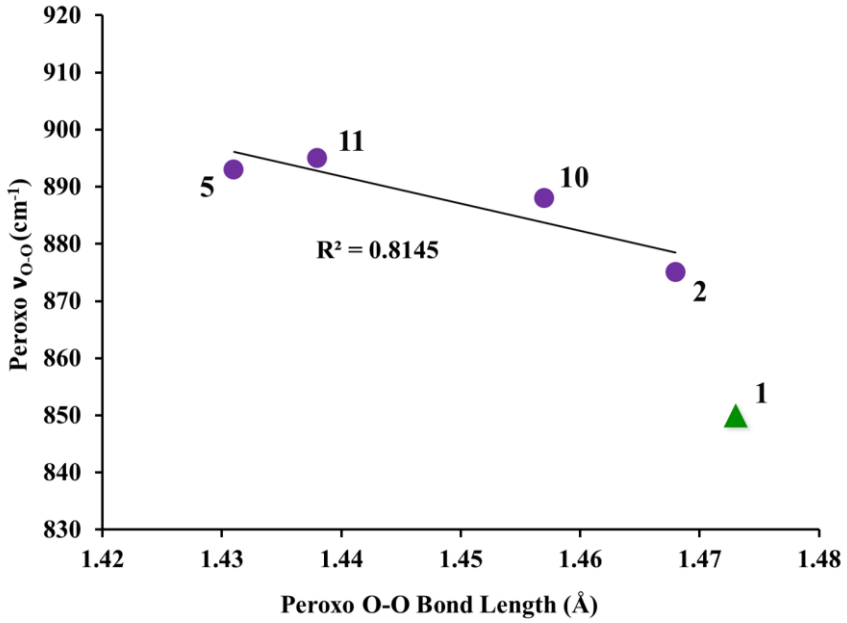

Figure 5.13 Correlation between peroxo O—O stretching frequency and peroxo O—O bond length, showing alkoxide-ligated **1** (green triangle) vs thiolate-ligated **2**, **5**, **10**, and **11** (purple circles).

5.2.5 Stability of Alkoxide-Ligated 1 Relative to Thiolate-Ligated 2

One might expect the stability of a peroxo to be primarily dictated by the ν_{O-O} and O—O bond strength, the latter of which is reflected in the distance. Based on these parameters alone, one would therefore predict that alkoxide-ligated Mn^{III}-OOR **1** and thiolate-ligated Mn^{III}-OOR **2** would have similar stabilities (***Table 5.2***). However, despite the similarities, alkoxide-ligated Mn^{III}-OOR **1** was considerably more stable (***Figures 5.14*** and **5.15**) than the corresponding thiolate derivative **2**. At 20 °C, DCM solutions of thiolate-ligated **2** were stable for ~30 minutes ($t_{1/2}^{293K}$ = 249 sec, k_1^{293K} = 2.78 x 10^{-3} sec^{-1}),[19] whereas DCM solutions of **1**, were stable for several hours at 25 °C ($t_{1/2}^{298K}$ = 6730 sec, k_{obs}^{298K} = 1.03 x 10^{-4} = 1.03 x 10^{-4} sec^{-1}, ***Figure 5.14***, ***Table 5.2***) Alkoxide-ligated **1** was not only more stable than thiolate-ligated *tert*-butylperoxo-**2**, but it was also more

stable than thiolate-ligated $[Mn^{III}(S^{Me2}N_4(6\text{-Me-DPPN}))(OO^tBu)]^+$ (**5**), $[Mn^{III}(S^{Me2}N_4(quinoEN))(OO^tBu)]^+$ (**10**), and $[Mn^{III}(S^{Me2}N_4(quinoPN))(OO^tBu)]^+$ (**11**) (***Table 5.3***), demonstrating a consistent trend.[19] Carboxamide-ligated $[Mn^{III}(OO^tBu)(dpaq^{2Me})]^+$ (**9**) also decayed at a slower rate ($t_{1/2}^{258K}$ = 3200 sec, k^{258K} = 2.17 x 10^{-4} s^{-1}),[30] relative to the thiolate-ligated **2**, **5**, **10**, and **11**.

The remainder of **Chapter 5** will discuss the DFT calculations calibrated to the experimental results and the insight they provided into the relative stability of the alkoxide alkylperoxo species **1**. In order to obtain insights into the relative stabilities of thiolate-ligated **2** versus alkoxide-ligated **1**, DFT and time-dependent DFT (TD-DFT) calculations were performed using the experimentally obtained electronic absorption spectrum (***Figure 5.7***), vibrational spectrum (***Figure 5.11***), and crystal structure (***Table 5.2***, ***Figure 5.2***) as calibration points.

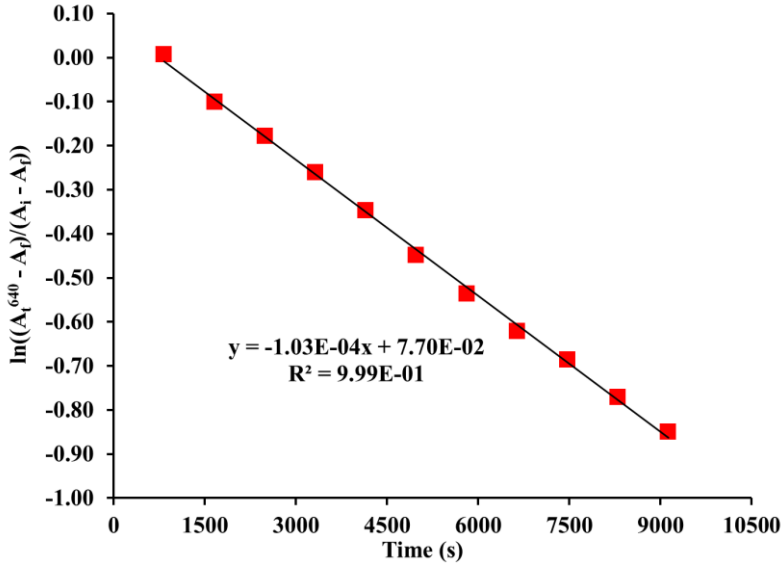

Figure 5.14 First order kinetics plot for the decay of **1** at 298 K. The observed rate constant, k_{obs}, was obtained from the slope.

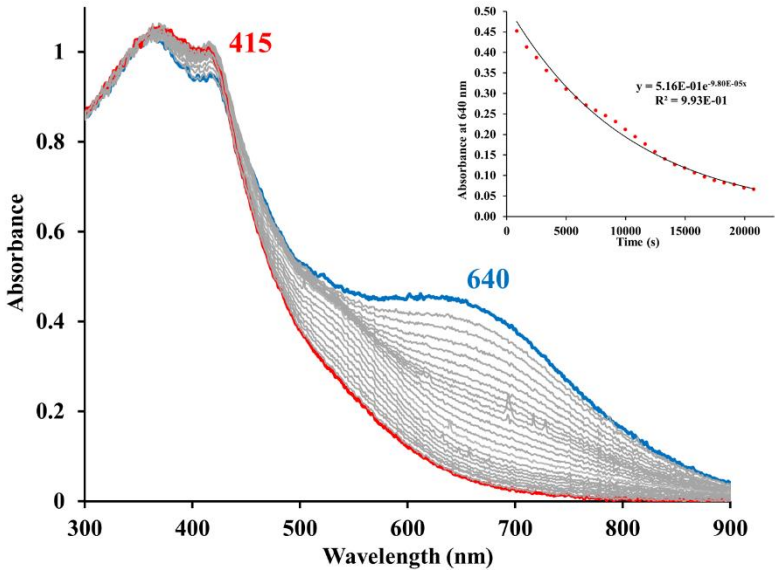

Figure 5.15 EAS spectrum monitoring the decay of $[Mn^{III}(O^{Me2}N_4(6\text{-Me-DPEN}))(OO^tBu)](BPh_4)$ (**1**) in DCM at 298 K over 5.76 hours, demonstrating its increased stability relative to the thiolate derivative $[Mn^{III}(S^{Me2}N_4(6\text{-Me-DPEN}))(OO^tBu)]^+$ (**2**). Insert shows the exponential decay curve at 640 nm. Spectrum recorded in 13.8 minutes interval. $[Mn^{II}$ (**8**)] = 1.0 mM.

5.3 Computational Details

All calculations were performed using the ORCA v.4.1.1 quantum chemistry package developed by Neese and coworkers,[48] and employed either the def2-TZVP or 6-31G* basis sets and the def2/J auxiliary basis set for Coulomb fitting, the atom-pairwise dispersion correction of Grimme (D3BJ).[49] Tight convergence criteria, together with Grid5 (GridX5) and FinalGrid6 (FinalGridX6) integration grid size, were required for self-consistent field (SCF) solutions. Geometry optimization were performed using either B3LYP, PBE0 or TPSS functionals, with the resolution of identity (RI) chain-of-spheres (RIJCOSX) approximation,[50,51] and initiated from the crystallographic coordinates when available. Analytical frequency calculations were performed on all optimized structures to determine whether the obtained stationary points correspond to local minima. Hybrid time-dependent DFT (TD-DFT) calculations employed the RIJCOSX and the

Tamm-Dancoff approximations (TDA).[52,53] Excited states from TD-DFT calculations were analyzed using Natural Transition Orbitals (NTOs) and by visualizing their difference densities between the ground and excited states. Canonical molecular orbital isosurfaces and natural transition orbitals in the TD-DFT were visualized using Chemcraft.[54]

5.4 Density Functional Theory (DFT) Geometry Optimizations

The crystallographically determined structures for the Mn complexes described above offered a starting point to minimize the energy of the system and calibrate further DFT calculations that modeled spectral features and described the electronic environments. The experimentally determined bond lengths and key angles around the Mn ions will be compared to the minimized structures to confirm the model was a good reproduction of the system.

5.4.1 Geometry Optimization of $[Mn^{III}(O^{Me2}N_4(6\text{-Me-DPEN})(OO^tBu))]^+$ (1)

Starting from the X-ray determined coordinates optimized geometries, using three functionals (B3LYP, PBE0, and TPSS), were calculated for alkoxide-ligated **1** and resulted in the coordinates shown in ***Figure 5.16*** and described in ***Table 5.4***. The key angles around the Mn ion are summarized in **Table 5.5**. A variety of functionals were used to find the best match for the experimentally obtained data. All three provided a good match (1.05 – 2.05 % error) to the crystallographically determined coordinates. Importantly, the DFT calculated structures display elongated $Mn\bullet\bullet\bullet N^{Ar}$ bonds, well outside the sum of covalent radii, in agreement with the crystal structure.

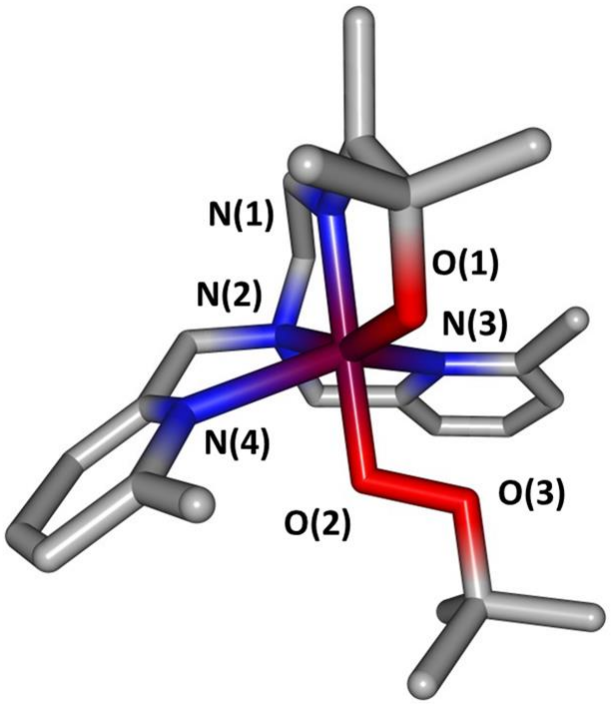

Figure 5.16 DFT optimized geometry for **1**, with B3LYP functional. Atoms are shown as Mn (purple); O (red); N (blue); and C (gray).

Table 5.4 DFT calculated versus crystallographically measured bond distances for alkoxide-ligated $[Mn^{III}(O^{Me2}N_4(6\text{-Me-DPEN}))(OO^tBu)](BPh_4)$ (**1**).

Bond	X-ray Bond Distance (Å)	B3LYP Calculated Bond Distance (Å)	% Error	PBE0 Calculated Bond Distance (Å)	% Error	TPSS Calculated Bond Distance (Å)	% Error
Mn—N(1)	2.004	2.025	1.05	2.021	0.85	1.999	0.25
Mn—N(2)	2.161	2.247	3.98	2.248	4.03	2.219	2.68
Mn—N(3)	2.355	2.316	1.66	2.327	1.19	2.330	1.06
Mn—N(4)	2.431	2.362	2.84	2.349	3.37	2.385	1.89
Mn—O(1)	1.854	1.837	0.92	1.844	0.54	1.851	0.16
Mn—O(2)	1.856	1.836	1.08	1.84	0.86	1.839	0.92
O(2)—O(3)	1.473	1.454	1.29	1.421	3.53	1.467	0.41
		Average error	1.83		2.05		1.05

Table 5.5 DFT calculated versus crystallographically measured bond angles (°) for alkoxide-ligated $[Mn^{III}(O^{Me2}N_4(6\text{-Me-DPEN}))(OO^tBu)](BPh_4)$ (**1**).

Angle	X-ray Bond Angle (°)	B3LYP Calculated Bond Angle (°)	% Error	PBE0 Calculated Bond Angle (°)	% Error	TPSS Calculated Bond Angle (°)	% Error
O(1)-Mn-N(1)	81.20	80.82	0.47	80.38	1.01	81.11	0.11
O(1)-Mn-N(3)	113.08	113.15	0.06	111.92	1.03	113.56	0.42
O(1)-Mn-N(4)	107.98	109.51	1.42	110.41	2.25	107.72	0.24
O(1)-Mn-O(2)	98.26	98.88	0.63	99.57	1.33	99.71	1.48
N(1)-Mn-N(3)	100.76	97.29	3.44	97.23	3.50	98.51	2.23
N(1)-Mn-N(4)	103.32	104.26	0.91	103.26	0.06	103.49	0.16
O(2)-Mn-N(3)	83.02	82.00	1.23	82.48	0.65	82.45	0.69
O(2)-Mn-N(4)	73.12	76.68	4.87	77.07	5.40	74.96	2.52
N(2)-Mn-N(1)	78.58	77.37	1.54	77.05	1.95	78.33	0.32
N(2)-Mn-N(3)	73.09	71.76	1.82	71.73	1.86	72.03	1.45
N(2)-Mn-N(4)	75.01	74.62	0.52	74.81	0.27	75.27	0.35
N(2)-Mn-O(2)	101.77	102.95	1.16	103.00	1.21	100.80	0.95
Average error			1.51		1.71		0.91

5.4.2 Geometry Optimization of $[Mn^{III}(S^{Me2}N_4(6\text{-Me-DPEN})(OO^tBu))^+$ 2

Starting from the X-ray determined coordinates of **2**, optimized geometries, using three functionals (B3LYP, PBE0, and TPSS), were calculated for thiolate-ligated **2** and resulted in the coordinates shown in ***Figure 5.17*** and described in ***Table 5.6***. The key angles around the Mn ion are summarized in ***Table 5.7*****.** A variety of functionals were attempted to find the best match for the experimentally obtained data. All three provided a good match (0.71 -1.92 % error) to the crystallographically determined coordinates. Importantly, the DFT calculated structures display elongated $Mn\bullet\bullet\bullet N^{Ar}$ bonds, well outside the sum of covalent radii, in agreement with the crystal structure.

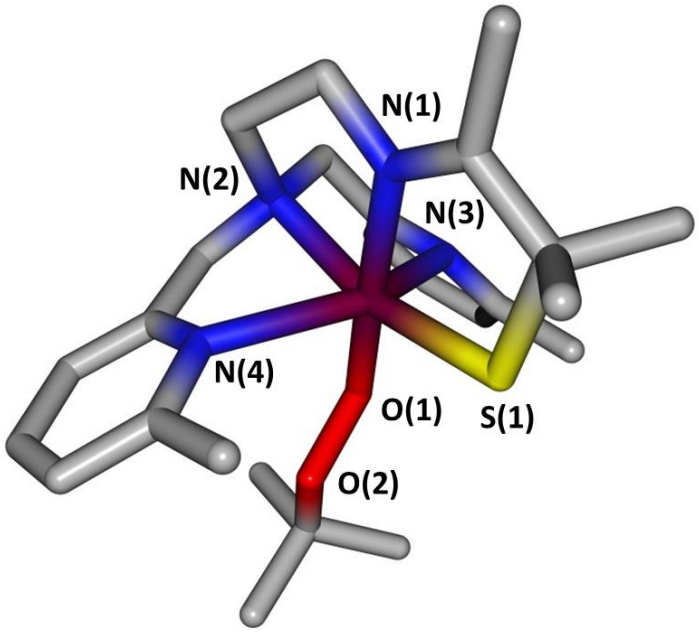

Figure 5.17 DFT optimized geometry for **1**, with B3LYP functional. Atoms are shown as Mn (purple); O (red); N (blue); S (yellow); and C (gray).

Table 5.6 DFT calculated versus crystallographically measured bond distances for thiolate-ligated $[Mn^{III}(S^{Me2}N_4(6\text{-Me-DPEN}))(OO^tBu)](BPh_4)$ (**2**).

Bond	X-ray Bond Distance (Å)	B3LYP Calculated Bond Distance (Å)	% Error	PBE0 Calculated Bond Distance (Å)	% Error	TPSS Calculated Bond Distance (Å)	% Error
Mn—N(1)	2.015	2.041	1.29	2.055	1.99	2.018	0.15
Mn—N(2)	2.163	2.200	1.71	2.241	3.61	2.191	1.29
Mn—N(3)	2.353	2.346	0.30	2.38	1.15	2.373	0.85
Mn—N(4)	2.470	2.521	2.06	2.512	1.70	2.447	0.93
Mn—S(1)	2.241	2.252	0.49	2.253	0.54	2.229	0.54
Mn—O(1)	1.852	1.824	1.51	1.831	1.13	1.831	1.13
O(1)—O(2)	1.469	1.451	1.23	1.42	3.34	1.468	0.07
		Average error	1.23		1.92		0.71

Table 5.7 DFT calculated versus crystallographically measured bond angles (°) for thiolate-ligated $[Mn^{III}(O^{Me2}N_4(6\text{-Me-DPEN}))(OO^tBu)](BPh_4)$ (**2**).

Angle	X-ray Bond Angle (°)	B3LYP Calculated Bond Angle (°)	% Error	PBE0 Calculated Bond Angle (°)	% Error	TPSS Calculated Bond Angle (°)	% Error
S(1)-Mn-N(1)	83.59	84.21	0.74	83.25	0.41	84.53	1.12
S(1)-Mn-N(3)	109.13	105.48	3.34	109.01	0.11	109.23	0.09
S(1)-Mn-N(4)	112.41	114.10	1.50	115.32	2.59	110.52	1.68
S(1)-Mn-O(1)	94.95	96.69	1.83	95.20	0.26	96.47	1.60
N(1)-Mn-N(3)	103.69	103.81	0.12	105.41	1.66	103.13	0.54
N(1)-Mn-N(4)	101.13	98.67	2.43	99.03	2.08	96.69	4.39
O(1)-Mn-N(3)	72.90	72.13	1.06	73.20	0.41	74.69	2.46
O(1)-Mn-N(4)	83.20	84.60	1.68	84.40	1.44	84.82	1.95
N(2)-Mn-N(1)	79.09	80.10	1.28	78.59	0.63	80.61	1.92
N(2)-Mn-N(3)	73.98	74.50	0.70	73.10	1.19	75.19	1.64
N(2)-Mn-N(4)	72.79	72.77	0.03	71.32	2.02	71.74	1.44
N(2)-Mn-O(1)	102.22	98.67	3.47	102.83	0.60	98.38	3.76
Average error			1.52		1.12		1.88

5.4.3 Geometry Optimizations of Mn^{II} Starting Complex 8

In order to support the protonated state of the Mn^{II} starting complex in the absence of an IR spectrum with an OH stretch, DFT calculations were investigated. ***Figure 5.18*** shows the B3LYP optimized geometry, with the proton present on the alkoxide ligand arm. ***Table 5.8*** summarizes the bond distances in comparison to the crystal structure obtained for **8**. The bond distances are in good agreement with an average error of 0.90%. ***Table 5.9*** summarizes the bond angles in comparison to the crystal structure bond angles around the Mn center. There was a higher level of error in comparison to the structure with average error of 4.34%.

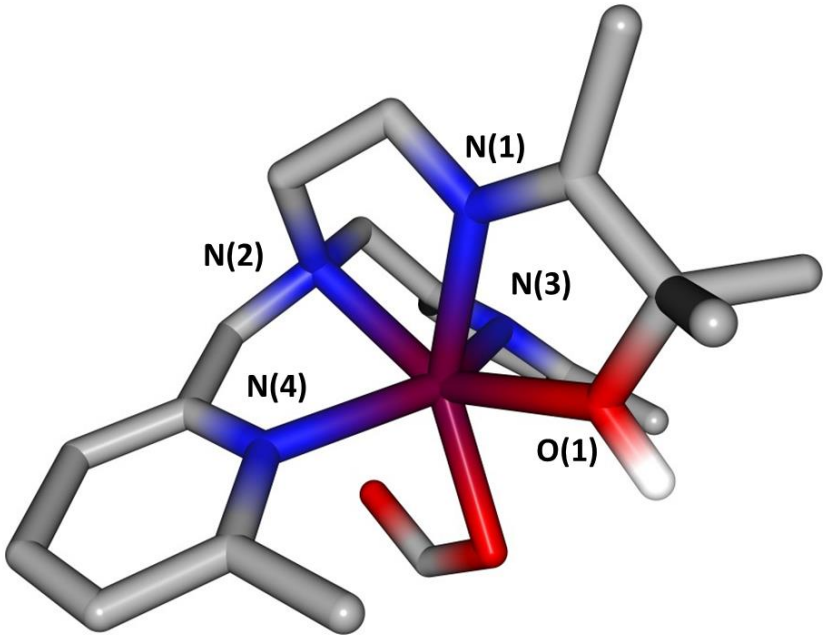

Figure 5.18 B3LYP optimized geometry for formate-bound Mn^{II} starting material, $[Mn^{II}(HO^{Me2}N_4(6\text{-Me-DPEN})(CHO_2))]^+$ (**8**).

Table 5.8 DFT calculated versus crystallographically measured bond distances for alkoxide-ligated $[Mn^{II}(HO^{Me2}N_4(6\text{-Me-DPEN})(CHO_2))]^+$ (**8**).

Bond	X-ray Bond Distance (Å)	B3LYP Calculated Bond Distance (Å)	% Error
Mn—N(1)	2.246	2.317	3.16
Mn—N(2)	2.308	2.320	0.52
Mn—N(3)	2.306	2.304	0.09
Mn—N(4)	2.291	2.284	0.31
Mn—O(1)	2.233	2.252	0.85
Mn—O(2)	2.120	2.1304	0.49
		Average error	0.90

Table 5.9 DFT calculated versus crystallographically measured bond angles (°) for thiolate-ligated $[Mn^{III}(O^{Me2}N_4(6\text{-Me-DPEN}))(OO^tBu)](BPh_4)$ (**2**).

Angle	X-ray Bond Angle (°)	B3LYP Calculated Bond Angle (°)	% Error
O(1)-Mn-N(1)	68.65	66.46	3.19
O(1)-Mn-N(3)	106.10	109.80	3.49
O(1)-Mn-N(4)	110.51	111.03	0.47
O(1)-Mn-O(2)	87.12	78.30	10.12
N(1)-Mn-N(3)	86.63	97.36	12.39
N(1)-Mn-N(4)	106.37	100.82	5.22
O(2)-Mn-N(3)	92.98	96.41	3.69
O(2)-Mn-N(4)	88.98	89.45	0.53
N(2)-Mn-N(1)	75.77	74.06	2.26
N(2)-Mn-N(3)	76.29	76.72	0.56
N(2)-Mn-N(4)	74.20	73.61	0.80
N(2)-Mn-O(2)	128.85	140.97	9.41
Average error			4.34

5.5 Time-Dependent Density Functional Theory (TD-DFT) Calculated Spectra

5.5.1 TD-DFT Calculated Spectra for 1

The next experimental calibration point to calculate was the electronic absorption spectrum modeled with time-dependent density function theory (TD-DFT). The calculated electronic absorption spectrum of alkoxide-ligated **1** was in good agreement with the experimental spectrum (***Figure 5.19***) when calculated with either the B3LYP or PBE0 functionals. The TPSS functional did not provide a good model of the experimental spectrum as the alkylperoxo bands were shifted by ~100 nm from the experimentally observed λ_{max} = 650 nm (***Figure 5.21***).

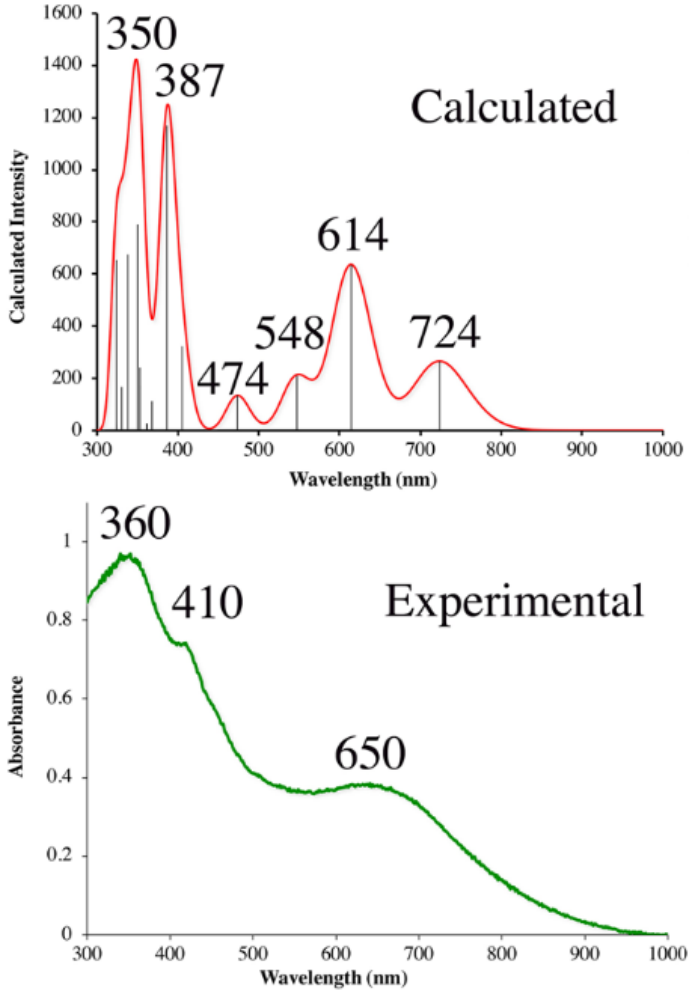

Figure 5.19 B3LYP TD-DFT calculated (top) versus experimental (bottom) electronic absorption spectra of alkoxide ligated RO-Mn-OOR (**1**).

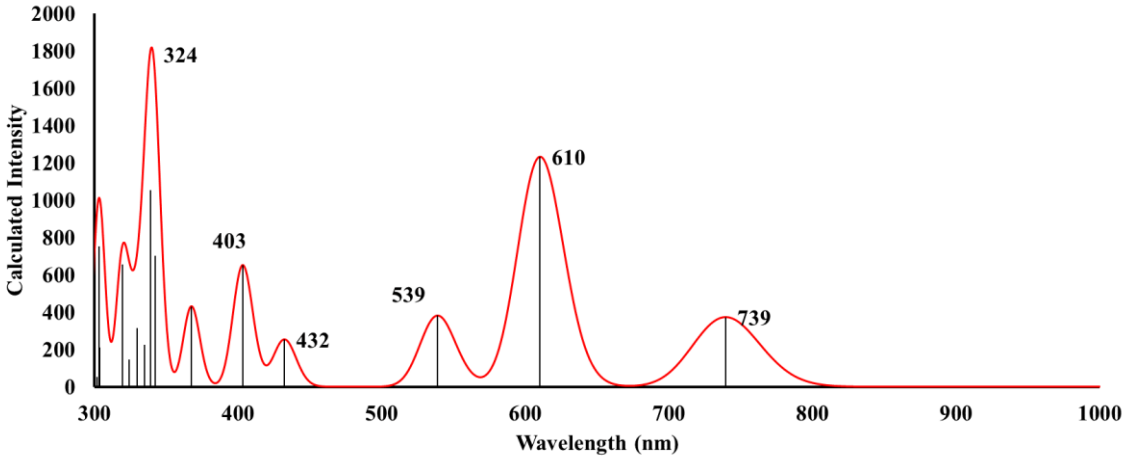

Figure 5.20 PBE0 TD-DFT calculated electronic absorption spectra of alkoxide ligated RO-Mn-OOR (**1**).

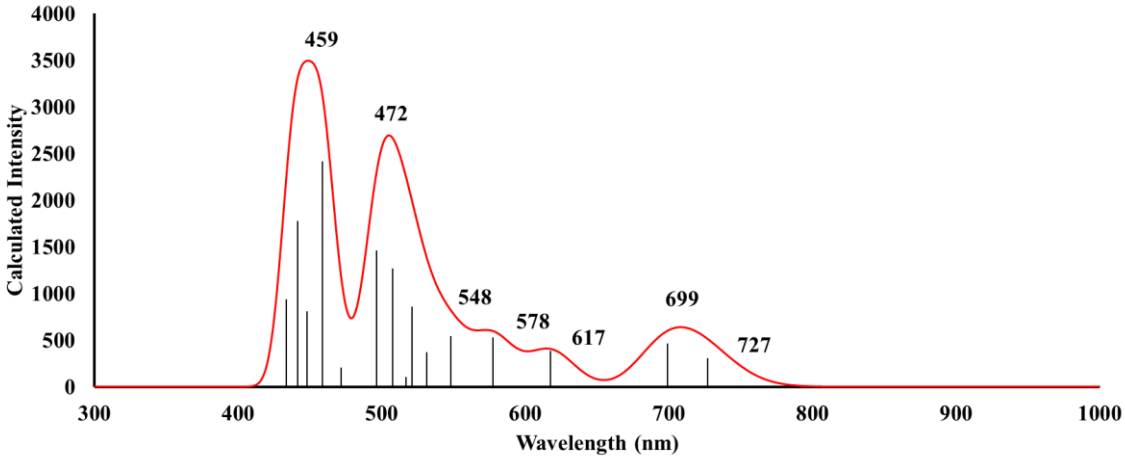

Figure 5.21 TPSS TD-DFT calculated electronic absorption spectra of alkoxide ligated RO-Mn-OOR (**1**).

5.5.2 TD-DFT Calculated Spectra for 2

The B3LYP TD-DFT calculated electronic absorption spectrum of thiolate-ligated **2** was also in good agreement with the experimentally obtained spectrum (***Figure 5.22***). The TD-DFT calculated spectrum using the PBE0 functional (***Figure 5.23***) was not a good match in this case with bands shifted to low energy (754 nm) over 100 nm away from the most intense band of the

experimental spectrum (λ_{max} = 600 nm). ***Figure 5.24*** shows the TPSS calculated spectrum that did not demonstrate the correct relative intensity expected for the bands. Across the two alkylperoxo complexes the B3LYP functional modeled the experimental result the most accurately in both cases and as such further calculations used the B3LYP functional.

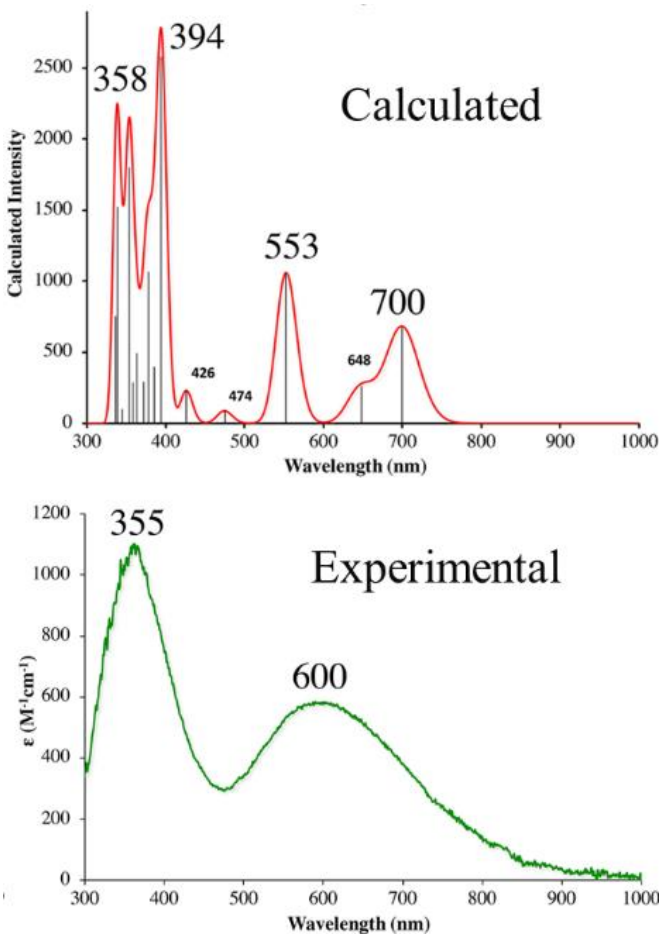

Figure 5.22 B3LYP TD-DFT calculated (top) versus experimental (bottom) electronic absorption spectra of thiolate-ligated RS-Mn-OOR (**2**).

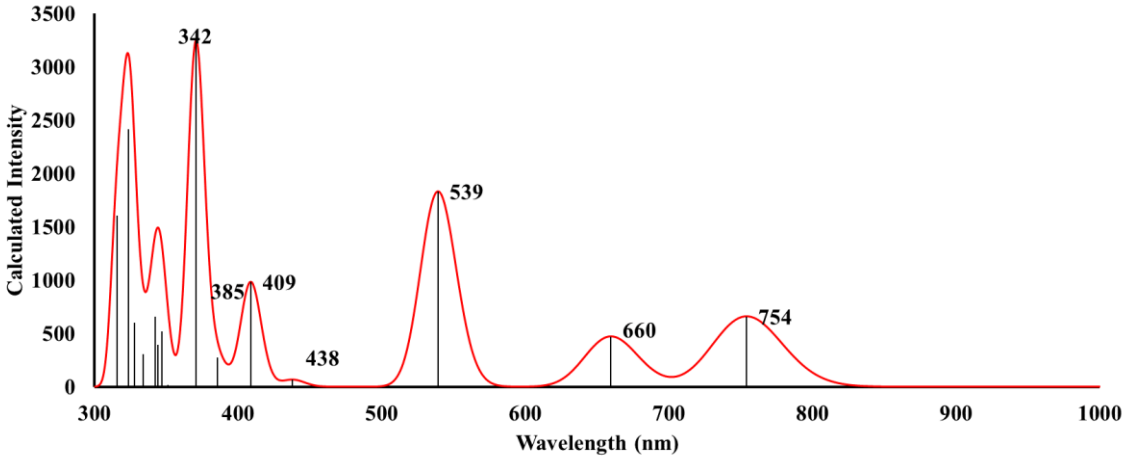

Figure 5.23 PBE0 TD-DFT calculated electronic absorption spectra of thiolate-ligated RS-Mn-OOR (**2**).

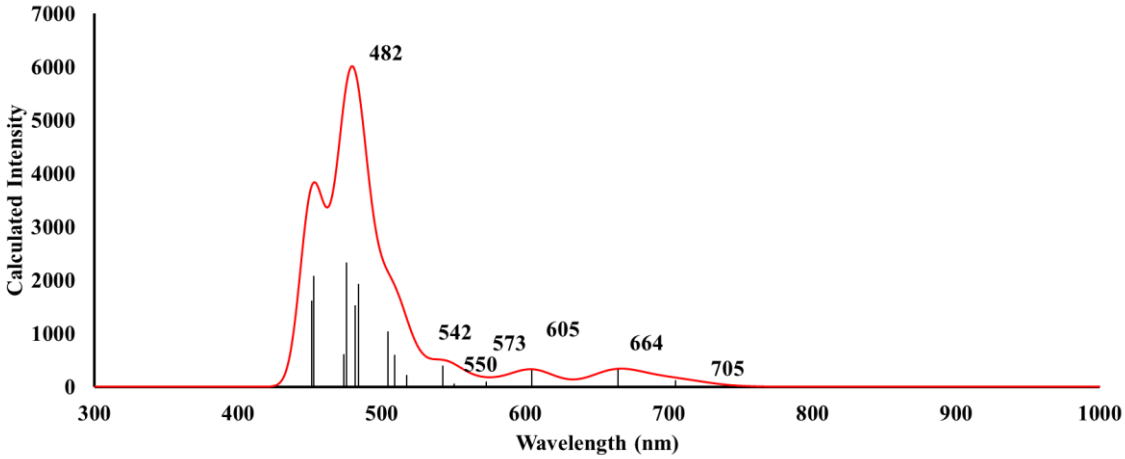

Figure 5.24 TPSS TD-DFT calculated electronic absorption spectra of thiolate-ligated RS-Mn-OOR (**2**).

5.6 Vibrational Data Calculations and Comparisons

The calculated vibrational spectra (***Figure 5.25***) and isotopic shifts ($\Delta(^{16}O-^{18}O)$; ***Figure 5.26*** and ***Figure 5.27***) for the vibrations associated with **1** and **2** were also in agreement with the experimentally obtained spectra (***Figure 5.11***).[55] The DFT- calculated isotopic shifts $\Delta(^{18}O-^{16}O)$ for the ν_{O-O} (880 cm^{-1}) and ν_{O-O} (925 cm^{-1}) vibrations of alkoxide-ligated **1** were 28 and 36 cm^{-1},

respectively, compared to a theoretical shift of 50 cm^{-1} based on Hooke's law. Deviations from theoretical isotopic shifts reflected the mixing between ν_{O-O} vibrations and vibrations involving other portions of the molecule (e.g., ^{t}Bu, ν_{C-C} and alkoxide ν_{C-O} vibrations), as depicted in the frequency displacement diagrams of ***Figures 5.28-5.34***. The DFT-calculated isotopic shift, $\Delta(^{16}O-^{18}O)$, for the ν_{Mn-O} (686 cm^{-1}) of alkoxide-ligated **1** was 37 cm^{-1} compared to a theoretical shift of 30 cm^{-1} based on Hooke's law. For thiolate- ligated **2,** the DFT-calculated isotopic shifts, $\Delta(^{16}O-^{18}O)$, for the ν_{O-O} (880 cm^{-1}) and ν_{O-O} (925 cm^{-1}) were 23 and 39 cm^{-1}, respectively, and the DFT-calculated isotopic shift, $\Delta(^{16}O-^{18}O)$, for the ν_{Mn-O} (692 cm^{-1}) of thiolate-ligated **2** was 34 cm^{-1}.

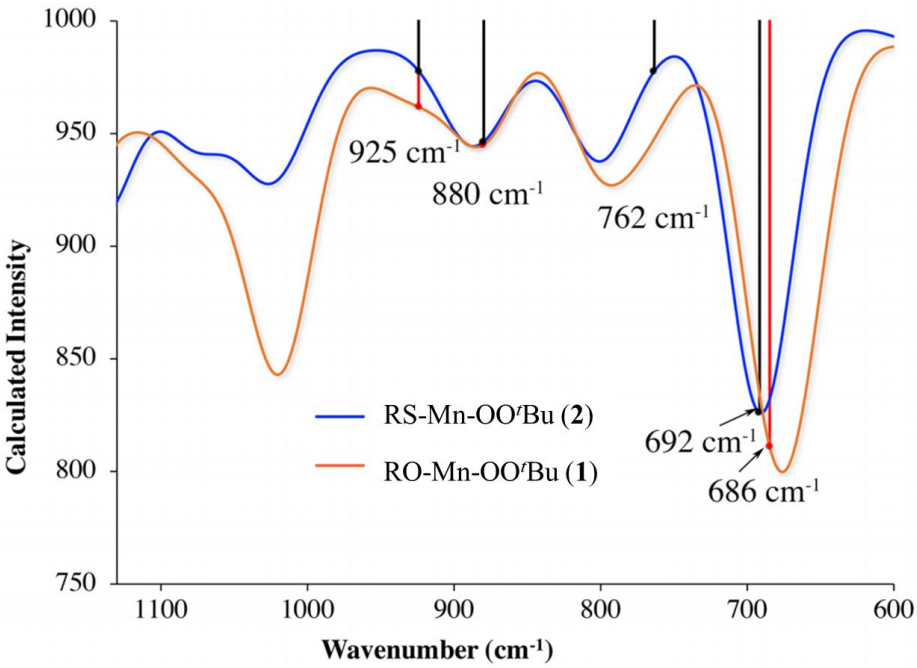

Figure 5.25 DFT calculated vibrational spectrum for alkoxide-ligated **1** (orange) versus thiolate-ligated **2** (blue). The calculated IR consists of a smoothed line formed from Gaussian fits to all of the calculated vibrational modes of the molecule. Frequencies represented by the sticks correspond to the vibrations that include major participation from the alkylperoxo O—O atoms, based on gif visualization of the vibrations and depicted in the frequency displacement diagrams.

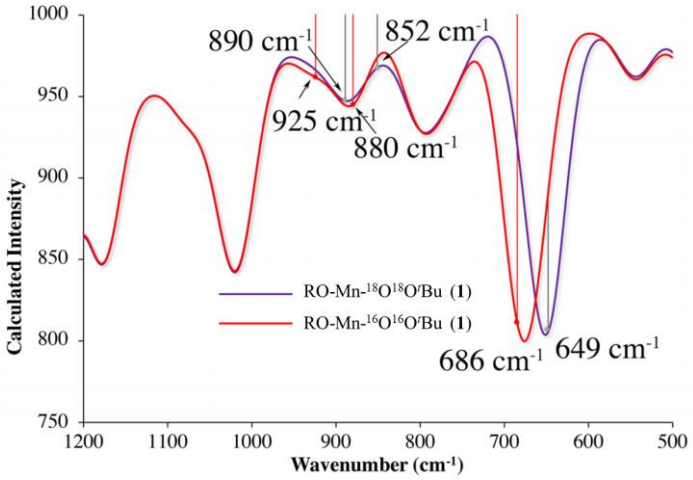

Figure 5.26 DFT calculated vibrational spectrum for alkoxide-ligated **1** showing calculated isotopic shifts as the separation between red and gray sticks. The calculated IR consists of a smoothed line formed from Gaussian fits to all of the calculated vibrational modes of the molecule. Frequencies represented by the sticks correspond to the vibrations that include major participation from the alkylperoxo O—O atoms, based on gif visualization of the vibrations and depicted in the frequency displacement diagrams.

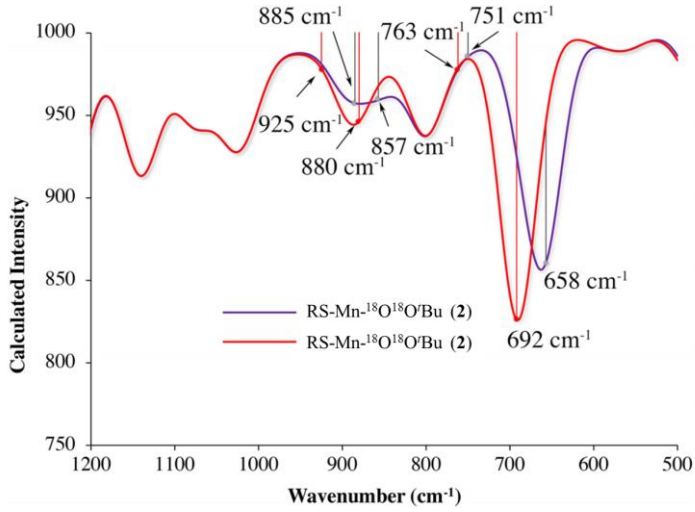

Figure 5.27 DFT calculated vibrational spectrum for thiolate-ligated **2** showing calculated isotopic shifts as the separation between red and gray sticks. The calculated IR consists of a smoothed line formed from Gaussian fits to all of the calculated vibrational modes of the molecule. Frequencies represented by the sticks correspond to the vibrations that include major participation from the alkylperoxo O—O atoms, based on gif visualization of the vibrations and depicted in the frequency displacement diagrams.

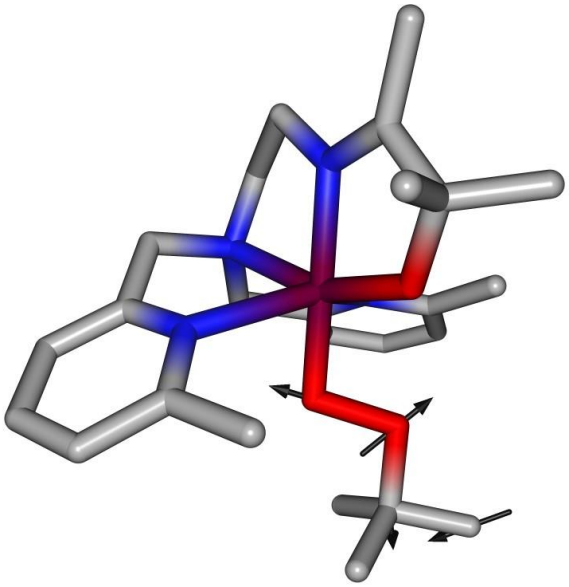

Figure 5.28 Frequency displacement diagram for the 880 cm^{-1} $\nu_{O\text{-}O}$ wag of alkoxide-ligated **1** showing the involvement of the t-Bu group in the vibration. The displacement arrows indicated the directions of the majority components of the vibrations.

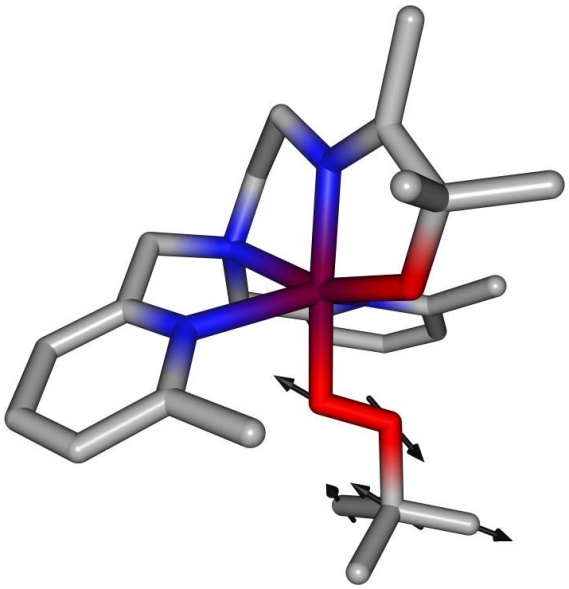

Figure 5.29 Frequency displacement diagram for the 925 cm^{-1} $\nu_{O\text{-}O}$ stretch of alkoxide-ligated **1** showing the involvement of the t-Bu group in the vibration.

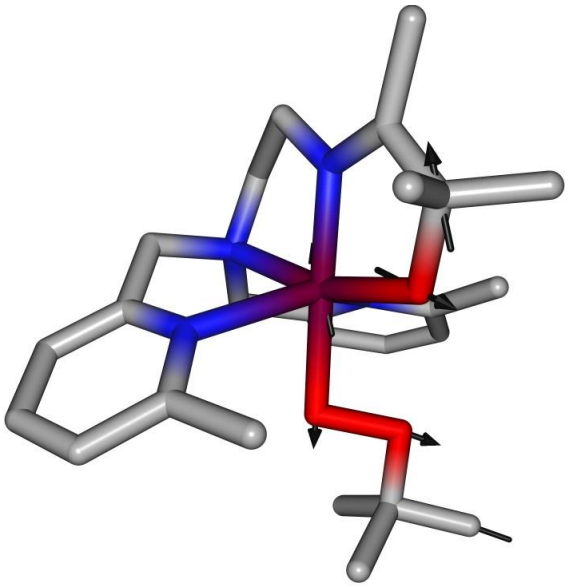

Figure 5.30 Frequency displacement diagram for the 686 cm^{-1} ν_{Mn-O} stretch of alkoxide-ligated **1** showing the involvement of the alkoxide O-C group in the vibration. The displacement arrows indicated the directions of the majority components of the vibrations.

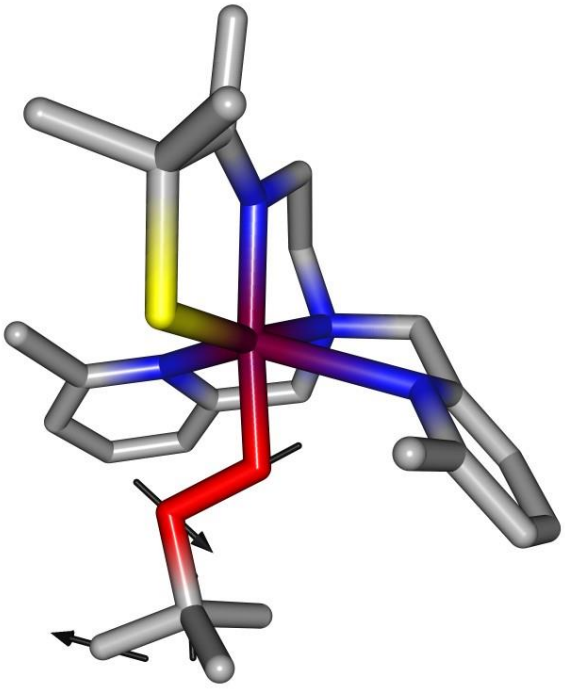

Figure 5.31 Frequency displacement diagram for the 880 cm^{-1} ν_{O-O} wag of thiolate-ligated **2** showing the involvement of the t-Bu group in the vibration. The displacement arrows indicated the directions of the majority components of the vibrations.

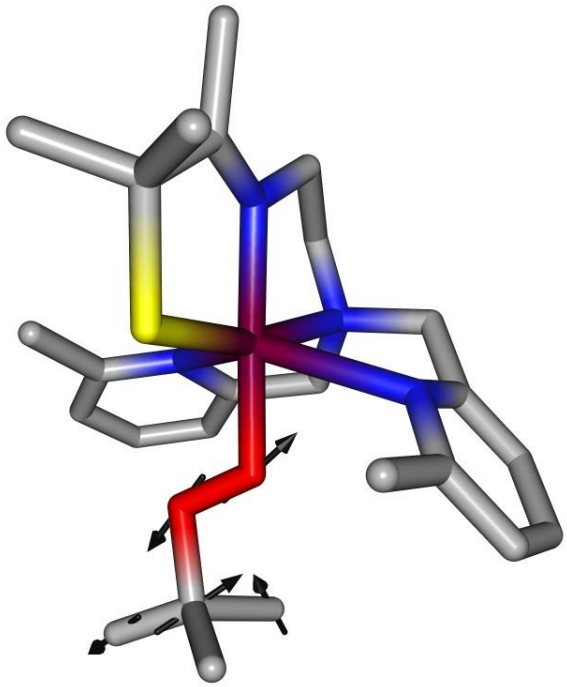

Figure 5.32 Frequency displacement diagram for the 925 cm^{-1} $\nu_{O\text{-}O}$ stretch of thiolate-ligated **2** showing the involvement of the t-Bu -group in the vibration.

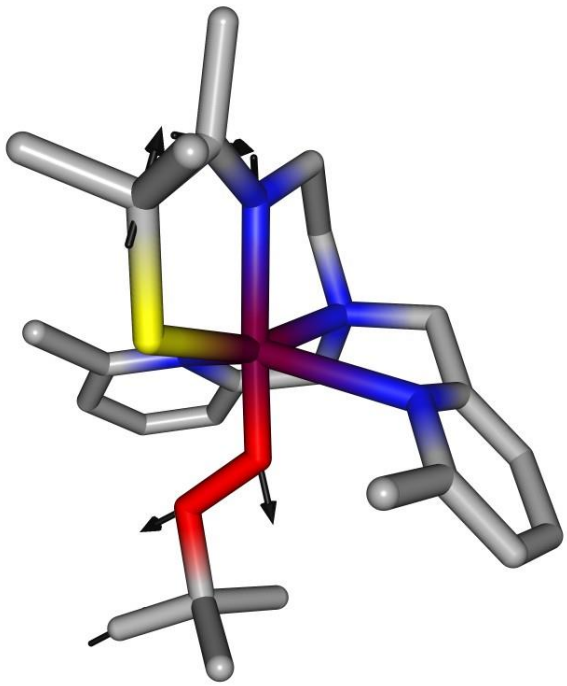

Figure 5.33 Frequency displacement diagram for the 692 cm^{-1} $\nu_{Mn\text{-}O}$ stretch of thiolate-ligated **2** showing the involvement of thiolate/imine C—C wag in the vibration.

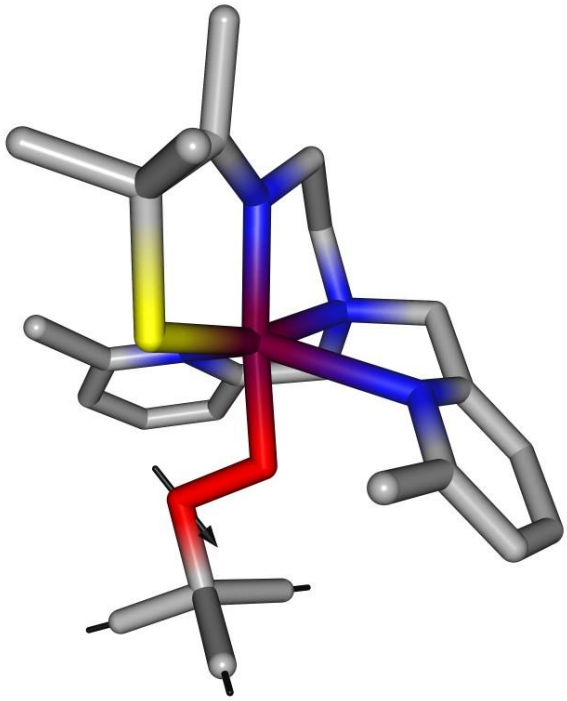

Figure 5.34 Frequency displacement diagram for the 762 cm^{-1} peroxo $\nu_{O\text{-}O}$ bend of thiolate-ligated **2** showing the involvement of the t-Bu-group.

5.7 Natural Transition Orbital (NTO) Descriptions

The low energy bands in the ~600 nm region of the spectra were shown to involve a peroxo π^*(O—O) → σ^*(Mn(d_{xy})-O, N) charge transfer transition with **1** (***Figure 5.35***), and a π^*(O—O) + S_π → σ^*(Mn(d_{xy})-S, N) charge transfer transition with **2** (***Figure 5.36***). The highest occupied molecular orbital (HOMO) of thiolate-ligated **2** possessed significant thiolate sulfur character, in contrast to the HOMO of alkoxide-ligated **1**, which possessed very little alkoxide character. As shown in ***Figure 5.37***, the predominant character of both of these HOMO orbitals was peroxo π^*(O—O) that would weaken the peroxo O—O bond, and contrasted with the bonding interaction of alkoxide-ligated **1**. This provided insight as to why the peroxo O—O bond of **2** cleaved more readily than that of **1**.

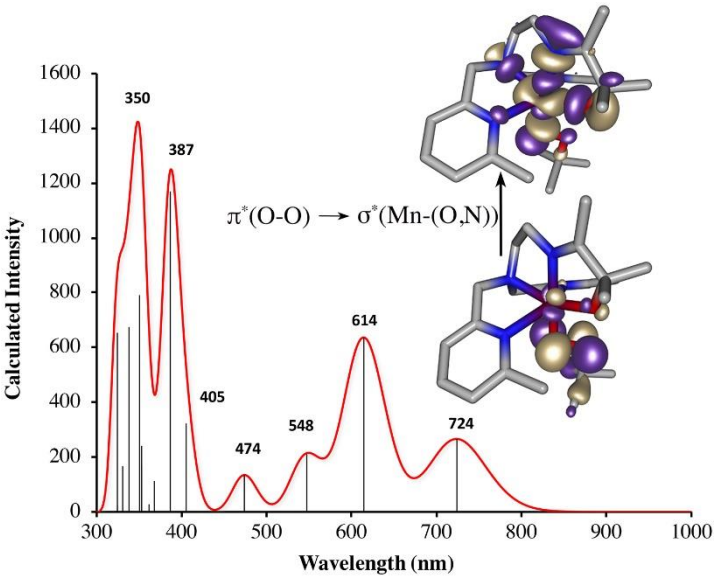

Figure 5.35 Time-dependent density functional theory (TD-DFT) calculated electronic absorption spectrum of alkoxide-ligated RO-Mn-OOR (**1**) including natural transition orbitals (NTO) describing the charge transfer (CT) transitions. Illustrated is the low energy peroxo π*(O—O) → σ*(Mn-L) transition and the associated donor and acceptor orbitals.

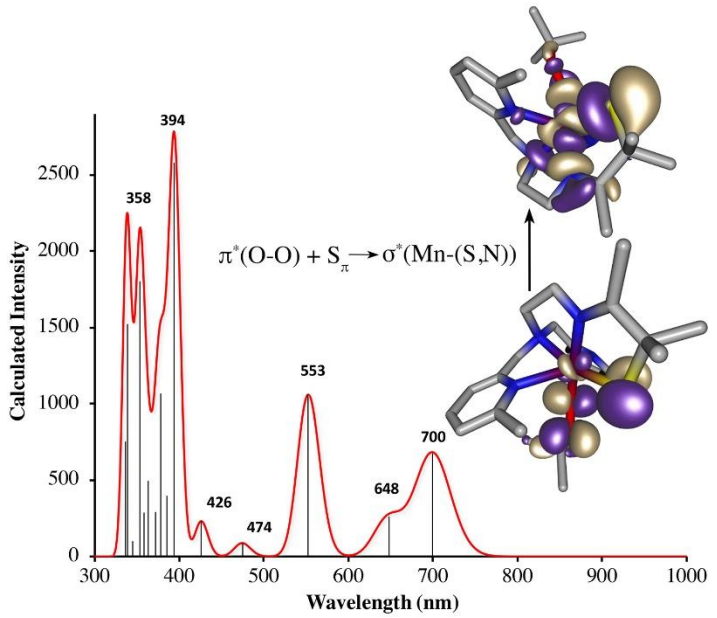

Figure 5.36 Time-dependent density functional theory (TD-DFT) calculated electronic absorption spectrum of thiolate-ligated RS-Mn-OOR (**2**) including natural transition orbitals (NTO) describing the charge transfer (CT) transitions. Illustrated is the low energy peroxo S_π + π*(O—O) → σ*(Mn-L) transition and the associated donor and acceptor orbitals.

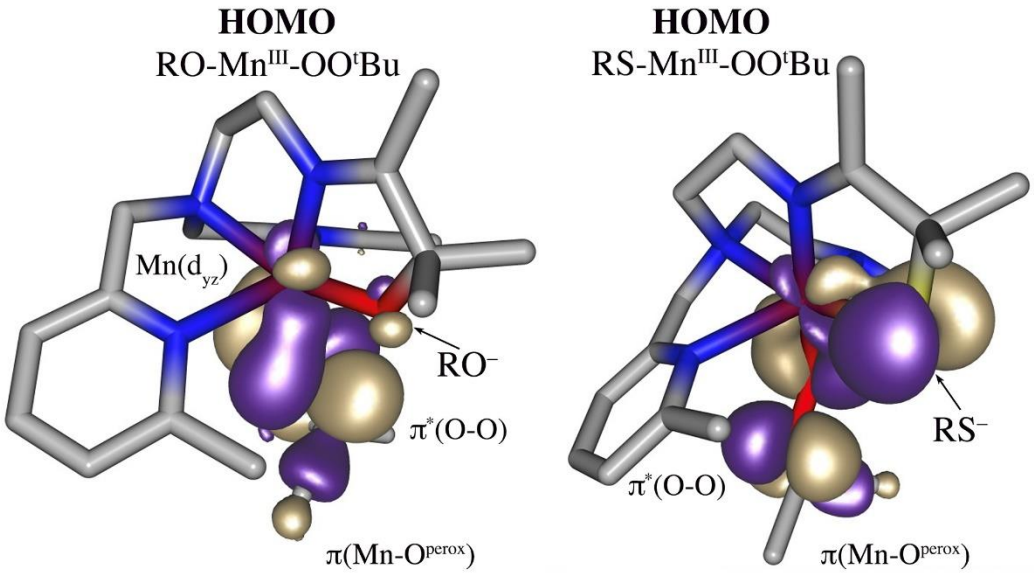

Figure 5.37 Electronic structure calculations show that the highest occupied orbital of **2** (right) contains significant thiolate sulfur character, in contrast to that of **1** (left), which has less alkoxide oxygen character

5.7 Comparing Lewis Acidity

The relative stability of alkoxide-ligated **1** versus thiolate-ligated **2** also correlated with the metal ion Lewis acidity. Previous studies in the Kovacs group showed similar results where, albeit for peroxo-bridged dimers, the relative stability of Mn-peroxo intermediates ($t_{1/2}$(6-Me-pyridine) = 249 sec, $t_{1/2}$(quinoline) = 23 sec, and $t_{1/2}$(6-MeO-pyridine) = 11.5 sec) correlates with metal ion Lewis acidity.[25] In the previous study, the primary coordination sphere atoms were identical and only the ligand scaffold and substituents were varied. The stability of the peroxo species was mainly shown to be dictated by the mean Mn•••N^{Ar} distance (2.56 Å (6-Me-pyridine), 2.5 Å (quinoline), and 2.413 Å (6-MeO-pyridine).[25] While preferrable, experimentally measured redox potentials were not used, since the limited stability of the peroxo complexes precluded their measurement.

In the current study, one heteroatom was varied in the primary coordination sphere (RO^- versus RS^-) while maintaining an otherwise identical ligand framework. As shown in ***Table 5.10***, the calculated Mulliken charge, and thus metal ion Lewis acidity, was greater for alkoxide-ligated **1** (+0.451) relative to thiolate-ligated **2** (+0.306). The change reflected the electron donating properties of thiolates. The fact that the alkoxide was less electron donating wa reflected in the higher negative Mulliken charge of the alkoxide oxygen (-0.531) relative to the thiolate sulfur (-0.327).

Table 5.10 Comparison of DFT calculated Mulliken charges for thiolate-ligated **2** versus alkoxide-ligated **1**.

Atom	Alkoxide-ligated 1	Thiolate-ligated 2
Mn	+0.451	+0.306
$\mathbf{O^{Alkoxide}}$	-0.531	N/A
$\mathbf{S^{Thiolate}}$	N/A	-0.327
$\mathbf{O^{Peroxo,\ proximal}}$	-0.396	-0.375
$\mathbf{O^{Peroxo,\ distal}}$	-0.180	-0.166

5.8 Conclusions

The work herein showed that peroxo O—O bonds cleave more readily when there is a thiolate in the coordination sphere through a combination of wet chemistry experiments and calculations on the rare, isolated Mn-complexes. The previously established correlations between structural and spectroscopic parameters were adhered to, even when an alkoxide was incorporated into the coordination sphere in place of a thiolate. Despite their structural and spectroscopic similarities, however, alkoxide-ligated RO-Mn^{III}-OO^tBu, was shown to be an order of magnitude more stable than the corresponding thiolate-ligated RS-Mn^{III}-OO^tBu derivative. Insight into the

factors responsible was provided by DFT and TD-DFT calculations. The highest occupied molecular orbital (HOMO) of thiolate-ligated RS-Mn^{III}-$OO^{t}Bu$ was shown to possess significant sulfur character and π-backdonation from the thiolate competes with π-backdonation from the peroxo π^*(O—O). The latter helped to stabilize the peroxo O—O bond since it facilitates the removal of electron density from an antibonding orbital. In addition, DFT calculated Mulliken charges showed that the Mn ion of alkoxide-ligated RO-Mn^{III}-$OO^{t}Bu$ was more Lewis acidic than that of thiolate-ligated RS-Mn^{III}-$OO^{t}Bu$. The significance of these results was that it helps to explain why the majority of Mn-enzymes incorporate O- and/or N-ligands as opposed to ^{cys}S-ligands. This is especially important for the photosynthetic oxygen evolving complex, which catalyzes O—O bond formation as opposed to cleavage. This work also provides experimental evidence to support the proposed role of cysteinates in promoting O—O bond cleavage in key metalloenzyme intermediates.

5.9 Chapter 5 References

(1) Cotruvo, J. A.; Stubbe, J. An Active Dimanganese(III)-Tyrosyl Radical Cofactor in Escherichia Coli Class Ib Ribonucleotide Reductase. *Biochemistry* **2010**, *49* (6), 1297–1309.

(2) Jackson, T. A.; Karapetian, A.; Miller, A.-F.; Brunold, T. C. Probing the Geometric and Electronic Structures of the Low-Temperature Azide Adduct and the Product-Inhibited Form of Oxidized Manganese Superoxide Dismutase. *Biochemistry* **2005**, *44* (5), 1504–1520.

(3) Ewa Skrzypczak-Jankun, *; Rebecca A. Bross; Richard T. Carroll; Willam R. Dunham, and; Max O. Funk, J. . Three-Dimensional Structure of a Purple Lipoxygenase. *J. Am. Chem. Soc.* **2001**, *123* (44), 10814–10820.

(4) Oliw, E. H.; Jernerén, F.; Hoffmann, I.; Sahlin, M.; Garscha, U. Manganese Lipoxygenase Oxidizes Bis-Allylic Hydroperoxides and Octadecenoic Acids by Different Mechanisms. *Biochim. Biophys. Acta - Mol. Cell Biol. Lipids* **2011**, *1811* (3), 138–147.

(5) Kovaleva, E. G.; Lipscomb, J. D. Crystal Structures of Fe2+ Dioxygenase Superoxo, Alkylperoxo, and Bound Product Intermediates. *Science (80-.).* **2007**, *316* (5823), 453–457.

(6) Mbughuni, M. M.; Chakrabarti, M.; Hayden, J. A.; Meier, K. K.; Dalluge, J. J.; Hendrich, M. P.; Münck, E.; Lipscomb, J. D. Oxy Intermediates of Homoprotocatechuate 2,3-Dioxygenase: Facile Electron Transfer between Substrates. *Biochemistry* **2011**, *50* (47), 10262–10274.

(7) Liu, W.; Groves, J. T. Manganese Catalyzed C-H Halogenation. *Acc. Chem. Res.* **2015**, *48* (6), 1727–1735.

(8) Shook, R. L.; Peterson, S. M.; Greaves, J.; Moore, C.; Rheingold, A. L.; Borovik, A. S. Catalytic Reduction of Dioxygen to Water with a Monomeric Manganese Complex at Room Temperature. *J. Am. Chem. Soc.* **2011**, *133* (15), 5810–5817.

(9) Christian R. Goldsmith; Adam P. Cole, and; Stack*, T. D. P. C−H Activation by a Mononuclear Manganese(III) Hydroxide Complex: Synthesis and Characterization of a Manganese-Lipoxygenase Mimic? *J. Am. Chem. Soc.* **2005**, *127* (27), 9904–9912.

(10) Murphy, A.; Stack, T. D. P. Discovery and Optimization of Rapid Manganese Catalysts for the Epoxidation of Terminal Olefins. *J. Mol. Catal. A Chem.* **2006**, *251* (1–2), 78–88.

(11) Cox, N.; Pantazis, D. A.; Neese, F.; Lubitz, W. Biological Water Oxidation. *Acc. Chem. Res.* **2013**, *46* (7), 1588–1596.

(12) Paul, S.; Neese, F.; Pantazis, D. A. Structural Models of the Biological Oxygen-Evolving Complex: Achievements, Insights, and Challenges for Biomimicry. *Green Chem.* **2017**, *19* (10), 2309–2325.

(13) Suga, M.; Akita, F.; Hirata, K.; Ueno, G.; Murakami, H.; Nakajima, Y.; Shimizu, T.; Yamashita, K.; Yamamoto, M.; Ago, H.; et al. Native Structure of Photosystem II at 1.95A° Resolution Viewed by Femtosecond X-Ray Pulses. *Nature* **2015**, *517* (7532), 99–103.

(14) Gilbert, N. C.; Bartlett, S. G.; Waight, M. T.; Neau, D. B.; Boeglin, W. E.; Brash, A. R.; Newcomer, M. E. The Structure of Human 5-Lipoxygenase. *Science.* **2011**, *331* (6014), 217–219.

(15) Sheng, Y.; Gralla, E. B.; Schumacher, M.; Cascio, D.; Cabelli, D. E.; Valentine, J. S. Six-Coordinate Manganese(3+) in Catalysis by Yeast Manganese Superoxide Dismutase. *Proc.*

Natl. Acad. Sci. U. S. A. **2012**, *109* (36), 14314–14319.

(16) Wu, A. J.; Penner-Hahn, J. E.; Pecoraro, V. L. Structural, Spectroscopic, and Reactivity Models for the Manganese Catalases. *Chem. Rev.* **2004**, *104* (2), 903–938.

(17) Gunderson, W. A.; Zatsman, A. I.; Emerson, J. P.; Farquhar, E. R.; Que, L.; Jr.; Lipscomb, J. D.; Hendrich, M. P. Electron Paramagnetic Resonance Detection of Intermediates in the Enzymatic Cycle of an Extradiol Dioxygenase. *J. Am. Chem. Soc.* **2008**, *130* (44), 14465.

(18) Hamberg, M.; Chao, S.; Oliw, E. Manganese Lipoxygenase. *J. Biol. Chem.* **1998**, *273* (21), 13080–13088.

(19) Coggins, M. K.; Martin-Diaconescu, V.; Debeer, S.; Kovacs, J. A. Correlation between Structural, Spectroscopic, and Reactivity Properties within a Series of Structurally Analogous Metastable Manganese(III)-Alkylperoxo Complexes. *J. Am. Chem. Soc.* **2013**, *135* (11), 4260–4272.

(20) Geiger, R. A.; Wijeratne, G. B.; Day, V. W.; Jackson, T. A. Steric and Electronic Influences on the Structures of Peroxomanganese(III) Complexes Supported by Tetradentate Ligands. *Eur. J. Inorg. Chem.* **2012**, *2012* (10), 1598–1608.

(21) Geiger, R. A.; Chattopadhyay, S.; Day, V. W.; Jackson, T. A. A Series of Peroxomanganese(III) Complexes Supported by Tetradentate Aminopyridyl Ligands: Detailed Spectroscopic and Computational Studies. *J. Am. Chem. Soc.* **2010**, *132* (8), 2821–2831.

(22) Geiger, R. A.; Leto, D. F.; Chattopadhyay, S.; Dorlet, P.; Anxolabéhère-Mallart, E.; Jackson, T. A. Geometric and Electronic Structures of Peroxomanganese(III) Complexes Supported by Pentadentate Amino-Pyridine and -Imidazole Ligands. *Inorg. Chem.* **2011**, *50* (20),

10190–10203.

(23) Coggins, M. K.; Kovacs, J. A. Structural and Spectroscopic Characterization of Metastable Thiolate-Ligated Manganese(III)-Alkylperoxo Species. *J. Am. Chem. Soc.* **2011**, *133* (9), 12470–12473.

(24) Coggins, M. K.; Sun, X.; Kwak, Y.; Solomon, E. I.; Rybak-Akimova, E.; Kovacs, J. A. Characterization of Metastable Intermediates Formed in the Reaction between a Mn(II) Complex and Dioxygen, Including a Crystallographic Structure of a Binuclear Mn(III)−Peroxo Species. *J. Am. Chem. Soc.* **2013**, *135*, 5631–5640.

(25) Poon, P. C. Y.; Dedushko, M.; Sun, X.; Yang, G.; Toledo, S.; Hayes, E. C.; Johansen, A.; Rees, J. A.; Stoll, S.; Rybak-Akimova, E.; et al. How Metal Ion Lewis Acidity and Steric Properties Influence the Barrier to Dioxygen Binding, Peroxo O-O Bond Cleavage, and Reactivity. *J. Am. Chem. Soc.* **2019**, *141*, 15046–15057.

(26) Kovacs, J. A. Tuning the Relative Stability and Reactivity of Manganese Dioxygen and Peroxo Intermediates via Systematic Ligand Modification. *Acc. Chem. Res.* **2015**, *48* (10), 2744–2753.

(27) Borovik, A. S. Bioinspired Hydrogen Bond Motifs in Ligand Design: The Role of Noncovalent Interactions in Metal Ion Mediated Activation of Dioxygen. *Acc. Chem. Res.* **2005**, *38* (1), 54–61.

(28) Stone, K. L.; Borovik, A. S. Lessons from Nature: Unraveling Biological C–H Bond Activation. *Curr. Opin. Chem. Biol.* **2009**, *13* (1), 114–118.

(29) Shook, R. L.; Gunderson, W. A.; Greaves, J.; Ziller, J. W.; Hendrich, M. P.; Borovik, A. S. A

Monomeric MnIII-Peroxo Complex Derived Directly from Dioxygen. *J. Am. Chem. Soc.* **2008**, *130* (28), 8888–8889.

(30) Parham, J. D.; Wijeratne, G. B.; Rice, D. B.; Jackson, T. A. Spectroscopic and Structural Characterization of Mn(III)-Alkylperoxo Complexes Supported by Pentadentate Amide-Containing Ligands. *Inorg. Chem.* **2018**, *57* (5), 2489–2502.

(31) Downing, A. N.; Coggins, M. K.; Chaau Yan Poon, P.; Kovacs, J. A. Influence of Thiolate versus Alkoxide Ligands on the Stability of Crystallographically Characterized Mn(III)-Alkylperoxo Complexes. *J. Am. Chem. Soc.* **2021**, *143* (16), 6104–6113.

(32) Coggins, M. K.; Toledo, S.; Shaffer, E.; Kaminsky, W.; Shearer, J.; Kovacs, J. A. Characterization and Dioxygen Reactivity of a New Series of Coordinatively Unsaturated Thiolate-Ligated Manganese(II) Complexes. *Inorg. Chem.* **2012**, *51* (12), 6633–6644.

(33) Coggins, M. K. Small Molecule Activation Studies Involving Thiolate-Ligated Manganese(II) Complexes and Biologically-Relevant Oxidants, Univeristy of Washington, Seattle, 2012.

(34) Kennepohl, P.; Neese, F.; Schweltzer, D.; Jackson, H. L.; Kovacs, J. A.; Solomon, E. I. Spectroscopy of Non-Heme Iron Thiolate Complexes: Insight into the Electronic Structure of the Low-Spin Active Site of Nitrile Hydratase. *Inorg. Chem.* **2005**, *44* (6), 1826–1836.

(35) Kovacs, J. A.; Brines, L. M. Understanding How the Thiolate Sulfur Contributes to the Function of the Non-Heme Iron Enzyme Superoxide Reductase. *Acc. Chem. Res.* **2007**, *40* (7), 501–509.

(36) Coggins, M. K.; Kovacs, J. A. Structural and Spectroscopic Characterization of Metastable Thiolate-Ligated Manganese(III)-Alkylperoxo Species. *J. Am. Chem. Soc.* **2011**, *133* (32),

12470–12473.

(37) Shannon, R. D. Revised Effective Ionic Radii and Systematic Studies of Interatomie Distances in Halides and Chaleogenides. *Acta Crystallogr. Sect. A* **1976**, *32*, 751–767.

(38) Annaraj, J.; Cho, J.; Lee, Y.-M.; Kim, S. Y.; Latifi, R.; de Visser, S. P.; Nam, W. Structural Characterization and Remarkable Axial Ligand Effect on the Nucleophilic Reactivity of a Nonheme Manganese(III)-Peroxo Complex. *Angew. Chemie Int. Ed.* **2009**, *48* (23), 4150–4153.

(39) Vanatta, R. B.; Strouse, C. E.; Hanson, L. K.; Valentine, J. S. [Peroxotetraphenylporphinato]Manganese(III) and [Chlorotetraphenylporphinato]Manganese(II) Anions: Syntheses, Crystal Structures, and Electronic Structures. *J. Am. Chem. Soc.* **1987**, *109* (5), 1425–1434.

(40) Kitajima, N.; Komatsuzaki, H.; Hikichi, S.; Osawa, M.; Moro-oka, Y. A Monomeric Side-On Peroxo Manganese(III) Complex: Mn(O2)(3,5-IPr2pzH)(HB(3,5-IPr2pz)3). *J. Am. Chem. Soc.* **1994**, *116* (25), 11596–11597.

(41) Singh, U. P.; Sharma, A. K.; Hikichi, S.; Komatsuzaki, H.; Moro-Oka B, Y.; Akita, M. Hydrogen Bonding Interaction between Imidazolyl N-H Group and Peroxide: Stabilization of Mn(III)-Peroxo Complex Tp IPr2 Mn(g 2-O 2)(Im Me H) (Im Me H = 2-Methylimidazole) Q. *Inorganica Chim. Acta* **2006**, *359*, 4407–4411.

(42) Kim, J.; Zang, Y.; Costas, M.; Harrison, R. G.; Wilkinson, E. C.; Que, L. A Nonheme Iron(II) Complex That Models the Redox Cycle of Lipoxygenase. *J. Biol. Inorg. Chem.* **2001**, *6* (3), 275–284.

(43) Coggins, M. K.; Downing, A. N.; Kaminsky, W.; Kovacs, J. A. Comparison of Two Mn IV Mn IV -Bis-μ-Oxo Complexes {[Mn IV (N 4 (6-Me-DPEN))] 2 (μ-O) 2 } 2+ and {[Mn IV (N 4 (6-Me-DPPN))] 2 (μ-O) 2 } 2+. *Acta Crystallogr. Sect. E Crystallogr. Commun.* **2020**, *76* (7), 1042–1046.

(44) Coggins, M. K.; Downing, A. N.; Kaminsky, W.; Kovacs, J. A. Comparison of Two Mn ^{IV} Mn ^{IV} -Bis-μ-Oxo Complexes {[Mn ^{IV} (N $_4$ (6-Me-DPEN))] $_2$ (μ-O) $_2$ } $^{2+}$ and {[Mn ^{IV} (N $_4$ (6-Me-DPPN))] $_2$ (μ-O) $_2$ } $^{2+}$. *Acta Crystallogr. Sect. E Crystallogr. Commun.* **2020**, *76* (7), 1042–1046.

(45) Coggins, M. K.; Sun, X.; Kwak, Y.; Solomon, E. I.; Rybak-Akimova, E.; Kovacs, J. A. Characterization of Metastable Intermediates Formed in the Reaction between a Mn(II) Complex and Dioxygen, Including a Crystallographic Structure of a Binuclear Mn(III)-Peroxo Species. *J. Am. Chem. Soc.* **2013**, *135* (15), 5631–5640.

(46) Badger, R. M. The Relation between the Internuclear Distances and Force Constants of Molecules and Its Application to Polyatomic Molecules. *J. Chem. Phys.* **1935**, *3* (11), 710–714.

(47) Green, M. T. Application of Badger's Rule to Heme and Non-Heme Iron-Oxygen Bonds: An Examination of Ferryl Protonation States. *J. Am. Chem. Soc.* **2006**, *128* (6), 1902–1906.

(48) Neese, F. The ORCA Program System. *Wiley Interdiscip. Rev. Comput. Mol. Sci.* **2012**, *2* (1), 73–78.

(49) Grimme, S.; Ehrlich, S.; Goerigk, L. Effect of the Damping Function in Dispersion Corrected Density Functional Theory. *J. Comput. Chem.* **2011**, *32* (7), 1456–1465.

(50) Adamo, C.; Barone, V. Toward Reliable Density Functional Methods without Adjustable Parameters: The PBE0 Model. *J. Chem. Phys.* **1999**, *110* (13), 6158–6170.

(51) Neese, F.; Wennmohs, F.; Hansen, A. Efficient and Accurate Local Approximations to Coupled-Electron Pair Approaches: An Attempt to Revive the Pair Natural Orbital Method. *J. Chem. Phys.* **2009**, *130* (11), 114108–114018.

(52) Hirata, S.; Head-Gordon, M. *Time-Dependent Density Functional Theory within the Tamm-Dancoff Approximation*; 1999; Vol. 314.

(53) Neese, F.; Olbrich, G. Efficient Use of the Resolution of the Identity Approximation in Time-Dependent Density Functional Calculations with Hybrid Density Functionals. *Chem. Phys. Lett.* **2002**, *362*, 170–178.

(54) Chemcraft - Graphical Program for Visualization of Quantum Chemistry Computations. Ivanovo, Russia 2005.

(55) Coggins, M. K.; Martin-Diaconescu, V.; DeBeer, S.; Kovacs, J. A. Correlation Between Structural, Spectroscopic, and Reactivity Properties Within a Series of Structurally Analogous Metastable Manganese(III)−Alkylperoxo Complexes. *J. Am. Chem. Soc.* **2013**, *135*, 4260–4272.

VITA

Alexandra Nicole Downing completed her Bachelor's of Science in Chemistry at the University of Puget Sound in 2016, with a minor in Spanish. During undergraduate research, she explored the synthesis of potential metallo-hydrogelator molecules with Professor Jo Crane. Upon starting the graduate program in Chemistry at the University of Washington in 2016, she joined the Kovacs research lab investigating the reactivity of thiolate-ligated biomimetic transition metal complexes under the guidance of Professor Julie Kovacs.